TLM

Silicon Drift Detector R&D for a keV Sterile Neutrino Search at KATRIN

Korbinian Urban

Vollständiger Abdruck der von der TUM School of Natural Sciences der Technischen Universität München zur Erlangung des akademischen Grades eines

Doktors der Naturwissenschaften (Dr. rer. nat.)

genehmigten Dissertation.

Vorsitz:
    Prof. Dr. Frank Pollmann

Prüfende der Dissertation:
    1. Prof. Dr. Susanne Mertens
    2. Prof. Dr. Lothar Oberauer

Die Dissertation wurde am 08.10.2024 bei der Technischen Universität München eingereicht und durch die TUM School of Natural Sciences am 02.12.2024 angenommen.

Abstract

Neutrinos are fundamental constituents of the Standard Model of particle physics. However, their non-zero mass remains unknown and proves the existence of physics beyond the standard model. A minimal extension of the standard model is the inclusion of sterile neutrinos, which could explain the neutrino mass and, if their mass is in the keV range, serve as a viable dark matter candidate. Sterile neutrinos could leave a subtle imprint in the electron spectra of β-decay through the mixing with active neutrinos. In this way, there is a potential avenue for detecting sterile neutrinos through laboratory experiments.

The TRISTAN project within the KATRIN experiment is dedicated to searching for the signature of keV-scale sterile neutrinos in the electron spectrum of tritium β-decay. In this context, the KATRIN beamline will be equipped with a novel detector system designed for high-rate electron spectroscopy. The detector system targets a total event rate of 10^8 counts per second and an energy resolution of 300 eV FWHM for 20 keV electrons. To overcome these challenging requirements, the TRISTAN detector exploits the silicon drift detector (SDD) technology, implemented as a multi-pixel focal plane array.

Detecting the signature of a sterile neutrino demands a precise understanding of all systematic effects that could influence the measured spectral shape. This work consists of five main parts: In the first part, a simplified sensitivity study of a keV-scale sterile neutrino search using KATRIN and the TRISTAN detector is performed. The study shows the influence of basic detector-related systematic effects, like detector calibration and energy resolution, on the sterile neutrino sensitivity. In the second part, a detailed simulation framework for the SDD signals and a model for the electronic noise components are introduced. These simulations help to understand the complex processes of the charge drift and signal formation in the TRISTAN SDD detector. The third part focuses on the development of dedicated calibration tools, which are essential for a comprehensive experimental characterization of the detector. One highlight is the development of a thermionic electron gun tailored explicitly to the TRISTAN detector characterization. The fourth part of this thesis describes a detailed characterization of the SDD system, including three main aspects: 1) General detector performance measurements are shown, including studies of the pulse shape and the noise performance. These measurements confirm the validity of the previously developed simulations and models. 2) The effect of crosstalk between pixels is addressed. Based on a thorough investigation of the underlying mechanisms, the crosstalk effect was significantly mitigated within an iterative refinement of the SDD readout design. 3) A model for the effect of charge sharing at the pixel borders is developed and supported by a measurement. The final part of this work involves simulating and specifying the DAQ system for the TRISTAN detector. The treatment of pileup in the digital pulse-height analysis plays a crucial role in the shape of the final spectrum. A strategy for the treatment of pileup is presented, and its impact on the spectral shape is studied with a detailed trace-level Monte Carlo simulation.

In conclusion, this work comprises detailed detector simulations and characterizations, as well as the development of calibration tools and a data acquisition system essential for the realization of the TRISTAN project.

Zusammenfassung

Neutrinos sind ein grundlegender Bestandteil des Standardmodells der Teilchenphysik. Ihre Masse ist allerdings noch immer unbekannt und beweist die Existenz von Physik jenseits des Standardmodells. Eine minimale Erweiterung des Standardmodells ist die Einführung von sterilen Neutrinos, welche die Neutrinomasse erklären und, falls sie eine Masses im keV Bereich haben, auch als Kandidat für dunkle Materie dienen könnten. Sterile Neutrinos könnten durch die Mischung mit aktiven Neutrinos einen winzigen Fußabdruck in den Elektronenspektren des β-Zerfalls hinterlassen. Auf diese Weise besteht die Möglichkeit, sterile Neutrinos in Experimenten nachzuweisen.

Das TRISTAN-Projekt im Rahmen des KATRIN-Experiments hat zum Ziel, im Elektronenspektrum des Tritium-β-Zerfalls nach der Signatur von sterilen Neutrinos im keV-Bereich zu suchen. Dazu wird die KATRIN-Beamline mit einem neuartigen Detektorsystem für Elektronenspektroskopie bei hoher Rate ausgestattet. Das Detektorsystem strebt eine Zählrate von 10^8 Elektronen pro Sekunde und eine Energieauflösung von 300 eV FWHM für 20 keV Elektronen an. Um diese anspruchsvollen Anforderungen zu erfüllen, nutzt der TRISTAN-Detektor die Silizium-Drift-Detektor-Technologie (SDD), umgesetzt als großflächiges Detektor-Array mit vielen Pixeln.

Die Erkennung der Signatur eines sterilen Neutrinos erfordert ein genaues Verständnis aller systematischen Effekte, die die gemessene Spektralform beeinflussen könnten. Diese Arbeit besteht aus fünf Hauptteilen: Im ersten Teil wird eine vereinfachte Sensitivitätsstudie für die Suche nach sterilen Neutrinos im keV-Bereich mit KATRIN und dem TRISTAN-Detektor durchgeführt. Die Studie zeigt den Einfluss grundlegender detektorbezogener systematischer Effekte, wie Detektorkalibrierung und Energieauflösung, auf die Sensitivität für sterile Neutrinos. Im zweiten Teil werden detaillierte Simulationen für die SDD-Signale und ein Modell für die elektronischen Rauschkomponenten vorgestellt. Diese Simulationen helfen, die komplexen Prozesse des Ladungsdrifts und der Signalbildung im TRISTAN SDD-Detektor zu verstehen. Der dritte Teil konzentriert sich auf die Entwicklung spezieller Kalibrationswerkzeuge, die für eine umfassende experimentelle Charakterisierung des Detektors entscheidend sind. Ein Highlight ist die Entwicklung einer Elektronenkanone, die speziell auf die Charakterisierung des TRISTAN-Detektors zugeschnitten ist. Der vierte Teil dieser Arbeit beschreibt eine detaillierte Charakterisierung des SDD-Systems, die wiederum drei Aspekte umfasst: 1) Es werden allgemeine Messungen der Detektorperformance gezeigt, einschließlich Untersuchungen der Pulsform und des Rauschverhaltens. Diese Messungen bestätigen die Gültigkeit der zuvor entwickelten Simulationen und Modelle. 2) Die Auswirkung des Übersprechens zwischen den Pixeln wird behandelt. Mit Hilfe einer Analyse der zugrundeliegenden Mechanismen konnte dieser Effekt im Rahmen einer schrittweisen Optimierung des SDD-Auslesedesigns deutlich abgeschwächt werden. 3) Es wird ein Modell für den Charge-Sharing-Effekt an den Pixelgrenzen entwickelt und durch eine Messung untermauert. Der letzte Teil dieser Arbeit umfasst die Simulation und Spezifikation des DAQ-Systems für den TRISTAN-Detektor. Vor allem die Behandlung von Pileup in der digitalen Pulshöhenanalyse spielt eine entscheidende Rolle für die Form des endgültigen Spektrums. Es wird eine Strategie für die Behandlung von Pileup vorgestellt, und die Auswirkungen auf die Form des Spektrums werden mit einer detaillierten Monte-Carlo-Simulation untersucht.

Insgesamt umfasst diese Arbeit detaillierte Detektorsimulationen und -charakterisierungen sowie die Entwicklung von Kalibrierungswerkzeugen und des Datenerfassungssystems, die entscheidend zur Realisierung des TRISTAN-Projekts beitragen.

Contents

Contents

1 Neutrino physics

The Standard Model of particle physics describes all known elementary particles and their interactions with great precision. The first two sections 1.1 and 1.2 briefly introduce the unique role of neutrinos in the standard model. Sterile neutrinos, a minimal but fruitful extension of the standard model, are described in section 1.3. Sterile neutrinos with a keV mass are a viable dark matter candidate, as presented in section 1.4. Finally, section 1.5 shows how laboratory experiments can search for sterile neutrinos.

1.1 Neutrinos in the Standard Model

Neutrinos are elementary particles described by the standard model (SM) of particle physics. An overview of all 17 elementary particles is shown in figure 1.1. The three main interactions (electromagnetism, strong interaction, and weak interaction) are described in the SM by the coupling of fermions (quarks and leptons) to gauge bosons (photon, gluon, W/Z boson, respectively) [1].

The fermions do not couple to all gauge bosons equally, but the interaction depends on the quantum numbers involved. Three categories are found: Quarks participate in all three fundamental interactions, charged leptons (electron, muon, and tau) participate in electromagnetic and weak interaction, and the three neutrinos ν_e, ν_μ, and ν_τ are the only fermions interacting solely via the weak interaction.

The quantum field theoretic description of fermions distinguishes four different states for each fermion: The particle can either be a particle or antiparticle, and it can be right-handed or left-handed. The strong and electromagnetic interactions behave the same if the handedness is flipped (parity) or all particles are exchanged by their antiparticles (charge conjugation). The weak interaction, however, was found experimentally to violate parity [2, 3]. Actually, the weak interaction turns out to have maximal parity violation, meaning that the interaction only involves left-handed particles or right-handed antiparticles.

A right-handed neutrino does not participate in any SM interactions and is thus not considered a physical particle. A consequence of the missing right-handed neutrino is that the Higgs mechanism, which is responsible for all known fermion masses, cannot be applied to the neutrino. Therefore, neutrinos are considered massless in the SM [4]. Finally, the concept of a Majorana particle becomes possible for neutrinos, in which case the neutrinos would be its own antiparticle.
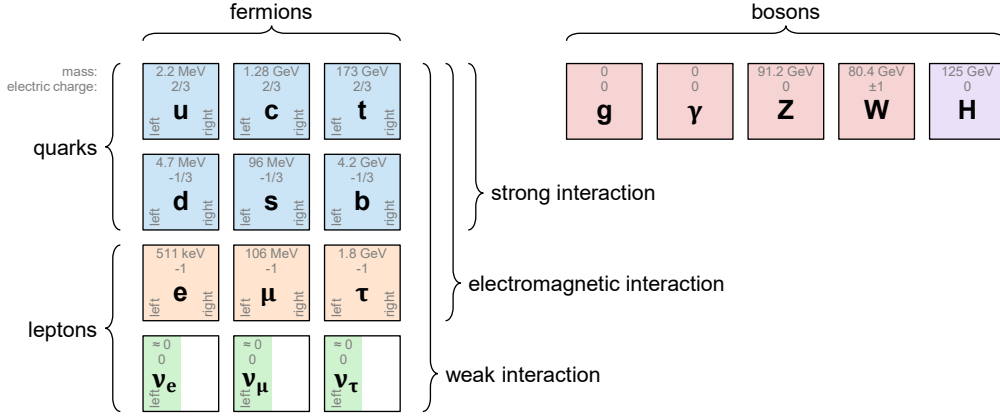
Figure 1.1: Elementary particles in the standard model (SM) of particle physics. The figure stresses that the three neutrinos are the only fermions in the SM, which appears solely left-handed. Values from [5].

1.2 The mystery of the neutrino mass

Although the SM prefers neutrinos to be massless, the observation of neutrino oscillations proves the opposite. The discovery of the non-zero neutrino mass started with a deficit in detected solar neutrino flux in the Homestake experiment in the late 1960s [6, 7]. Compared to the theoretical prediction, fewer neutrinos were observed. This disagreement, known as the solar neutrino problem, was later confirmed by other solar neutrino experiments.

The solar neutrino problem can be explained if the three flavor eigenstates $|\nu_e\rangle$, $|\nu_\mu\rangle$ and $|\nu_\tau\rangle$ are a non-trivial superposition of three mass eigenstates $|\nu_1\rangle$, $|\nu_2\rangle$ and $|\nu_3\rangle$. The mixing of flavor and mass eigenstates is described by the Pontecorvo-Maki-Nakagawa-Sakata (PMNS) matrix

$$\begin{pmatrix} |\nu_e\rangle \\ |\nu_\mu\rangle \\ |\nu_\tau\rangle \end{pmatrix} = \begin{pmatrix} U_{e1} & U_{e2} & U_{e3} \\ U_{\mu1} & U_{\mu2} & U_{\mu3} \\ U_{\tau1} & U_{\tau2} & U_{\tau3} \end{pmatrix} \begin{pmatrix} |\nu_1\rangle \\ |\nu_2\rangle \\ |\nu_3\rangle \end{pmatrix}. \tag{1.1}$$

Thanks to the mixing, neutrinos can change their flavor during propagation [8]. In 2001, the SNO experiment finally proved that the missing solar ν_e flux corresponds to an appearing ν_μ flux [9]. Other experiments like KamLAND [10] and Super-Kamiokande [11] measured flavor conversion also for neutrinos originating from reactors and the atmosphere and finally confirmed the effect of neutrino oscillation. These measurements imply a non-zero squared mass difference $\Delta m_{ij}^2 = m_i^2 - m_j^2$ between the neutrino mass eigenstates $|\nu_i\rangle$. Figure 1.2 illustrates the relation between the three neutrino masses. The oscillation experiments constrain the mass of the heaviest of the three neutrinos to at least $\approx 50\,\text{meV}$. This lower limit is more than seven orders of magnitudes lighter than the mass of the electron with $m_e = 511\,\text{keV}$, which is the lightest charged lepton.

There are many theoretical approaches introducing neutrino masses. However, they all require new physics beyond the SM [14, 15]. All charged fermions in the SM obtain their mass via the Higgs mechanism, which couples a right-handed fermion state to a left-handed one. Such a Dirac mass term, if applied to the neutrino, requires a right-handed (and thus sterile) neutrino. Furthermore, an unnatural small coupling constant is required to explain the lightness of neutrinos.

$$\Delta m_{21}^2 \approx 7.4 \cdot 10^{-5} \text{ eV}^2$$
$$\Delta m_{32}^2 \approx 2.5 \cdot 10^{-3} \text{ eV}^2$$
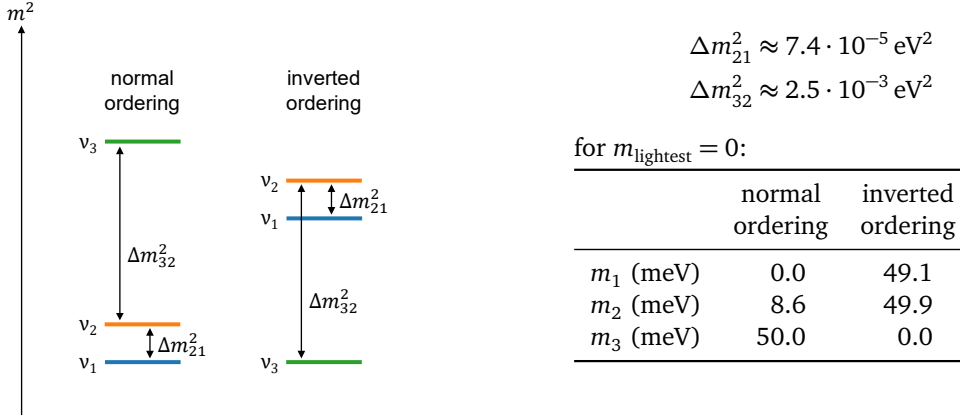
for $m_{\text{lightest}} = 0$:

	normal ordering	inverted ordering
m_1 (meV)	0.0	49.1
m_2 (meV)	8.6	49.9
m_3 (meV)	50.0	0.0

Figure 1.2: Neutrino mass differences as obtained from a global analysis of oscillation experiments (from NuFIT 5.3 [12, 13]). The uncertainty is less than 3 % for all stated values.

A central question regarding neutrino masses is whether neutrinos are of Majorana nature or not. Majorana's theory states that there is no fundamental difference between neutrinos and antineutrinos except for their handedness. Assuming the Majorana nature, additional Lorenz-invariant terms in the neutrino Lagrangian become possible, referred to as Majorana mass terms [15]. These mass terms directly couple, for instance, a left-handed neutrino field to a right-handed antineutrino field [16]. A major implication of Majorana mass terms is that they introduce a lepton number violation. Thus, lepton number violating processes would be allowed, like the neutrinoless double β-decay.

Both the Dirac and Majorana mass terms can, in general, have arbitrary mass. For the Dirac mass term, however, it is natural to expect a mass on the same scale as the known masses of charged fermions (511 keV to 173 GeV) [15]. The famous seesaw mechanism combines a Dirac mass term with mass m_D and a Majorana mass term of a right-handed neutrino of mass M, assuming $M \gg m_D$. If constructed appropriately, the result is an effective neutrino mass [16]

$$m_{\text{eff}} = \frac{m_D^2}{M} \ll m_D. \tag{1.2}$$

The name seesaw reflects the fact that a heavier M corresponds to a lighter mass m_{eff}. The seesaw mechanism could elegantly explain the lightness of the known neutrino. Besides the described seesaw mechanism of type 1, there are more types of seesaw mechanisms and other approaches to introduce the very light neutrino masses [15]. In most theories, right-handed neutrinos are introduced with varying mass ranges.

Searches for the absolute neutrino mass   Neutrino oscillation experiments started the neutrino mass puzzle by proofing their non-zero mass. However, the absolute value of the mass cannot be probed by oscillation experiments and remains unknown to this day. Three different approaches allow to constrain the neutrino mass by a measurement: 1) cosmological observations, 2) search for neutrinoless double β-decay, and 3) direct measurements based on the kinematics of β-decay.

   1. **Cosmology** Today, the universe is filled with around 340 neutrinos per cm^3, which are relics from the Big Bang. The relic neutrinos were relativistic at early times in the universe and turned non-relativistic later. The temperature of the relic neutrinos corresponds to around 0.2 meV today, and at least two out of the three neutrino mass eigenstates are

non-relativistic [5]. The time of the transition to non-relativistic particles depends on the mass of the neutrinos. The sum of the neutrino masses

$$\sum m_\nu := \sum_{i=1,2,3} m_i \,, \tag{1.3}$$

therefore, has two main implications on cosmological observables. First, as relativistic neutrinos do not cluster gravitationally, m_ν influences the large-scale structure formation of the universe. Second, the transition from radiation-like to matter-like mass density of neutrinos influences the evolution of the scale parameter $a(t)$ of the universe [17, 18, 19]. Based on the precision measurement of the cosmic microwave background, the Planck collaboration in 2018 provided an upper limit $\sum m_\nu < 0.26\,\text{eV}$ at 95 % CL [20]. Depending on which data is included and on the details of the underlying ΛCDM model, the limit can change from around $\sum m_\nu < 0.09\,\text{to}\,0.54\,\text{eV}$ [5]. Another limit was recently published by the DESI collaboration (in combination with Planck), which measures the angular scale of the baryonic acoustic oscillations by a spectroscopic measurement of millions of extra-galactic objects [21]. With $\sum m_\nu < 0.072\,\text{eV}$ their result approaches the minimal allowed value from oscillation experiments $\sum m_\nu > 0.059\,\text{eV}$ (see figure 1.2).

2. **Search for neutrinoless double β-decay** The double β-decay ($2\nu\beta\beta$) can be observed in several isotopes where the single β-decay is energetically forbidden, e.g. ^{76}Ge or ^{136}Xe. While $2\nu\beta\beta$ produces two neutrinos, the neutrinoless double beta decay ($0\nu\beta\beta$) describes the case where no neutrino is emitted. $0\nu\beta\beta$ is not allowed in the SM and was not observed experimentally until today. Its observation would have implications on the neutrino: The neutrino would be required to be of Majorana nature and to have a non-zero effective Majorana mass [22, 23]

$$m_{\beta\beta} = \left| \sum_i U_{ei}^2 m_i \right| \,. \tag{1.4}$$

Consequently, the non-observation of $0\nu\beta\beta$ gives an upper limit on $m_{\beta\beta}$. The leading limits of the half-life of $0\nu\beta\beta$ come from ^{76}Ge (e.g. GERDA, LEGEND, MAJORANA) and ^{136}Xe (e.g. KamLAND-Zen) with values $T_{1/2}^{0\nu} > 10^{26}\,\text{yr}$ [24, 25, 26]. The corresponding limits on the neutrino mass are $m_{\beta\beta} < 79\,\text{to}\,180\,\text{meV}$ for ^{76}Ge [27] and $m_{\beta\beta} < 28\,\text{to}\,122\,\text{meV}$ for ^{136}Xe [25]. All limits are at 90 % confidence level (CL). The spread of the $m_{\beta\beta}$ limits reflect the limited knowledge of the nuclear matrix elements, which are necessary for calculating $m_{\beta\beta}$ from $T_{1/2}^{0\nu}$.

3. **Direct measurement by kinematics** The third and most direct way to measure the absolute neutrino mass is the investigation of the kinematics of processes involving neutrinos [28, 29]. For example, the time-of-flight measurement of neutrinos of supernova SN 1987A puts a limit $m_{\bar{\nu}_e} < 5.7\,\text{eV}$ (90 % CL) [30]. Another option is the study of weak decays, which have a neutrino in the final state. The most stringent limit on the absolute neutrino mass comes from measuring the electron spectrum of tritium β^- decay

$$^3\text{H} \to {}^3\text{He} + e + \bar{\nu}_e \,. \tag{1.5}$$

In the decay, the total available kinetic energy (neglecting the small nuclear recoil energy) is shared between the electron e and the neutrino $\bar{\nu}_e$. Following the Fermi theory, the resulting

spectral distribution $\frac{d\Gamma}{dE}$ of the kinetic energy of the electron E is

$$\frac{d\Gamma}{dE} = C \cdot F_C(E) \cdot \underbrace{\sqrt{(E+m_e)^2 - m_e^2}}_{p_e} \cdot \underbrace{(E+m_e)}_{E_e^{\text{tot}}} \cdot \underbrace{\sqrt{(E_0-E)^2 - m_\nu^2}}_{p_\nu} \cdot \underbrace{(E_0-E)}_{E_\nu^{\text{tot}}} . \tag{1.6}$$

Here, C is a constant that absorbs the nuclear matrix element and the Fermi function $F_C(E)$ accounts for the electromagnetic interaction of the outgoing electron with the daughter nucleus. Furthermore, the endpoint energy E_0 is the maximal possible electron energy in case $m_\nu = 0$. The underbraced factors in equation 1.6 originate from the phase-space density of the electron and the neutrino and entail their momentum p and total energy E^{tot}, respectively [29]. The neutrino mass m_ν directly enters into p_ν and changes the spectral shape close to the endpoint where $E_0 - E$ is almost zero. Equation 1.6 considers a single neutrino mass m_ν for simplicity. The actual tritium β-decay spectrum is the superposition of three spectral contributions corresponding to the three neutrino mass eigenstates. Further details on calculating the differential tritium spectrum can be found in [28].

The leading experimental effort to constrain m_ν via β-decay is the KATRIN (KArlsruhe TRItium Neutrino) experiment. KATRIN measures the spectral shape of the tritium β-decay utilizing an electromagnetic spectrometer of MAC-E type (Magnetic Adiabatic Collimation combined with an Electrostatic filter). Its latest result states that the measured spectrum is compatible with a neutrino mass of zero. The deducted upper limit on the effective electron antineutrino mass

$$m_\beta = \sqrt{\sum_i |U_{ei}|^2 \cdot m_i^2} \tag{1.7}$$

is $m_\beta < 0.45\,\text{eV}$ at 90 % CL [31]. KATRIN targets a final sensitivity better than 0.3 eV. To further improve the sensitivity in the future, novel approaches like using atomic tritium and a differential energy measurement are necessary. E.g. the CRES (Cyclotron Radiation Electron Spectroscopy) technology is currently being developed within the PROJECT 8 collaboration [32]. An alternative approach to constrain the neutrino mass by β-decay kinematics is the calorimetric measurement of the electron capture decay of ^{163}Ho. Today, this approach is followed by ECHo [33] and HOLMES [34], with an upper limit of $m_\beta < 28\,\text{eV}$ at 90 % CL [35].

The three above-mentioned methods have complementary observables $\sum m_\nu$, $m_{\beta\beta}$, and m_β. Up to today, none of the approaches has seen evidence for a non-zero neutrino mass, although the experiments are slowly pushing the limits to probe the lower bound from oscillation experiments.

1.3 Sterile neutrinos

Sterile neutrinos are a minimal extension of the standard model. If sterile neutrinos would exist, several open questions in particle physics and cosmology could be addressed. The simplest sterile neutrino scenario extends equation 1.1 by an additional neutrino flavor eigenstate ν_s and mass

eigenstate ν_4 (3+1 scenario). The neutrino mixing from equation 1.1 then becomes:

$$
\begin{pmatrix} |\nu_e\rangle \\ |\nu_\mu\rangle \\ |\nu_\tau\rangle \\ |\nu_s\rangle \end{pmatrix} = \begin{pmatrix} U_{e1} & U_{e2} & U_{e3} & U_{e4} \\ U_{\mu1} & U_{\mu2} & U_{\mu3} & U_{\mu4} \\ U_{\tau1} & U_{\tau2} & U_{\tau3} & U_{\tau4} \\ U_{s1} & U_{s2} & U_{s3} & U_{s4} \end{pmatrix} \begin{pmatrix} |\nu_1\rangle \\ |\nu_2\rangle \\ |\nu_3\rangle \\ |\nu_4\rangle \end{pmatrix}.
\tag{1.8}
$$

ν_s is a sterile neutrino, which does not interact by any SM interaction. A mass eigenstate ν_4 with mass m_4 is introduced along with the sterile flavor eigenstate. The new mass eigenstate ν_4 can mix with the active flavor eigenstates ν_e, ν_μ, ν_τ, similar to the known neutrino mixing. With $\sin^2\theta = |U_{e4}|^2$ [1], the amount of mixing is given by the mixing angle θ. The shown scenario adds two new parameters: The mass m_4 and mixing amplitude $\sin^2\theta$.

The right-handed neutrino, introduced in section 1.2 for providing a neutrino mass mechanism, can be interpreted as sterile neutrino in the picture of 1.8. In this case, m_4 corresponds to the mass eigenstate dominated by the Majorana mass M and one of m_1, m_2 or m_3 corresponds to the light effective mass m_{eff}.

The preferred value of m_4 and $\sin^2\theta$ depends on the motivation for introducing the sterile neutrino. A very heavy mass m_4 is suitable to provide a mechanism for the light active neutrino masses m_1, m_2, and m_3 via the seesaw mechanism [15]. The mass m_4 can be up to 10^{23} GeV, in this case. A sterile neutrino with a light mass m_4 of $\mathcal{O}(1\,\text{eV})$ could explain some anomalies observed in neutrino oscillation experiments. These anomalies encompass the LSND/MiniBooNE anomalies (e.g [36, 37]), the Reactor antineutrino anomaly (e.g. [38]) and the Gallium anomaly (e.g. [39]). The debate about their sterile neutrino interpretation is ongoing, while some anomalies were weakened or became inconsistent with other experiments (e.g. [40, 41]).

In cosmology, a sterile neutrino could also answer fundamental questions. Most notably, with a mass in the keV-range, sterile neutrinos could be the constituents of dark matter [42]. Details about the constraints for sterile neutrino dark matter are described in the next section 1.4.

There can be more than one sterile neutrino. A scenario where three sterile neutrinos (in this context labeled N_1, N_2, and N_3) are introduced is the Neutrino Minimal Standard Model (νMSM) [43, 44]. The νMSM can solve three open questions of physics and cosmology simultaneously: N_1 has a mass in the keV regime, serving as a dark matter candidate. N_2 and N_3 are two heavy sterile neutrinos with masses of around 150 MeV and 100 GeV, which could explain the lightness of the neutrino masses and also provide a mechanism to explain the baryon asymmetry in the universe.

1.4 keV sterile neutrino as dark matter candidate

The fundament of modern cosmology is the ΛCDM model [5]. It describes the evolution of the energy and matter density of the universe from the Big Bang until now and explains cosmological observations with surprising precision. The central ingredients in the ΛCDM model are ordinary (or baryonic) matter, radiation, dark matter, and dark energy. The late universe consists of 70 %

---

[1] In the β-decay context of this work, θ considers solely the mixing from ν_4 to ν_e. In other contexts the mixing angle is often defined as $\sin^2\theta = |U_{e4}|^2 + |U_{\mu4}|^2 + |U_{\tau4}|^2$. Furthermore, in oscillation experiments, $\sin^2 2\theta$ is often given instead of $\sin^2\theta$. For small θ, the conversion is $\sin^2\theta \approx \theta^2 \approx 0.25\sin^2 2\theta$.

dark energy, 25 % dark matter, and only 5 % baryonic matter. Dark matter, in particular, poses a mystery for particle physicists, as its constituents remain unknown. It is certain, however, that the dark matter particles have mass and interact very weakly, if at all, with known particles. There are many dark matter candidates, mainly extensions of the Standard Model, that have been discussed and experimentally investigated for many years, including WIMPs (Weakly Interacting Massive Particles), Axions (named after a brand of cleaning detergent), and sterile neutrinos. So far, no suitable particle has been discovered. The following will briefly examine sterile neutrinos as a dark matter candidate and is mostly based on review literature [5, 45, 42, 46].

Sterile neutrinos[2] fulfill the fundamental requirements of dark matter, as they are massive and almost not interacting. To be a plausible dark matter candidate, however, a production mechanism should also be provided. For sterile neutrinos, the production can be achieved via the mixing amplitude $\sin^2 \theta \ll 1$ between active neutrinos and the sterile mass eigenstate m_4. Sterile neutrinos are best suited for dark matter when their mass is in the keV regime. They are highly relativistic (hot) during their production shortly after the Big Bang. During the expansion of the universe, keV sterile neutrinos soon become non-relativistic (or cold). They are thus counted as warm dark matter (WDM).

WDM is preferred over cold dark matter (CDM) in the context of structure formation in the universe. The "small scale challenges" state that cold dark matter cannot reproduce the structure in the universe on small scales below around 1 Mpc (for comparison: the size of the milky way is around 50 kpc) well. The "small scale challenges" comprise the "missing satellites problem", the "cusp-core problem", and the "too-big-to-fail problem". These challenges could be solved with WDM. However, also other solutions not involving WDM are possible.

The constraints on the mass m_4 and the mixing $\sin^2 \theta$ for sterile neutrino dark matter are pictured in figure 1.3 and summarized in the following:

- **Sterile neutrino decay** A keV sterile neutrino is not stable but decays as drawn in figure 1.4. The lifetime, however, is longer than the age of the universe in most cases. If m_4 is too heavy and the mixing amplitude $\sin^2 \theta$ is too large, the lifetime drops below the age of the universe. In this case, sterile neutrinos cannot be dark matter.
- **X-ray telescopes** A small fraction of sterile neutrino decays emit a photon with $E = \frac{m_4}{2}$ (see 1.4b). Therefore, X-ray telescopes should see an X-ray line from objects with large dark matter density (for example, the Milky Way or galaxy clusters) if sterile neutrinos were dark matter. The non-observation of an X-ray line puts a stringent limit on the parameter space of m_4 and $\sin^2 \theta$.
- **Production mechanism** Sterile neutrinos can be produced thermally in the early universe through oscillation from active neutrinos and scattering-induced decoherence. The Dodelson-Widrow mechanism [49] proposed such a production for the first time in 1994 and thereby attracted attention to sterile neutrinos as a dark matter candidate. This robust mechanism produces a large amount of sterile neutrino during the hot beginning of the universe, depending on m_4 and $\sin^2 \theta$. The right amount of sterile neutrinos for explaining dark matter would be produced along a line in the parameter space, shown in figure 1.3. The parameter space above the line (larger $\sin^2 \theta$) is excluded as it would correspond to an overproduction of sterile neutrinos. The parameter space below the line, on the other hand, requires some enhancement or additional mechanism to produce enough sterile neutrinos. Such an

---

[2]The term sterile neutrino is here used for the additional mass eigenstate.
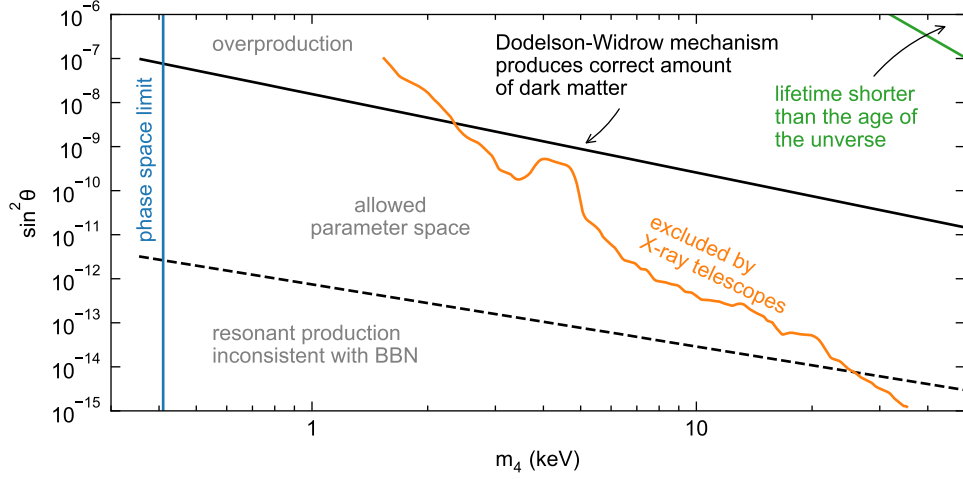
Figure 1.3: Cosmological bounds on keV sterile neutrino dark matter. Sterile neutrinos with low mass $m_s < 0.4\,\text{keV}$ cannot be all dark matter due to the limited phase space density of fermions in galaxies with high dark matter density ([47, 48]). Along the solid black line, the Dodelson-Widrow mechanism [49] would produce the right amount of dark matter [42]. The area above is excluded as too much dark matter would be produced. Below the black dashed line, even the resonant production described in the Shi-Fuller mechanism cannot produce enough sterile neutrinos for dark matter [42]. The X-ray exclusion comes from the non-observation of galactic X-rays from sterile neutrino decay. The line combines three analyses with data from the X-ray satellite Chandra [50], NuStar [51], and XMM-Newton [52].
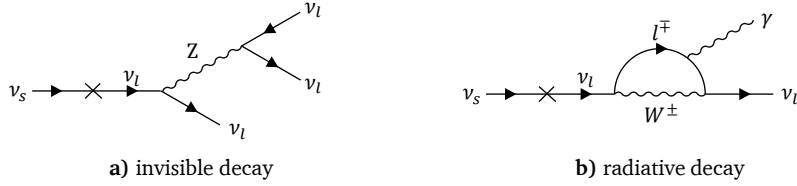

a) invisible decay   **b)** radiative decay

Figure 1.4: Leading Feynman diagrams for sterile neutrino decay. The sterile neutrino mass eigenstate ν_4 couples to the weak gauge bosons W and Z via the mixing amplitude $\sin^2\theta$ to the active neutrino flavor eigenstates ν_l. The invisible decay into three active neutrinos (a) dominates the overall decay rate. The radiative decay into one active neutrino and a photon (b) has a second diagram (not shown), where the photon couples to the W boson.

enhancement is provided by the resonant production of sterile neutrinos proposed by X. Shi and F. Fuller [53], where a lepton number density in the early universe changes the neutrino flavor transition, similar to the MSW effect in the sun. Depending on the lepton number density, the resonant production lowers the required $\sin^2\theta$ by several orders of magnitude. A lower limit for $\sin^2\theta$ arises, where the required lepton asymmetry is not compatible with the big bang nucleosynthesis anymore (BBN).´

- **Phase-space limit** A robust lower bound on the mass of fermionic dark matter particles comes from Pauli's exclusion principle. If the dark matter particle is too light, the dark matter density in dwarf spheroidal galaxies will exceed that of the degenerate Fermi gas [48]. The exact value of this bound depends on the dark matter density model. A conservative limit is $m_s > 0.41\,\text{keV}$ (from [48]).

Following the considerations from above, a mixing amplitude $\sin^2\theta \ll 10^{-7}$ is required for sterile neutrinos to be a reasonable dark matter candidate. When comparing these limits to laboratory
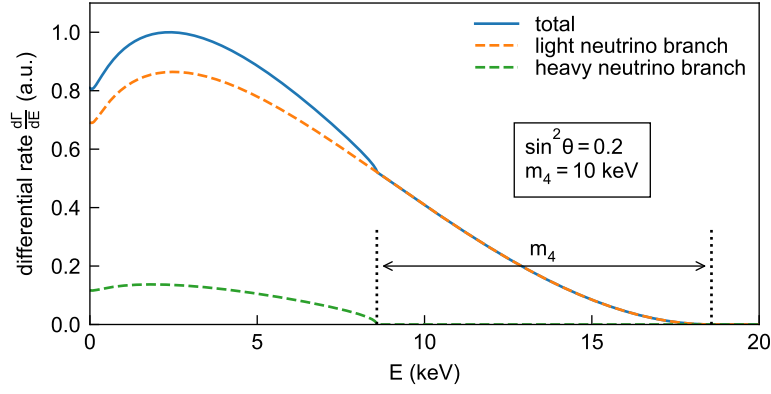
Figure 1.5: Electron spectrum of tritium β-decay with a strong sterile neutrino signature. The spectrum follows equation 1.9 with $m_4 = 10\,\text{keV}$ and $\sin^2\theta = 0.2$.

searches, it is important to stress the model dependence of the cosmological considerations. Many assumptions about the early universe enter into these. In [54], several ways to weaken both the limits from the production mechanism and X-ray telescope observations are presented. The proposed modifications can shift the limits by several orders of magnitude, potentially making sterile neutrino dark matter detectable in laboratory experiments. However, they typically remove some of the simplicity of sterile neutrino dark matter. The most straightforward modification is a dark matter cocktail, where sterile neutrinos build only a fraction of the total dark matter. This would weaken the X-ray telescope constraints. Another way to weaken the X-ray constraints is by assuming a suppressed radiative sterile neutrino decay, for example, by suitable new terms in the decay Lagrangian. The overproduction constraint can be weakened if the thermal production of sterile neutrinos is suppressed above a critical temperature T_c. If $T_c = 5\,\text{MeV}$, the correct amount of sterile neutrinos would be produced at $\sin^2\theta \approx 10^{-4}$.

1.5 Laboratory search for keV sterile neutrinos

The investigation of β-decay allows for a laboratory-based search for sterile neutrinos, similar to the searches for the neutrino mass via equation 1.6. A small admixture of a heavy mass eigenstate m_4 to the electron antineutrino emitted in a β-decay would cause the electron spectrum to be a superposition of two branches:

$$\frac{\mathrm{d}\Gamma_{\text{tot}}}{\mathrm{d}E} = \cos^2\theta \underbrace{\left.\frac{\mathrm{d}\Gamma}{\mathrm{d}E}\right|_{m_\nu\approx 0}}_{\substack{\text{light neutrino} \\ \text{branch}}} + \sin^2\theta \underbrace{\left.\frac{\mathrm{d}\Gamma}{\mathrm{d}E}\right|_{m_\nu=m_4}}_{\substack{\text{heavy neutrino} \\ \text{branch}}}. \tag{1.9}$$

Here, $\frac{\mathrm{d}\Gamma}{\mathrm{d}E}$ is the electron spectrum depending on the mass of the emitted neutrino m_ν, given by equation 1.6 in the case of tritium decay. An exemplary tritium spectrum according to equation 1.9 with a hypothetical sterile neutrino is shown in figure 1.5. The the maximal energy of the heavy neutrino branch is lowered by m_4. Furthermore, the heavy neutrino branch has a steep gradient at its maximal energy. Therefore, the characteristic signature of a keV sterile neutrino is a kink-like distortion at $E = E_0 - m_4$. The amplitude of the kink-like distortion scales with the mixing
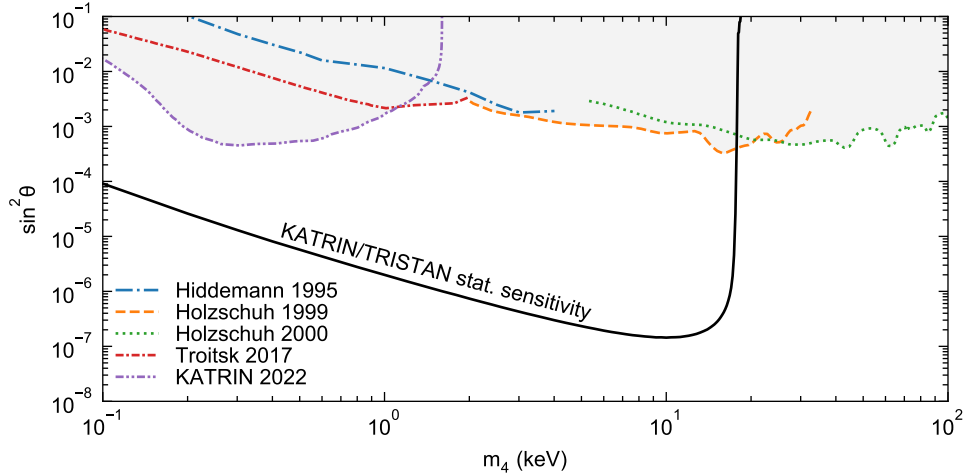
Figure 1.6: Leading laboratory exclusion limits for keV sterile neutrinos. "Hiddemann 1995" [55] used a magnetic $\pi\sqrt{13}/2$-spectrometer with a solid tritium source. "Holzschuh 1999" [56] and "Holzschuh 2000" [57] used a magnetic spectrometer of Tret'yakov type with source isotopes ^{63}Ni and ^{35}S, respectively. "Troitsk 2017" [58] and "KATRIN 2022" [59] used a MAC-E spectrometer with a windowless gaseous tritium source. The projected statistical sensitivity of the TRISTAN detector at the KATRIN experiment is also shown. The curve is calculated in section 3 of this work and is based on one year of data-taking at 10^8 cps. Systematic effects are not included.

amplitude $\sin^2\theta$. With a β-decaying isotope of endpoint energy E_0, masses $0 < m_4 < E_0$ can be probed.

The best laboratory limits today are summarized in figure 1.6. A historical summary is given in [60]. Some of the early experiments used Germanium (e.g. [61]) or lithium-doped silicon Si(Li) (e.g. [62]) semiconductor detectors for β-spectroscopy. However, the best limits shown in figure 1.6 were achieved with magnetic spectrometers or MAC-E filters. The most important β-decay isotopes in this context encompass ^{35}S ($E_0 = 167$ keV), ^{63}Ni ($E_0 = 67$ keV), and tritium ^{3}H ($E_0 = 18.7$ keV).

The search for the signature of a sterile neutrino can also use the recoil spectrum of the daughter nucleus. In this case, electron capture decay can be used, where no electron is emitted. The BeEST experiment, for instance, measures the nuclear recoil spectrum of ^{7}Be electron capture decay by superconducting tunnel junction quantum sensors [63]. This approach is sensitive to sterile neutrinos in the 100 keV to 860 keV mass range. Another approach, followed by the HUNTER experiment, is a total energy-momentum reconstruction of single electron capture decays of ^{131}Cs [64]. This approach measures the nuclear recoil and all atomic deexcitations following the decay to reconstruct each decay's missing mass. If a small fraction of decays would have a keV sterile neutrino in the final state, it could be detected on a single-event basis.

The precise understanding of the measured spectrum is a big challenge for keV sterile neutrino searches. This is seen by many false-positive sterile neutrino signals published in the past [65]. For example, in [66], a $m_4 = 17$ keV sterile neutrino signal with a mixing of $\sin^2\theta = 0.03$ was claimed after analyzing tritium β-decay spectra captured with a Si(Li) detector. Other experiments falsely confirmed the result, some of which also used different isotopes (e.g. [61, 67]). Later, the 17 keV sterile neutrino was excluded (e.g. [62]). The previously published signatures turned out

to originate from experimental effects, mostly from scattering of electrons in the experimental apparatus [65].

keV sterile neutrino search with KATRIN

The KATRIN experiment is designed to measure the endpoint region of the tritium β-spectrum in order to constrain the neutrino mass. The acquired tritium spectrum can also be used to search for sterile neutrinos. Due to the limited analysis window (last 40 eV) of the acquired β-spectrum, such a sterile neutrinos search is restricted to light masses m_4 in the eV range [68].

A keV sterile neutrino search was possible during the commissioning of the KATRIN experiment, where the source activity was reduced to 0.5 %. This activity reduction was necessary, as the current FPD detector can only handle rates up to around 1 Mcps [69], and allowed for extending the measured energy range down to 1.6 keV below the endpoint. The resulting exclusion limit [59] in the sterile neutrino parameter space is shown in figure 1.6. The exclusion reaches $\sin^2 \theta < 5 \cdot 10^{-4}$ at $m_4 \approx 0.3$ keV and improves the leading laboratory-based exclusion limits in the mass range $0.1 \, \text{keV} < m_4 < 1.0 \, \text{keV}$.

The goal of the TRISTAN project within the KATRIN experiment is to exploit the full potential of a keV sterile neutrino search with KATRIN. If equipped with a new detector, optimized for high-rate electron spectroscopy, a statistical sensitivity below $\sin^2 \theta \approx 10^{-6}$ could be achieved in a mass range up to 18.6 keV, assuming a one-year acquisition at a total count rate of 10^8 cps (counts per second), as illustrated in figure 1.6. This measurement could improve the current laboratory limits on $\sin^2 \theta$ by several orders of magnitude. Thereby, the laboratory search for sterile neutrinos would significantly approach the preferred parameter space for sterile neutrino dark matter, presented figure 1.3 in section 1.4 of this work.

2 The KATRIN experiment and the TRISTAN detector

This chapter first provides an overview of the KATRIN experiment in section 2.1. Following that, section 2.2 describes the concept of the TRISTAN detector upgrade for a keV sterile neutrino search at KATRIN. The last two sections of this chapter focus on the technical realization of the TRISTAN detector. Section 2.3 introduces the Silicon Drift Detector (SDD) working principle. Finally, section 2.4 focuses on the design of the TRISTAN detector.

2.1 KATRIN overview

The KArlsruhe TRitium Neutrino experiment (KATRIN) is a tritium β-decay experiment aiming to measure the effective electron antineutrino mass with a sensitivity of 0.2 eV at 90 % CL. To achieve this goal, KATRIN combines a very stable, high-intensity, windowless gaseous tritium source with a high-precision electron spectrometer based on the MAC-E filter principle [70]. In 2019, KATRIN started the acquisition of spectral data within the endpoint region (last 40 eV) of tritium β-decay. Based on the first five measurement campaigns, containing 259 live days of data, the collaboration reported an upper limit $m_\nu < 0.45$ eV at 90 % C. L. [31]. The fourteenth measurement campaign is running at the time of writing, and data-taking will continue until end of 2025.

The 70 m long beamline of KATRIN is shown in figure 2.1. The main sections are described in the following. All details about the experimental setup are documented by the KATRIN collaboration in [70].

Windowless gaseous tritium source

The source of KATRIN is a windowless gaseous tritium source (WGTS). It consists of a 10 m stainless steel tube with a diameter of 9 cm. In the middle of the tube, molecular tritium gas is injected with a pressure of 3 μbar. Superconducting magnets create a longitudinal magnetic field of 2.5 T to guide the electrons emitted in the gas by β-decay along the beam tube. Pumps along the WGTS remove the tritium molecules so only electrons can reach the spectrometer section. A closed tritium loop system cleans the pumped tritium gas and feeds it back to the injection capillary. The WGTS is designed to have a T_2 column density of $5 \cdot 10^{17}$ cm^{-2} corresponding to a total activity of around 10^{11} Bq.
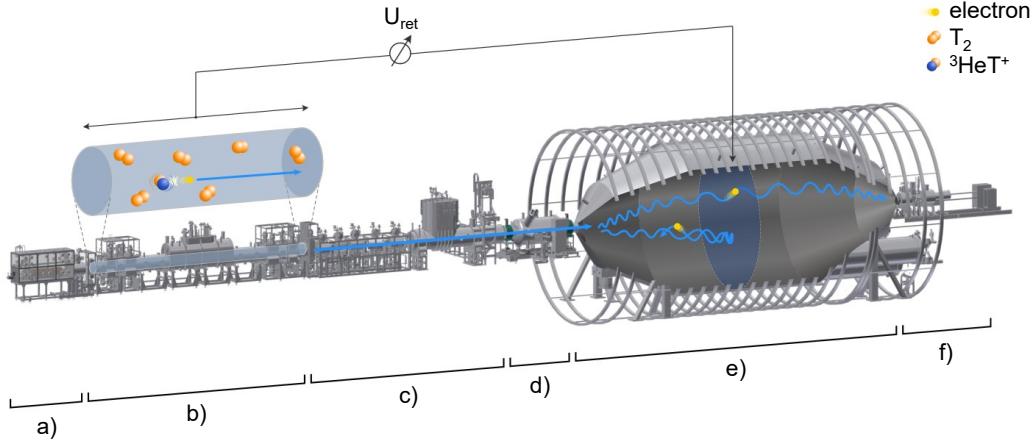
Figure 2.1: Electron beamline of the KATRIN experiment. **a)** rear section, **b)** windowless gaseous tritium source (WGTS), **c)** transport section, **d)** pre-spectrometer, **e)** main spectrometer, and **f)** detector section. Figure kindly provided by L. Köllenberger.
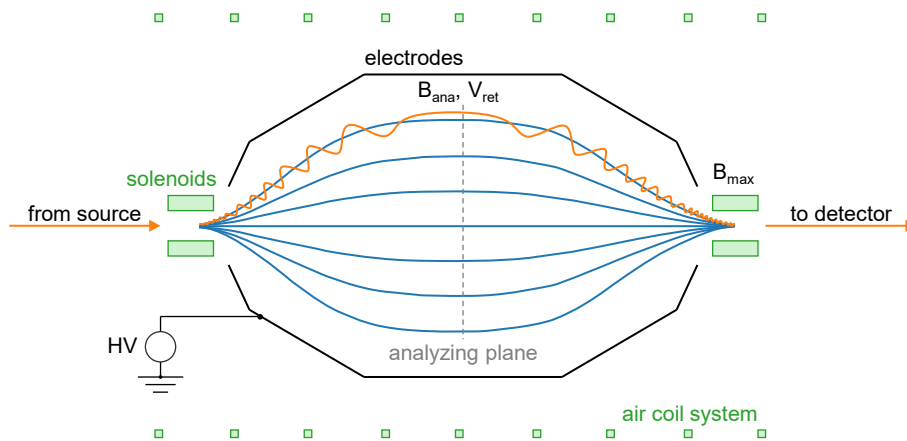

Figure 2.2: Functional principle of a MAC-E filter. The magnetic field is minimal at the analyzing plane. Magnetic field lines are drawn in blue, and the trajectory of an example electron is shown in orange.

Transportation section and spectrometer section

The transportation section magnetically guides the β-electrons to the spectrometer section. It is equipped with two more pumping sections, where the amount of tritium in the beam tube is further reduced. Furthermore, parts of the beam tube in the transport section are tilted by 20°, preventing a direct line of sight between the source and spectrometer to stop ions from reaching the spectrometer.

KATRIN uses a spectrometer based on the MAC-E (Magnetic Adiabatic Collimation combined with an Electrostatic filter) principle. Compared to solely magnetic spectrometers, the MAC-E filter is superior in combining a good energy resolution with a high luminosity [71, 72]. The working principle of the MAC-E filter is illustrated in figure 2.2. In a large spectrometer vacuum vessel, an electrostatic retarding potential V_{ret} blocks all electrons with a longitudinal kinetic energy $E_\parallel$ below eV_{ret}. The plane where the potential reaches its maximum is called the analyzing plane. In order to

Table 2.1: Magnetic field strength along the KATRIN beam line

source	$B_{\mathrm{src}} = 2.5\,\mathrm{T}$
transportation section	$B_{\mathrm{ts}} = 4\,\mathrm{T}$
analyzing plane	$B_{\mathrm{ana}} = 0.6\,\mathrm{mT}$
pinch magnet	$B_{\mathrm{max}} = 4.2\,\mathrm{T}$

obtain a good energy resolution ΔE on $E_{\mathrm{kin}} = E_\perp + E_\parallel$, the transversal energy must be converted to longitudinal energy before the analyzing plane. This is achieved by magnetic adiabatic collimation, which uses the conservation of the magnetic moment μ of each electron along the beamline

$$\mu = \frac{E_\perp}{B} = \mathrm{const}. \tag{2.1}$$

A low magnetic field strength B_{ana} thus leads to a reduced $E_\perp$ at the analyzing plane. The energy resolution of the filter ΔE scales with the ratio of the magnetic field strength B_{ana} in the analyzing plane to the maximal magnetic field strength B_{max} in the beamline

$$\Delta E = \frac{B_{\mathrm{ana}}}{B_{\mathrm{max}}} \cdot E_{\mathrm{kin}}. \tag{2.2}$$

Table 2.1 lists the magnetic field strength along the KATRIN beamline. With the high ratio $\frac{B_{\mathrm{ana}}}{B_{\mathrm{max}}}$ of $\mathcal{O}(10^{-4})$, an energy resolution of $\Delta E = 2.7\,\mathrm{eV}$ is achieved at the endpoint energy $E_{\mathrm{kin}} = 18.6\,\mathrm{keV}$ of tritium β-decay. Besides the electrostatic rejection of electrons in the spectrometer, there is also a magnetic rejection of electrons depending on their starting angle. The critical starting angle angle θ_{crit} is given by

$$\theta_{\mathrm{crit}} = \arcsin \sqrt{\frac{B_{\mathrm{src}}}{B_{\mathrm{max}}}}, \tag{2.3}$$

where B_{src} is the magnetic field strength in the source. The magnetic mirror effect will reflect electrons with a starting angle larger than θ_{crit}. In the KATRIN beamline, all electrons starting in the source with an angle larger than $\theta_{\mathrm{crit}} = 51°$ are rejected. As the electrons are emitted isotropically in the source, the fraction ϵ of electrons that are magnetically transmitted can be calculated by the solid angle:

$$\epsilon = \frac{\Omega}{4\pi} = \frac{1 - \cos \theta_{\mathrm{crit}}}{2} \approx 0.19 \tag{2.4}$$

Due to the huge ratio $\frac{B_{\mathrm{src}}}{B_{\mathrm{ana}}}$, the flux tube of electrons broadens to several meters at the analyzing plane. Therefore, the main spectrometer vessel of KATRIN has an inner diameter of 9.8 m and a length of 23 m. The volume of 1400 m³ is under ultra-high vacuum of 10^{-11} mbar. The ultra-high vacuum is necessary to keep the detected background at a minimum, as every electron created by the ionization of residual gas atoms close to the analysis plane is not distinguishable from a tritium electron.

The KATRIN beamline has two MAC-E filters: The above-described main spectrometer and a smaller pre-spectrometer, which is not used during tritium data acquisition [73]. Furthermore, a third spectrometer, the monitor spectrometer, is located in a separate building next to the KATRIN beamline. It uses the hardware of the predecessor experiment in Mainz [74]. The monitor spectrometer can be used to perform long-term stability tests of the high-voltage system of KATRIN by periodically
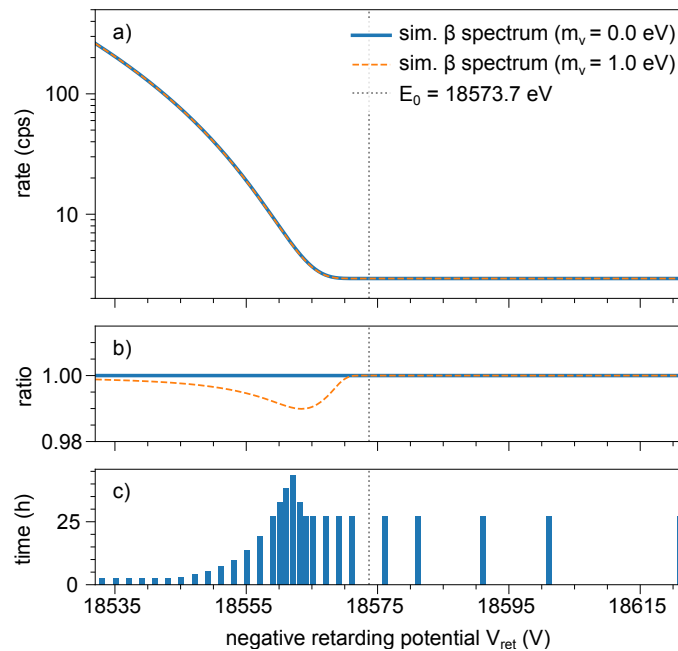
Figure 2.3: Illustration of the spectrum for the KATRIN neutrino mass analysis. Plot a) is the integral tritium spectrum, corresponding to the count rate at 28 different retarding potential setpoints of the main spectrometer. The ratio plot b) shows the signature of a nonzero effective neutrino mass $m_\nu = 1\,\mathrm{eV}$. The bottom plot (c) shows the measurement time distribution that encodes the total time spent at each of the 28 retarding potential setpoints. Figure adapted from [70].

scanning a monoenergetic line of a condensed ^{83m}Kr source [75]. Currently, the monitor spectrometer is primarily used as a test bench for new hardware, such as the modules of the TRISTAN detector.

Focal plane detector

The focal plane detector (FPD) counts the number of electrons passing the main spectrometer. The FPD is implemented as a monolithic multi-pixel silicon PIN-diode array, containing 148 pixels on a circular area with 90 mm diameter [69]. Electrons from the main spectrometer reach the FPD with an energy of around 28.6 keV, corresponding to the endpoint energy plus a 10 keV post acceleration. The post acceleration is achieved by setting the entire detector on a 10 kV positive voltage. This reduces detector systematic effects and shifts the signals into an energy region with fewer background events. The energy resolution of the detector is around 2.8 keV Full Width at Half Maximum (FWHM) [76]. The count rate is determined by summing all counts within a region-of-interest (ROI), typically ranging from 14 keV to 32 keV.

The tritium electron spectrum is measured as the count rate at a defined number of retarding potential setpoints. The resulting curve is an integral version of the spectrum, as illustrated in figure 2.3. In the data analysis, the effective neutrino mass m_ν and the endpoint energy E_0 are extracted from the integral spectrum by fitting a model prediction. The model prediction is constructed by convolving the differential spectrum $\frac{d\Gamma}{dE}$ (equation 1.6) with the instrumental response function [77].
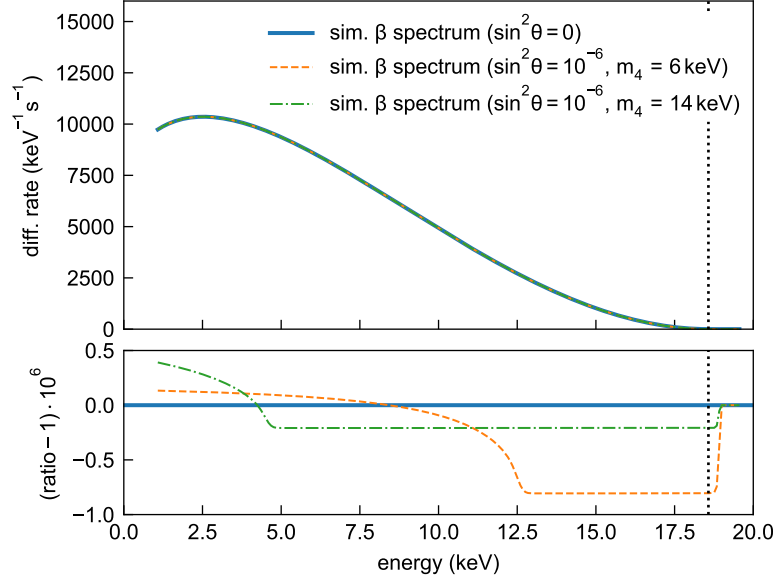
Figure 2.4: Illustration of the spectrum for keV sterile neutrino search with the TRISTAN detector. The simulated spectrum (top) is based on equation 1.6, convoluted with a Gaussian energy resolution (300 eV FWHM). The spectra with sterile neutrinos are normalized to have the same total number of counts as the spectrum without sterile neutrinos. The ratio plot (bottom) reveals the signature of a sterile neutrino with an amplitude on the same scale as the mixing amplitude, which is $\sin^2 \theta = 10^{-6}$ in this plot.

2.2 keV sterile neutrino search with the TRISTAN detector

After the neutrino mass measurement is completed, a keV sterile neutrino search is foreseen with the KATRIN setup. To this end, the entire energy range (0 keV to 18.6 keV) of the tritium β-decay spectrum will be acquired, which allows for probing sterile neutrinos with masses up to 18.6 keV. The sterile neutrino search will be carried out with a new detector, called the TRIS-TAN detector, optimized for high-rate electron spectroscopy. The idea of the TRISTAN detector is to measure the tritium spectrum without scanning the MAC-E spectrometer but by utilizing the spectroscopic performance of the silicon detector. The energy resolution of the silicon detector (FWHM $\approx$ 300 eV) is significantly larger than the width of the transmission function of the MAC-E spectrometer ($\Delta E \approx$ 3 eV). Despite the larger resolution, the spectroscopic measurement with the silicon detector is beneficial for achieving a good sensitivity on the sterile mixing angle $\sin^2 \theta$ due to the differential nature of the acquired spectrum. In a one-year measurement at a total count rate of 10^8 cps, a statistical sensitivity below $\sin^2 \theta \approx 10^{-6}$ could be achieved at $m_4 \approx 10$ keV, which would improve current laboratory limits by several orders of magnitude (see figure 1.6). The calculation of the statistical sensitivity is addressed in detail in section 3. A simplified illustration of the differential tritium spectrum, as it could be acquired with the TRISTAN detector, is shown in figure 2.4.

The two key challenges for detecting a sterile neutrino signature are the following:

1. The statistical sensitivity on $\sin^2 \theta_{\text{crit}}$ scales with the number of collected electrons N according to $\sin^2 \theta_{\text{crit}} \propto N^{-\frac{1}{2}}$. Thus, a high-rate measurement is required. The goal of the first TRISTAN measurement phase is to collect $3 \cdot 10^{15}$ electrons within one year, corresponding to a total count rate of 10^8 cps.

2. A precise understanding of the instrumental response is essential. The spectral analysis requires a model that describes the measured tritium spectrum precise enough to detect a sterile neutrino signature on the 10^{-6} level. The instrumental response entails all components of the beamline, like scattering of electrons in the source gas, backscattering of electrons at the rear section of the beamline, non-adiabaticity effects in the spectrometer, backscattering at the detector, and detector effects like crosstalk, pixel-edge effects, and pileup. A detailed description of all relevant effects is found in [78]. Most of these effects can be minimized by hardware modification of the beamline. For instance, the rearwall material is planned to be changed for a material with a lower backscattering coefficient.

The largest modification of the beamline to address the two challenges listed above is the installation of the TRISTAN detector. The TRISTAN detector is a semiconductor detector based on the Silicon Drift Detector (SDD) technology. A general overview of detector technologies suitable for detecting ionizing radiation is found in the appendix A.1.

The development of the TRISTAN detector started in 2017 with 7-pixel prototype detectors. In 2022, the first fully functional detector modules with 166-pixel became available. The first physics measurement campaign with nine detector modules is planned for 2026 after the current KATRIN measurement campaign on the neutrino mass has finished.

2.3 Silicon Drift Detector: working principle

A semiconductor detector [79, 80, 81] uses the depleted volume of a pn-junction for detecting ionizing radiation. Ionization creates electron-hole pairs, which do not recombine but are separated by the electric field in the depleted volume. In silicon, on average, one electron-hole pair is created every 3.63 eV of ionizing energy deposition [82]. The positive holes and negative electrons move to the electrodes and are measured as a reverse current in the diode. The thickness d of the depleted volume depends on the doping concentration N of the silicon and can be enlarged by reverse biasing the diode with an external voltage V_b

$$d \approx \sqrt{\frac{2\epsilon_0\epsilon_r(V_b + 0.7\,\mathrm{V})}{Ne}}. \tag{2.5}$$

Here, ϵ_0 and $\epsilon_r = 11.9$ are the vacuum permittivity and the relative permittivity of silicon, respectively.

A typical silicon detector geometry is the PIN (positive, intrinsic, negative) diode, shown in figure 2.5. The PIN diode detector uses a silicon wafer of low (intrinsic) n-type doping concentration $N \approx \mathcal{O}\left(10^{12}\,\mathrm{cm}^{-3}\right)$ to yield a large depleted volume. A reverse bias voltage $\mathcal{O}(100\,\mathrm{V})$ is sufficient to reach a depletion thickness d similar to the wafer thickness $\mathcal{O}(500\,\mu\mathrm{m})$. To achieve a good energy resolution at a high rate, a low anode capacitance C_a is essential (details about the noise calculations are shown in section 4.2). With the plate capacitor design of the PIN diode, the lower limit for the capacitance C_a depends on the area A, and the thickness d by

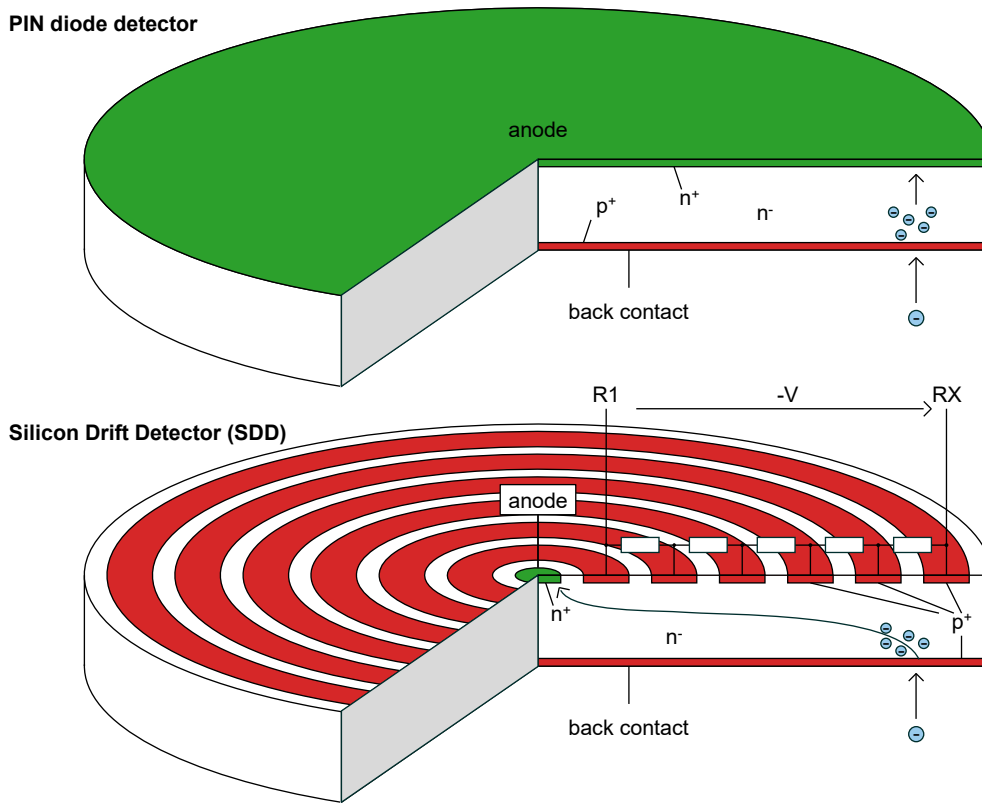$$C_a = \epsilon_0\epsilon_r\frac{A}{d}. \tag{2.6}$$

Figure 2.5: Illustration of a circular PIN diode detector and an SDD. The entrance window is on the bottom side of the detector.

The KATRIN FPD is a PIN diode detector with a pixel area of $44\,mm^2$ and a design capacitance of around $8.2\,pF$ per pixel [69]. It reaches an energy resolution of $1.4\,keV$ FWHM at the $59.5\,keV$ γ-ray line of ^{241}Am, which corresponds to an equivalent noise charge of around 150 electrons[1].

The Silicon Drift Detector (SDD) improves the noise performance compared to the PIN diode detector by reducing the anode to an almost point-like contact [83]. To keep the detector area large at the same time, the principle of side-ward depletion is used [84]. The design of the PIN diode detector and the SDD are compared in figure 2.5. The negatively biased p-type silicon of an SDD extends not only on the bottom (entrance window) side of the detector but also on several drift rings surrounding the anode. In this geometry, all electrons generated in the depleted volume of the detector are guided to the small anode. The drift ring voltage increases proportional to the radius. A voltage divider is implemented on the chip to supply the drift rings. The anode capacitance of an SDD is typically as low as $\mathcal{O}(100\,fF)$ and almost independent of the device area. A detailed study of the electric field and the signal formation in the TRISTAN SDD will be shown in section 4.

Today, SDDs are widely used in energy-dispersive X-ray spectrometry (EDS), for example, in electron microscopy [85]. Current state-of-the-art SDDs reach an anode capacitance of less than $\mathcal{O}(50\,fF)$ and, thus, an equivalent noise charge of only 3 electrons at short peaking time $\mathcal{O}(1\,\mu s)$ [86]. Typical input count rates range from $10\,kcps$ to $1\,Mcps$, and a typical detector area is $10\,mm^2$ per

---

[1]This value is calculated with equation 4.37.

cell. A significant advantage of SDDs, compared to most other semiconductor detectors like Si(Li) or HPGe detectors, is that they can be operated at room temperature or moderate cooling. This is due to the low leakage current achieved in modern silicon semiconductor processing.

2.4 TRISTAN detector design

The TRISTAN SDD detector chip was designed and is manufactured at the Halbleiterlabor der Max-Planck-Gesellschaft (HLL)[2]. The in-vacuum readout electronics is developed at Politecnico di Milano. The TRISTAN detector must meet specific criteria that go beyond state-of-the-art SDDs. These encompass:

- **multipixel system** The TRISTAN detector should have $\mathcal{O}(1000)$ pixels in order to distribute the high input rate.
- **focal plane array** The final detector, composed of several detector modules, must have a diameter of at least 12 cm to cover the entire electron flux tube of the KATRIN beamline.
- **electron spectroscopy** The TRISTAN detector is applied for electron spectroscopy. In this case, the spectroscopic response is very different from the typical case of X-ray detection. The detector response to electrons is very sensitive to surface effects at the entrance window of the detector.
- **environment** The KATRIN detector section is a challenging environment: The SDD will be placed in an ultra-high vacuum, at a magnetic field strength of $\mathcal{O}(1\,\text{T})$, and on a high voltage of up to 20 kV to boost the kinetic energy of the electrons (post acceleration).

The general design choices, like pixel size and pixel number, are discussed in [87, 88, 78].

The TRISTAN detector uses a modular design. The first detector, planned for a one-year science campaign, comprises nine identical and independent detector modules. A rendering of the 9-module TRISTAN detector is shown in figure 2.6. Each TRISTAN module, shown in figure 2.7, comprises a monolithic SDD chip, a copper holding structure, and the frontend readout electronics. The readout electronics is split into two identical boards (ASIC boards), comprising 83 channels each. The ASIC board has a high analog readout line density and is implemented as a 12-layer printed circuit board (PCB) with a minimal track width and distance of only 75 µm [89]. The boards are mounted on the top and bottom sides of the holding structure to allow for a margin-less side-by-side arrangement of several TRISTAN modules. An overview of the characteristics of one TRISTAN detector module is given in table 2.2.

SDD chip design The TRISTAN SDD is implemented on a $38 \times 40 \times 0.45\,\text{mm}^3$ chip of high resistivity n-type silicon (resistivity 4 kΩcm). Each chip comprises 166 hexagonal detector cells, as shown in figure 2.8. The hexagonal geometry allows for a seamless arrangement with the highest possible area-to-border ratio. The hexagons' height of 2.856 mm was chosen to match the 7.1 mm^2 area of a circular cell with 3 mm diameter. The 166-pixel[3] array is surrounded by a small margin for routing and bond pads. The active area ratio of the chip is 77.1 %. Each SDD cell features an n-channel junction field-effect transistor (JFET) and a feedback capacitor, both directly integrated into the anode (see [90] for a similar implementation). The integrated JFET allows for a minimal anode capacitance, independent of the long readout lines of several cm between the SDD chip and

---

[2]www.hll.mpg.de
[3]Throughout this thesis, a detector pixel is used as a synonym for a detector cell.
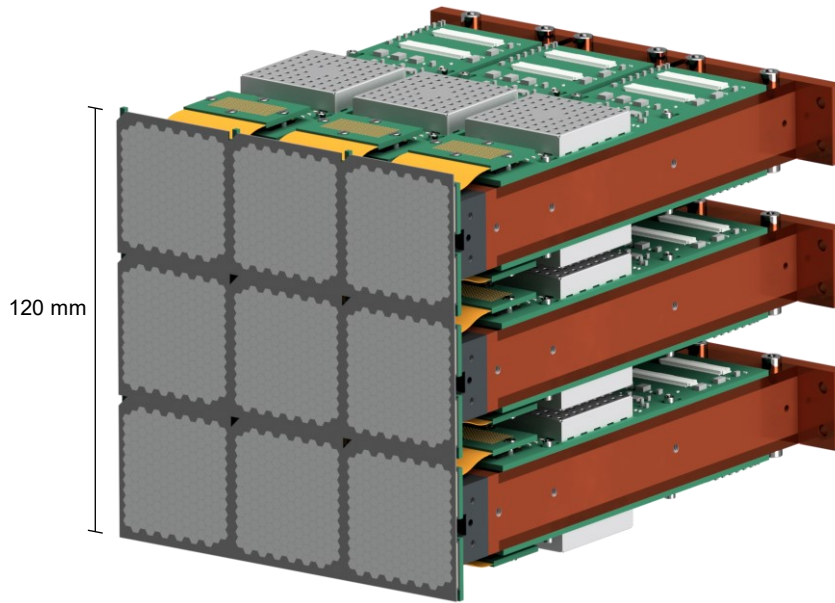
Figure 2.6: Rendering of the TRISTAN detector as planned for the first science campaign. The detector has nine identical modules.
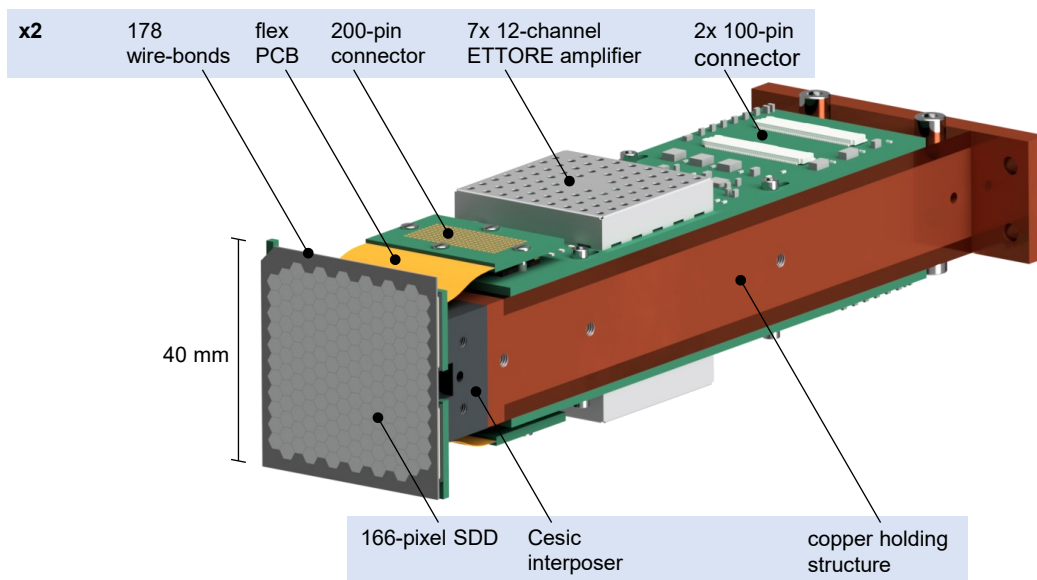

Figure 2.7: Rendering of one TRISTAN detector module. The readout electronics (top labels) exists two times on top and bottom of the copper holding structure, reading out the upper 83 channels (northern hemisphere) and the lower 83 channels (southern hemisphere) of the SDD, respectively.

the readout electronics board. The readout uses the ETTORE application-specific integrated circuit (ASIC) [91]. Further details about the readout circuit are given in section 4.2.

Table 2.2: Characteristics of one TRISTAN detector module

SDD		
	area	$40 \times 38\,\mathrm{mm}^2$
	pixel number	166
	active area ratio	77.1 %
	number of supply voltages[a]	7
	supply voltage range	$-120\,\mathrm{V}$ to $7\,\mathrm{V}$
	power consumption[b]	$\approx 400\,\mathrm{mW}$
	connection	2×178 wire-bond pads
readout		
	amplifiers	14×12-channel ETTORE ASIC
	supply voltage	$3.9\,\mathrm{V}$
	power consumption[c]	$\approx 4400\,\mathrm{mW}$ ($24\,\mathrm{mW/ch}$)
	connection	4×100-pin cables
	target event rate	$16.6\,\mathrm{Mcps}$ ($100\,\mathrm{kcps/ch}$)
	dynamic range[d]	$226\,\mathrm{keV}$
general		
	target temperature	$-30\,°\mathrm{C}$
	dimensions	$200 \times 40 \times 38\,\mathrm{mm}^3$ ($l \times h \times b$)
	weight (with copper block)	$\approx 800\,\mathrm{g}$

[a]explicitly: V_{BC}, V_{BF}, V_{R1}, V_{RX}, V_{IG}, V_{D}, V_{RST}
[b]calculated from ring-voltage divider ($5\,\mathrm{M\Omega/ch}$) with $V_{\mathrm{R1}} - V_{\mathrm{RX}} = 110\,\mathrm{V}$
[c]includes ETTORE and JFET supply
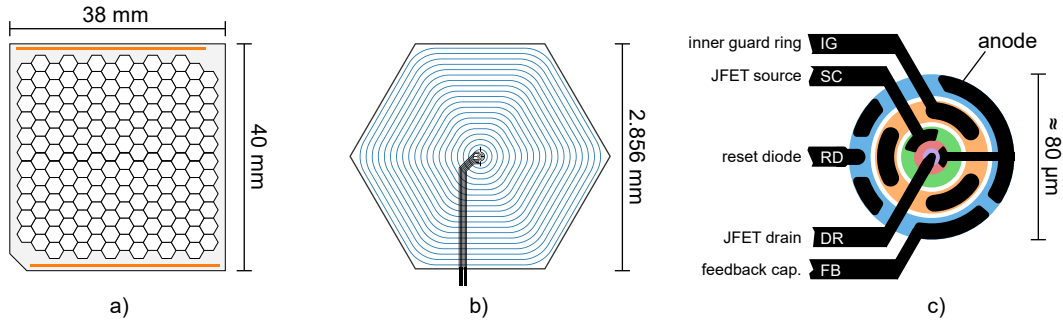[d]maximal value with ETTORE second stage in low gain mode

Figure 2.8: The TRISTAN SDD chip geometry. Drawing **a)** shows a monolithic silicon chip that comprises 166 hexagonal detector cells. The orange area indicates the region of bond pads. Drawing **b)** sketches one detector cell. The 21 drift rings (gaps drawn as blue lines) and the readout lines (black) are visible. Drawing **c)** shows the anode region of one cell. A circular JFET, a feedback capacitor (FB), and a reset diode (RST) are implemented at the ring-like anode. An inner guard ring (IG) isolates the JFET from the anode.

3 TRISTAN sensitivity

A simplified sensitivity study is presented in this chapter. The study estimates the potential of a sterile neutrino search with a tritium source and a TRISTAN-like detector, There were many calculations of the TRISTAN sensitivity in the past (e.g., in [88, 92, 93, 94, 78]). Currently, considerable effort is being put into estimating the sensitivity with realistic experimental systematic effects. These studies are very complex due to the computationally challenging task of calculating a model of the spectrum with $\mathcal{O}(10^{-6})$ precision. Many systematic effects rely on correctly describing the scattering of low-energy (keV-scale) electrons in matter, which is a challenging physics case. A recent work that shows the status of the modeling effort is given by [78].

The study presented in this section does not focus on describing the experimental effects of the KATRIN beamline and the TRISTAN detector with high accuracy but tries to put light on the general origin of the sensitivity curve. This work treats the unknown experimental parameters as free nuisance parameters in a maximum likelihood spectrum fit. A disadvantage of this approach is that it quickly becomes demanding when many unknown parameters are included. Therefore, this work considers the detector calibration and energy resolution to be the only experimental effects.

This chapter first introduces the method for calculating the sensitivity curve (section 3.1) and the model used to describe the measured data (section 3.2). Section 3.3 calculates the statistical sensitivity, assuming all parameters (like calibration and energy resolution) to be perfectly known. The statistical sensitivity is then compared to the sensitivity with free nuisance parameters, calculated in section 3.4. Finally, the influence of the choice of the energy region-of-interest is studied in section 3.5.

3.1 Method

The sensitivity of the experiment in the $\{m_4, \sin^2\theta\}$ space is obtained by a χ^2 difference (or $\Delta\chi^2$) test, which was also used in previous work. Central for the calculation is a model $\vec{N}(\sin^2\theta, m_4, \vec{p})$, which describes the expected number of counts in a binned histogram as a function of $\sin^2\theta$, m_4 and a set of experimental parameters $\vec{p}$. The method for the studies in this work is as follows:

1. In the first step a reference spectrum $\vec{N}_{\mathrm{ref}}$ is calculated. The reference spectrum is a simulated spectrum based on the null hypothesis model $\vec{N}_0$ of no sterile mixing. The sensitivity study is done with unfluctuated data, which means that the reference data and the null hypothesis model are equivalent:

$$\vec{N}_{\mathrm{ref}} = \vec{N}_0 = \vec{N}(\sin^2\theta = 0, \vec{p}_0).$$

$\vec{p}_0$ is a set of experimental parameters with their estimated true values. The reference spectrum is shown in figure 3.1.
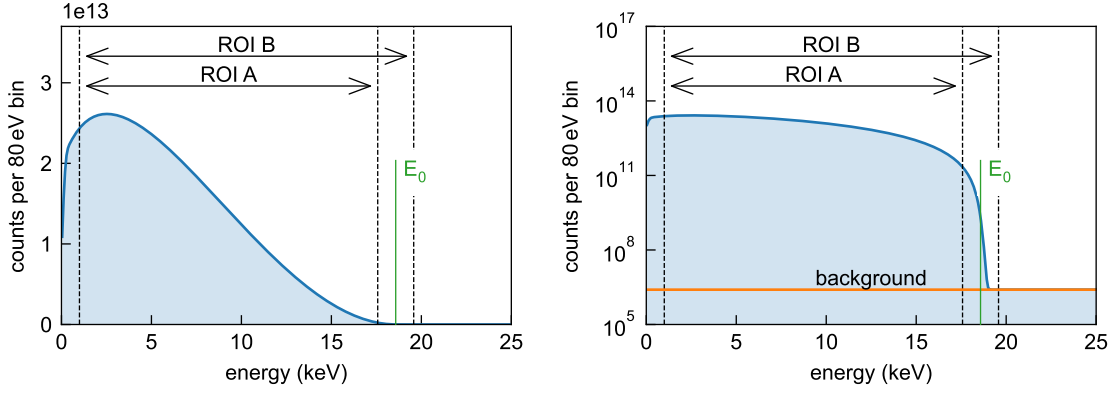
Figure 3.1: Reference spectrum $\vec{N}_{\mathrm{ref}}$ with no sterile mixing, in linear (left) and logarithmic (right) scale. $\vec{N}_{\mathrm{ref}}$ uses the default experimental parameters from table 3.1. The sensitivity study uses two different regions of interest (ROIs). ROI A excludes the endpoint E_0, and ROI B includes E_0.

2. A loop iterates through discrete values of m_4 from 0 to 18.6 keV. For each m_4 a value $\sin^2 \theta_{\mathrm{lim}}$ is determined. To this end, a hypothesis model

$$\vec{N}_1(\sin^2 \theta, m_4, \vec{p})$$

is compared to the null hypothesis model $\vec{N}_0$. The test statistic, which is used to decide if the hypothesis is rejected or not, is

$$\Delta \chi^2 = \chi_1^2 - \underbrace{\chi_0^2}_{=0} = \sum_i \frac{\left(N_{1,i} - N_{\mathrm{ref},i}\right)^2}{N_{1,i}}.$$

Conveniently, χ_0^2 of the null hypothesis is zero due to using unfluctuated $\vec{N}_{\mathrm{ref}}$. The hypothesis model $\vec{N}_1$ adds two additional parameters $\sin^2 \theta$ and m_4 to the null hypothesis model. Therefore, $\Delta \chi^2$ is expected to follow a χ^2 distribution with two degrees of freedom, and the $\vec{N}_1$ hypothesis is rejected at 95 % CL if $\Delta \chi^2 > 5.99$ [95]. The contour of the sensitivity lies at $\sin^2 \theta_{\mathrm{lim}}$, which is the minimal $\sin^2 \theta$, for which $\Delta \chi^2 > 5.99$ while taking into account the best-fit nuisance parameters $\vec{p}^*$.

To find $\sin^2 \theta_{\mathrm{lim}}$, a Markov Chain Monte Carlo method is used in this work, which samples the parameter space of $\{\sin^2 \theta, \vec{p}\}$. The sampling algorithm uses the `emcee` python package [96]. The χ^2 function serves as a negative logarithmic likelihood

$$-2 \log \mathscr{L}(\sin^2 \theta, \vec{p}) = \Delta \chi^2(\sin^2 \theta, \vec{p}).$$

The output samples in $\{\sin^2 \theta, \vec{p}\}$ space are not used to extract an interval for $\sin^2 \theta$ directly (although it could be in a Bayesian approach). Here, the values of $\vec{p}^*$ and $\sin^2 \theta_{\mathrm{lim}}$ are extracted by searching the sample with largest $\sin^2 \theta$, which still fulfills $\Delta \chi^2 > 5.99$. In this case, the Markov Chain Monte Carlo is used as a tool to find $\sin^2 \theta_{\mathrm{lim}}$ and the parameters $\vec{p}^*$ of maximal likelihood or minimal χ^2.

3. The relation between $\sin^2 \theta_{\mathrm{lim}}$ and m_4 is plotted. Sterile neutrinos with parameters above the line (at larger $\sin^2 \theta$) can hypothetically be excluded by the experiment if no sterile neutrino in the relevant mass range exists in nature.

Table 3.1: Default values of nuisance parameters for the sensitivity study

name	symbol	default value
normalization	N	$N_0 = 3.15 \cdot 10^{15}$, corresponding to a 1 year acquisition with 10^8 cps total output rate.
gain	G	$G_0 = 1$
offset	C	$C_0 = 0\,\mathrm{eV}$
energy resolution	σ_{en}	$\sigma_{\mathrm{en}\,0} = 127.4\,\mathrm{eV}$, corresponding to 300 eV FWHM.

3.2 Model

The studies in this section use a model $\vec{N}(\sin^2\theta, m_4, \vec{p}^*)$. It predicts the number of expected measured counts in a binned energy histogram with a bin width of 80 eV. The model is constructed in the following way:

1. The theoretical tritium spectrum is calculated and integrated within each bin. A sterile neutrino with parameters m_4 and $\sin^2\theta$ is included according to equation 1.9.
2. The histogram is convolved with a Gaussian kernel with width σ_{en}, accounting for the general energy resolution of the detector.
3. A linear calibration is applied, which has two parameters: gain G and offset C. The central position of each bin after the calibration is $E_{\mathrm{out}\,i} = E_{\mathrm{in}\,i} \cdot G + C$. A rebinning method redistributes the counts to a fixed output binning.
4. A normalization is applied, such that the total number of counts in the histogram is N.
5. A flat background is added with a constant (more or less arbitrary) rate of $\Gamma_{\mathrm{bkg}} = 1\,\mathrm{cps/keV}$. The background rate has no significant influence on the results of the studies in this section but still is present in the model.
6. The histogram is cut by a region of interest (ROI). There are two options: ROI A extends from 1 keV to $E_0 - 1$ keV. This ROI is a conservative choice, as it excludes the two interesting spectral regions around $E = 0\,\mathrm{keV}$ and $E = 18.6\,\mathrm{keV}$, where the spectrum has a large logarithmic slope. These regions may be difficult to model, as the shape there depends strongly on the detector response. On the other hand, if modeled correctly, including these regions could also help to constrain nuisance parameters like gain, offset, and energy resolution. An alternative ROI, labeled ROI B, used later in this chapter, includes the endpoint region.

In summary, the model is a function of six parameters, of which two are the parameters of interest, and four are experimental parameters:

$$\vec{N}(\sin^2\theta, m_4, \vec{p}) = \vec{N}(\sin^2\theta, m_4, N, G, C, \sigma_{\mathrm{en}}). \tag{3.1}$$

Table 3.1 gives an overview of the experimental parameters and their default values $\vec{p}_0$. The model without sterile mixing ($\sin^2\theta = 0$) and default parameters is shown in figure 3.1.

3.3 Statistical sensitivity

The statistical sensitivity curve is calculated with only the normalization N as a free parameter. The other parameters gain G, offset C, and energy resolution σ_{en} are assumed to be perfectly known in the experiment and are kept fixed at their default value according to table 3.1. Even with a perfect
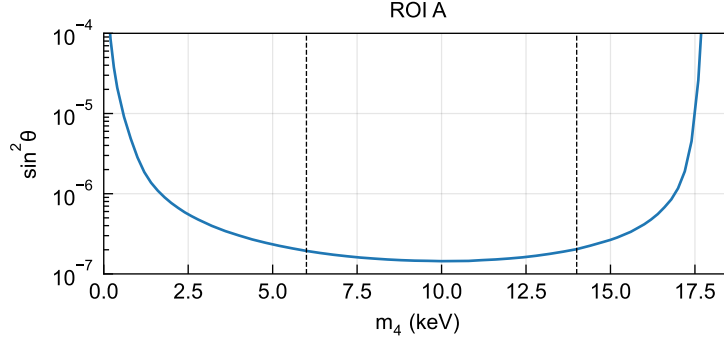
Figure 3.2: Statistical sensitivity (95 % CL) in the sterile neutrino parameter space. The curve is based on the default experimental parameters from table 3.1 and uses ROI A (see figure 3.1).

experiment, the normalization N cannot be fixed, as the uncertainty on the half-life of tritium is not known sufficiently. As no experimental parameters are considered to have uncertainties, the sensitivity curve is called "statistical" sensitivity.

Figure 3.2 shows the sensitivity curve, assuming one year of measurement time with a total detected rate of 10^8 cps. In line with previous work (e.g. [78]), the sensitivity curve reaches $\sin^2 \theta = 1.5 \cdot 10^{-7}$ in the central mass region $m_4 \approx 10$ keV. The statistical sensitivity on $\sin^2 \theta$ scales with the total amount of collected electrons according to

$$\sin^2 \theta_{\text{lim}} \propto \frac{1}{\sqrt{N}} \tag{3.2}$$

Increasing the measurement time to three years instead of one year would, therefore, reduce $\sin^2 \theta_{\text{lim}}$ by a factor $\sqrt{3} \approx 1.73$. On the other hand, a total measurement time of only one day would already reach around $\sin^2 \theta = 3 \cdot 10^{-6}$ at $m_4 \approx 10$ keV.

The signature of a sterile neutrino is visible in the residual plot in figure 3.3. The figure shows the residuals for $m_4 = 6$ keV and $m_4 = 14$ keV at the contour with mixing $\sin^2 \theta_{\text{lim}}$. By construction, the squared sum of the residuals is

$$\chi_1^2 = \Delta \chi^2 = \sum \text{residuals}^2 = 5.99 \tag{3.3}$$

for both cases. As expected, the residuals show an apparent kink at $E_0 - m_4 \approx 12.6$ keV and $E_0 - m_4 \approx 4.6$ keV respectively. The normalization, which is the only free fit parameter, can vertically move and distort the residual shape, but it cannot compensate for the kink-like feature. It is interesting to note that the sensitivity in figure 3.3 extends below $m_4 = 1$ keV, although the ROI ends 1 keV below the endpoint. The sensitivity at $m_4 < 1$ keV, therefore, must originate from the spectral shape distortion rather than the kink itself. The spectral shape distortion can originate either from the different shape of the sterile neutrino branch in the spectrum, which is similar to the active neutrino mass signal in the current KATRIN analysis. Furthermore, the energy resolution causes a small smearing of the kink.
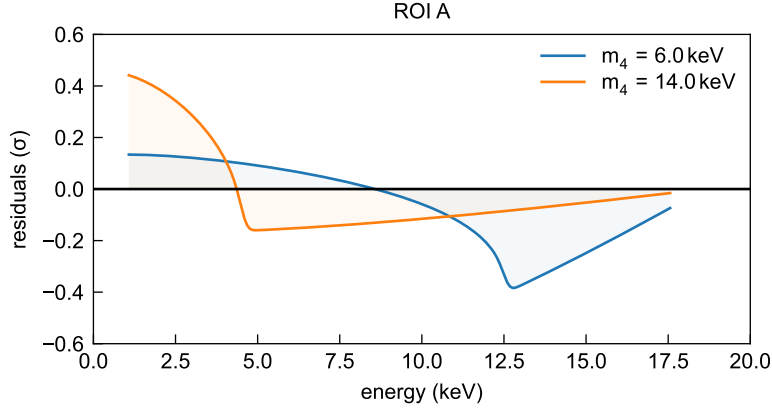
Figure 3.3: Residuals of a sterile neutrino with $m_4 = 6\,\text{keV}$ and $m_4 = 14\,\text{keV}$ at $\sin^2 \theta_{\text{lim}}$ using ROI A. The residuals belong to two values of m_4 on the statistical sensitivity curve of figure 3.2. The kink-like signature can be recognized at $E_0 - m_4$.

3.4 Nuisance parameters

Now, the influence of nuisance parameters on the sensitivity is studied. Nuisance parameters can be any experimental effect that has a non-perfectly known magnitude. In the case studied here, the calibration (with parameters gain G and offset C) and the energy resolution (with parameter σ_{en}) are considered nuisance parameters. These parameters were fixed for the statistical sensitivity.

Figure 3.4 shows how the sensitivity curve evolves if G, C and σ_{en} are freed one-by-one. With each additional free parameter, the sensitivity curve covers less parameter space. This matches the expectation, as the free parameters can compensate for part of the sterile neutrino signal. Figure 3.4 also shows the relative difference between the best-fit values for the nuisance parameters and their default value. The relative value of the difference is tiny: At $m_4 = 14\,\text{keV}$, for instance, a change of the gain to $G = 1 + 1.4 \cdot 10^{-7}$ and an offset $C = 2.5\,\text{meV}$ is sufficient to reduce the $\sin^2 \theta_{\text{lim}}$ by a factor 2.8. The smallness of the values, by which the nuisance parameters change to compensate for the sterile neutrino signal, is an important result of the study. One consequence is that it will be almost impossible to constrain the calibration parameters sufficiently from an external measurement. For comparison, an experimental assessment of the calibration stability is given in [97]: in a 60 h measurement of an X-ray line position, an offset stability of batter than 5 eV in most pixels was observed, which is still more than three orders of magnitudes above the offset variation along the sensitivity curve in figure 3.4.

The effect of the nuisance parameters is also visible in the residual plots in figure 3.5. The structure in the residuals becomes more and more local around the kink as more nuisance parameters are added. This is related to the fact that nuisance parameters, like the calibration and energy resolution, change the spectrum shape smoothly. Such smooth changes cannot mimic the kink-like signature of a sterile neutrino. This effect was also studied in [94], where the smoothness of a parameter was quantified by its correlation length. A smaller correlation length leads to a larger degradation of the sensitivity.

In figure 3.5, freeing the nuisance parameters G and C increases $\sin^2 \theta_{\text{lim}}$ by more than a factor 2 for almost all values of m_4. The nuisance parameter σ_{en} further reduces $\sin^2 \theta_{\text{lim}}$, depending on m_4.
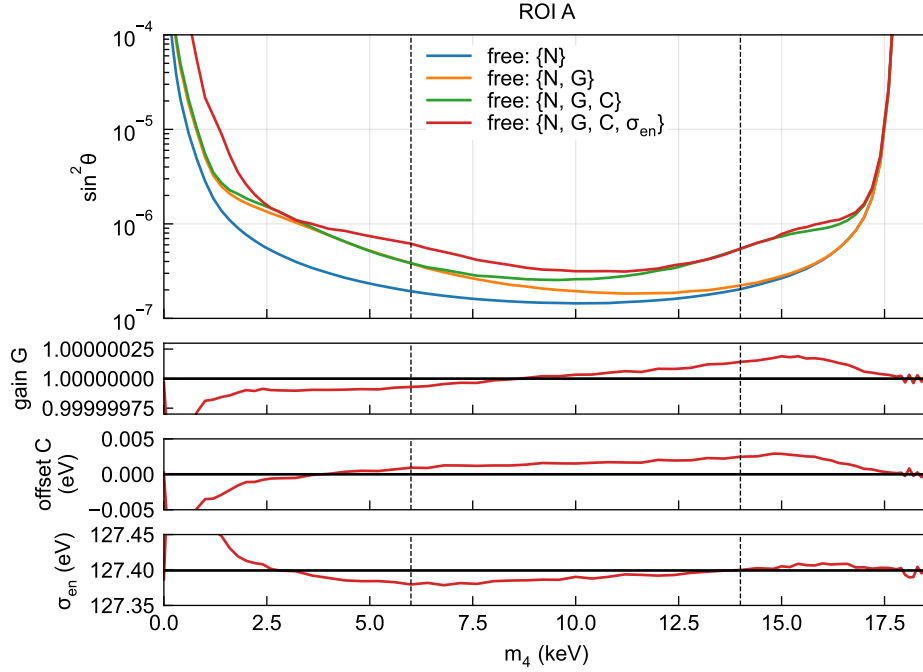
Figure 3.4: Sensitivity (95 % CL) in the sterile neutrino parameter space. The curves are based on the default experimental parameters from table 3.1 and use ROI A (see figure 3.1). The normalization N is a free parameter in all shown cases. The parameters gain G, offset C, and σ_{en} are made free in the fit one-by-one. The best-fit nuisance parameters in the bottom half of the figure correspond to the sensitivity contour with all parameters free (red). The fitted parameters show a small deviation from their default values, compensating for a sterile neutrino signature and worsening the sensitivity.
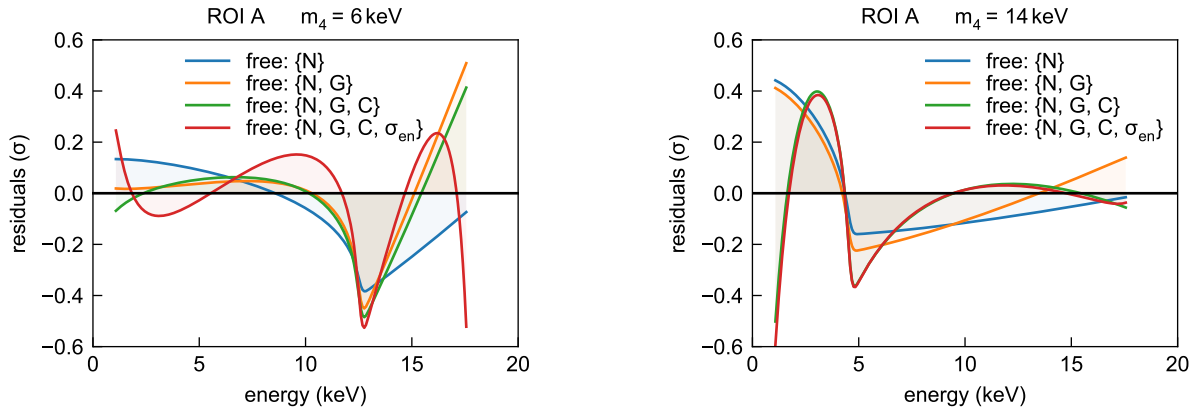
Figure 3.5: Residuals of a sterile neutrino with $m_4 = 6\,\mathrm{keV}$ (left) and $m_4 = 14\,\mathrm{keV}$ (right) at $\sin^2 \theta_{\mathrm{lim}}$ using ROI A. The parameters gain G, offset C and σ_{en} are made free one-by-one. The residuals belong to two values of m_4 on the statistical sensitivity curve of figure 3.4. The kink-like feature at $E_0 - m_4$ gets more and more local. All four lines have the same significance, but the kink gets more spiky as the $\sin^2 \theta_{\mathrm{lim}}$ increases.

The nuisance parameters in this study are implemented as entirely free parameters. Any external information, for example from a calibration measurement, could reduce the parameter's negative effect by adding a pull-term in the χ^2 calculation. However, for all parameters shown here, the expected precision of an external measurement will not be sufficient to constrain the parameter significantly.

3.5 Region-of-interest

Nuisance parameters can be constrained by extending the ROI. So far, the spectrum between $1\,\mathrm{keV}$ and $(E_0 - 1\,\mathrm{keV})$ was used for the analysis. If the endpoint E_0 is included in the fit, the steep logarithmic slope at the endpoint constrains nuisance parameters. To demonstrate this effect, the sensitivity study is repeated with an alternative ROI (labeled ROI B), which includes the endpoint (see figure 3.1). Figure 3.6 shows the sensitivity contour and the best-fit nuisance parameters, calculated with ROI B. Figure 3.7 shows the corresponding residuals for two values of m_4.

Compared to the sensitivity using ROI A (figure 3.4), $\sin^2 \theta_{\mathrm{lim}}$ is overall slightly lower, corresponding to a better sensitivity. Especially when σ_{en} is made free, there is almost no loss in sensitivity with ROI B, while there is a significant loss with ROI A. This is explained by the large imprint of the energy resolution σ_{en} in the endpoint region of the spectrum. Including the endpoint region in the fit thereby constrains σ_{en} precisely. This is also visible by the almost negligible deviation of the fitted σ_{en} from its default value in figure 3.6.

Similar to the endpoint region, one could include the spectrum down to zero, or even below the tritium spectrum, if a post acceleration is used. As demonstrated above, extending the ROI above and below the main tritium spectrum has the advantage of constraining nuisance parameters. However, this only works if the model is precise enough to fit the spectrum in these regions. This is the case by construction in the sensitivity study, as the same model is used for simulating the reference spectrum and fitting. In the actual experiment, a small discrepancy between the model and the experiment could already be a problem when fitting the spectrum above and below the main tritium spectrum, where the spectrum shape is dominated by the detector response. In this case, fitting only the main tritium spectrum without endpoint regions is probably more robust at the cost of a worse sensitivity.

3.6 Summary

A sensitivity study for a keV sterile neutrino search in the tritium β-decay spectrum was performed within this work. The study does not focus on a detailed description of experimental effects. Instead, the key of the study is the controlled introduction of fundamental nuisance parameters, explicitly the detector calibration and the detector resolution. The study shows how these nuisance parameters worsen the sensitivity significantly over the entire energy range by at least a factor of two.

The studies in this chapter were done with a simplified spectrum model. Many effects, like a post acceleration, charge sharing, backcattering at the rearwall and so on, will significantly change the shape of the actual spectrum compared to the one shown in figure 3.1. Therefore, the sensitiv-
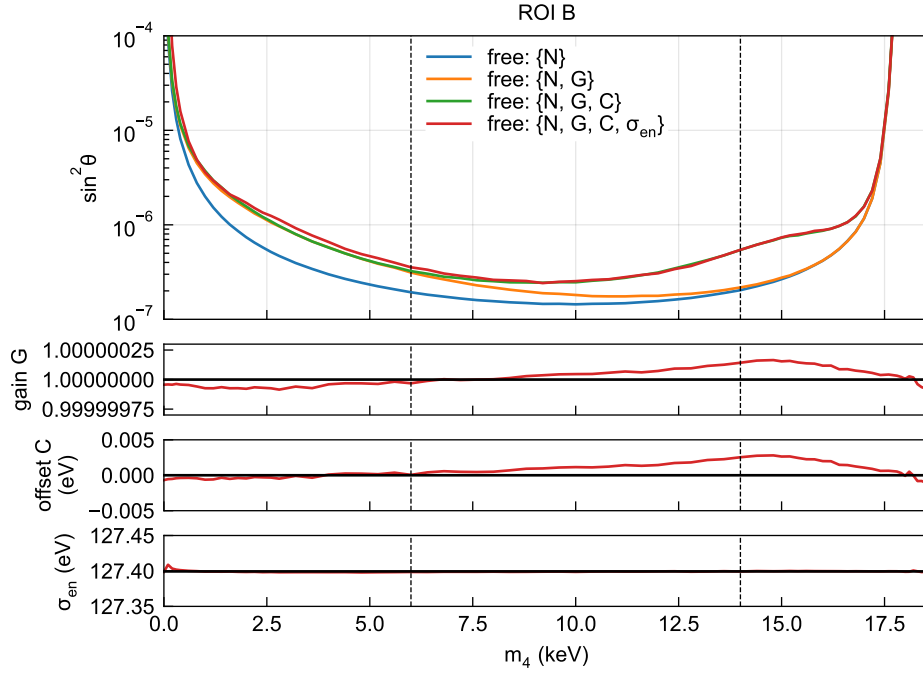
Figure 3.6: Sensitivity (95 % CL) in the sterile neutrino parameter space. The curves are based on the default experimental parameters from table 3.1 and use ROI B (see figure 3.1). The only difference to figure 3.4 is the ROI, which includes the endpoint region in this plot. The sensitivity is improved by including the endpoint region.
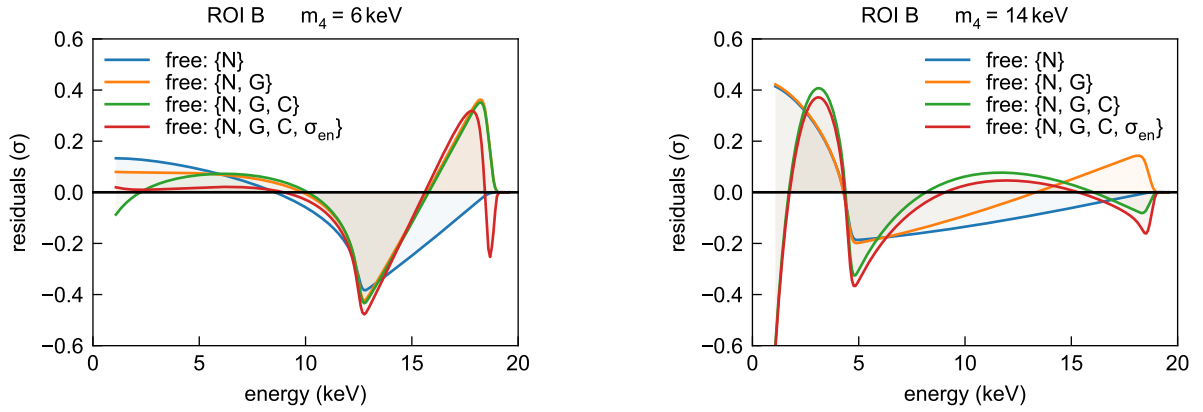

Figure 3.7: Residuals of a sterile neutrino with $m_4 = 6\,\text{keV}$ (left) and $m_4 = 14\,\text{keV}$ (right) at $\sin^2\theta_{\text{lim}}$ using ROI B. The only difference to figure 3.5 is the ROI, which includes the endpoint region in this plot. Besides the kink of the sterile neutrino, a second feature arises at the endpoint, which strongly constrains nuisance parameters.

ity shown here should not be interpreted as a quantitative assessment of systematic effects for TRISTAN.

A unique feature of the study is that the nuisance parameters are implemented as free fit parameters, avoiding the covariance matrix approach used in many previous studies. This gives a more reliable result and, most importantly, allows for studying the best-fit value of the nuisance parameters. Assuming a one-year acquisition at 10^8 cps, the two nuisance parameters of the calibration (gain G and offset C) deviate by $\Delta G = \mathcal{O}\left(10^{-7}\right)$ and $\Delta C = \mathcal{O}(1\,\mathrm{meV})$ to reduce the sensitivity roughly by a factor three. The small values obtained for ΔG and ΔC define the required precision of an external calibration to improve the sensitivity.

This study also shows that the choice of the ROI for the analysis plays an important role. Extending the ROI above the lower and higher end of the tritium spectrum helps to constrain nuisance parameters and thus improves the sensitivity. However, this also comes with the danger of underestimating nuisance parameters in a sensitivity study with a large ROI. The reason is that the edge regions of the spectrum can be fitted without problems in the sensitivity study, although these regions will be challenging to model with the required precision in the actual experiment.

4 Modelling of the SDD signals

This chapter studies the signal properties of the SDD, including the signal formation in the detector diode and readout effects. The details about the SDD signals are essential for understanding the spectroscopic response of the detector.

Section 4.1 presents a simulation of the charge cloud drift within the depleted silicon volume. The simulation calculates the intrinsic pulse shape of the detector and reveals the pulse shape's dependence on the primary interaction location. The subsequent section 4.2 addresses the readout circuit, which influences the pulse shape. A detailed model for the electronic noise, which arises in the used readout circuit, is derived in the third section 4.3. It will also be shown how the electronic noise, given as a power density spectrum, is connected to the observed energy resolution of the detector.

4.1 Signal simulation

In order to study and understand the signal formation inside the TRISTAN SDD, the simulation code `driftsim` was developed within the scope of this work. The simulation consists of three parts. First, the depleted silicon volume's electric field is calculated. Second, a Monte Carlo approach simulates the charge cloud drift inside the depleted volume. Third, the induced signal shape at the anode is calculated from the electron trajectories.

4.1.1 Part 1: electric field

The electric potential Φ inside depleted silicon follows the Poisson equation

$$\triangle \Phi = -\frac{Ne}{\epsilon_0 \epsilon_r},$$

(4.1)

where N is the intrinsic doping concentration. The electrodes of the device form boundary constraints at the surface of the depleted volume with fixed potentials. To facilitate the numerical calculation of the field two important approximations are applied:

1. The field simulation uses a cylindrical coordinate system (r, z, ϕ) as shown in figure 4.1 and approximates the geometry to be symmetric in ϕ. This approximation simplifies the field calculation to a two-dimensional calculation in the r-z plane. The hexagonal shape of the pixels is accounted for by mapping the calculated two-dimensional potential in the r-z plane to a hexagonal pixel volume in three dimensions.
2. The simulation assumes constant doping concentration and full depletion of the entire detector volume. In a real detector the depleted region does not reach the device surface but
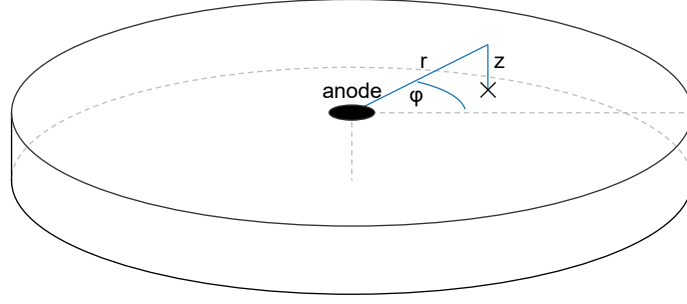
Figure 4.1: Cylindrical coordinates (r, z, ϕ) used for the field calculation. The black disc on the center of the top face illustrates the anode of the detector.
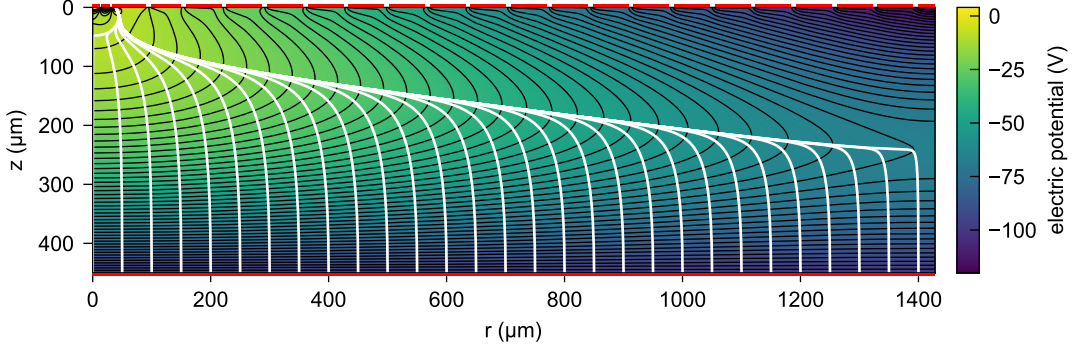

Figure 4.2: Simulated electric potential in the SDD volume. Equipotential lines are drawn every 2 V. Red lines indicate electrodes at a defined potential. White lines show the gradient walk (or electric field lines) starting at different radii at the entrance window.

> ends in the implantation doped n^+ and p^+ silicon layers. Due to the small depth of implantation doping of typically less than $1\,\mu m$ the approximation of depletion to the surface can be applied.

The field is solved on a regular grid in the r-z plane with 451×1429 grid points which corresponds to a resolution of $1\,\mu m$. For solving the equation the finite elements method, implemented in the `sfepy` python package, is used [98]. Details about the formulation of the Poisson equation 4.1 in ϕ-symmetric cylindrical coordinates are given in appendix A.2.

The calculated field is shown in figure 4.2. The electrode dimensions and the applied voltages were adapted to the TRISTAN SDD layout provided by HLL. The electric potential has a positive gradient from the entrance window to the anode. Thus, all field lines, shown in figure 4.2, reach the anode of the device. The potential in the device has two saddle points:

- At the border to a neighboring pixel, symmetry prohibits any radial component of the electric field. The positive space charge in the depleted bulk forms a saddle point, where the electric field is zero, deep in the detector volume. The simulated field shows this spot at a depth of $z \approx 250\,\mu m$. The electric field in this region defines the properties of charge sharing, which is studied in section 6.5.
- Another saddle point is located at the anode region of the device. Figure 4.3 provides a close-up view of this region. In the field simulation, the JFET is represented by a single electrode with a voltage of 4 V (in reality, it consists of a gate, drain, and source). The JFET has the most positive voltage in the device, causing electrons to drift toward the JFET channel instead
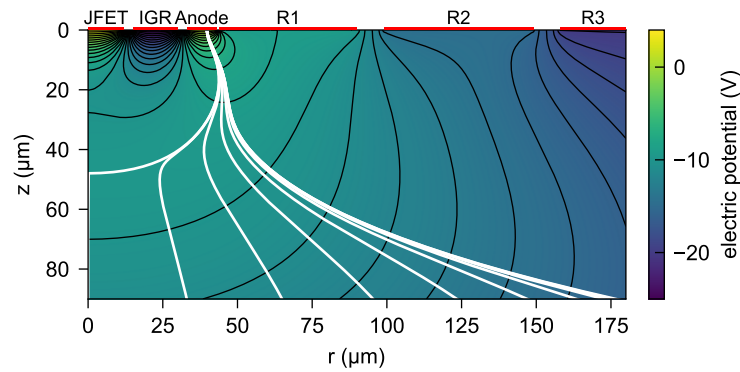
Figure 4.3: Zoom to the simulated electric potential in the SDD volume at the anode region (compare 4.2). Equipotential lines are drawn every 1 V.

of the anode. These electrons do not reach the JFET gate and would consequently be lost for signal formation. An inner guard ring (IG), which surrounds the JFET at a negative potential of -25 V, addresses this issue by building a negative barrier around the JFET. Consequently, a saddle point of the electric potential at a depth $z \approx 40\,\mu$m is formed on the central axis of the device.

The back contact voltage $V_{BC} = -100$ V is applied to the entrance window of the detector and has a central influence on the electric field in the device. There is a plateau region for the allowed back contact voltage where the electric field lines and, therefore, the drifting electrons reach the anode. In the following, the two cases of a too positive and too negative V_{BC} are shortly illustrated:

The detector volume will not be fully depleted if the back contact voltage is too positive. Figure 4.4 shows a simulation with $V_{BC} = -80$ V. The figure indicates that the electric field lines do not reach the anode but terminate at a potential minimum within the detector volume at $z \approx 80\,\mu$m. Consequently, electrons accumulate at this minimum, forming a "lake" that gradually fills until it connects with the anode. This implies that the anode effectively extends into the intrinsic silicon volume of the detector. Although signal formation remains possible in a partially depleted detector, the noise performance and signal rise time will significantly degrade due to the increased anode geometry and capacitance.

Figure 4.5 shows a simulation with a too-negative back contact voltage $V_{BC} = -120$ V. In this scenario, most field lines from the entrance window do not reach the anode but end at the innermost drift ring. One can picture this situation as if the field from the negative back contact (pushing electrons to the readout side surface) dominates compared to the field from the positive space charge of the depleted silicon (pulling electrons into the volume) so that the electrons are pushed to the rings.

The simulation of several different values for V_{BC} indicates a V_{BC} range from -95 V to -110 V where all electrons reach the anode and the detector is in a proper field configuration. Nevertheless, the correct setpoint of V_{BC} has to be measured for each detector device due to limited input knowledge of the simulation. For example, a slight change in the intrinsic doping concentration of the wafer has a direct influence on the optimal back contact voltage.
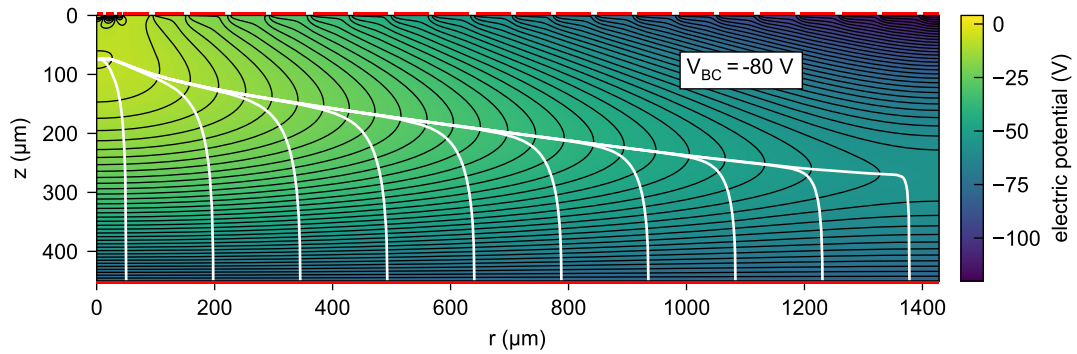
Figure 4.4: Simulated electric potential with too-positive back contact voltage $V_{BC} = -80\,\text{V}$ (compare figure 4.2). A potential maximum forms deep below the anode, where the electric field lines end. In practice, this region would get fill up with electrons.
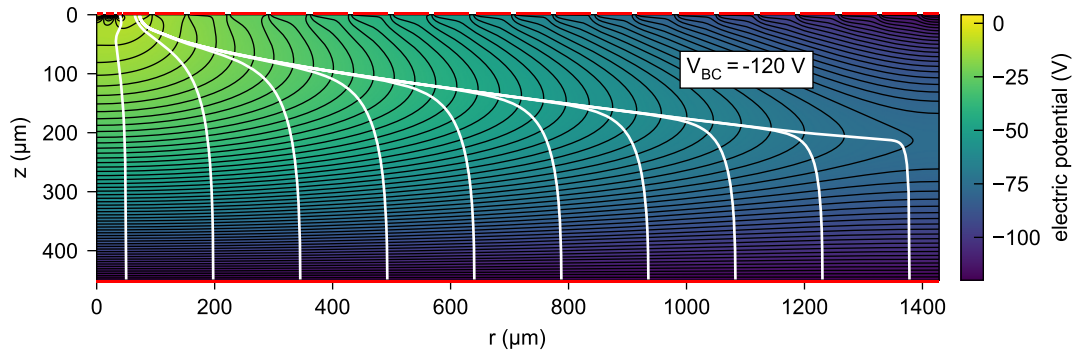

Figure 4.5: Simulated electric potential with too-negative back contact voltage $V_{BC} = -120\,\text{V}$ (compare figure 4.2). Most field lines reach the innermost drift ring and signal electrons would be lost between the drift rings.
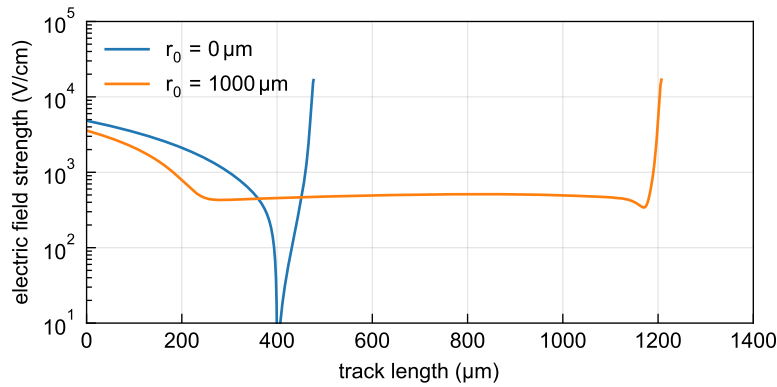
Figure 4.6: Electric field strength along two field lines starting at $r_0 = 0\,\mu m$ and $r_0 = 1000\,\mu m$ (compare figure 4.2). The field line starting at $r_0 = 0\,\mu m$ passes through the saddle point below the JFET, where the electric field is zero.

The electric field strength $\mathscr{E}$ (here written curly to distinguish from energy symbol E) is now evaluated. $\mathscr{E}$ is calculated by the divergence of Φ

$$\vec{\mathscr{E}} = \vec{\nabla}\Phi\,. \tag{4.2}$$

Figure 4.6 shows the electric field strength $\left|\vec{\mathscr{E}}\right|$ along two field lines from figure 4.2 starting at the entrance window at radii $r_0 = 0\,\mu m$ and $r_0 = 1000\,\mu m$. The $r_0 = 1000\,\mu m$ field line starts with an electric field strength of around 4 kV/cm which quickly decreases to around 500 V/cm in the potential valley at a depth of around 250 µm. During the radial drift, the electric field strength stays at an almost constant magnitude and only increases again to around 20 kV/cm in the last 20 µm towards the anode. Similar features can also be seen for the electric field strength along the field line starting at $r_0 = 0\,\mu m$. In the latter case, the radial drift is missing and is replaced by the almost field-free region above the JFET. This simulation of the electric field is an important input to the simulation of the drift of electrons in the detector.

4.1.2 Part 2: charge cloud drift

Based on the calculated electric field (see previous section 4.1.1), the next step simulates the drift of the electron charge cloud from the initial event location to the anode. The drift of holes to the back contact does not contribute significantly to the anode signal and is neglected. There are different approaches to simulate the drift:

- A collective charge cloud approach, as implemented in some germanium detector simulations ([99] and [100]), simulates the entire charge cloud as single object with a location and size. This approach is not very suitable for an SDD, as the charge cloud is relatively large compared to the features of the electric field.
- A density approach would overcome this issue by simulating the time evolution of the full three-dimensional electron density in the detector volume. However, the computational effort is currently prohibiting the use of this approach.
- In a multi-body approach, the track of each single of the $\mathscr{O}(10000)$ electrons in the charge cloud is simulated individually in a Monte Carlo fashion. This approach allows a true three-dimensional simulation with almost infinite spatial resolution and is used in this work.
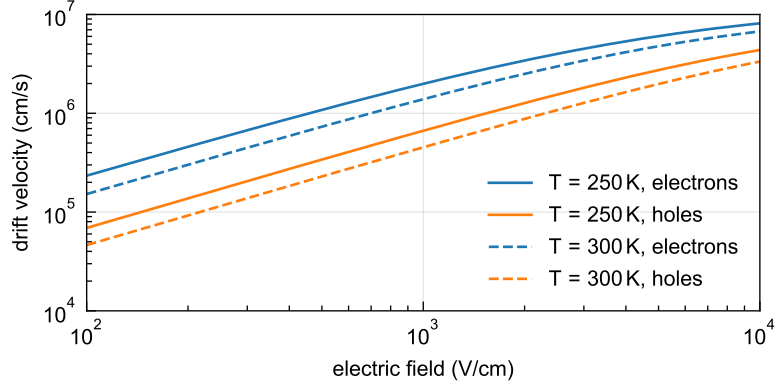
Figure 4.7: Empirical relation between drift velocity and electric field strength in silicon [101]. At low field strength, there is a linear relation with a slope given by the mobility μ.

The velocity of each electron is calculated from the electric field at the electron location. The simulation uses an empirical velocity model $v(\mathscr{E})$ as illustrated in figure 4.7 from [101].

The empirical model indicates that cooling the detector from room temperature ($T \approx 300\,\mathrm{K}$) to $T \approx 250\,\mathrm{K}$ leads to an increase of the drift velocity by around 50 %. At a small electric field strength $\left|\vec{\mathscr{E}}\right| < 1\,\mathrm{kV/cm}$, the velocity is linearly depending on $\vec{\mathscr{E}}$

$$\vec{v} = \mu\vec{\mathscr{E}}, \tag{4.3}$$

with mobility $\mu \approx 2400\,\mathrm{cm^2/Vs}$ at $T = 250\,\mathrm{K}$. During the radial drift in the SDD volume the electric field has a magnitude of around $0.5\,\mathrm{kV/cm}$ (see figure 4.6), which gives a drift speed of $1.1 \cdot 10^6\,\mathrm{cm/s}$ or $11\,\mathrm{\mu m/ns}$. Consequently, the drift time from the edge of the detector at $r = 1400\,\mathrm{\mu m}$ to the anode takes around $130\,\mathrm{ns}$.

The effect of diffusion is added by a random walk of each individual electron. The spatial spread within one simulation time step Δt is described by the diffusion law [81]

$$\sigma_x = \sqrt{2D\Delta t}. \tag{4.4}$$

The diffusion constant D depends on the temperature T and the mobility μ by

$$D = \frac{k_B T}{\mu e}, \tag{4.5}$$

with the Boltzmann constant k_B and elementary charge charge e. At $T = 250\,\mathrm{K}$ one obtains $D = 51.2\,\mathrm{cm^2/s}$ for electrons.

The coulomb repulsion is currently neglected in the simulation, as it is a small effect, compared to diffusion, for low energy events ($E \lessapprox 30\,\mathrm{keV}$) [88]. The initial charge cloud size is also neglected for the same reason. The simulation of an event with energy E is initialized by creating $n = E/w$ electrons (see table A.1) at a single point at a depth of $2\,\mathrm{\mu m}$, close to the entrance window. The drift of each electron is simulated for small steps in time $\Delta t = 10\,\mathrm{ps}$. At each step, the new position of each electron is calculated according to the following algorithm:

1. The electric field $\vec{\mathscr{E}}$ is evaluated at the location of the electron.
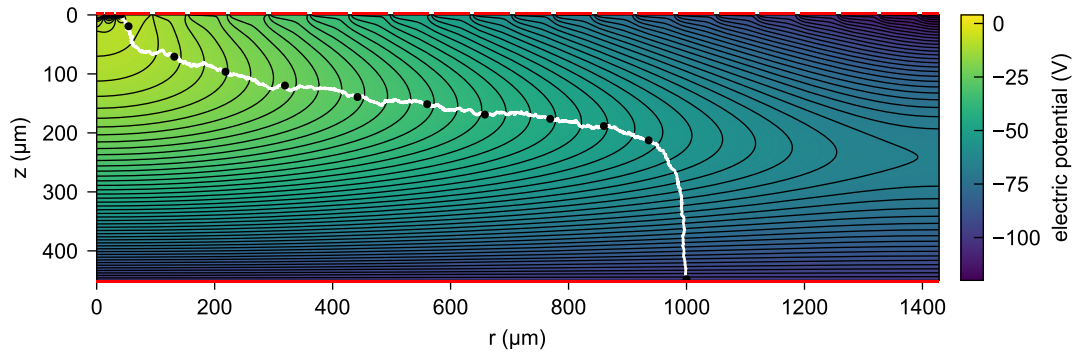2. The velocity of the electron $\vec{v}_{\mathrm{drift}}$ is calculated using the mobility model.

Figure 4.8: Simulated drift trajectory of a single electron. The trajectory starts at the entrance window and ends at the anode of the detector. Each black dot corresponds to 1000 simulation steps or a time span of 10 ns.

3. Three random numbers for the random motion vector $\vec{dx}_{\mathrm{diff}}$ by diffusion are drawn from a distribution with spread according to equation 4.4.
4. The position change of the electron is the sum of the term from its drift velocity and its random motion $\vec{x}_{\mathrm{new}} = \vec{x}_{\mathrm{old}} + \vec{v}_{\mathrm{drift}} \cdot \Delta t + \vec{dx}_{\mathrm{diff}}$

An example of the simulated drift path of a single electron starting at a radius $r_0 = 1000\,\mu\mathrm{m}$ is shown in figure 4.8. In the example, the drift takes 102 ns, which corresponds to 10 200 simulation steps. Compared to the electric field lines in figure 4.2, the random walk from diffusion is visible.

Figure 4.9 shows the drift of a 30 keV event ($n = E/w = 8219$ electrons). The figure compares the drift of events with four different incident radii: The first simulation starts at the pixel center, the second and third at radii 100 μm and 1000 μm and the last at the pixel border. In all cases, all electrons arrive at the anode, independent of the starting position. Only for the event at the pixel border, half of the electrons reach the anode of the shown pixel. The other half drifts to the anode of the neighboring pixel, which was included in the simulation but is not shown.

A detailed view of the anode region for the same simulations of the four drifting charge clouds is shown in figure 4.10. At the anode region, the inner guard ring electrode (IG) plays an important role and the effect of shielding the JFET is visible.
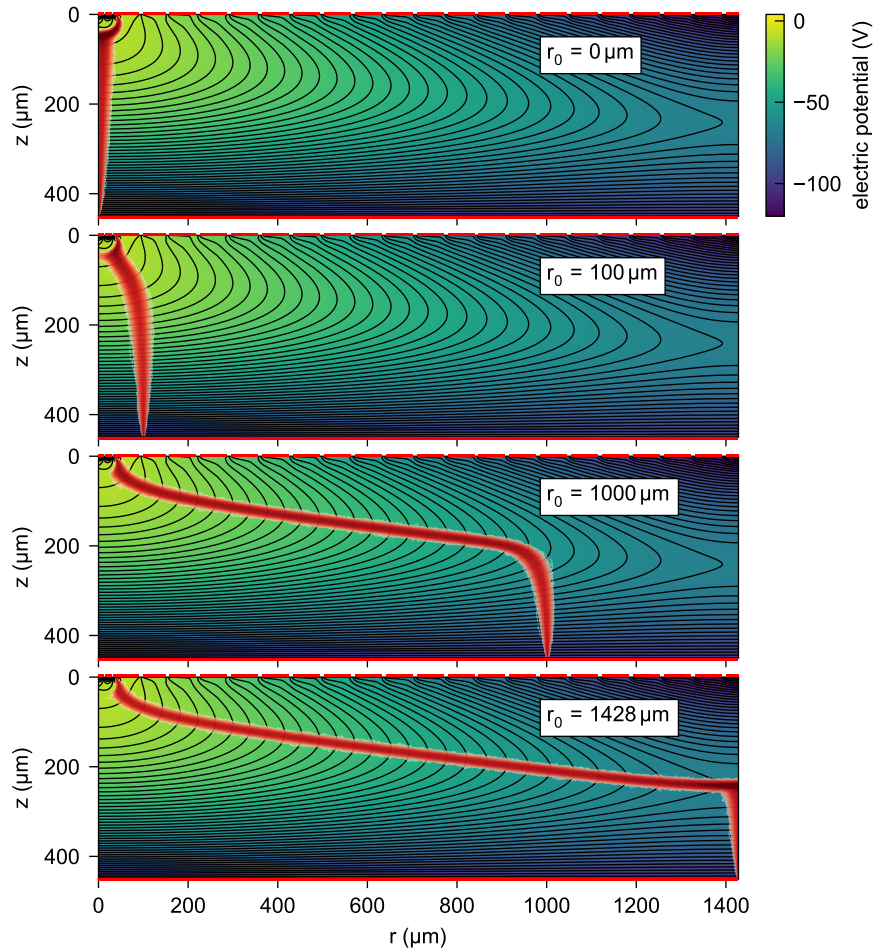
Figure 4.9: Simulated drift of a 30 keV event at different incident radii r_0. The red color map shows the time-integrated electron density. The effect of diffusion causes a broad band of trajectories, compared to the electric field lines in figure 4.2.
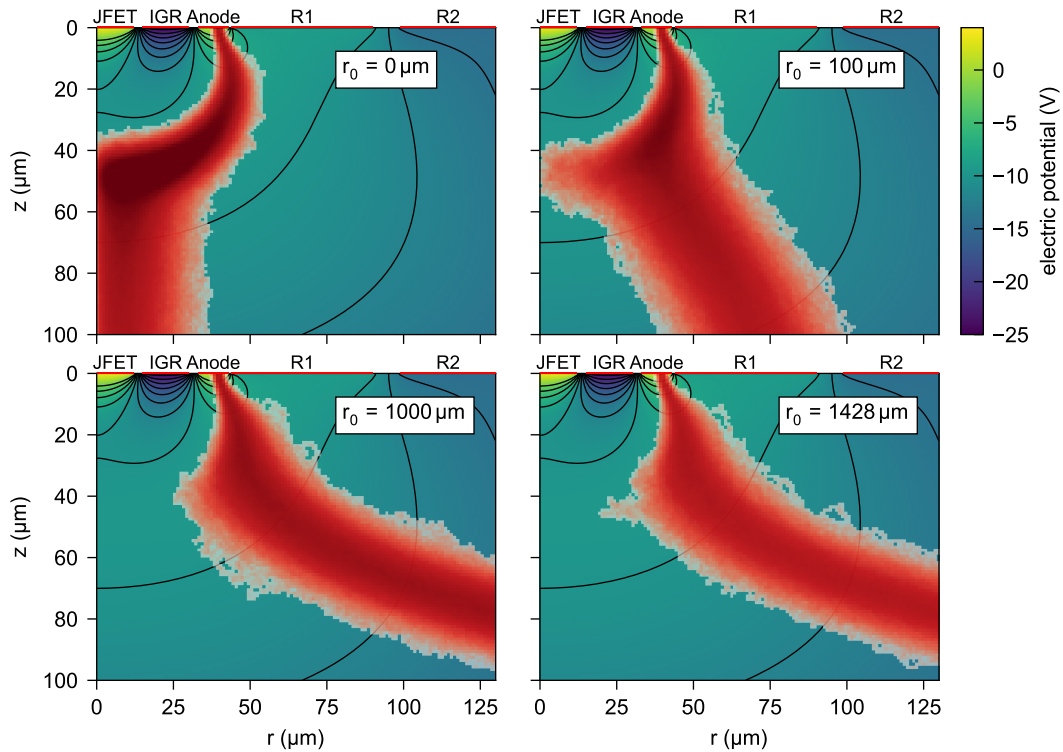
Figure 4.10: Zoom to the anode region of the simulated drift of a 30 keV event at different incident radii r_0 (see figure 4.9). The inner guard ring (IG) prohibits the electron trajectories from reaching the JFET.

4.1.3 Part 3: signal formation

In the last step of the simulation, the signal shape at the anode is calculated. According to the theorem of Shockley-Ramo, the amplitude of the induced signal $Q(t)$ on the anode depends on the weighting potential $\Phi_w(\vec{x})$ of the anode at the position of the charge q [102, 103]. The total signal at the anode is obtained by summing over all drifting electrons:

$$Q(t) = \sum_{i=0}^{n} q \cdot \Phi_w(\vec{x}_i(t)). \tag{4.6}$$

The weighting potential $\Phi_w(\vec{x})$ is calculated by solving the electric potential in the SDD for all electrodes grounded except the anode, which is set to unity. The space charge is neglected for the calculation of $\Phi_w(\vec{x})$. The resulting weighting potential is shown in figure 4.11.

Due to the ring electrodes and the inner guard ring, which sit close to the anode on the readout side of the detector, Φ_w is zero in most of the detector volume. Only in the last tens of µm around the anode, Φ_w is significantly greater than zero. This means that the majority of the total signal is only induced at the anode when the electron charge cloud drifts through the anode region of the device.

The calculated signals of the four previously studied events at different radii are shown in figure 4.12. Depending on the incident radius r_0, the signal shape varies significantly. The drift time varies between 25 ns and 240 ns. Furthermore, the 10 % to 90 % rise time varies between 10 ns and 76 ns.
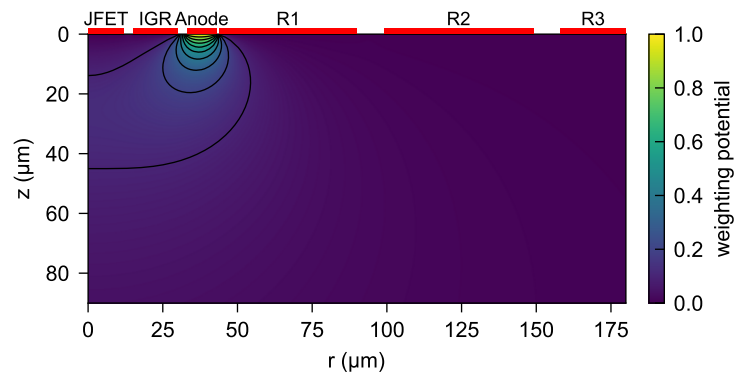
Figure 4.11: Weighting potential Φ_w of the anode. Not the full SDD crosssection is shown, but only a zoom to the anode region. The outermost equipotential line corresponds to $\Phi_w = 0.05$.
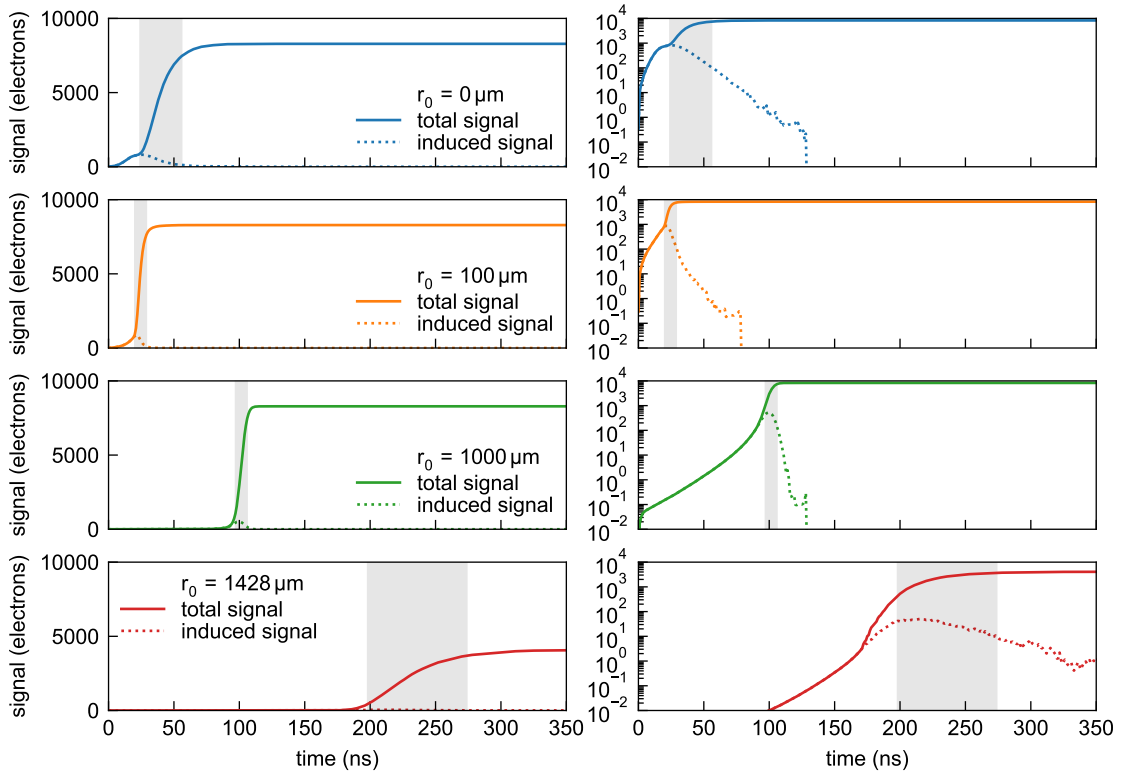

Figure 4.12: Simulated signals for four different events with incident radii $r_0 = 0\,\mu\text{m}$, $100\,\mu\text{m}$, $1000\,\mu\text{m}$, and $1428\,\mu\text{m}$, respectively. The drift of the four events is detailed in figures 4.9 and 4.10. The right column is identical to the left column but has a logarithmic y-axis. At $t = 0$, a 30 keV charge cloud (8219 electrons) is injected at the entrance window side of the detector. The dashed signal is the contribution of drifting electrons, and the solid line includes the electrons already collected at the anode. The shaded span marks the 10 % to 90 % rise time.
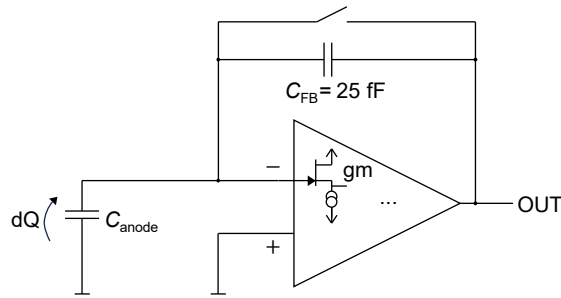
Figure 4.13: Conceptual circuit of a charge sensitive amplifier. The first transistor is often implemented as JFET, as shown here, or as MOSFET.

The two special cases at the pixel center ($r_0 = 0\,\mu$m) and the pixel border ($r_0 = 1428\,\mu$m) show a relatively slow signal rise time of 32 ns and 76 ns, respectively. This is explained by the slow drift at the two saddle points of the electric field in the device, which are above the JFET center and at the pixel border. The signal at the pixel border has only half of the full amplitude, as half of the electrons drift to the neighboring pixel.

In summary, `driftsim` proves to be a powerful tool to study the shape of SDD pulses. Here only a small study of four example pulses at different incident radii was shown, which sheds light on the intrinsic drift time and signal speed of the TRISTAN SDD. Many more studies, for example, of the dependency of the pulse shape on the bias voltages, temperature etc., are possible. Most importantly, the simulation helps to understand and illustrate the fundamental drift process in the TRISTAN SDD.

4.2 Low-noise readout

The low-noise readout of the TRISTAN detector has the task to amplify the SDD anode signals with minimal noise to yield a good energy resolution. Furthermore, the readout is fast (the bandwidth limit is around 7 MHz) to preserve a good timing information of the events and to resolve individual events at high rate. In this section the readout circuit of the TRISTAN detector is described. Furthermore, the front-end circuit is studied with a circuit simulation.

4.2.1 Charge sensitive amplifier

The readout circuit of the TRISTAN detector is a Charge Sensitive Amplifier (CSA). The basic concept of the CSA is shown in figure 4.13. A detected event leads to a short charge pulse ΔQ at the anode. The anode is connected to the negative input of an operation amplifier. A feedback capacitor C_{FB} connects the output of the amplifier to the anode and thereby closes a negative feedback loop. With this negative feedback configuration, the voltage at the output is proportional to the total charge which arrived at the anode

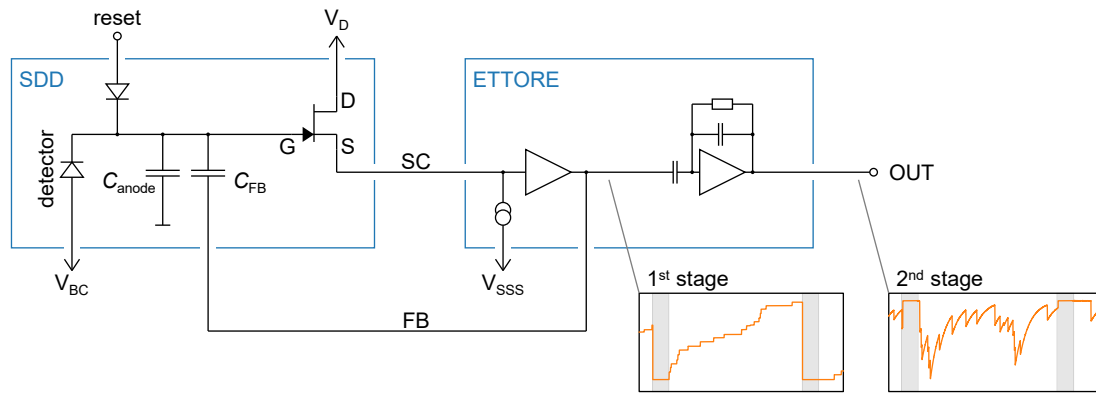$$\Delta V_{\mathrm{out}}(t) = \frac{\Delta Q}{C_{\mathrm{FB}}}. \tag{4.7}$$

Figure 4.14: Simplified readout circuit of one TRISTAN detector pixel. The charge sensitive amplifier loop is shared between the SDD and the ETTORE ASIC. The two orange waveforms illustrate the first stage and second stage signals during one reset cycle.

The concept of a CSA has two beneficial properties:

- The voltage at the anode is kept constant, so that there is no change in the electric field in the detector after an event. This also means that the anode capacitance does not need to be perfectly constant over voltage, as its working point is kept constant by the feedback loop.
- The amplitude of the resulting output pulse depends only on ΔQ and the feedback capacitance. By choosing the feedback capacitance small (here $C_{\mathrm{FB}} = 25\,\mathrm{fF}$), large output signals are achieved with a single amplifier stage.

The CSA circuit is used commonly for reading out radiation detectors (including SDDs, SiPMs, germanium detectors and many more, for example in [104, 105, 106]). The first transistor usually dominates the total noise performance of a CSA. If a JFET is used, the noise power density at the output scales with the ratio $\frac{C_{\mathrm{a}}}{g_m}$, where C_{a} is the anode capacitance (including the JFET gate) and g_m is the JFET transconductance. This means that a small anode capacitance and a large JFET transconductance are preferred. Details on the noise contributions are found in section 4.3.

4.2.2 TRISTAN readout circuit

The TRISTAN detector readout uses the ETTORE Application-Specific Integrated Circuit (ASIC), which is a 12-channel front-end ASIC for SDDs with an integrated JFET [91]. Figure 4.14 shows a simplified circuit diagram of the readout circuit for each channel. A JFET and a feedback capacitor are both directly integrated into the detector silicon at the anode of the pixel. Each SDD pixel is connected to the ETTORE ASIC by two lines: the source (SC) and feedback (FB). The readout circuit can tolerate relatively large stray capacitance of up to $40\,\mathrm{pF}$ for these lines, which is important to allow for the mechanically required distance between the SDD and ETTORE. The amplifier operates in pulsed reset mode, where the accumulating charge at the feedback capacitor is periodically removed by a short pulse applied to a reset diode. The pulsed reset mode is advantageous compared to a continuous reset mode, especially for maintaining a good energy resolution at high count rates above $10\,\mathrm{kcps}$ [104]. The output signal of the pulsed reset CSA (labeled ETTORE first stage) is a sawtooth signal, with a step-like increase for each event.

Additional to the first stage, a second amplifier stage is implemented in ETTORE. The second stage has a programmable voltage gain of -5 or -10 and adds an exponential decay with fixed time constant $\tau = 15\,\mu\mathrm{s}$ to the signals. The exponentially decaying output signals are beneficial for
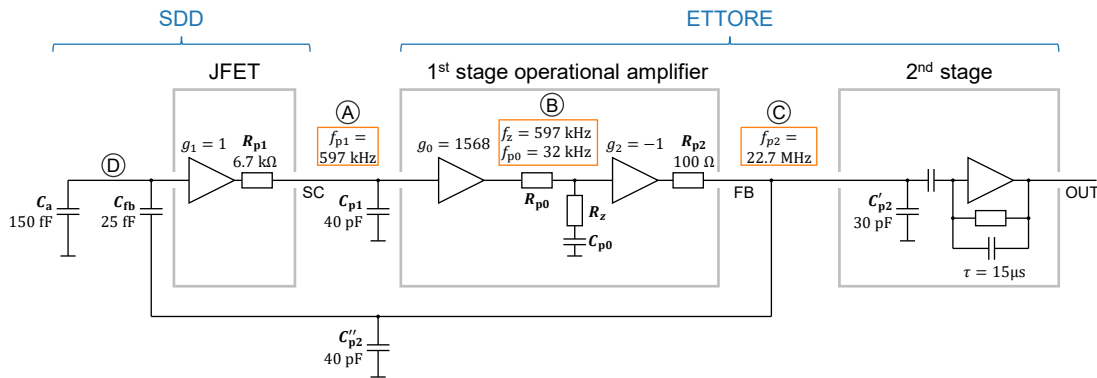
Figure 4.15: Equivalent circuit used for the simulation of the TRISTAN readout.

digitization, as the ADC range is used more efficiently compared to digitizing the first stage signal. The first and second stage waveforms are illustrated for a high input count rate of 100 kcps in figure 4.14.

4.2.3 Readout circuit simulation

This section studies the response of the TRISTAN amplifier utilizing an electric circuit simulation. Most circuit descriptions and calculations in this section are adapted from [89] and [107]. The focus of this section is to shed light on the main concepts and functional basics of the TRISTAN amplifier in a technical correct but not too detailed description.

The readout circuit simulation uses a linearized circuit of the TRISTAN CSA, as shown in figure 4.15. The main differences compared to the circuit in figure 4.14 are as follows:

- The JFET is described at its working point as a unity gain buffer with an output resistor $R_{p1} = \frac{1}{g_m}$. This represents the source follower configuration of the JFET, where the output voltage corresponds to the input voltage. A change at the input voltage corresponds to a change of the output current according to the transconductance.
- The first stage operational amplifier is modeled by a combination of two buffers. This models the frequency response of the ETTORE amplifier as described in [89].
- Two stray capacitances C_{p1} and C''_{p2} of 40 pF are added for the FB and SC lines to mimic the stray capacitance of the lines. Furthermore the second stage has a 30 pF input capacitance C'_{p2}.

The linearized circuit is evaluated using two approaches. First, the open loop gain of the system is calculated in frequency domain. This allows us to learn about the speed and stability of the amplifier loop. Following that, the response of the system to an input signal is calculated in time domain.

Open loop calculation The open loop gain characterizes the speed and stability of an amplifier loop. To calculate the open loop gain of the TRISTAN amplifier, the circuit from figure 4.15 is cut at any position where no current is flowing. Here the loop is cut at the input of the JFET. The frequency dependent complex gain $A(\omega)$ of the loop is calculated analytically by solving the system for an input $V_{\text{in}} = V_0 \cdot e^{i\omega t}$ and an output $V_{\text{out}} = A(\omega) \cdot V_0 \cdot e^{i\omega t}$. The loop is divided up into four

Table 4.1: Overview of zeros and poles in the amplifier loop of figure 4.15. The time constants and characteristic frequencies $f = (2\pi\tau)^{-1}$ are extracted from equations 4.8 to 4.10.

name	time constant	characteristic frequency	origin
zero (z)	$\tau_z = R_z C_{p0}$	$f_z = 597\,\text{kHz}$	ETTORE internal
pole (p0)	$\tau_{p0} = (R_z + R_{p0})C_{p0}$	$f_{p0} = 32\,\text{kHz}$	ETTORE internal
pole (p1)	$\tau_{p1} = R_{p1}C_{p1}$	$f_{p1} = 597\,\text{kHz}$	JFET + SC line
pole (p2)	$\tau_{p2} = R_{p2}C_{p2}$	$f_{p2} = 22.7\,\text{MHz}$	ETTORE + FB line

parts Ⓐ to Ⓓ. Each part can be calculated analytically:

$$\text{Ⓐ} \quad A_A(\omega) = g_1 \cdot \frac{1}{i\omega R_{p1}C_{p1} + 1} \qquad = g_1 \cdot \frac{1}{i\omega\tau_{p1} + 1} \tag{4.8}$$

$$\text{Ⓑ} \quad A_B(\omega) = g_0 \cdot \frac{i\omega R_z C_{p0} + 1}{i\omega(R_z + R_{p0})C_{p0} + 1} = g_0 \cdot \frac{i\omega\tau_z + 1}{i\omega\tau_{p0} + 1} \tag{4.9}$$

$$\text{Ⓒ} \quad A_C(\omega) = g_2 \cdot \frac{1}{i\omega R_{p2}C_{p2} + 1} \qquad = g_2 \cdot \frac{1}{i\omega\tau_{p2} + 1} \tag{4.10}$$

$$\text{Ⓓ} \quad A_D(\omega) = \frac{C_{fb}}{C_a + C_{fb}} \cdot \tag{4.11}$$

The combined gain of the feedback loop is

$$A(\omega) = \underbrace{g_0 g_1 g_2 \frac{C_{fb}}{C_a + C_{fb}}}_{= A_0} \cdot \underbrace{\frac{(i\omega\tau_z + 1)}{(i\omega\tau_{p0} + 1)(i\omega\tau_{p1} + 1)(i\omega\tau_{p2} + 1)}}_{\text{poles and zeros}}. \tag{4.12}$$

This equation has two parts: The first part A_0 is the DC-gain at $\omega = 0$. The second part is a quotient with a polynomial in the numerator and denominator, which describes the frequency-dependence of the gain. In engineering language, each term in brackets corresponds to a "zero" of the gain if it is in the numerator and a "pole" if it is in the denominator. The name pole and zero originate from the Laplace space, where $i\omega$ is replaced by $s = i\omega + \sigma$. In the 2D plane of ω and σ a pole or zero corresponds to a mathematical pole or zero at $\omega = 0$ and $\sigma = -\tau^{-1}$.

The DC-gain of the feedback loop is $A_0 = -224$ (or 47 dB). Equation 4.12 has one zero and three poles which are listed in table 4.1. The loop gain is fully characterized by the DC-gain and the characteristic frequencies of the poles and zeros.

Pole-zero matching in ETTORE   Table 4.1 indicates that the frequencies of the pole (p1) is matched by the frequency of the zero (z). This leads to the fact that the two corresponding terms in equation 4.12 cancel, which yields:

$$A(\omega) = g_0 g_1 g_2 \frac{C_{fb}}{C_a + C_{fb}} \cdot \frac{1}{(i\omega\tau_{p0} + 1)(i\omega\tau_{p2} + 1)}. \tag{4.13}$$

This method is sometimes called pole-zero matching. In the case of the TRISTAN detector it helps to get rid of the unwanted (but unavoidable) pole p1 [89, 91]. The loop gain after pole-zero matching (equation 4.13) contains only one pole below the target bandwidth at around 7 MHz
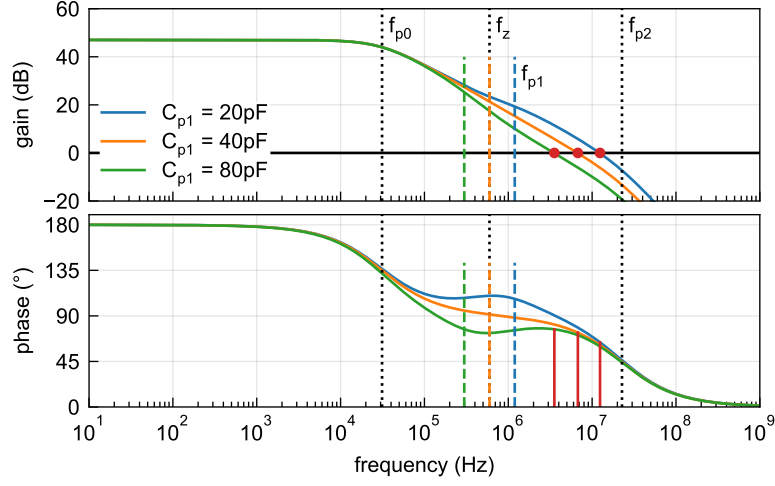
Figure 4.16: Bode plot of the open loop gain of the TRISTAN amplifier (equation 4.12). The frequency dependence is characterized by three poles p0, p1, and p2, as well as one zero z. In the nominal case, shown in orange, the pole p1 is matched by the zero z (pole-zero matching). If the SC line capacitance C_{p1} differs from its nominal value of 40 pF, the frequencies f_z and f_{p1} do not match (blue and green). Consequently, the bandwidth limit (red dots) and phase margin (red lines) varies significantly. The corresponding step response is shown in figure 4.17.

and one pole above the target bandwidth. This situation is beneficial for an amplifier, as explained in [108].

Equation 4.12 can also be expressed in a Bode plot, which shows the absolute amplitude $|A(\omega)|$ and the complex phase as a function of frequency $f = \frac{\omega}{2\pi}$, as shown in figure 4.16. The Bode plot of the open loop gain shows two important properties of the TRISTAN amplifier:

1. The bandwidth limit of the closed loop amplifier is given by the frequency where the gain is one (0 dB). In case of the TRISTAN front-end amplifier the bandwidth limit is $f_{BW} = 6.8\,\text{MHz}$. The 10 % to 90 % output rise time to a step-like input signal can be estimated by [89]

$$t_{\text{rise}} = \frac{0.35}{f_{BW}} \approx 50\,\text{ns}. \tag{4.14}$$

2. The shape of the rising edge of the output signal depends on the so-called phase margin of the amplifier loop [108]. The phase margin is the complex phase of the gain at the bandwidth limit f_{BW} and is marked as red line in figure 4.16. The optimal phase margin is around 60°, causing a fast step response without overshoot. Lower values of the phase margin correspond to an overshoot in the amplifier's step response or even oscillations. Larger values of the phase margin cause a long exponential rise time.

The pole-zero matching requires the characteristic frequencies of the pole p1 and the zero z to be the same. The frequency of the pole $f_{p1} = \frac{1}{2\pi R_{p1} C_{p1}} = \frac{g_m}{2\pi C_{p1}}$ is given by the transconductance of the JFET and the line capacitance of the SC-line. These parameters are determined by the JFET and readout geometry and are constrained by the used technology. The zero z, implemented in ETTORE, aims to match the hardware frequency f_{p1}. In case of a mismatch of f_z and f_{p1}, for example due to a variation of the SC line capacitance C_{p1}, both the bandwidth and the phase margin change significantly. Figure 4.16 illustrates this situation and plots the gain for three different SC-line capacitances C_{p1}. To prevent a mismatch of the pole-zero matching, ETTORE has a dedicated
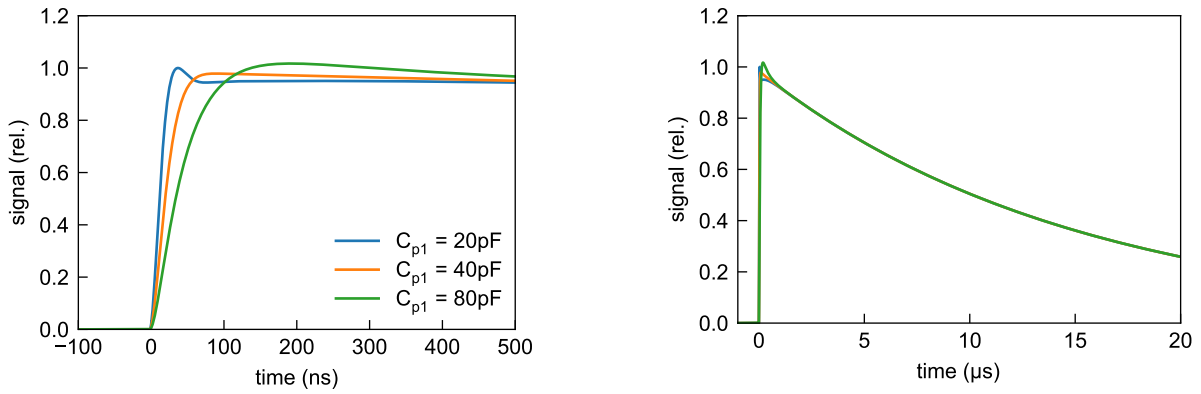
Figure 4.17: Simulated step response of the TRISTAN readout circuit. The simulation uses circuit 4.15 with three different values for SC-line capacitances C_{p1}. The plotted signal corresponds to the inverted OUT voltage. $C_{p1} = 40\,\text{pF}$ is the nominal scenario, where the pole-zero matching in the CSA loop works properly. If C_{p1} varies, the pulses show a slight overshoot and differ significantly in speed. The right plot is a zoomed-out version of the left plot, which shows the $\tau = 15\,\mu s$ decay from the second amplification stage.

BW input voltage, which allows for tuning the frequency of the zero z. The BW voltage should be adjusted to the present JFET transconductance and SC-line capacitance.

In practice this tuning of the BW voltage is difficult, as it can only be set globally for all pixels. In the current version of the ASIC board, the BW voltage cannot be tuned externally and is fixed to its default. For this reason a slight variation of the rising edges for different pixels is expected.

Closed loop simulation   The study of the open loop gain showed, that the SC line capacitance C_{p1} has a significant influence on the bandwidth limit and the phase margin of the amplifier. The bandwidth limit and the phase margin define the speed and shape of the amplifier's response in time domain. The time domain response of the TRISTAN amplifier is now calculated by a full (closed loop) simulation of the circuit of figure 4.15. To this end, a time domain solver was implemented in python, which calculates the currents, voltages and charges in each capacitor of the circuit at small time steps. The step response of the circuit is simulated by injecting a charge at time $t = 0$ to the anode capacitor C_a. The resulting output signal is shown in figure 4.17. A signal rise time of around 50 ns is observed for the nominal setting, as expected from equation 4.14. As already anticipated by the Bode plot, the signal shows a significantly faster or slower rise time if C_{p1} differs from the nominal value. Furthermore, in case of a mismatch, over and undershoots appear. The simulated variation of the pulse shape, observed with $C_{p1} = 20\,\text{pF}$ and $C_{p1} = 80\,\text{pF}$, is similar to the measured variation of pulse shapes within the channels of the 166-pixel TRISTAN device (see section 6.2.2).

In summary, this section illustrated and simulated how the TRISTAN amplifier works. One important feature of the TRISTAN amplifier is a pole-zero matching, which is essential for the fast readout of SDDs with integrated JFET. It is especially interesting to see which parameters in the hardware define the performance of the amplifier. It was found that the capacitance of the SC line, which involves the SDD routing, ASIC board routing, wire bonds etc. has a direct influence on the speed and shape of the signal rise. Moreover, the circuit simulation enables the study of further readout effects. For instance, section 6.3.2 uses the circuit simulation to investigate crosstalk, where a capacitive coupling between two neighboring amplifier circuits is present.
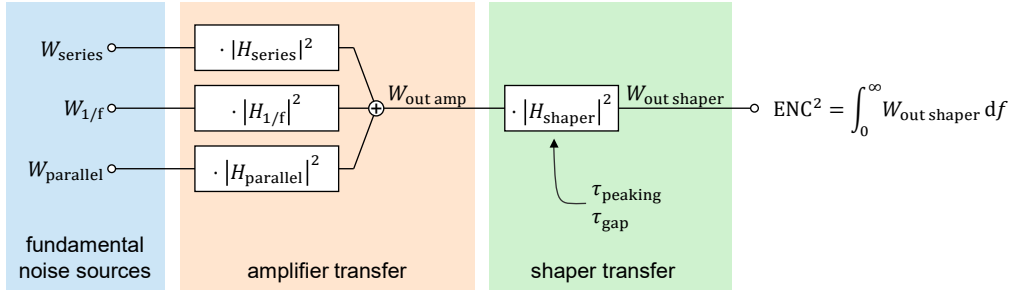
Figure 4.18: Simplified circuit diagram for the noise calculation. The parallel noise is a current noise source parallel to the detector diode, originating from the quantized nature of the leakage current. The series noise and 1/f noise originate from the JFET and are voltage noise sources in series to the detector diode.

4.3 Noise model

The electronic noise on the signals is an important performance parameter of a detector. The term "electronic noise" refers here to the fundamental noise sources that are not avoidable in electric circuits, like the thermal noise of resistors (also known as Johnson-Nyquist noise) or shot noise from the quantized nature of a current. These effects cause random noise on the analog detector signals. Effects like electromagnetic interference or oscillations are not addressed in this section.

The search for the best readout circuit to measure the charge signal of a detector has been carried out for a long time. Two very useful summaries, which include different readout options and the practical calculation of the expected noise contribution, are from the 1980s by E. Gatti and P. F. Manfredi [84] and by V. Radeka [109]. Most of the following calculations are based on their approaches and are carried out in the frequency domain, where noise is characterized by its frequency-dependent power density, denoted as W. The resulting uncertainty of the measured pulse height due to noise is usually quantified by the equivalent noise charge (ENC), which gives the 1σ uncertainty of the measured charge of an event. This section presents a model which describes W and ENC of the TRISTAN amplifier circuit as a function of the fundamental circuit parameters, like the anode capacitance and the JFET transconductance.

4.3.1 Fundamental sources of noise

The noise calculation uses a simplified CSA circuit, shown in figure 4.18. The circuit includes three sources of noise:

- **Parallel noise** One noise source originates from the quantized nature of the leakage current in the detector diode. This noise source is labeled parallel noise in the following description because of its location in the circuit relative to the detector diode. The parallel noise is modeled as a current source with the noise power density [109]

$$W_{\text{parallel}} = 2eI. \qquad \left[\frac{\text{A}^2}{\text{Hz}}\right] \tag{4.15}$$

- **Series noise** A second noise contribution comes from the JFET channel. It is called series noise because it is modeled as a voltage source at the JFET gate in series to the detector

Figure 4.19: Conceptual sketch of the noise calculation. The transfer functions of the amplifier and the shaping filter are applied to the noise power density of the three fundamental noise sources.

diode with the noise power density

$$W_{\text{series}} = \frac{4k_B T a_n}{g_m} \ . \qquad \left[\frac{\text{V}^2}{\text{Hz}}\right] \tag{4.16}$$

This equation is similar to the thermal noise of a resistor $W_{\text{series}} = 4k_B TR$ where the resistance R is replaced by the inverse transconductance g_m^{-1}. The additional factor a_n is specific for the used JFET and has a typical value of $a_n \approx \frac{2}{3}$ [109], which is the value used for the noise calculation in this work.

- **1/f noise** A third noise contribution is the 1/f noise from the JFET. It is modeled as a voltage source in series to the detector diode, similar to the series noise. The noise power density is given by

$$W_{1/\text{f}} = \frac{A_f}{2\pi f} \ . \qquad \left[\frac{\text{V}^2}{\text{Hz}}\right] \tag{4.17}$$

This noise source scales with the inverse frequency f^{-1}. Therefore, compared to the series noise of equation 4.16, it dominates at low frequencies. The value of the 1/f noise constant A_f is specific to the JFET device.

In order to evaluate the contributions of these noise sources to the total noise power density at the amplifier output $W_{\text{out amp}}$, the noise power must be propagated to the amplifier output signal, where the three contributions are summed. After that, the shaping filter transfer is applied to obtain the ENC value. Figure 4.19 shows a conceptual sketch of the calculation. The propagation of a given noise power density $W_{\text{in}}(f)$ through a system is done by a multiplication with the transfer function in frequency domain $H(f)$:

$$W_{\text{out}}(f) = W_{\text{in}}(f)\,|H(f)|^2\ . \tag{4.18}$$

This simple formalism is possible because all involved systems (the amplifier circuit and the shaping filter) are linear and time-invariant[1].

---

[1]This means that the systems are linear for the input and output signal: If two arbitrary input signals v_{in1} and v_{in2} give the two output signals v_{out1} and v_{out2}, the sum of the input signals $v_{\text{in1}} + v_{\text{in2}}$ will give the output signal $v_{\text{out1}} + v_{\text{out2}}$. Furthermore the system does not depend on the absolute time. Such a linear time-invariant system is fully defined by its transfer function $H(f)$, which describes the systems response in frequency domain. A similar approach was already used for the open loop characterization of the TRISTAN amplifier in section 4.2.3, which is also a linear time-invariant system.

Table 4.2: Parameters used for the noise calculation. The two configurations of a room temperature and a moderately cooled detector differ in temperature parameter T. Furthermore, the leakage current I of the detector diode has a strong intrinsic temperature dependence.

parameter	description	value warm	value cold
I	leakage current	10 pA	0.1 pA
C_a	total anode capacitance	203 fF	203 fF
A_f	1/f constant	$3 \cdot 10^{-11}\,\text{V}^2$	$3 \cdot 10^{-11}\,\text{V}^2$
T	temperature	250 K	300 K
g_m	JFET transconductance	150 µA/V	150 µA/V

4.3.2 Noise power density at the amplifier output

The total noise power density at the amplifier output is

$$W_{\text{out amp}} = W_{\text{series}}|H_{\text{series}}|^2 + W_{1/\text{f}}|H_{1/\text{f}}|^2 + W_{\text{parallel}}|H_{\text{parallel}}|^2. \tag{4.19}$$

The three transfer functions H_{series}, $H_{1/\text{f}}$ and H_{parallel} are calculated from the circuit in figure 4.18:

$$H_{\text{series}} = \frac{C_{\text{FB}} + C_{\text{anode}}}{C_{\text{FB}}} \qquad\qquad |H_{\text{series}}|^2 = \frac{(C_{\text{FB}} + C_{\text{anode}})^2}{C_{\text{FB}}} \tag{4.20}$$

$$H_{1/\text{f}} = \frac{C_{\text{FB}} + C_{\text{anode}}}{C_{\text{FB}}} \qquad\qquad |H_{1/\text{f}}|^2 = \frac{(C_{\text{FB}} + C_{\text{anode}})^2}{C_{\text{FB}}} \tag{4.21}$$

$$H_{\text{parallel}} = \frac{1}{i2\pi f\,C_{\text{FB}}} \qquad\qquad |H_{\text{parallel}}|^2 = \frac{1}{(2\pi)^2 f^2 C_{\text{FB}}^2} \tag{4.22}$$

It should be noted that the transfer function H_{parallel} maps from a current source to an output voltage, so the unit is $\frac{V}{A}$, while the other two transfer functions H_{series} and $H_{1/\text{f}}$ map from a voltage source to a output voltage, so the unit is 1. The resulting total noise power density at the amplifier output is obtained by plugging equations 4.20-4.22 and 4.15-4.17 into equation 4.19:

$$W_{\text{out amp}} = \underbrace{\frac{(C_{\text{FB}} + C_{\text{anode}})^2 4k_B T a_n}{C_{\text{FB}}^2 g_m}}_{\text{series}} + \underbrace{\frac{(C_{\text{FB}} + C_{\text{anode}})^2 A_f}{C_{\text{FB}}^2}\frac{1}{2\pi f}}_{1/\text{f}} + \underbrace{\frac{2eI}{C_{\text{FB}}^2}\frac{1}{(2\pi f)^2}}_{\text{parallel}}. \tag{4.23}$$

Here, the three terms series, 1/f, and parallel noise are sorted by their frequency dependence. Equation 4.23 describes the voltage noise power density at the output, the corresponding unit is $\frac{\text{V}^2}{\text{Hz}}$. Converting the unit to the equivalent input charge by $\mathrm{d}q = \mathrm{d}V_{\text{out}} \cdot C_{\text{FB}}$ is advantageous to later calculate the ENC. To this end, equation 4.23 is multiplied by C_{FB}^2 and is now given in the unit $\frac{\text{C}^2}{\text{Hz}}$:

$$W_{\text{out amp}}^{\text{ENC}} = \underbrace{\frac{C_a^2 4k_B T a_n}{g_m}}_{\text{series}} + \underbrace{C_a^2 A_f \frac{1}{2\pi f}}_{1/\text{f}} + \underbrace{2eI \frac{1}{(2\pi f)^2}}_{\text{parallel}}. \tag{4.24}$$

This equation uses the total anode capacitance $C_a = C_{\text{anode}} + C_{\text{FB}}$. The resulting noise power density spectrum is plotted in figure 4.20 for two configurations listed in table 4.2. The two cases correspond to a room temperature configuration and a configuration at moderate cooling at $T \approx -30\,°\text{C}$.
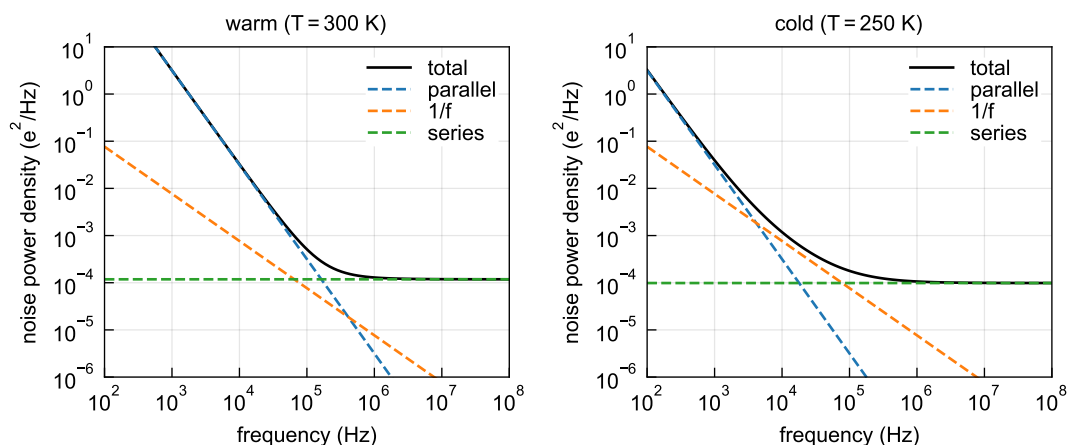
Figure 4.20: Noise power density at the output of the TRISTAN amplifier according to equation 4.24. The parameters of the circuit in warm and cold configuration are listed in table 4.2.

Cooling reduces the leakage current strongly, here a factor 100 is assumed. Therefore, cooling suppresses the parallel noise component, which dominates at low frequencies. At higher frequencies above $\mathcal{O}(100\,\text{kHz})$, the noise power is dominated by the series noise, which has only a slight, linear, temperature dependence. Some parameters like the JFET transconductance g_m and the 1/f coefficient A_f may also have a small temperature dependence but are assumed to be constant here.

The model for the noise power density spectrum (equation 4.24) is a powerful tool for noise investigations, as it can be compared to a measured noise power density spectrum of the detector system. This method allows the extraction of the fundamental circuit parameters, like leakage current or the anode capacitance, from a direct measurement.

4.3.3 Equivalent noise charge and noise curve

The equivalent noise charge (ENC) value is now calculated from the noise power density given in equation 4.24 of the previous section. The used shaping filter is central for this calculation, and the ENC value depends strongly on the used filter shape and its characteristic time constants.

The shaping filter turns the step-like output signal of an event after the CSA into a defined signal shape of finite length. This is advantageous for maximizing the signal-to-noise ratio and avoiding pileup effects at high rates. The TRISTAN data acquisition system (DAQ) uses a trapezoidal shaping filter, so the shaping filter output of a physical event is a trapezoid with rise time τ_{peaking} and flat top time τ_{gap}[2]. The impulse response, step response, and transfer function of a trapezoidal filter with $\tau_{\text{gap}} = 0.5 \cdot \tau_{\text{peaking}}$ are shown in figure 4.21. The transfer function is calculated analytically

---

[2]In this thesis the names τ_{peaking} and τ_{gap} are used. Some other references use the names τ_{rise} and τ_{flattop}, which mean the same thing.
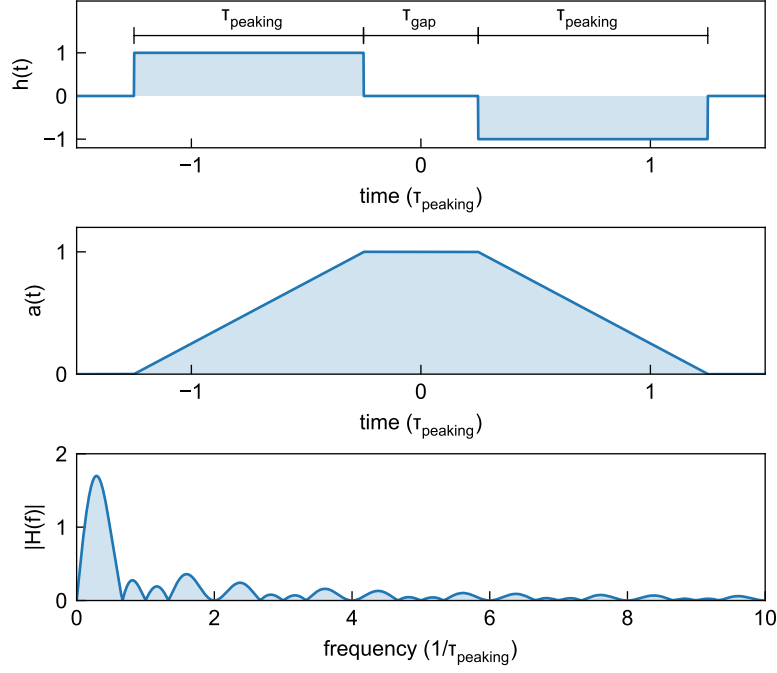
Figure 4.21: Impulse response $h(t)$, step response $a(t)$ and transfer function $|H(f)|$ of a trapezoidal shaping filter with $\tau_{\text{gap}} = 0.5\tau_{\text{peaking}}$. The filter is normalized such that the step response has amplitude 1. If $\tau_{\text{peaking}} = 1\,\mu\text{s}$ the maximum of the frequency response $|H(f)|$ is at $f = 420\,\text{kHz}$

by the Fourier transform of the impulse response:

$$H_{\text{trap}}(f) = \int_{-\infty}^{\infty} e^{-i2\pi f t} h(t) \mathrm{d}t \tag{4.25}$$

$$= \frac{1}{\tau_{\text{peaking}}} \frac{1}{i\pi f} \left[\cos\left(\pi f (\tau_{\text{gap}} + 2\tau_{\text{peaking}}) \right) - \cos\left(\pi f \tau_{\text{gap}} \right) \right]. \tag{4.26}$$

This transfer function allows the calculation of the noise power density $W_{\text{out trap}}^{\text{ENC}}$ after the trapezoidal filter, following equation 4.18.

The DAQ system evaluates the trapezoidal filter output pulse of each event at one point in time within the flat top of the trapezoid. The obtained value is an estimator for the deposit charge of the physical event. The ENC value is the standard deviation of the estimated charge due to noise. It is calculated by integrating the noise power density at the trapezoidal filter output $W_{\text{out trap}}^{\text{ENC}}$:

$$\text{ENC}^2 = \int_0^{\infty} W_{\text{out trap}}^{\text{ENC}}(f) \mathrm{d}f = \int_0^{\infty} W_{\text{out amp}}^{\text{ENC}}(f) |H_{\text{trap}}(f)|^2 \mathrm{d}f . \tag{4.27}$$

Equation 4.24 is plugged in, and the integral is split into three terms:

$$\text{ENC}^2 = \underbrace{\frac{C_a^2 4 k_B T a_n}{g_m} B_{\text{series}}}_{\text{series}} + \underbrace{C_a^2 A_f \cdot B_{1/f}}_{1/f} + \underbrace{2eI \cdot B_{\text{parallel}}}_{\text{parallel}}, \tag{4.28}$$

51
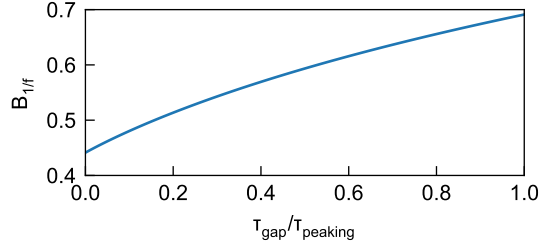
Figure 4.22: The 1/f noise integral $B_{1/f}$ as a function of $\frac{\tau_{\text{gap}}}{\tau_{\text{peaking}}}$. The integral is calculated numerically according to equation 4.30.
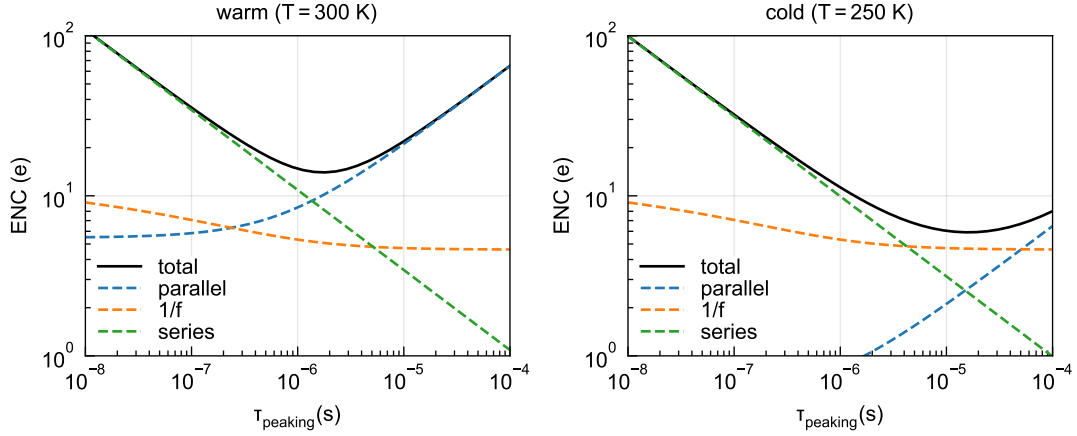
Figure 4.23: Calculated noise curves of the TRISTAN readout in a warm (left) and cold (right) configuration. The curves are calculated with equation 4.28 and parameters from table 4.2 and constant $\tau_{\text{gap}} = 480\,\text{ns}$.

with

$$B_{\text{series}} = \int_0^\infty |H_{\text{trap}}(f)|^2 \mathrm{d}f \qquad = \frac{1}{\tau_{\text{peaking}}} \tag{4.29}$$

$$B_{1/f} = \int_0^\infty \frac{1}{2\pi f} |H_{\text{trap}}(f)|^2 \mathrm{d}f \qquad \approx 0.59 \quad (\text{if } \tau_{\text{peaking}} = 2\tau_{\text{gap}}) \tag{4.30}$$

$$B_{\text{parallel}} = \int_0^\infty \frac{1}{(2\pi f)^2} |H_{\text{trap}}(f)|^2 \mathrm{d}f \qquad = \frac{\tau_{\text{peaking}}}{3} + \frac{\tau_{\text{gap}}}{2}. \tag{4.31}$$

These three integrals describe how the three noise terms scale with the trapezoidal filter parameters τ_{peaking} and τ_{gap}. The integrals B_{series} and B_{parallel} were solved analytically. The integral $B_{1/f}$ was calculated numerically. With increasing τ_{peaking} the series noise contribution decreases, while the parallel noise contribution increases. The 1/f noise is almost independent of τ_{peaking} but has a small dependence on the ratio $\tau_{\text{peaking}}/\tau_{\text{gap}}$, as plotted in figure 4.22. In case $\tau_{\text{peaking}} = 2\tau_{\text{gap}}$, which is realistic for the TRISTAN readout, $B_{1/f}$ is 0.59.

The plot of the ENC as a function of the time constant of the shaping filter is called noise curve. In the case of the trapezoidal filter, only τ_{peaking} is varied, while τ_{gap} is kept constant at $\tau_{\text{gap}} = 480\,\text{ns}$. Figure 4.23 shows the calculated noise curve from equation 4.28 for the warm and cold configura-

tion. The noise curve has a minimum, where the series and parallel noise contributions are roughly equal. In the warm setup, this minimum is at $\tau_{\text{peaking}} \approx 2\,\mu s$, and in the cold setup, it is close to $\tau_{\text{peaking}} \approx 20\,\mu s$.

At a low rate, the best spectroscopic performance is obtained at this minimum of the electronic noise. At high rates, however, another constraint on τ_{peaking} comes from the accepted amount of pileup. In order to keep the total amount of pileup below around 20 % at an input count rate of 100 kcps, a peaking time of $\tau_{\text{peaking}} \leq 1\,\mu s$ is required. In this case, the series noise dominates the electronic noise. The expected equivalent noise charge at $\tau_{\text{peaking}} = 960\,ns$ is 11.5 electrons.

4.3.4 Optimum filter

The optimum filter is the shaping filter which has the lowest possible ENC value for a given noise situation. This section briefly elaborates on what the optimal filter for the TRISTAN detector would look like and compares its performance to that of a trapezoidal filter.

The shape of the optimum filter depends on the noise power density spectrum of the amplifier output signal. If the noise power density spectrum comprises only a parallel and a series noise component, the optimal filter shape can be calculated analytically, as demonstrated for example in [109]. The resulting filter shape is a cusp with a characteristic time constant τ_c:

$$h(t) = e^{-\frac{|t|}{\tau_c}}. \tag{4.32}$$

The optimum filter for the full noise model of a cooled detector (compare table 4.2) has to be calculated numerically. The calculation utilizes a time-discrete filter with a sampling rate of 62.5 MHz and free filter coefficients. The filter coefficients are then fitted to minimize the ENC value, calculated with equation 4.27. The resulting optimum filter for the full noise model has a very similar shape to equation 4.32 with $\tau_c \approx 10\,\mu s$ and reaches an ENC of 4.6 electrons. This value should be compared to the ENC of the best possible trapezoidal filter with $\tau_{\text{peaking}} = 17\,\mu s$ and $\tau_{\text{gap}} = 0\,\mu s$, which is 5.8 electrons.

So far, the derivation of the optimum filter did not have constraints on its output shape. However, there are good reasons to apply constraints on the filter output shape in an actual detector setup. First, the length where the filter output is different than zero should be limited to constrain the pileup amount. Second, there should be a region around the filter's maximum where the shaping filter output is flat. A flat filter top reduces the influence of a timestamp jitter on the energy resolution. Furthermore, a flat filter top makes the reconstructed pulse height independent of the signal rise time. The last point is especially important for detectors with long drift times, like the SDD, where the pulse rise time can vary with the primary interaction position. The cusp-shaped optimum filter does not fulfill these constraints, as it has infinite tails and a sharp tip.

Now the optimum filter which fulfills the two constraints mentioned above is calculated. In particular, a flat top of 300 ns is required and the window before and after the flattop is constrained to 1 μs. The resulting constrained optimal filter is shown in figure 4.24. The figure also shows the trapezoidal filter with the same constraints and the optimal filter without constraints. The ENC values of the filters are compared in table 4.3. The trapezoidal filter and the optimum filter with constraints have similar response shapes and ENC values. The difference on the 10^{-3} level is neg-
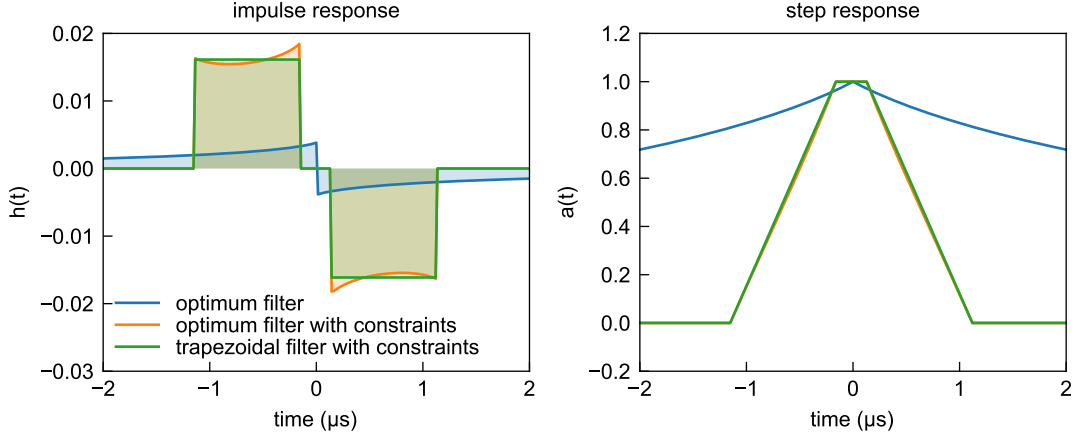
Figure 4.24: Comparison of the impulse response $h(t)$ (left) and step response $a(t)$ (right) of optimum filters and the trapezoidal filter. The filters are optionally constrained to have non-zero impulse response entries only within two windows of $1\,\mu s$ duration, separated by 300 ns.

Table 4.3: Comparison of the equivalent noise charge (ENC) of the trapezoidal filter and the optimum filter, calculated with equation 4.27.

filter	length	ENC
optimum filter	∞	4.6 e
trapezoidal filter	$\tau_{\text{peaking}} = 17\,\mu s;\ \tau_{\text{gap}} = 0\,\mu s$	5.8 e
optimum filter with constraints	$\tau_{\text{peaking}} = 1\,\mu s;\ \tau_{\text{gap}} = 0.3\,\mu s$	11.21 e
trapezoidal filter with constraints	$\tau_{\text{peaking}} = 1\,\mu s;\ \tau_{\text{gap}} = 0.3\,\mu s$	11.22 e

ligible in practice. If the filter is unconstrained, the optimum filter has a slightly lower ENC than the trapezoidal filter.

In conclusion, the TRISTAN readout would not benefit from an optimal filter. The optimal filter and the trapezoidal filter are almost identical in shape and performance. The main reason for this is the constraint of having a fast total filter response, which is necessary to reduce pileup at high rates. It should be noted that this holds only if the noise power density on the detector signals follows the model from section 4.3.2. If there are significant features in the noise power density spectrum, for example, from electromagnetic interference, the performance gain of the optimal filter compared to the trapezoidal filter could be more significant.

4.3.5 Series noise and capacitive matching

For many applications (such as TRISTAN), the series noise is the dominant noise in the detector. To explore the options to minimize the series noise, the corresponding term in equation 4.28 is now studied:

$$\text{ENC}^2_{\text{series}} = \frac{C_a^2 4 k_B T a_n}{g_m} \cdot \frac{1}{\tau_{\text{peaking}}}.$$ (4.33)

This term can be minimized by cooling due to its dependence on the absolute temperature T. Nevertheless, this is a limited handle, as the electronic readout has to be in its specified temperature

Table 4.4: Estimated capacitances at the TRISTAN detector anode.

description	symbol	capacitance
feedback	C_{FB}	25 fF
anode ring	C_{ar}	112 fF
line from anode ring to JFET gate	C_{stray}	10 fF
JFET gate	C_g	56 fF
total	C_a	203 fF

range, and cooling to cryogenic temperature is also technically challenging. The TRISTAN detector aims to operate at a moderate cooling of around $-30\,°C$, achieved by conventional cooling liquid circulation.

The most important handle on the series noise comes from the detector capacitance C_a, which goes linear into ENC_{series}. This leads to the significant gain in performance of the SDD ($C_a \approx 200\,fF$) compared to the conventional PIN diode, which has a total anode capacitance of at least $C_a \approx 2\,pF$ for a similar pixel area.

The third handle is the transconductance g_m of the front-end amplifier. In JFETs (and also in MOSFETs), the transconductance scales directly with the size of the device (or the width of the channel, to be more precise), and so does the gate capacitance C_g. This can be expressed by the constant gain bandwidth product of the device $\omega_T = \frac{g_m}{C_g} = \text{const}$, which does not depend on the width of the channel but only on the technological implementation of the JFET. Furthermore, the total anode capacitance C_a can be expressed as the sum of the JFET gate capacitance C_g and the remaining capacitance C_d, which includes all other anode capacitance contributions. This yields

$$\mathrm{ENC}_{series}^2 \propto \frac{C_a^2}{g_m} = \frac{(C_d + C_g)^2}{\omega_T C_g} = \frac{C_d}{\omega_T} \underbrace{\left(\sqrt{\frac{C_g}{C_d}} + \sqrt{\frac{C_d}{C_g}} \right)^2}_{F^2,\ \text{minimal for } C_g = C_d}. \tag{4.34}$$

The term in brackets is minimal if the size of the JFET is chosen such that $C_g = C_d$. This relation is sometimes referred to as "capacitive matching" [109, 84, 81]. With capacitive matching, the dependence of the series noise becomes proportional to $\sqrt{C_d}$, while it was proportional to C_d if the size of the JFET is kept constant. It should be noted that this capacitive matching only works if g_m scales with C_g. If this is not the case, for example for a stray capacitance connecting the detector and JFET, this capacitance has to be included in C_d and will worsen the series noise.

The estimated capacitances at the TRISTAN detector anode are listed in table 4.4. The gate capacitance is estimated to be $C_g = 56\,fF$ and the remaining anode capacitance is $C_d = 147\,fF$. In this case, the series noise would be reduced by 12 % if the JFET and thereby g_m and C_g would be increased by a factor $\frac{147}{56} = 2.6$.

This example shows that a moderate mismatch (up to roughly a factor 5) of C_d and C_g has a small effect on the series noise. Only if the capacitive matching is off by orders of magnitude, adapting the JFET size can significantly improve the series noise. In the design of the integrated JFET of
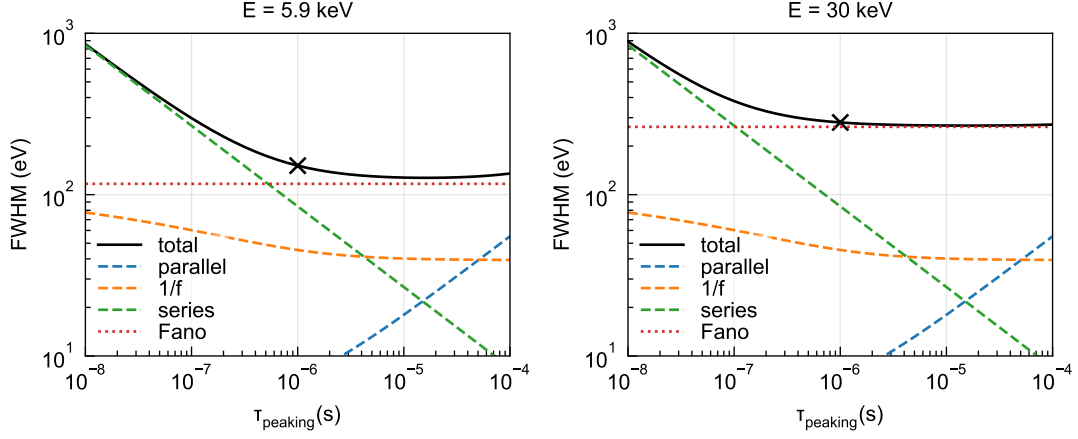
Figure 4.25: Energy resolution (FWHM) of the TRISTAN detector as a function of τ_{peaking} for two different deposit event energies $E = 5.9\,\text{keV}$ and $30\,\text{keV}$. τ_{gap} has the constant value $\tau_{\text{gap}} = 480\,\text{ns}$. The contribution of electronic noise (equation 4.28) and the Fano law A.3 are taken into account.
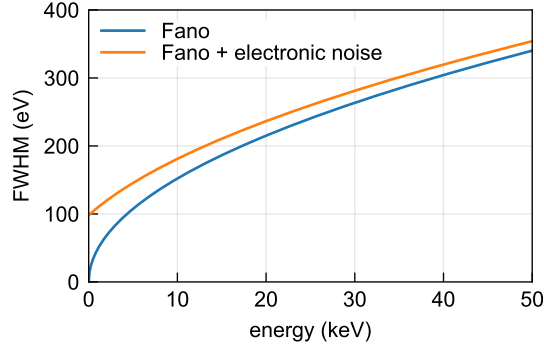
Figure 4.26: Energy resolution of the TRISTAN detector as a function of the deposit event energy. The contribution of electronic noise (equation 4.28) and the Fano law A.3 are taken into account, and the peaking time is fixed to $\tau_{\text{peaking}} = 1\,\mu\text{s}$.

the TRISTAN detector, the size of the JFET is limited by the available space within the anode. Therefore, the moderate mismatch is accepted.

4.3.6 Noise and energy resolution

The equivalent noise charge, calculated in section 4.3.3 contributes to the overall energy resolution of the detector by

$$\sigma_{\text{noise}} = \frac{w}{e}\text{ENC}, \tag{4.35}$$

where $w = 3.63\,\text{eV}$ is the pair creation energy in silicon (see table A.1). Another contribution to the energy resolution, which dominates in most cases, comes from the statistical fluctuations of the deposit number of electron-hole pairs in the charge cloud. This fluctuation is described by the Fano law (see section A.1)

$$\sigma_{\text{stat}} = \sqrt{wFE}, \tag{4.36}$$

with deposit energy E and Fano factor $F = 0.115$ for silicon. For electrons as incident particle, the partial charge collection at the entrance window is another relevant contribution. For X-rays with keV energy, the combination of σ_{stat} and σ_{noise} usually provides a good description of the energy resolution. As both the contributions are statistically independent, they are added in square. This yields

$$\text{FWHM} = 2\sqrt{2\ln 2} \cdot \sqrt{\sigma_{\text{noise}}^2 + \sigma_{\text{stat}}^2} = 2\sqrt{2\ln 2} \cdot \sqrt{\frac{w^2}{e^2}\text{ENC}^2 + wFE}. \qquad (4.37)$$

Due to the dependence of ENC from equation 4.28 on the peaking time of the shaping filter, the overall energy resolution depends on the peaking time.

Figure 4.25 plots the overall energy resolution for two different energies $E = 5.9\,\text{keV}$ and $E = 30\,\text{keV}$. With the target peaking time $\tau_{\text{peaking}} = 960\,\text{ns}$, the energy resolution is FWHM $= 151\,\text{eV}$ at $5.9\,\text{keV}$ deposit event energy and FWHM $= 281\,\text{eV}$ at $30\,\text{keV}$ deposit event energy. In both cases, the energy resolution is dominated by the Fano law. Figure 4.26 shows how the energy resolution, assuming ENC $= 11.5$ electrons, depends on the energy. The energy resolution from electronic noise, without Fano contribution, would be FWHM $= 98.2\,\text{eV}$. The Fano contribution dominates the energy resolution for all energies $E > 4.2\,\text{keV}$. A comparison of the modeled energy resolution from figure 4.26 to measurements with X-rays and electrons will be shown in section 6.2.4.

4.4 Summary

This chapter showed several studies of the properties of the SDD signals, focusing on signal formation in the detector and on readout effects. A signal simulation was developed to investigate the charge cloud drift in the TRISTAN detector, revealing drift times ranging from 25 ns to 200 ns and signal rise times between 32 ns and 76 ns, depending on the interaction location. Additionally, the TRISTAN preamplifier circuit was analyzed, showing that the rise time of output signals is significantly affected by the line capacitance between the SDD and ETTORE ASIC. These results about the rising edge of the SDD pulses will be compared to measurements in section 6.2.2.

Furthermore, a model for electronic noise was developed. The noise model predicts the noise power density and the equivalent noise charge of the TRISTAN detector based on fundamental design parameters, like the anode capacitance or the temperature. With the default parameters of TRISTAN, the model evaluation yields an equivalent noise charge of 11.5 electrons, which is in line with the TRISTAN target energy resolution of less than 300 eV FWHM. Furthermore, the concept of an optimum filter and the concept of capacitive matching were shortly discussed. The result is that the noise performance of the TRISTAN detector cannot be improved significantly by these methods.

5 Calibration sources

The calibration of the TRISTAN detector is crucial for comprehending and mitigating variations in its response. Section 5.1 of this work summarizes radioactive calibration sources available. The content of this work was the development of a thermionic electron gun, offering increased flexibility compared to radioactive sources. The development and commissioning of the electron gun is described in section 5.2. Finally, section 5.3 presents an approach developed within this work, wherein a pulsed laser is employed to precisely generate a charge cloud in the detector. A first demonstration measurement with a 7-pixel detector is also shown in this section.

5.1 Radioactive sources

Radioactive sources are a simple but precise source of radiation. They offer monoenergetic spectra e.g. with γ-rays from nuclear transitions or X-rays from atomic transitions. Besides these sources of photons, there are also decay mechanisms which provide monoenergetic electrons. Examples are electrons from internal conversion of nuclear transitions or Auger electron emission from atomic transitions.

X-ray sources

In the case of SDDs, the use of the radioactive iron isotope ^{55}Fe has become established as a standard source for comparing the detector performance (e.g. [83, 110, 85]). The ^{55}Fe nucleus undergoes an electron capture decay, transitioning into the ground state of ^{55}Mn with a half-life of 2.73 a [111]. The deexcitation of the vacancy in the inner electron shell results in the emission of characteristic X-rays of Mn. The obtained X-ray spectrum comprises the K_α and K_β lines at 5.9 keV and 6.5 keV respectively [112].

Another radioactive X-ray source that provides higher energetic photons, reaching up to 60 keV, is the americium isotope ^{241}Am. It decays with a half-life of 432 a into the long-lived ^{237}Np via α-decay, with γ-emissions at 26 keV and 60 keV [111]. Besides the two γ-lines, characteristic X-ray lines of Np are emitted, with interesting energies between 12 keV to 21 keV. The α particle is not pertinent for calibration and is retained in the source material. Depending on the encasing material, more characteristic X-ray lines can be present in the spectrum.

The attenuation length of X-rays is usually larger than the penetration depth of electrons. For $\mathcal{O}(15\,\text{keV})$ X-rays in silicon, the attenuation length is similar to the detector thickness of 450 μm. The absorption profiles for different X-ray energies are compared in figure 5.1. For energies above roughly 10 keV, the detection efficiency drops as part of the X-rays pass the detector without interaction.
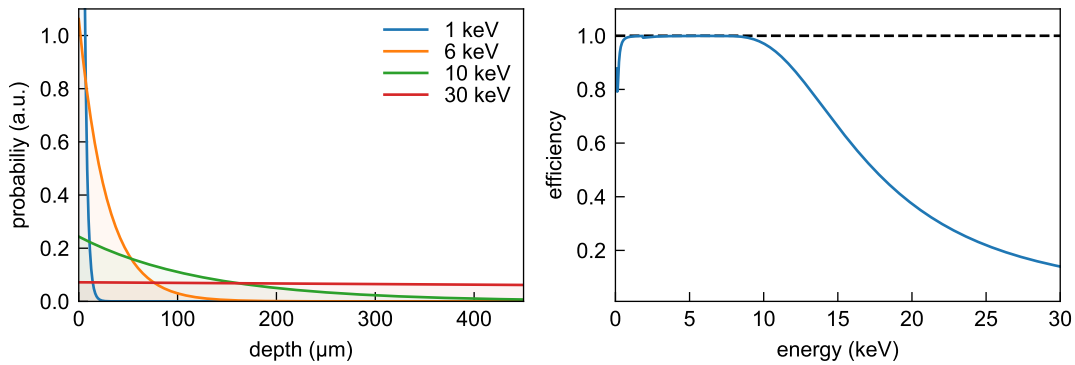
Figure 5.1: X-ray absorption profile (left) and detection efficiency (right) of a silicon detector. The detector is assumed to have a thickness of 450 μm and an insensitive layer of 10 nm at the entrance window. The curves are calculated based on attenuation coefficients from [112].

The entrance window limits the efficiency of low-energy X-rays. In between (from around 1 keV to 10 keV), the efficiency is approximately 1.

The absorption profile is an important input for interpreting a calibration measurement because the timing and drift characteristics of the detector depend on the depth of the primary charge cloud. The large penetration depth of X-rays before interacting means that the entrance window effects, which occur for electrons, are usually not visible in X-ray measurements. The line resolution of an X-ray calibration measurement is commonly used to quantify the noise situation for an SDD detector.

Electron sources

Within the KATRIN experiment, the decay of ^{83m}Kr is used to calibrate the beamline and spectrometer with monoenergetic electrons. ^{83m}Kr is generated by the decay of ^{83}Rb, which has a half live of 86 d. The isomeric state ^{83m}Kr subsequently decays via two γ-transitions with 32.2 keV and 9.4 keV and a half-life of 1.83 h. These two γ-transitions have a high conversion coefficient such that monoenergetic electrons are emitted. The kinetic energy of the emitted electron is reduced by the initial binding energy of the electron, which can come from a K, L, M, or N shell. The result is an electron spectrum with around twenty lines between 7.4 keV and 32.1 keV [113, 114].

A radioactive ^{83m}Kr source was used in previous investigations to characterize the TRISTAN detector with electrons [93]. Nevertheless, many challenges come with ^{83m}Kr as a calibration source:
  • Electrons may lose part of their kinetic energy in the source material, especially if the decaying atom does not sit exactly at the surface of the source material. This affects both gaseous and condensed sources.
  • The electrons are emitted isotropically in all directions, which leads to many scattered electrons from surrounding structures.
  • Due to the noble gas nature of ^{83m}Kr, it may vaporize from the surface of the source before it decays ($T_{1/2} = 1.8$ h).
  • The rate and energies are fixed.

5.2 Electron gun for TRISTAN

Besides the radioactive electron sources, there are many artificial sources of monoenergetic electrons (electron guns). In most electron guns, electrons are released from a metal surface, for example via the photoelectric effect, and subsequently accelerated by a defined electric potential difference. The KATRIN beamline features a sophisticated electron gun at its rear section, which is used to calibrate the electron transmission properties of the KATRIN gaseous source and spectrometer [115]. In addition, there is a UV-illuminated titanium plate, which can be inserted in the detector section of KATRIN to provide electrons for detector tests [70].

However, these electron sources cannot be used outside of the KATRIN beamline in a laboratory setup. Therefore, as part of this work, an electron gun was developed, which is suitable for characterization measurements of the TRISTAN detector modules in a laboratory environment outside of the KATRIN beamline. The key requirements of the electron source are to
1. provide monoenergetic electrons with kinetic energy up to 30 keV,
2. provide electron rates up to 100 kcps per pixel, and
3. illuminate the area of one TRISTAN detector module ($40 \times 38\,\mathrm{mm}^2$).

The first design choice for the laboratory setup is to not use superconducting magnets, which significantly simplifies the design and operation of the setup. Furthermore, the mechanism used to get free electrons is an important choice. There are three common options:
- **Photoelectric emission** A photocathode emits electrons when illuminated with light. The electron gun in the KATRIN rear section uses photoelectric emission from a backside-illuminated thin gold cathode [115].
- **Field emission** Field emission electron guns use a needle (typical tip size 100 nm) to create a strong electric field such that electrons can leave the metal surface via quantum tunneling [116].
- **Thermionic emission** A heated metal surface emits electrons. This technique is widespread in many devices, such as cathode ray tubes, electron microscopes, etc.

The electron gun developed in this work utilizes thermionic emission because of its robustness, flexibility in rate, and relatively simple design. One major challenge of a thermionic electron gun for detector characterization is the emission of light, which disturbs the detector. The development and commissioning of the thermionic electron gun was published in a journal article [117] and is summarized in the following sections.

5.2.1 Thermionic emission

At low temperatures, electrons in a metal are bound to the metal volume. The work function E_w is the work that electrons must carry out to escape the metal volume. A general formula for the emission flux F_{el} as a function of temperature T was derived by O. W. Richardson more than 100 years ago [118]:

$$F_{\mathrm{el}} = \frac{A'}{e} T^2 \exp\left(-\frac{E_w}{k_B T}\right). \tag{5.1}$$

Here, $A' \approx 1.2 \cdot 10^6\,\mathrm{A/K^2/m^2}$ is a constant [119], e is the elementary charge, and k_B is the Boltzmann constant. The exponential function in equation 5.1 dominates the electron flux dependence on temperature T. As an example, with realistic values $E_w = 4.25\,\mathrm{eV}$ and $T = 1500\,\mathrm{K}$, the electron flux doubles if the temperature increases by 32 K.

Table 5.1: Work functions of selected cathode materials

material	E_w
Tungsten (W)	4.55 eV [120]
Tantalum (Ta)	4.25 eV [120]
Yttrium oxide (Y_2O_3)	2.6 eV [121]
Barium oxide (BaO)	1.0 to 1.8 eV [121]
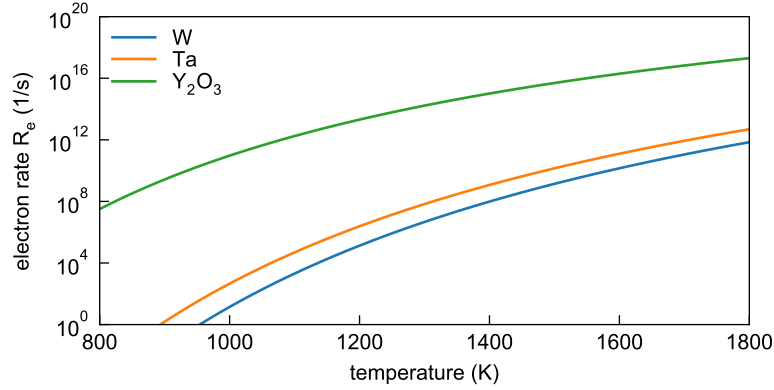
Figure 5.2: Electron emission rate R_{el} as a function of temperature. The rate is calculated by equation 5.1 and equation 5.2.

Typical work functions of cathode materials are listed in table 5.1. In general, a lower work function is advantageous for a thermionic electron source. Most metals have a work function around 4 eV to 5 eV. Oxide-coated cathodes, like BaO, have significantly lower work functions, reaching $E_W \approx 1$ eV. Nevertheless, their stability in air is usually a problem. The exposure to air is not avoidable during the assembly of the TRISTAN detector characterization setup. Thus, this work uses tantalum, which is mechanically robust and does not degrade in air [121]. Its work function $E_w = 4.25$ eV is lower than the work function of tungsten[1].

Figure 5.2 compares the emission rate R_{el} for the cathode materials W, Ta and Y_2O_3, using

$$R_{el} = F_{el} \cdot A \tag{5.2}$$

with an assumed emission area of $A = 0.157\,\mathrm{mm}^2$. To achieve a total rate of $\mathcal{O}(100\,\mathrm{kcps})$ a temperature of at least $T \approx 1100$ K is required with tantalum as cathode material.

5.2.2 Emission of light

When operating a glowing cathode in the vicinity of a silicon detector, light emission disturbs the detector. A photo current which adds to the diode's leakage current increases the parallel current noise of the amplifier (compare equation 4.28). The emitted light can be hindered geometrically, for example by having no line-of-sight between cathode and SDD. However, a small amount of light from reflecting surfaces was always present in electron gun measurements of this work. The emitted light spectrum and the SDD sensitivity to light is shortly addressed in the following.

---

[1]As an option in the future, the use of Y_2O_3 could be considered due to its low work function of $E_w = 2.6$ eV. However, the mechanical properties, stability, and durability in a frequently vented system remain to be tested.
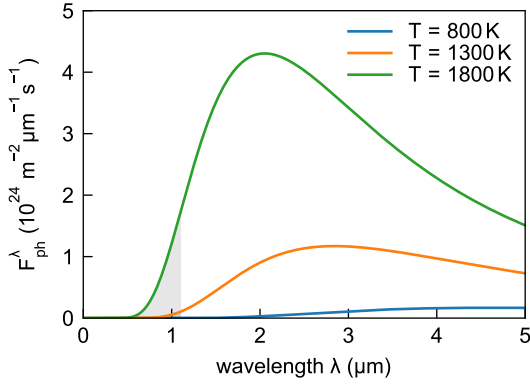
Figure 5.3: Spectral photon flux F_{ph} of blackbody radiation at three different temperatures, according to equation 5.3. The gray area roughly marks the wavelength range where a silicon detector has a high quantum efficiency.
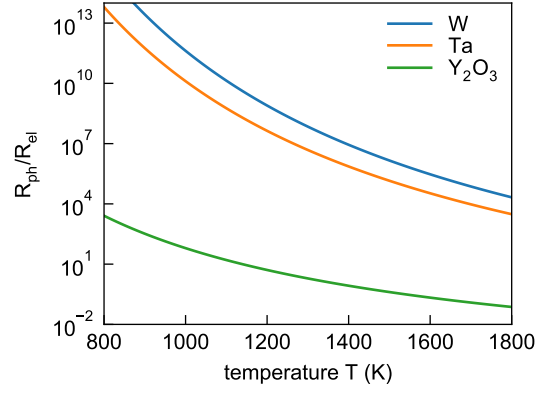
Figure 5.4: Ratio of the photon emission rate R_{photon} to the electron emission rate R_{el}. The ratio is smaller (or more favorable for the electron gun) at higher temperatures.

Planck's law for blackbody radiation relates the emitted spectral photon flux F_{ph}^{λ} to the wavelength λ and temperature T:

$$F_{ph}^{\lambda} = \frac{4\pi c}{\lambda^4} \frac{1}{e^{\frac{hc}{\lambda k_B T}} - 1}. \tag{5.3}$$

Here, h denotes the Planck constant, c the speed of light, and k_B the Boltzmann constant. This representation of Planck's law is derived from the common form (e.g. found in [122]) by dividing by hc/λ to get the photon density instead of the energy density and by multiplying with $c/2$ to get a surface flux instead of the volume content. The resulting spectral flux F_{ph}^{λ} is does not depend on cathode material and is plotted in figure 5.3. The peak of emission is in the infrared regime for typical temperatures of the filament.

The optical photon quantum efficiency of an SDD depends on the entrance window properties (e.g. the SiO_2 thickness and reflectivity) and the wavelength. Typically, the efficiency is high (around 70 % to 80 %) in the optical red and infrared range with wavelengths around $\lambda \approx 600\,\text{nm}$ to $1000\,\text{nm}$ [123, 124] and close to zero above $\lambda > 1100\,\text{nm}$. Therefore, the total harmful photon rate R_{ph} is roughly estimated here by integrating the tail of the spectrum up to $\lambda = 1100\,\text{nm}$ (marked gray in figure 5.3) and multiplying by the emission area A:

$$R_{ph} = A \cdot \int_0^{1.1\,\mu\text{m}} F_{ph}^{\lambda} d\lambda \tag{5.4}$$

Figure 5.4 compares the resulting photon rate R_{ph} to the electron rate R_{el} from Richardson's law in equation 5.2. At $T = 1500\,\text{K}$, a tantalum filament emits around 10^6 times more photons with $\lambda < 1100\,\text{nm}$ than electrons. Furthermore, figure 5.4 shows that the ratio R_{ph}/R_{el} is smaller (or more favorable for an electron gun) at high temperatures. This motivates a small size of the filament at a high temperature, rather than a large filament at lower temperature.

The estimations of electron and photon emission rates in the above paragraphs use many simplifications. For example, the temperature of the filament in reality is not constant, but has a gradient
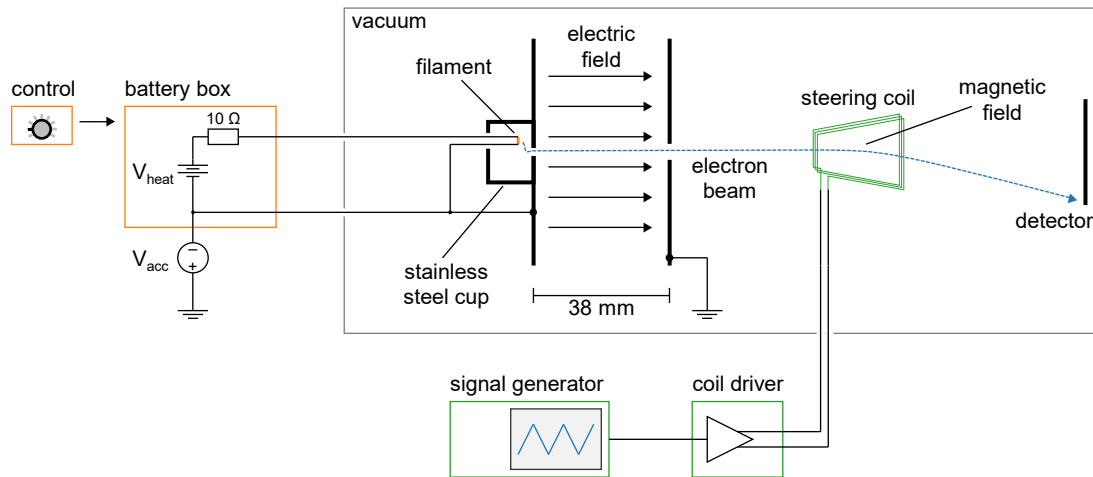
Figure 5.5: Schematic view of the electron gun and steering coil setup. The filament is inside a stainless steel cup to shield light from the glowing filament. The electric field between two plates on V_{acc} and ground accelerates the electrons from the filament to form an electron beam. Outside of the vacuum chamber is a high voltage power supply V_{acc}, a battery box with a galvanically-decoupled controller to adjust the voltage V_{heat} (orange boxes), and a steering coil driver.

from the center, where the temperature is highest, to the mounting points. However, the main conclusion of this section, which states that a small filament is favorable, is valid in any case.

5.2.3 Design of the electron gun

The considerations about electron and light emission in sections 5.2.2 and 5.2.1 lead to the choice of a thin tantalum wire as filament. Figure 5.5 shows a schematic view, and figure 5.6 shows pictures of the electron gun design. The main components are:

- **Filament** The filament is a tantalum wire with a diameter of $D = 25\,\mu$m and a length of $l \approx 5$ mm. Figure 5.6a shows a photograph of the filament. The calculated electric resistance R of the filament, given the electric resistivity of tantalum $\rho = 13.5 \cdot 10^{-8}\,\Omega$m [120] at room temperature, is

$$R = \rho\,\frac{4l}{\pi D^2} = 1.4\,\Omega. \tag{5.5}$$

  The filament is mounted between two copper wires. Two 180° bends of the copper wires pinch the ends of the filament. Additionally, the bends are soldered. Although the "solderability" of tantalum is questionable, this method showed an acceptable contact quality between the copper wires and the tantalum filament.

- **Stainless steel cup** The acceleration field is formed between a ground plate and a high-voltage plate made of stainless steel. A closed cup ($\varnothing$ 16 mm × 13 mm, see figure 5.6a) behind the HV plate forms an almost field-free region where the filament sits. The emitted electrons from the filament reach the high-field acceleration region in front of the plate through a small hole (diameter 1 mm). The two wires to connect the filament are fed into the cup via a small ceramic insert and a small drop of insulating glue (LOCTITE EA 3450).

- **HV feedthrough** Two high-voltage vacuum feedthroughs of type "LEMO HGP.3Y.425"[2] are used to feed the wires to the outside of the vacuum chamber. Compared to many other

---

[2]www.lemo.com/pdf/HGP.3Y.425.CLL.pdf
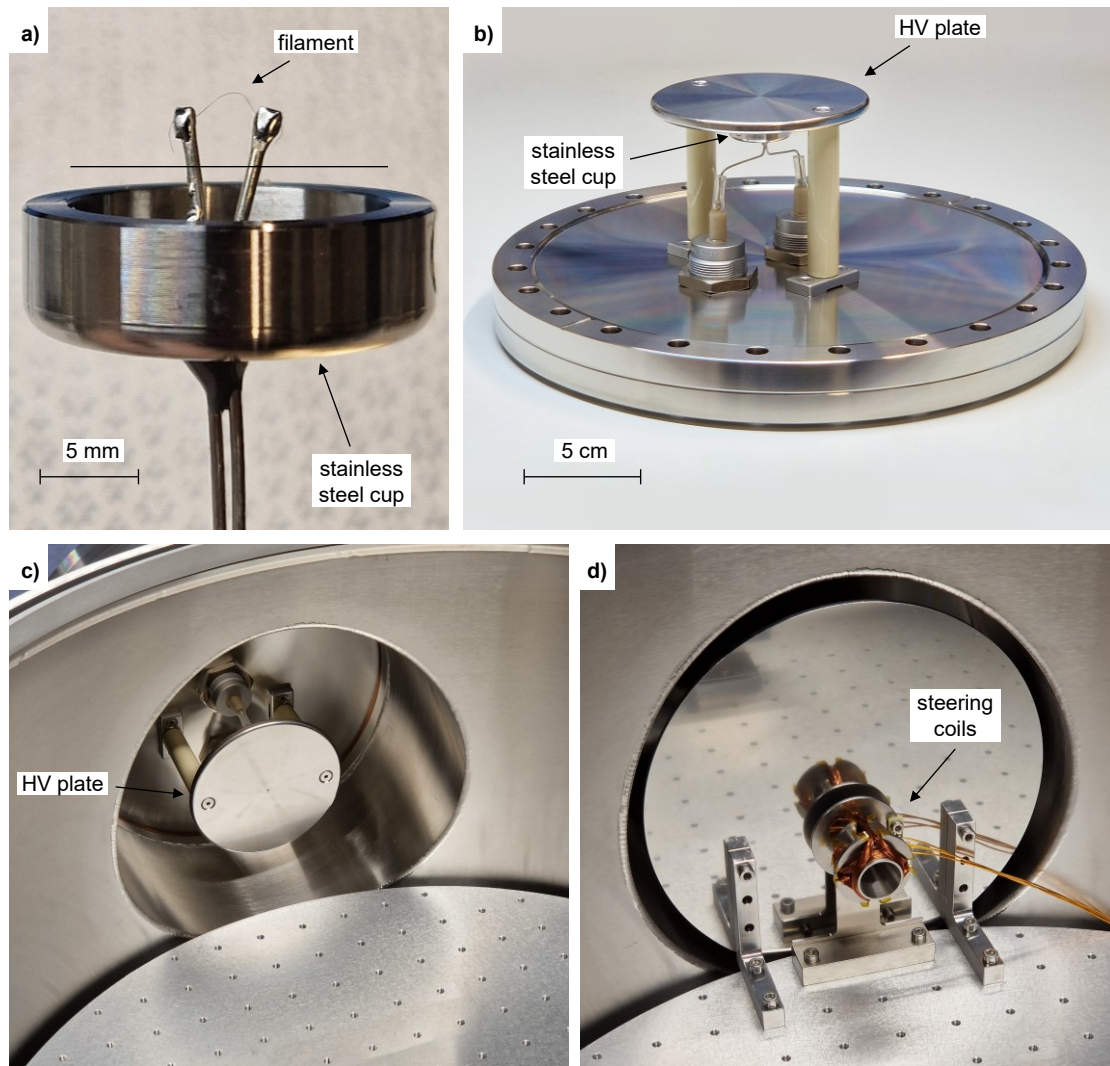
Figure 5.6: Photographs of the electron gun setup. **a)** filament, **b)** stainless steel cup with isolating standoffs, **c)**: vacuum chamber with electron gun and detector, and **d)** steering coil system.

high-voltage feedthroughs, this feedthrough has the advantage of a fully screened plug connector on the air side. The specified creepage distance of this connector is 25.5 mm, and the connector is tested up to a DC voltage of 52 kV by the manufacturer. However, this high-voltage resistance only holds if a heat-shrink tube with an inner melting coating seals the vacuum side of the feedthrough, where the contact is soldered. One of the first versions of the electron gun had a heat-shrink tube without an inner melting coating. As a result, a discharge appeared below the heat-shrink tube at $V_{\mathrm{acc}} \approx 28\,\mathrm{kV}$. Figure 5.7 shows the damaged insulator.

Consequently, a heat shrink tube with an inner melting coating has been used since then. In the current design of the electron gun, it would be preferred to have no heat shrink tube on the vacuum side of the feedthrough to avoid outgassing. Nevertheless, no suitable high-voltage feedthrough was found for this purpose. To prevent discharges at the HV feedthrough, the electrun gun is currently operated with high-voltages up to 25 kV only.
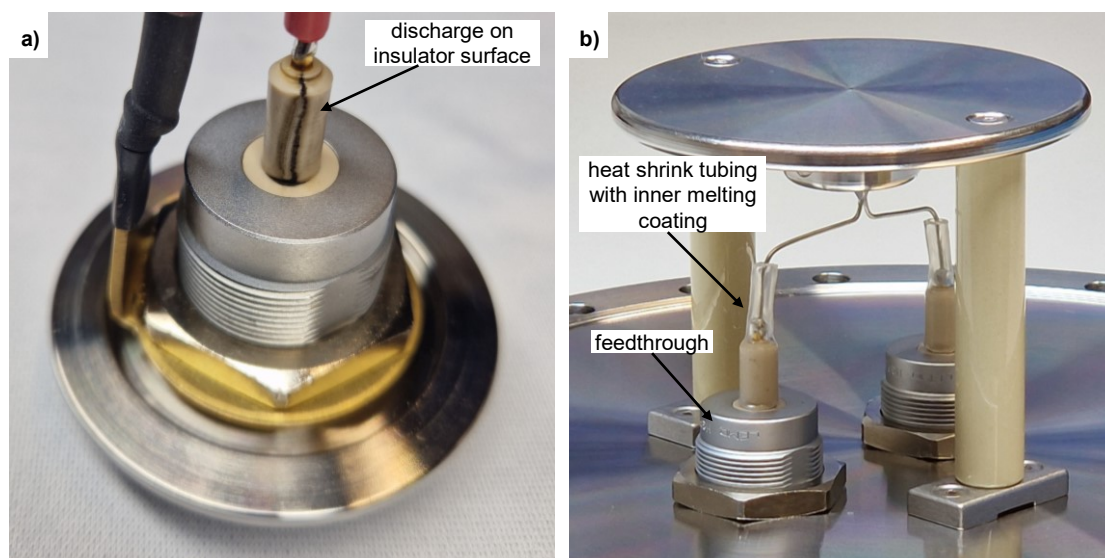
Figure 5.7: Photographs of the vacuum feedthroughs for the electron gun. **a)** shows a broken feedthrough after a high-voltage discharge. To prevent discharges, a heat shrink tubing with inner melting coating is added in the latest design, as shown in **b)**.

- **High-voltage supply** The negative high voltage V_{acc} is provided by a high-voltage laboratory power supply of type "Heinzinger LNC 30000 - 2 neg"[3]. This power supply has a nominal output stability of better than $15\,V$ within $8\,h$ and a maximum ripple of $6\,V_{pp}$ at $30\,keV$. This stability is sufficient to not significantly broaden the main peak width of a monoenergetic electron measurement.
- **Battery box** The supply of heating current for the filament, sitting on the negative high voltage, is realized with a battery system. The battery with a linear regulator circuit provides the heating voltage V_{heat}, which is connected to the filament via a series resistor ($10\,\Omega$). A galvanically decoupled high-voltage optocoupler circuit allows the user to set the value of V_{heat} from ground potential. The corresponding circuit diagram is found in the appendix in figure A.13.

5.2.4 Design of the steering coils

The electrons are emitted from the hot filament in all directions with a small kinetic energy due to the thermal energy distribution in the metal ($k_B T \approx 130\,meV$ at $T = 1500\,K$). The initial spread of starting momentum and starting position on the filament causes a slight divergence of the electron beam after the acceleration region. Simulations (see next section 5.2.5) indicate that the resulting divergence is around $1°$ at $20\,keV$ kinetic energy. Accordingly, the diameter of the beam at a distance of $30\,cm$ is approximately $5\,mm$, which is similar to the diameter of one detector pixel ($\varnothing\,3\,mm$). However, for many measurements, it is preferable to illuminate the entire sensitive detector area. In order to achieve a homogeneous illumination, several approaches can be taken: One method involves increasing the beam divergence, for example, by using electrostatic or magnetic electron lenses. Another approach is to increase the distance to the detector. The third method bends the beam to sequentially scan the detector surface, which is the approach implemented in this work.

---

[3]www.heinzinger.com/assets/uploads/downloads/LNC.pdf

Similar to the deflection yoke in an classic television tube, a steering coil system is employed around the electron beam to deflect the beam in horizontal and vertical direction. The coil system, depicted in figure 5.6d, consists of two coils on a stainless steel body, each with 80 turns. When a coil current of 1 A is used, a magnetic field perpendicular to the beam of $B_\perp = 2.8\,\text{mT}$ is achieved, resulting in a bending power of approximately $\int B_\perp \, \mathrm{d}s = 6 \cdot 10^{-5}\,\text{Tm}$. The deflection angle can be estimated using

$$\sin(\theta) = \frac{v_\perp}{v} \approx \frac{e \int B_\perp \, \mathrm{d}s}{\sqrt{2Em}}, \tag{5.6}$$

where $v_\perp$ represents the electron velocity component perpendicular to the beam, v denotes the total velocity, E is the kinetic energy, and m is the mass of the electron. The resulting deflection angle is $\theta \approx 7°$, corresponding to a displacement of 21 mm after 20 cm, which is sufficient for our purpose. The bending in horizontal and vertical directions can be controlled by adjusting the current in the horizontal and vertical coils, respectively. Applying triangular signals with a high frequency to the steering coils simulates a homogeneous illumination of the entrance window.

In addition to enabling the illumination of all detector pixels, the steering coil system also has the advantage of correcting for variations in the beam position caused by potential misalignments or the earth's magnetic field. At an electron energy of $E = 10\,\text{keV}$, the earth's magnetic field $B_{\text{earth}} \approx 48\,\mu\text{T}$ corresponds to a cyclotron radius (if perpendicular to the electron movement) of

$$r = \frac{\sqrt{2Em}}{eB_{\text{earth}}} = 7.0\,\text{m}. \tag{5.7}$$

The displacement Δs after $l = 30\,\text{cm}$ is

$$\Delta s = \frac{l^2}{2r} = 6.4\,\text{mm}, \tag{5.8}$$

which, although small, is not negligible.

5.2.5 Field and tracking simulation

To validate this design of the electron source, the electric field and the trajectories of several electrons were simulated. The field calculations are based on the `sfepy` package for python [98], which implements the finite element method. A simplified design, as depicted in figure 5.8, is used of the simulation. The figure shows the calculated electric potential and ten electron tracks. An interesting result of the simulation is the size of the beam spot at the detector. The simulation indicates that the beam spot has a diameter of several millimeter and therefore has a similar size as a detector pixel.

One challenge of the tracking simulation is to accurately simulate the cup and filament region. In this region, there are many free electrons with low kinetic energy ($E < 1\,\text{eV}$). Most electrons cannot escape the small potential well $\mathcal{O}(200\,\text{mV})$, which the cup forms, due to the connection of the negative end of the filament to the cup. These electrons are strongly affected by weak magnetic fields, like the earth's magnetic field or the stray field of the steering coils. As a consequence, most electrons follow a chaotic trajectory until they are either absorbed by the filament or the cup wall or eventually reach the acceleration region. Given the difficulty in simulating this mechanism, the exact size of the beam spot and the output electron rate need to be determined experimentally.
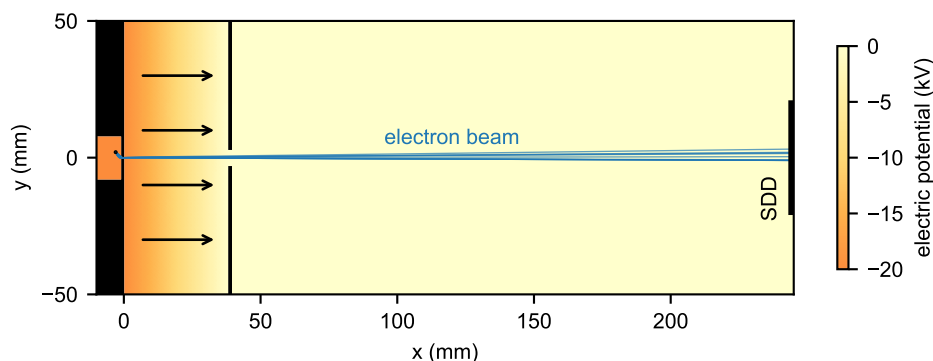
Figure 5.8: Simulation of the electric potential and ten electron tracks (blue) originating at the hot filament (small dot). The acceleration voltage is $V_{\text{acc}} = 20\,\text{kV}$. The figure shows only tracks that reach the acceleration region. The spot size at the detector has a diameter of around 4 mm.
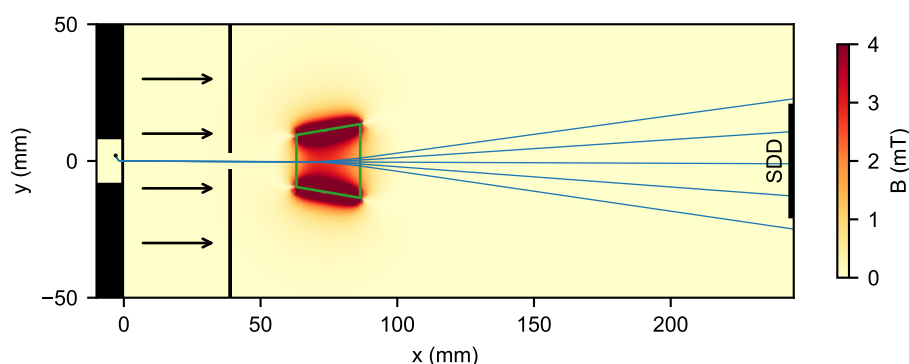
Figure 5.9: Simulation of the magnetic field of the steering coil for vertical deflection. The top view of the coil path is drawn in green. The five electron tracks correspond to a coil current of $I = -1\,\text{A}$, $-0.5\,\text{A}$, $0\,\text{A}$, $0.5\,\text{A}$, and $1.0\,\text{A}$. The acceleration voltage is $V_{\text{acc}} = 20\,\text{kV}$. With this range of the coil current, the electrons can reach the entire detector area of the SDD.

To validate the steering coil design, the electron trajectory for five different coil currents was calculated. Figure 5.9 illustrates the corresponding magnetic field and electron trajectories. The simulation demonstrates that the entire detector area can be reached by adjusting the currents of the two coils for horizontal and vertical deflection.

5.2.6 Vacuum chamber setup

The electron gun is installed in a vacuum chamber setup. This setup features a $\varnothing\,50\,\text{cm}$ cylindrical vacuum chamber (see figure 5.10a) with a pump port on the bottom. A turbomulecular pump is used to evacuate the chamber. The pressure during operation is around $1 \cdot 10^{-6}\,\text{mbar}$. The inside vacuum components are mounted on a liquid cooled aluminum base plate. An external chiller cools the plate to $-50\,°\text{C}$ during operation, and the detector reaches $-34\,°\text{C}$. The large top lid of the chamber allows for easy access and flexible configuration of the detector and electron gun. A 166-pixel TRISTAN detector, as described in section 2.4, is used for measurements presented in this section. An optional ^{55}Fe source, (not installed while making the photograph for figure 5.10a) can be installed in parallel to the electron beam. The detector is connected via four 100-pin microD
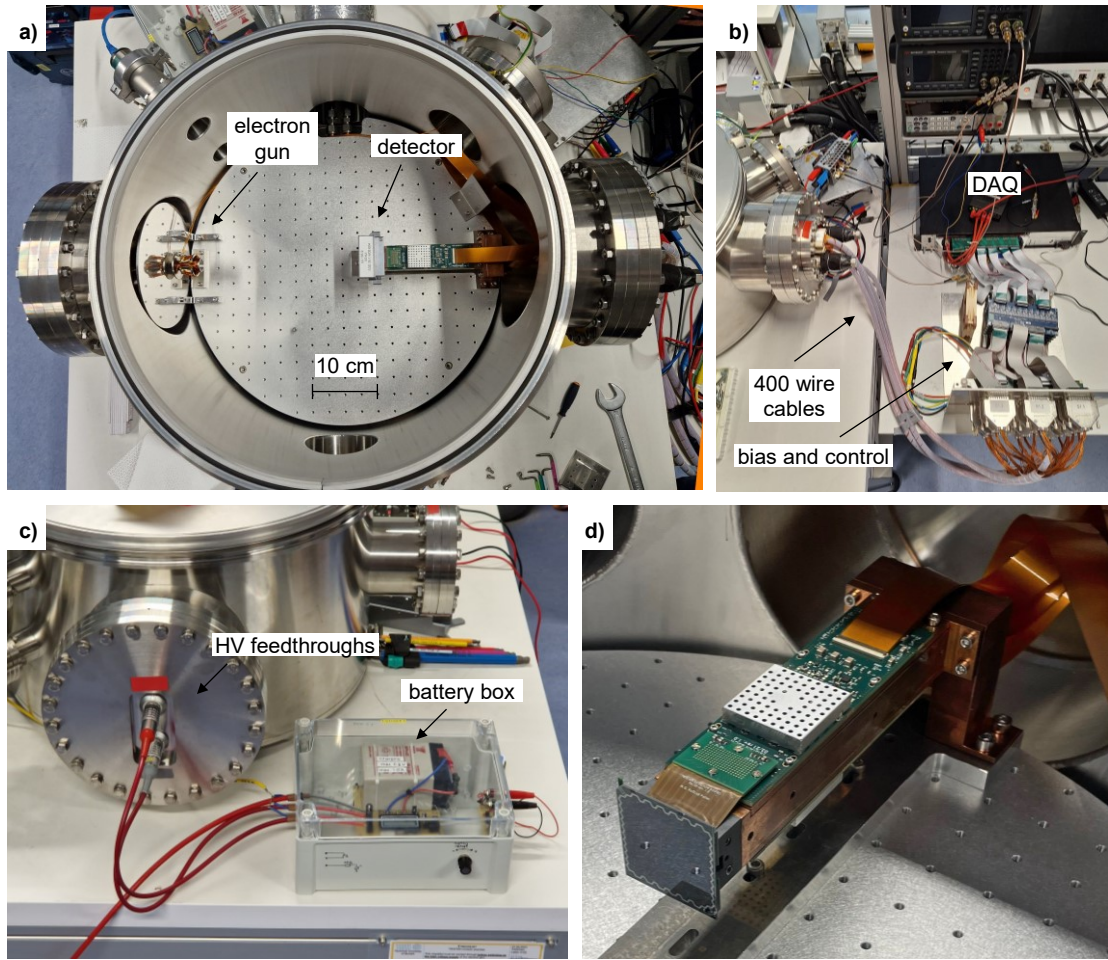
Figure 5.10: Photographs of the vacuum chamber setup. **a)** chamber with open lid, **b)** air-side detector bias and DAQ electronics, **c)** high voltage battery box, and **d)** mounted detector without cover.

vacuum feedthourghs to the bias and control electronics and to the DAQ system (see figure 5.10b). The DAQ system is based on full waveform digitization and digital pulse height analysis of each detector channel. The setup uses a commercial system[4], which features a sampling frequency of 100 Msps and an ADC resolution of 14 bit.

The vacuum chamber setup is used for commissioning of the electron gun, described in the next section. Furthermore, the same setup acts as a general purpose characterization test stand, which is used for most measurements presented in the characterization chapter of this work (chapter 6).

5.2.7 Commissioning

In the first step of commissioning the electron gun setup, a measurement of the filament voltage as a function of current was conducted. During this measurement, both the acceleration voltage and the detector were switched off. The resulting data, depicted in figure 5.11, demonstrates the expected non-linear behavior. This is due to the positive temperature coefficient of the electric

---

[4]3x CAEN VX2740
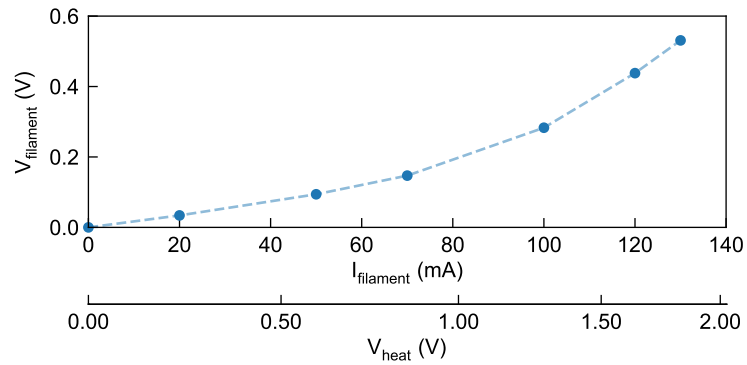
Figure 5.11: Measured voltage-current curve of the tantalum filament. Without heating, the resistance is $1.7\,\Omega$. When heating the filament with a current of $130\,\text{mA}$, the temperature increases, and the resistance changes to $4.1\,\Omega$. On the second x-axis, the corresponding value of V_{heat} is shown. V_{heat} is the voltage including a $10\,\Omega$ series resistor, see figure 5.5.
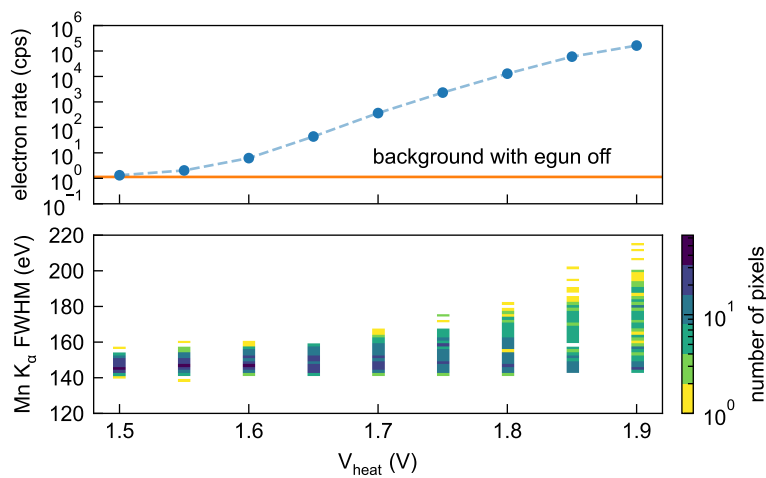
Figure 5.12: Measurement of the electron rate (top) and energy resolution (bottom) with the electron gun as a function of the heating voltage V_{heat}. The acceleration voltage was $V_{\text{acc}} = 15\,\text{kV}$. The rate measurement uses a threshold of $8\,\text{keV}$. The background rate of $1.3\,\text{cps}$ originates from pileup of two ^{55}Fe events. The energy resolution is determined by measuring the FWHM of the Mn K_α line with $V_{\text{acc}} = 0\,\text{kV}$. For high values of V_{heat}, the FWHM on some pixels is increased due to illumination of the detector with light.

resistivity in tantalum. In electron gun operation, the heating voltage V_{heat} is regulated (instead of I_{filament}) for controlling the electron emission rate. V_{heat} is shown as second x-axis in figure 5.11.

A second commissioning measurement focused on the emitted electron rate as a function of V_{heat}. To this end, the acceleration voltage was set to $V_{\text{acc}} = 15\,\text{kV}$, and the detector was switched on. To measure the total electron rate, all detected events above $8\,\text{keV}$ are counted. Figure 5.12 shows the detected rate. At $V_{\text{heat}} = 1.5\,\text{V}$, no electrons from the electron source are observed. At $V_{\text{heat}} \approx 1.55\,\text{V}$, the electron rate starts to increase. The rate reaches about $160\,\text{kcps}$ at $V_{\text{heat}} = 1.9\,\text{V}$. The total rate of $160\,\text{kcps}$ is sufficient for all characterization purposes shown in this work. Still, the rate can be increased further by raising V_{heat}.
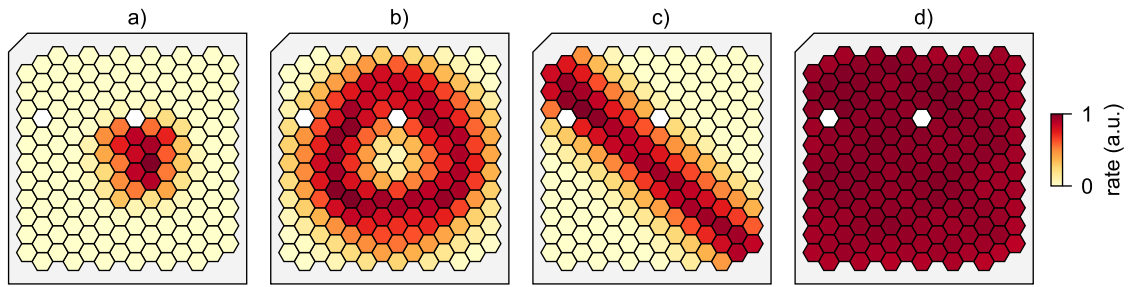
Figure 5.13: Illumination of the entrance window of a 166-pixel detector with electrons using four different patterns. Pixel map a) shows the count rate of electrons if the steering coils are switched off. Pixel map b) shows the rate distribution for an acquisition where two sinusoidal signals with 90° phase shift were applied to the steering coils to draw a circle. Acquisition c) had two synchronous triangular signals applied to draw a diagonal line. Acquisition d) had two non-synchronous triangular signals with different frequencies applied, leading to a homogeneous illumination of the detector chip. Two pixels of the detector (shown in white color) had to be disabled due to connection issues.

To quantify the effect of the emitted light from the electron gun, the energy resolution of all 160 active pixels was monitored via the Mn K_α line width of the ^{55}Fe calibration source. The distribution of the resulting FWHM is drawn on the bottom plot of figure 5.12. A slight increase in energy resolution on part of the pixels is observed starting at $V_\text{heat} \approx 1.7\,\text{V}$.

In a third commissioning measurement, the steering coil system was tested. Figure 5.13 shows the rate distribution, as measured by the 166-pixel detector, for four different signals applied to the steering coils. When the steering coils are switched off, the electron beam produces a spot with a FWHM of approximately 10 mm at the center of the chip. By applying synchronized signals to both coils, patterns such as a circle or a line can be drawn on the detector surface. Moreover, when two triangular signals with different frequencies are applied, the entire surface of the detector is illuminated. During this process, a rate variation of about 12 % was observed between the pixels under homogeneous illumination.

In summary, the thermionic electron gun developed within this work shows promising properties for calibrating and characterizing the TRISTAN detector. It provides monoenergetic electrons with a kinetic energy up to 25 keV. The kinetic energy is currently limited by the discharge robustness of the setup, especially the HV vacuum feedthroughs. The rate of electrons can be set between less than 1 cps and >100 kcps. Thanks to the off-axis mounting of the filament, the illumination of some detector pixels with light from the glowing filament causes only a moderate worsening of the energy resolution, even at the highest rates. The electron beam spot on the detector has a diameter of several millimeters. A steering coil system allows for extending the illuminated area to the entire detector entrance window, imitating a homogeneous illumination.
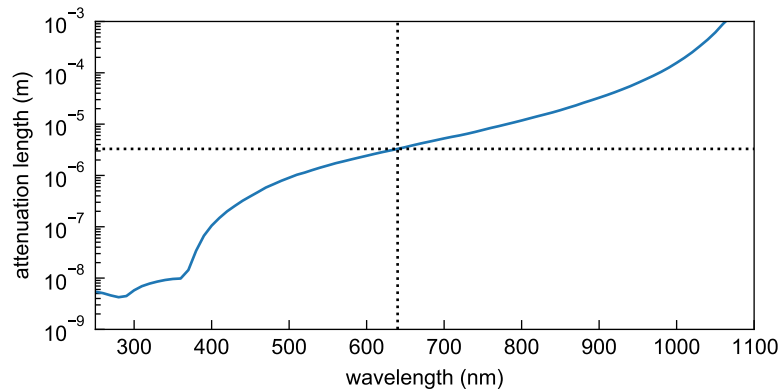
Figure 5.14: Attenuation length of light in intrinsic silicon, depending on the wavelength [130]. The dashed lines indicate an attenuation length of 3.3 μm for the wavelength of 640 nm, which is used in this work.

5.3 Pulsed light characterization

A silicon detector is sensitive to any ionization, that occurs inside its sensitive volume. The cause of ionization can be an ionizing particle like an X-ray or electron, but can also originate from optical light. Often, the sensitivity to optical photons is a drawback, as a particle detector has to sit in a fully dark environment during operation. But the sensitivity to optical photons can also be utilized to induce artificial signals in the detector, which can be helpful for characterization and calibration. This technique has been used in silicon detectors, mostly for high energy physics, extensively in the last decades. An example is the (scanning) transient current technique (TCT), described in [125] and [126]. But also in SDDs, this technique has been applied to studying timing effects [127, 128, 129] in the past.

This section first shows how the pulsed light characterization can be applied to the TRISTAN detector. After that, a test measurement, which confirms the validity of the drift simulations of section 4.1.3, is presented.

5.3.1 Charge cloud induced by light

In a semiconductor, optical photons can lift an electron from the valence band across the band gap (1.1 eV for silicon) into the conduction band. This process happens only for wavelengths shorter than around 1100 nm, as for longer wavelengths, the photon energy is not sufficient and silicon is almost transparent. A charge clouds induced by light are labeled "optically induced" in the following, and charge clouds caused by X-rays or electrons are labeled "particle-induced".

Charge cloud location   The location of an optically induced charge cloud on the entrance window surface (xy-direction) can be defined by optically focusing the light beam with a lens. The lens is mounted on an xy stage to scan the entire entrance window of a detector. In z-direction (depth), the charge cloud has an exponential profile. The wavelength and corresponding attenuation length of silicon define the depth of the profile. Figure 5.14 shows that a wavelength of $\lambda = 640$ nm corresponds to an attenuation depth of around 3.3 μm. This value is similar to the penetration depth of an electron with 30 keV energy [88]. This means that the optically induced and the particle-induced charge cloud are created at a similar depth.

71

Charge cloud statistics At an optically induced event, each electron-hole pair is independent from all other electron-hole pairs. This holds if the number of electron-hole pairs in the induced charge cloud is small compared to the number of photons created in the light pulse. In all realistic scenarios, this is fulfilled, as only very few electron-hole pairs ($\mathcal{O}(10000)$) are required in the detector. The independent electron-hole pairs lead to a Poisson distribution of the number N_{oi} and the variance is

$$\text{var}(N_{oi}) = \overline{N}_{oi}, \tag{5.9}$$

where $\overline{N}_{oi}$ is the expectation value for the number of electron-hole pairs from an optically induced event. Opposite to that, a particle-induced event has partially correlated electron-hole pairs, as they all originate from the same primary electron track and $\text{var}(N_{pi})$ is reduced by the Fano factor $F = 0.115$ (see section A.1):

$$\text{var}(N_{pi}) = F\overline{N}_{pi}. \tag{5.10}$$

Consequently, the spectral peak with (or energy resolution) of optically induced events is around $1/\sqrt{F} \approx 3$ times larger than particle-induced events with the same induced charge.

Calibration by pulsed light Equation 5.9 can be used for an energy calibration using the relative energy resolution σ_{rel} of optically induced events

$$\sigma_{rel} = \frac{1}{\sqrt{\overline{N}_{oi}}}. \tag{5.11}$$

The average pair creation energy of silicon $w = E/N = 3.63\,\text{eV}$ (see table A.1) can be used to substitute $\overline{N}_{oi}$ by E/w and solve for E:

$$E = \frac{w}{\sigma_{rel}^2}. \tag{5.12}$$

This equation allows one to directly calculate the energy of optically induced events for the measured relative peak width σ_{rel}. If this method is applied, other contributions to the measured σ_{rel}, like electronic noise, must be considered. As these contributions usually are independent of the energy, they can be disentangled by measuring σ_{rel} at several (arbitrary) energies. This approach was tested in [131], and a calibration on the 5 % level was achieved with a pulsed LED. Due to the relatively large uncertainty, the light calibration approach may be interesting mostly for applications where X-ray calibration sources are not available.

5.3.2 Setup for pulsed light characterization

The components of a setup for pulsed light characterization are shown in figure 5.15:

- An pulsed light source produces short light pulses. The pulses should be faster than the typical rise time of detector signals. A pulse duration of less than 20 ns is sufficient for this purpose. In the shown example a fast pulse generator in combination with a LED or laser diode (e.g. type ADL-65055[5] with wavelength 650 nm) is used.
- An optical fiber guides the light to the detector. With a typical single mode fiber, the light leaves the fiber end on a small spot of diameter $d_1 \approx 5\,\mu\text{m}$. The small size at the fiber opening is essential for obtaining a small beam spot on the detector. At the same time, the fiber removes all constraint for the brilliance of the light source itself (for example, it can be

---

[5]ADL-65055 datasheet
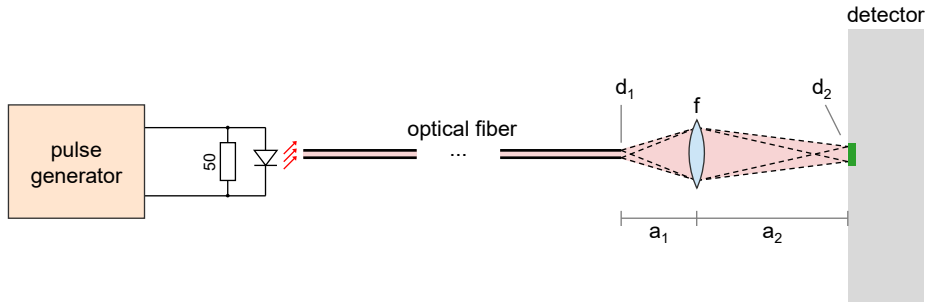
Figure 5.15: Schematic view of the light calibration setup

a simple wide-angle LED) and the only constraints of the light source are the timing and the wavelength.

- An optical lens with focal length $f = 2\,\text{mm}$ maps the end of the optical fiber onto the detector surface. The focus condition [132]

$$\frac{1}{a_1} + \frac{1}{a_2} = \frac{1}{f} \tag{5.13}$$

is fulfilled, for example, with $a_1 \approx 3\,\text{mm}$ and $a_2 \approx 6\,\text{mm}$. In this case, the final spot size on the detector is

$$d_2 = \frac{a_2}{a_1} d_1 \approx 10\,\mu\text{m}. \tag{5.14}$$

- An xyz stage is used to adjust the lens and fiber position relative to the detector. The z-position focuses the beam. The xy-position defines the location of the beam spot on the detector surface and is scanned to see for example location-dependent detector effects.

One challenge in the setup is the adjustment of the distances a_1 and a_2 to have a focused beam. Three possibilities are:

1. The diameter of the beam as a function of the distance to the lens can be measured by a rotating chopper wheel[6]. The SDD surface is afterwards placed at the distance of smallest beam diameter.
2. A fine pixelated CCD sensor can be used to measure the beam diameter. A standard (and cheap) webcam sensor turns out be be suitable and easy to readout.
3. The most direct way to measure the beam diameter would be the scan across a covering edge on the SDD itself. With this method, the setup does not have to be changed between focus determination and physical measurement. However, the entrance window of the TRISTAN detector does not have any structure where this method could be applied.

5.3.3 Measurement of drift time and rise time

A test measurement with the pulsed light setup and a 7-pixel TRISTAN detector at room temperature is shown in this section. The measurement is considered a test, as a manual xy stage and a very coarse beam focus was used. The beam spot width was determined to FWHM $< 50\,\mu\text{m}$ with the chopper wheel method described above. Later, more refined measurements, using a CCD sen-

---

[6]A helpful example is illustrated at thorlabs.com
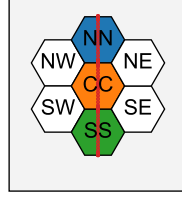
Figure 5.16: Scanning points for the pulsed light measurement on the entrance window of a 7-pixel SDD. The 118 scanning points cover three pixels NN, CC, and SS.
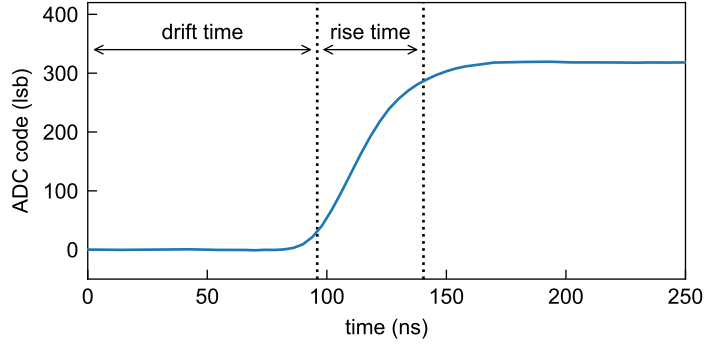
Figure 5.17: Acquired pulse shape at one scanning point. The pulse was triggered a $t = 0$. The signal is from pixel SS and the scan position was 8.5 mm (compare figure 5.18).

sor for focusing and a motorized xy stage were performed. The results, including detailed studied of the pixel border region and the JFET region, are reported in [133, 134, 131].

Despite its test character, the measurement presented in this section is used to determine the drift time T_{drift} and the signal rise time T_{rise} of events relative to their interaction location on the SDD on a 1D line across the entrance window. Figure 5.16 illustrates the scanning points of the 1D scan. At each datapoint, many pulse waveforms were recorded and averaged to reduce noise. Before averaging, the individual pulses were aligned to the known trigger timestamp of the optical pulse. An averaged pulse is plotted in figure 5.17. To extract the two quantities of interest T_{drift} and T_{rise}, the 10 % and 90 % crossing timestamps (t_{10} and t_{90}, respectively) of the pulses are determined relative to the trigger timestamp of the optical pulse at $t = 0$. Figure 5.18 shows the extracted drift time $T_{\mathrm{drift}} = t_{10}$ and signal rise time $T_{\mathrm{rise}} = t_{90} - t_{10}$ as a function of the position on the detector.

As expected, the drift time shows an almost linear dependence on the distance of the initial charge cloud to the anode with a slope of 146 ns/mm or a drift speed of $v_{\mathrm{drift\ meas}} = 6.8\,\mu\mathrm{m/ns}$. The drift speed can also be estimated from the empirical relation (compare figure 4.7) and the simulated electric field $E = 500\,\mathrm{V/cm}$ (see section 4.1.1) along the radial drift. This yields an expected drift speed of $v_{\mathrm{drift\ sim}} = 7.3\,\mu\mathrm{m/ns}$, which is similar to the measured value. It is important to note that these values are at room temperature ($T \approx 300\,\mathrm{K}$) and the drift in a cooled detector is significantly faster. The discrepancy between measurement and simulation of around 7 % can be explained, for example, by the tilted drift path in z-direction or by a small deviation of the SDD temperature. In conclusion, the measurement of the drift time confirms the general validity of the field simulation
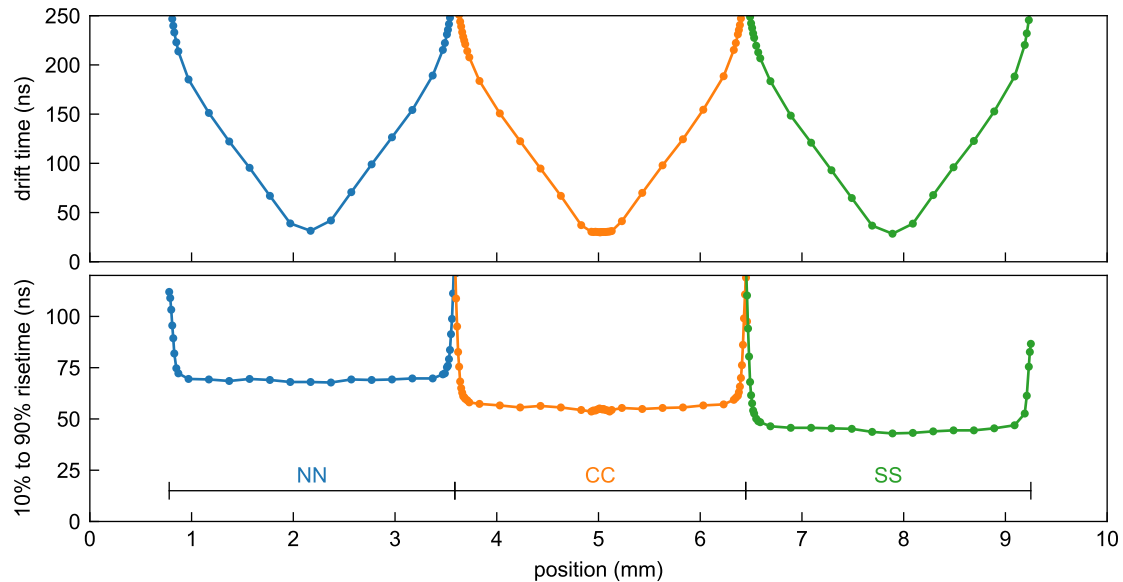
Figure 5.18: Drift time and signal rise time as a function of the position on a 1D line on a 7-pixel detector of production 1 (see figure 5.16 for the line arrangement). The values are extracted from the averaged pulse at each scanning point.

(section 4.1.1) and the empirical drift velocity model (figure 4.7) used for the signal simulation.

The signal rise time measurement in figure 5.18 shows a rapid increase of the rise time at the pixel border, reaching $T_{\text{rise}} > 120\,$ns. In this region, the low electric field at the saddle point between pixels causes very slow drifts and long rise times from diffusion. The observed rise time structure is in agreement with the simulations of section 4.1.3. Besides the increase at the pixel border, the rise time shows an overall difference for the three pixels. Pixel NN, which has the longest traces on the SDD has the largest overall rise time. This can be explained by the effect of the SC-line capacitance, as illustrated in the circuit simulation of section 4.2.3. A similar effect is observed in the rise time distribution of physical events within a 166-pixel detector module, presented in section 6.2.2.

5.4 Summary

This chapter introduced different tools for calibrating and characterizing the TRISTAN detector. Due to the absence of suitable electron sources for characterization measurements in a laboratory setup, a custom electron gun was developed within this work. The electron gun, based on thermionic electron emission, provides a beam of monoenergetic electrons of up to 25 keV with a rate up to more than 100 kcps. The design highlights include an off-axis mounting to mitigate the detector illumination with light and a coil system to magnetically steer the electron beam. The electron gun is an essential tool for many TRISTAN detector investigations. Most measurements of chapter 6 of this thesis use the electron gun. Due to the custom design and the flexible vacuum chamber setup without guiding magnetic fields, many investigations were possible, which are not part of this work, For instance, a measurement of electron backscattering from the detector is pre-

sented in [135]. A radiation hardness investigation, using the electron gun at rates above 10 Mcps, is presented in [136].

Finally, this chapter presented the concept of a pulsed light characterization. Within this method, a charge cloud is induced in the detector volume at a defined time and location by a short, focused pulse of red light. This allows for studying the drift and signal formation in the TRISTAN SDD. A test measurement demonstrating the method was presented in this work. More detailed investigations using the pulsed light characterization method were done by others [131, 134].

6 Detector characterization

This chapter presents measurements of the TRISTAN detector characteristics. These encompass general performance parameters of silicon detectors, like the noise curve and the detector response shape. Furthermore, the two effects of crosstalk and charge sharing are addressed in detail. Both effects are intrinsic to the multipixel design of the TRISTAN detector and have a significant impact on the detector's spectral response.

The first section 6.1 of this chapter briefly summarizes the history of the detector development to have a basis for later performance comparisons of different detector versions. After that, measurements of general TRISTAN detector characteristics are presented in section 6.2. These contain measurements of the leakage current, of the pulse shape, of the noise curve, and of the detector's response to electrons. Section 6.3 studies the effect of crosstalk, which originates from electric interference of neighboring channels in the detector readout. Besides the measurement of crosstalk, a study of possible crosstalk mechanisms is presented. Furthermore, based on the identified mechanisms, design modifications for mitigating crosstalk were applied and are evaluated in this section. The consecutive section 6.4 studies the impact of crosstalk on the spectroscopic performance by a trace-level Monte Carlo approach. The final section 6.5 in this chapter addresses the effect of charge sharing.

6.1 History of the detector development

The TRISTAN SDDs chips are manufactured at the Halbleiterlabor der Max-Planck-Gesellschaft (HLL)[1] in Munich. An overview of the TRISTAN detector productions is shown in figure 6.1.

Prototype 0   The development started in 2017 with prototype detectors ("prototype 0"). These 7-pixel devices were manufactured with various pixel diameters ranging from 0.25 mm to 2 mm. The prototype 0 detectors did not have an integrated JFET at the anode, but the anode was wire-bonded to external low-noise CMOS amplifiers [137]. Many measurements were performed with prototype 0 detectors, for example, characterization campaigns with x-ray and electrons [93, 88, 138, 139], sterile neutrino searches at the Troitsk ν-mass experiment [140, 141, 94], and a source monitoring application in the KATRIN beamline [142]. The prototype 0 detectors proved that the SDD technology is suitable for electron spectroscopy and the sterile neutrino search with KATRIN.

Production 1   The consecutive step in the detector development was the integration of a JFET into the anode of each pixel. This step is necessary to scale the detector to a large monolithic pixel array, where the wire-boding of each anode is impossible. The first production (here called production 1) contained 1-pixel, 7-pixel, 12-pixel, 47-pixel, and 166-pixel devices. The first devices

---

[1] www.hll.mpg.de

	prototype 0	production 1	production 1x	production 2
amount		6 wafers	2 wafers	10 wafers
year	2017	2020	2022	2023
used devices	7-pixel	7-pixel, ... , 166-pixel	7-pixel, ... , 166-pixel	7-pixel, ... , 166-pixel
	Ø = 2 mm, no integrated JFET		designs: 1a: reference 1b: moderate 1c: advanced	
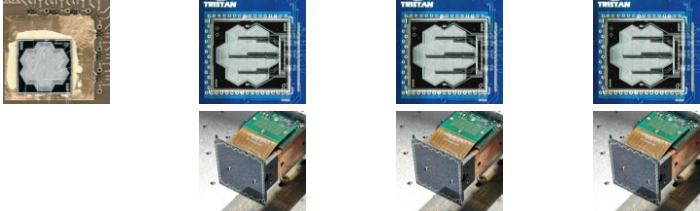
Figure 6.1: Overview of the four available generations of TRISTAN detectors.

were available in 2020. Several effects were noticed when the first 7-pixel devices of production 1 were tested (see also [89]):

- **Increased series noise** A worse-than-expected energy resolution at short shaping times was observed. One contribution to this effect came from an increased contact resistance at the JFET source connection.
- **Crosstalk** An unexpectedly strong crosstalk was present in pixels geometrically near readout lines.
- **Random telegraph signal** A binary noise (also called random telegraph signal) was present in a low fraction of the pixels, probably related to the trapping of single electrons close to the gate of the JFET.
- **Drain bus resistance** The supply line of the JFET drain had a too-high resistance, so a homogeneous biasing of all detector pixels was impossible.

In order to address these issues, two wafers of production 1 were processed with design improvements, here called production 1x. The design modifications were possible because two wafers still needed to be partially processed when the first detectors were tested. The increased contact resistance, the random telegraph signal, and the drain bus resistance were successfully mitigated in all devices of production 1x. Furthermore, three different readout designs were implemented to study the origin of crosstalk and possible design improvements. The designs are labeled as production 1a, 1b, and 1c.

Production 2 Production 2 is the second production of TRISTAN detector chips. The readout design is based on production 1b, although many more small modifications were implemented. For the first phase of the sterile neutrino search with the TRISTAN detector, nine 166-pixel detector chips will be used from this production. In production 2, enough chips are available for a second measurement campaing with more than twenty 166-pixel detectors.
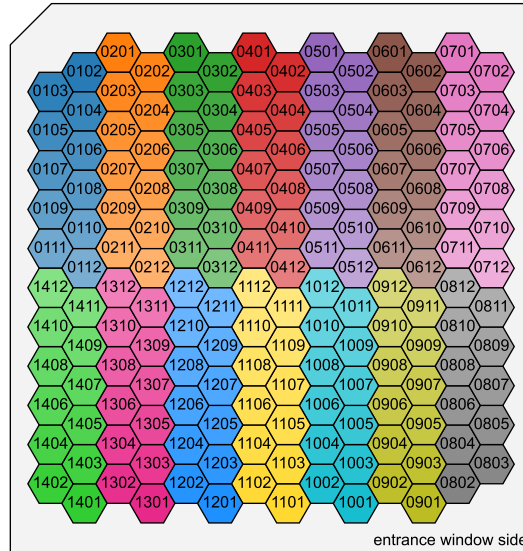
Figure 6.2: Pixel map with label and default color for each pixel of the 166-pixel detector module.

6.2 General characterization of the 166-pixel detector module

This section shows general characterization measurements of 166-pixel detector modules, including measurements of the

- leakage current,
- pulse shape,
- electronic noise (noise curve), and
- detector response to electrons.

All measurements were conducted in a vacuum chamber, described in section 5.2.6, at the TRISTAN laboratory at TUM. Two 166-pixel detector modules (labels S0-166-6 and S0-166-7) of the latest production 2 are used for the measurements presented in this section. The bias voltages and supply parameters are found in table A.7.

A consistent colormap and pixel labeling, illustrated in figure 6.2 are used in this work whenever possible. Each pixel of a 166-pixel detector is labeled with four characters, for example, 0102. The first two characters denote the readout group (01 to 14), and the second two characters denote the pixel number within the readout group (01 to 12).

6.2.1 Leakage current

The leakage current of the reverse biased detector diode contributes to the noise on the detector signals. Due to its strong temperature dependence, cooling reduces the leakage current efficiently. As a rough approximation, in a typical ideal diode, the leakage current is halved when lowering the temperature by $9\,\mathrm{K}$ [108]. This number is a rough estimation for an ideal diode.

In the case of the TRISTAN readout circuit, the leakage current I can be measured directly via the slope of the amplifier's first stage ramp. The slope is given by

$$\frac{\mathrm{d}V}{\mathrm{d}t} = \frac{I}{C_{\mathrm{FB}}}\,, \tag{6.1}$$
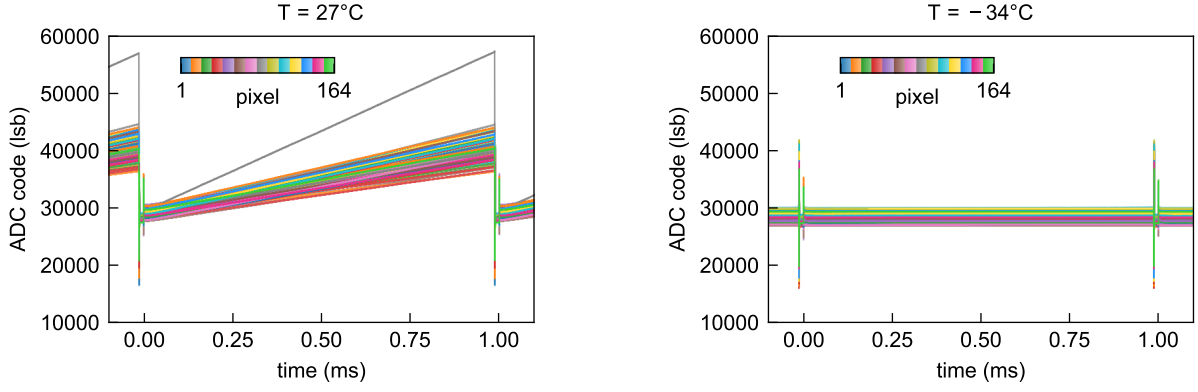
Figure 6.3: Signals of the amplifier's first stage with detector S0-166-7 at room temperature (left) and with cooling (right). One reset period is shown without event pulses.
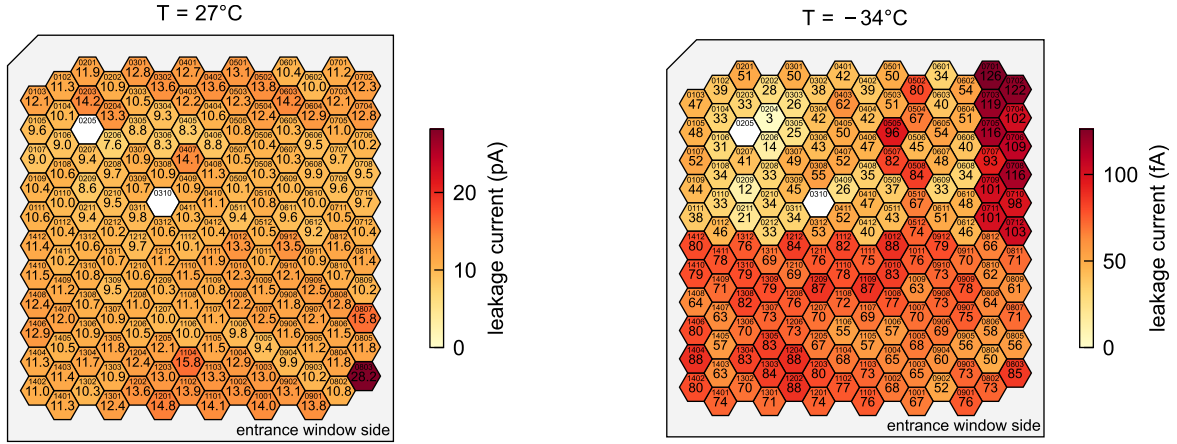
Figure 6.4: Pixel maps of the leakage current of detector S0-166-7 at room temperature (left) and with cooling (right). The leakage current is calculated with equation 6.1, using the slope from figure 6.3.

where $C_{\mathrm{FB}} \approx 25\,\mathrm{fF}$ is the feedback capacitance of the charge sensitive amplifier. Figures 6.3 and 6.4 show the first stage waveforms and the corresponding leakage current of detector S0-166-7. The median of the leakage current at room temperature (27 °C) is 10.9 pA. One pixel (label 0803) shows a significantly increased leakage current at room temperature. The increased leakage current of the outlier, however, vanishes if the detector is cooled. At −34 °C, the leakage current is below 130 fA for all pixels.

The relation between the leakage current I and the parallel noise on the detector signals was derived in equation 4.28. The contribution to the total equivalent noise charge (ENC) is

$$\mathrm{ENC}^2_{\mathrm{parallel}} = 2eI \left(\frac{\tau_{\mathrm{peaking}}}{3} + \frac{\tau_{\mathrm{gap}}}{2} \right). \tag{6.2}$$

Here, τ_{peaking} and τ_{gap} are the peaking time and gap time of a trapezoidal energy filter. With $\tau_{\mathrm{peaking}} = 960\,\mathrm{ns}$ and $\tau_{\mathrm{gap}} = 480\,\mathrm{ns}$, which are typical values for TRISTAN, the measured median leakage current of $I = 10.9\,\mathrm{pA}$ results in $\mathrm{ENC}_{\mathrm{parallel}} \approx 8.7\,\mathrm{e}$. With cooling, the parallel noise drops to $\mathrm{ENC}_{\mathrm{parallel}} \lesssim 1\,\mathrm{e}$, which is considered a negligible contribution to the overall noise. More details

on the noise contributions are found in section 4.3.3. All following measurements are done with a detector cooled to around −34 °C, where the leakage current is not a concern.

6.2.2 Pulse shape

The pulse shape of electron events is now studied regarding two aspects: First, the rising edge is addressed. Second, the exponential decay is studied. All pulses are acquired using the second amplifier stage of ETTORE.

Rising edge

A fast rise time of the signals is important for an effective pileup treatment at high rates (see section 7.2). The rising edge of the TRISTAN detector signals depends on several effects:

- **SDD signal formation** The drift simulation of section 4.1.3 shows that the charge signal at the anode has a typical rise time[2] between 10 ns and 50 ns and can reach even higher values for events at the pixel border.
- **CSA bandwidth** The charge sensitive amplifer (CSA), implemented by ETTORE and the JFET integrated in the SDD chip, has a design bandwidth limit of around 7 MHz, which corresponds to a rise time of around 50 ns for a step-like charge signal at the anode. The step-response of the CSA depends on the stray capacitance of the line between ETTORE and the SDD chip. Due to the individual routing of the channels, the stray capacitance, and thus the rise time, may be pixel-dependent. A simulation of the influence of the stray capacitance on the pulse shape is given in section 4.2.3.
- **Cable length at ETTORE output** ETTORE is designed to drive a limited capcitive load of 40 pF at its output [107]. With long cables between the in-vacuum electronics and the DAQ, this value is easily exceeded, which leads to an increased signal rise time. The measurements in this work use a cable length of around 45 cm. The final TRISTAN detector, however requires a cable length of almost 2 m.

To assess the pulse shape experimentally, a triggered waveform acquisition of 25 keV electron events from the electron gun (see section 5.2) is used. Figure 6.5 shows an overlay of many acquired pulses for two detector pixels. A pixel map of the extracted median rise time of each pixel is shown in figure 6.6a. The distribution of rise times within one pixel is shown in figure 6.6b for three selected pixels.

The two pixels, compared in figure 6.5, show a significantly different pulse shape. The most probable explanation for the observed difference is a varying source (SC) line stray capacitance. This hypothesis is supported by the similarity of the observed pulse shapes and the simulated pulse shapes for varying stray capacitance of the SC-line C_{p1} in figure 4.17. The fast rise and slight overshoot at pixel 0102 in this picture corresponds to a low capacitance C_{p1}. The slow exponential rise at pixel 1311 fits an increased capacitance C_{p1}. The observation is also consistent with the location of the two pixels: pixel 0102 is close to the bond pads and has a shorter track length of the SC-line compared to pixel 1311, which sits close to the detector center. The trend of an increasing rise time with increasing track length from the bond pads is observed globally on the pixel map of figure 6.6a. A similar effect, where the pulse shape depends on the track length on the SDD, was also observed in pulsed-light-investigations of 7-pixel TRISTAN detectors [133]. In principle, a varying line capacitance of the SC-line can be accounted for in ETTORE by adjusting the BW input

---

[2]the rise time is always given as 10 % to 90 % rise time, even if it is not stated explicitly.
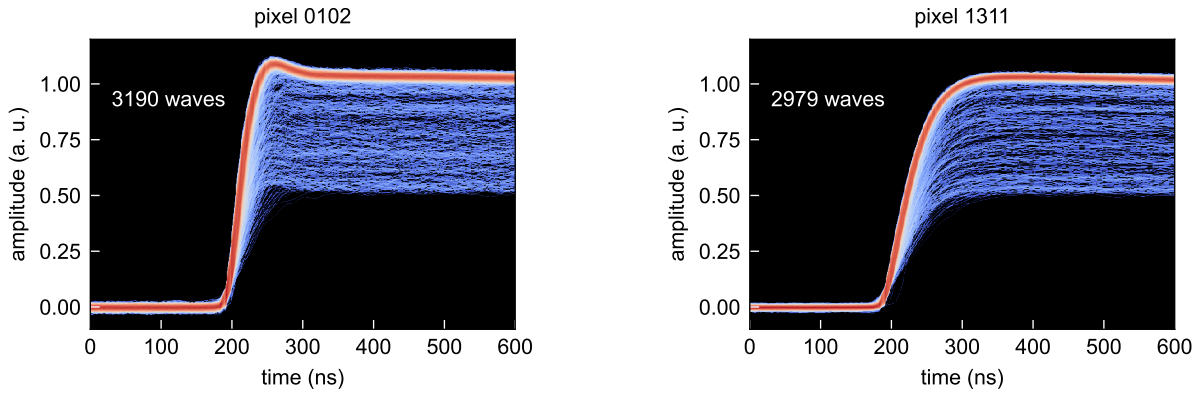
Figure 6.5: Overlay of many waveforms of electrons events with 25 keV kinetic energy. The color code denotes the density of lines, where red is a high density. Detector S0-166-6 is used, cooled to −34 °C. The left plot corresponds to pixel 0102 which is the pixel with the fastest median rise time of 35.7 ns in the detector. The right plot corresponds to the pixel 1311, which is the pixel with the slowest median rise time of 76.1 ns. Only events with a reconstructed energy between 12.5 keV and 27 keV are shown. The pulses are aligned such that the they cross the 0.05 level at the same time. A comparison of the averaged waveforms in all pixels of the same acquisition is shown in figure A.23 in the appendix.
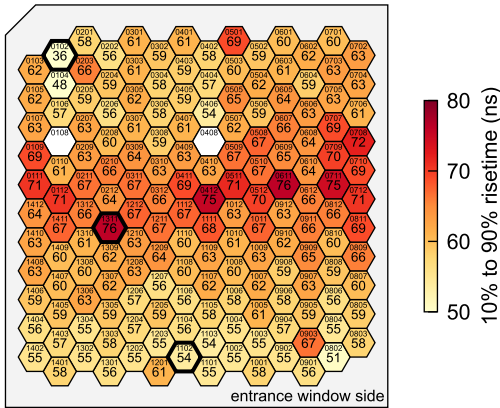
Figure 6.6: Pixel map of the median 10 % to 90 % rise time for 25 keV electron events. Figure 6.5 shows corresponding example pulses. The rise time distrution of the three bold circumfenced pixels are plotted in figure 6.7. Detector S0-166-6 is used, cooled to −34 °C, with two pixels deactivated due to connection issues.
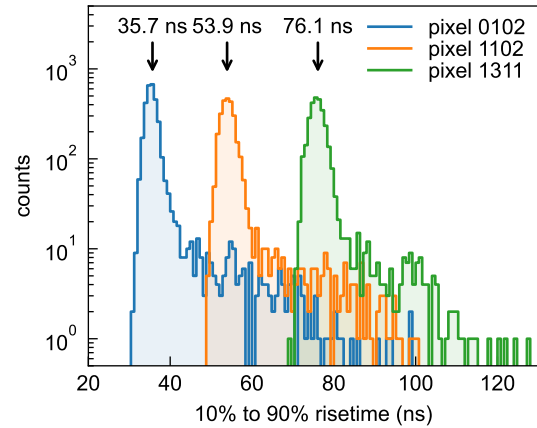
Figure 6.7: Distribution of rise times of three selected pixels of figure 6.6. The annotated value is the median risetime of the three distributions.

voltage (see section 4.2.3). However, the BW voltage cannot be set on a pixel level and is fixed in the current ASIC board layout.

It should be mentioned that the variation of the observed pulse shape is within the specified range of ETTORE production edge cases[3]. In such an edge case, variations of the processing parameters during the ASIC production can cause, for example, an overshooting pulse shape. However, the track length dependence in the pixel map of figure 6.6a hints towards an effect originating from the SDD. When more ASIC boards are available for testing, more insight into the reproducibility of the rise time with different ETTORE ASICs can be expected.

Despite the pixel-dependent pulse shape, the distribution of rise times within each pixel in figure 6.6b shows a tail towards higher values. This effect is expected from the signal formation in the SDD, as simulated in section 4.1.3. The measurement confirms the simulated maximal rise time of around 80 ns for events at the pixel border, which is where the tail ends for pixel 0102. The tail in the rise time distribution motivates the use of a rise time cut. Rejecting events with large rise time would remove events at the pixel border, where part of the charge cloud can be lost to the adjacent pixel[4]. Figure 6.7 shows that an overall increased rise time is disadvantageous for a rise time cut. In this case, the tail becomes less pronounced. The varying median rise times, seen in figure 6.6, make the application of the rise time cut at least challenging for the TRISTAN acquisition. Furthermore, the increase of the cable length from 45 cm in the measurements shown here to almost 2 meter in the final detector will probably further reduce the effectiveness of a rise time cut. Therefore, a rise time cut is currently not considered in the TRISTAN acquisition.

Exponential decay

After the rising edge of a pulse follows an exponential decay with a time constant $\tau \approx 15\,\mu\text{s}$, originating from the second stage of ETTORE. In the digital event reconstruction, the exponential decay is "deconvoluted". The deconvolution only works correctly when the decay time τ and the signal baseline (in the following called offset) of the pulses are known and constant over time. Furthermore, the decaying pulses must not contain any non-exponential shape.

The shape of the pulse decay is now studied with digitized pulses of electron events with a kinetic energy of 25 keV at a high event rate $\mathcal{O}(100\,\text{kcps})$. The high rate is advantageous to assess the signal at higher levels than a single 25 keV pulse due to tail pileup. Figure 6.8 shows the digitized signal of one detector pixel. Each decaying waveform is modeled by

$$y(t) = \text{amp} \cdot e^{\frac{t_0 - t}{\tau}} + \text{offset}, \tag{6.3}$$

with event amplitude amp, event timestamp t_0 and the two shape parameters τ and offset. The fit of equation 6.3 to $\mathcal{O}(10000)$ decaying waveforms yields the average fit parameters

$$\tau = 13.94\,\mu\text{s} \tag{6.4}$$

$$\text{offset} = 3927.8\,\text{lsb}[5] \tag{6.5}$$

---

[3] see figure 17 in "Report on development of ETTORE RUN2" [107]

[4] More details about the effect of charge sharing are found in section 6.5.
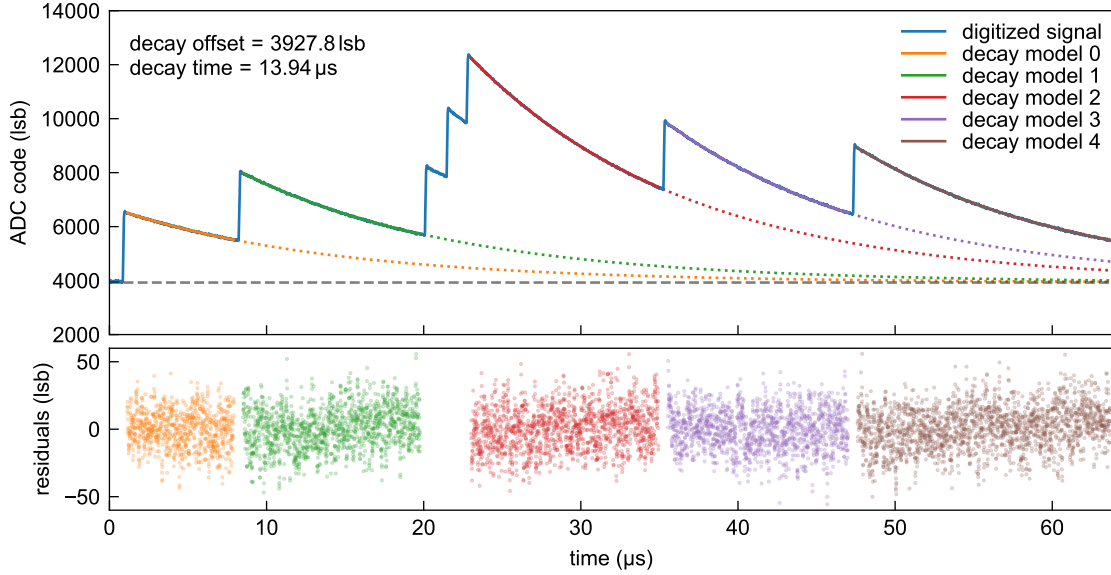
Figure 6.8: Comparison of the decaying waveform to an exponential model. The pulses originate from electron events with a kinetic energy of 25 keV. The models share the same decay offset and decay time. Pixel 0604 of detector S0-166-6 is used, cooled to −34 °C.

In order to check if all individual decay shapes are compatible with these values, a second fit was performed with τ and offset fixed to the averaged values from equations 6.4. Figure 6.8 depicts the corresponding residuals between the model and data. The residuals show no significant distortions from an exponential decay with fixed τ and offset. Slight structures in the residuals are not easy to interpret, as the waveform contains 1/f noise and shot noise, causing correlated residuals. A sophisticated MC study would be necessary to evaluate the significance of residual structures.

So far, the study of exponential decay has focused on a single pixel. The same method is now applied to all pixels of a detector module. The extracted τ and offset for all pixels are plotted in figure 6.9. The decay time varies from 13.2 µs to 14.3 µs. The variation is well covered by production variations[6] of the ETTORE ASIC. The pixel map of the offset parameter in figure 6.9 shows a clear structure. There is a difference of around 1000 lsb between the two hemispheres of the detector and a slight increase of the offset at the pixel center. These two observations originate from two different effects:

- The increased offset at the detector center can be related to an illumination of the detector with light from the filament of the electron gun. The resulting additional detector current causes an increase of the detector baseline. This effect is only present for high-rate electron gun measurements.
- The origin of the offset deviation between the northern and southern hemispheres, corresponding to a voltage deviation of around 150 mV, is unclear. One possible explanation could be a difference of the V_{REF} voltage, which internally defines the second stage baseline on each ASIC board[107]. The difference could also be related to different ground potentials on the two ASIC boards. More investigations are necessary to find the origin.

---

[5]The digital unit of one ADC code is called least significant bit (lsb) in this work.
[6]see figure 16 in "Report on development of ETTORE RUN2" [107]
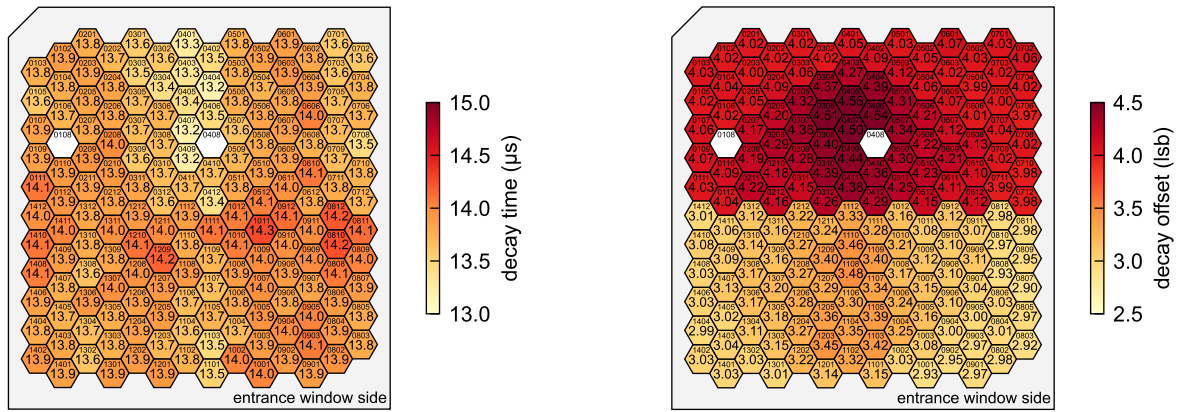
Figure 6.9: Pixel maps of the pulse decay time (left) and decay offset (right), extracted from 25 keV electron events with detector S0-166-6, cooled to $-34\,°\text{C}$.

If calibrated appropriately, the observed pixel dependence of the offset and decay time does not degrade the detector's performance. The influence of a wrongly calibrated decay constant on the spectroscopic performance, for example, due to a drift over time, is studied in the DAQ chapter of this work (section 7.3.4).

6.2.3 Noise curve

The noise curve is measured to quantify the electronic noise on the detector signals (see section 4.3 for an electronics noise model). The noise curve displays the equivalent noise charge (ENC) as a function of the time constant τ_{peaking} of the trapezoidal energy filter. There are two common methods to determine ENC:

1. One measures the width of a physical peak in a recorded spectrum and estimates the ENC by subtracting known effects like the Fano resolution.
2. The shaping filter output[7] output is evaluated without the presence of a physical pulse (base-line evaluation). The standard deviation of the evaluated value directly reflects the ENC.

This second option is used here, as it is a more direct measurement of the electronic noise In the following, a waveform acquisition of X-ray events from the decay of ^{55}Fe is used for calculating the noise curve. The investigation uses all 164 activated pixels of detector S0-166-7. Figure 6.10 shows an example of a digitized pulse with the shaping filter output and the trigger filter output. Both filter outputs are calculated offline, i.e. after the measurement, from the digitized signals. For each pulse, the energy filter output is evaluated two times. The first evaluation is at the trigger timestamp. This evaluation yields the height of the physical pulse. The second evaluation is 10 µs before the trigger timestamp and measures the electronic noise. The spectra of the two evaluations are shown in figure 6.11. The baseline evaluation spectrum is a Gaussian distribution centered around zero, referred to as "zero peak". The pulse evaluation yields the physical spectrum of the ^{55}Fe source with the Mn-K$_\alpha$ line at 5.9 keV and Mn-K$_\beta$ line at 6.5 keV. In order to extract the peak widths, a model is fitted to the zero peak and the physical spectrum. The model contains the peak amplitudes, peak widths and two parameters for a linear calibration as free parameters. In the shown example, the zero peak has a width $\Delta E_{\text{FWHM zero}} = 92\,\text{eV}$. This value is used for the ENC calculation, while the pulse evaluation spectrum is fitted only for a robust energy calibration. The

---

[7]For TRISTAN, the shaping filter is a trapezoidal filter, described in section A.4.4
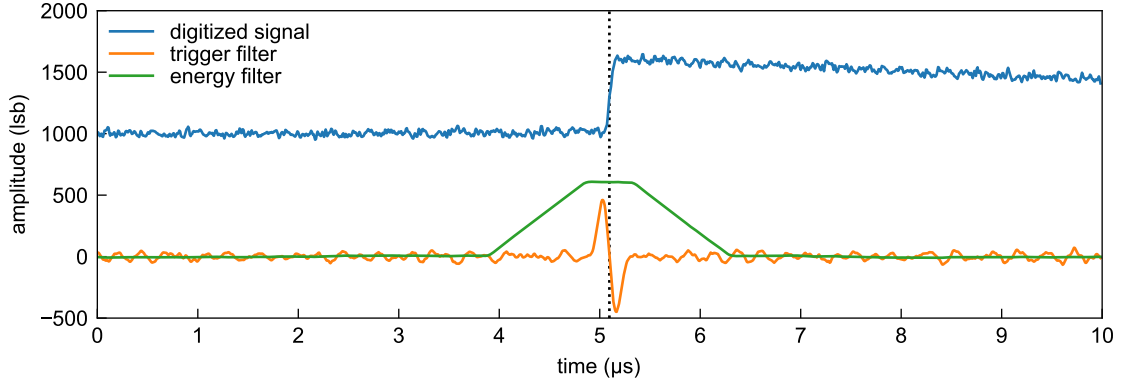
Figure 6.10: Example pulse waveform of an ^{55}Fe X-ray pulse on pixel 0102, used for the noise curve calculation. The output of the trapezoidal energy filter and the bipolar trigger filter are also shown. The trapezoidal energy filter has the parameters $\tau_{\text{peaking}} = 960\,\text{ns}$ and $\tau_{\text{gap}} = 480\,\text{ns}$. The energy is evaluated at the pulse (gray dashed line) and at $10\,\mu s$ before the pulse (outside of the plot window) to get the zero peak.
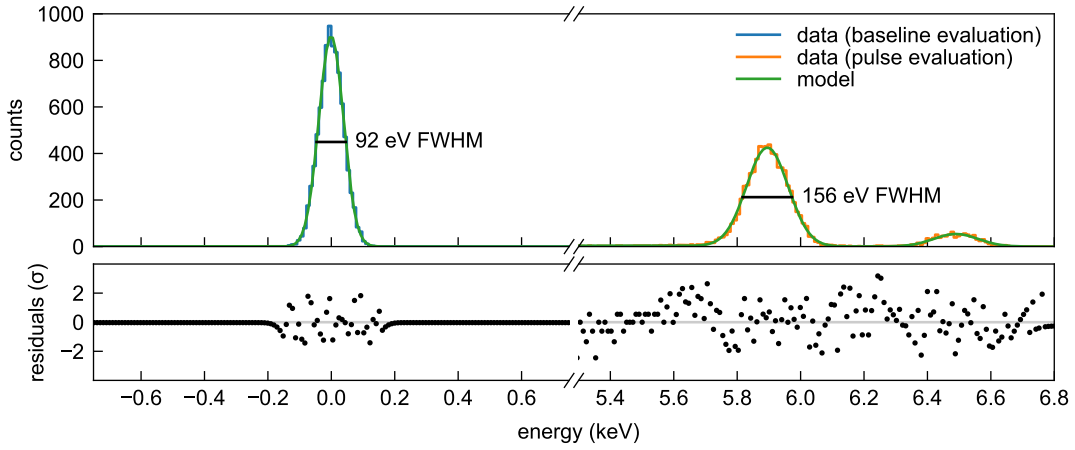
Figure 6.11: Fit of the zero peak and the ^{55}Fe spectrum, used for the noise curve calculation. The spectrum is calculated with a trapezoidal filter with the parameters $\tau_{\text{peaking}} = 960\,\text{ns}$ and $\tau_{\text{gap}} = 480\,\text{ns}$. The width of the Gaussian zero peak is used to calculate the ENC.

ENC value is calculated by

$$\text{ENC} = \frac{\Delta E_{\text{FWHM zero}}}{2\sqrt{2\ln 2} \cdot w} e \,, \tag{6.6}$$

where $w = 3.63\,\text{eV}$ is the pair creation energy of silicon. The factor $2\sqrt{2\ln 2} \approx 2.3548$ originates from converting the FWHM to the standard deviation. The ENC for the example in figure 6.11 is $\text{ENC} = 10.8\,\text{e}$.

As a crosscheck, the measured width of the Mn-K$_\alpha$ line is compared to the calculated width with Fano noise and ENC $= 10.8\,\text{e}$ (see equation 4.37). The measured width $\Delta E_{\text{FWHM}} = 156\,\text{eV}$ is slightly larger than the calculated value $\Delta E_{\text{FWHM}} = 149\,\text{eV}$. There are several possible explanations for the slight difference. For example:

1. The measured X-ray line width could be broadened due to incomplete charge collection at the entrance window or from charge sharing at the pixel border.
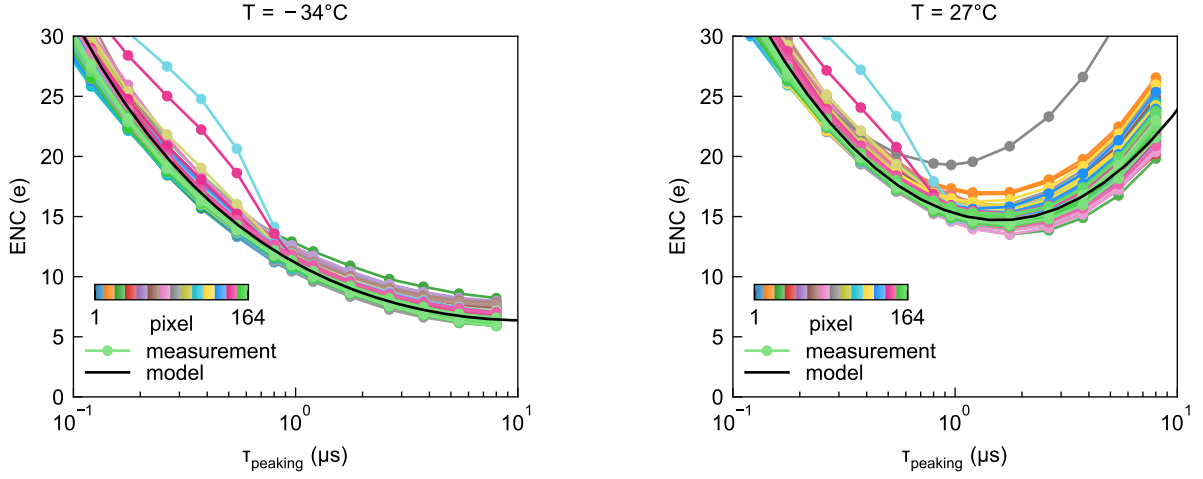
Figure 6.12: Noise curves of detector S0-166-7 with the detector cooled (left) and at room temperature (right). A trapezoidal energy filter with fixed $\tau_{gap} = 480\,\text{ns}$ is used. The standard deviation of the zero peak (see text) is used to extract the equivalent noise charge (ENC) from a measurement of ^{55}Fe pulses. The model uses equation 4.28 with parameters from table 4.2.

2. The Gaussian model, fitted to the X-ray lines, may not describe the spectral shape correctly. This is also seen in a slight structure in the residuals of figure 6.11.

3. The ^{55}Fe K_α peak is not a single line but consists of two lines with a distance of around 10 eV. The procedure to extract ENC is repeated with varying $\tau_{peaking}$ of the energy filter to obtain a noise curve. The result for all pixels of a detector module is shown in figure 6.12. The figure compares a measurement with a cooled detector to a measurement at room temperature.

Overall, the measured noise curves agree with the model developed in section 4.3. The measured ENC values of all pixels are

$$\text{ENC} = 33.2^{+5.5}_{-2.9}\,\text{e} \qquad \text{at} \qquad \tau_{peaking} = 0.08\,\mu\text{s},$$
$$\text{ENC} = 11.3^{+1.6}_{-0.9}\,\text{e} \qquad \text{at} \qquad \tau_{peaking} = 0.96\,\mu\text{s},$$
$$\text{ENC} = 6.7^{+1.5}_{-0.8}\,\text{e} \qquad \text{at} \qquad \tau_{peaking} = 8.0\,\mu\text{s}.$$

The stated value is the median of 164 pixels, and the range is the minimum and maximum appearing value.

The noise curves of three pixels deviate from the model:
- Pixel 0803 has a worse performance for large $\tau_{peaking}$ at room temperature. If the detector is cooled, the performance of pixel 0803 is recovered.
- Pixel 1012 and pixel 1303 show an increased ENC for $\tau_{peaking} < 0.8\,\mu\text{s}$, independent of the temperature.

The origin of the increased noise of these three pixels is further studied by comparing their noise power density spectrum. To this end, the noise power density spectrum is calculated from the digitized baseline waveform at room temperature. The result is shown in figure 6.13. Additionally, the noise power density model, developed in section 4.3, is plotted. Pixel 0102 represents a nominal pixel, for which a good agreement of the measured noise power and the model is observed. Pixel 0803 has an increased parallel noise component, fitting to the increased leakage current, which
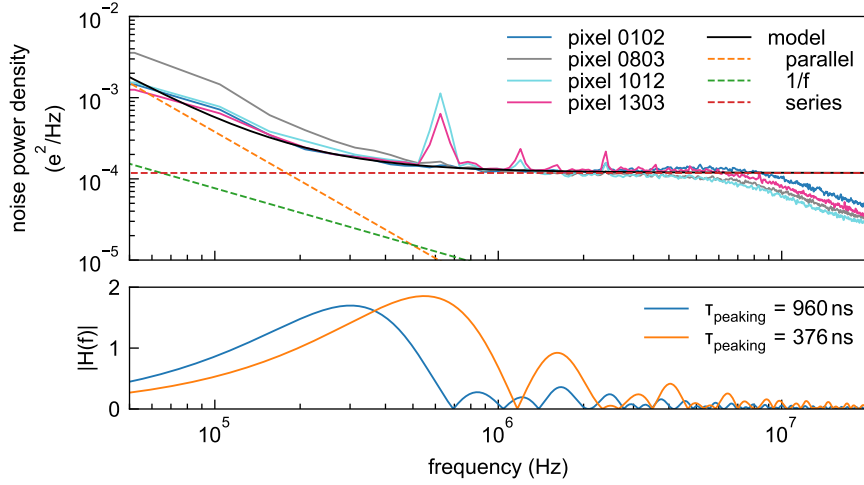
Figure 6.13: Noise frequency analysis of four selected pixels of detector S0-166-7 at room temperature. The noise power density (top) is calculated from many baseline snippets of 19.2 μs length from a triggered waveform acquisition. The model uses equation 4.28 with the room temperature parameter from table 4.2. The transfer function $|H(f)|$ (bottom) of the trapezoidal energy filter with two different τ_{peaking} and fixed $\tau_{\text{gap}} = 480$ ns is also shown. The equation for $|H(f)|$ is given in equation 4.26.

was detected already in section 6.2.1. The two remaining outlying pixels 1012 and pixel 1303 both show a noise excess at the frequency $f \approx 600$ kHz. Depending on the trapezoidal filter's peaking time τ_{peaking} $|H(f)|$, this frequency has a strong effect (i. e. at $\tau_{\text{peaking}} = 376$ ns) or a negligible effect (i. e. at $\tau_{\text{peaking}} = 960$ ns) on the ENC. A possible cause for excess noise at $f \approx 600$ kHz noise frequency is electromagnetic interference from switched-mode DC-DC converters, for example, present on the XGlab bias and control board.

Two more plots of the noise curve of the TRISTAN detector model are produced: Figure 6.14 directly compares the median noise curves at room temperature and with cooling. Furthermore, figure 6.15 compares the median noise curve to the noise model developed in section 4.3. Which of the three noise components (parallel, 1/f, and series noise) dominates depends on the temperature and the energy filter peaking time.

In conclusion, the 166-pixel module S0-166-7 shows an excellent noise performance, in line with the analytical estimations of section 4.3. A median ENC of 11.3 e at a trapezoidal peaking time $\tau_{\text{peaking}} = 960$ ns confirms a central feature of the TRISTAN detector, which is the high-rate operation with good energy resolution. The noise level is homogeneously distributed for all pixels of the detector module. Furthermore, the investigation of the noise power density spectrum revealed the origin of three slightly outlying pixels: Two pixels show an increased sensibility to electromagnetic interference, and one pixel shows an increased leakage current at room temperature. However, with the correct settings ($\tau_{\text{peaking}} = 960$ ns and detector cooled), these three pixels have a good performance and can be used for physics measurements.
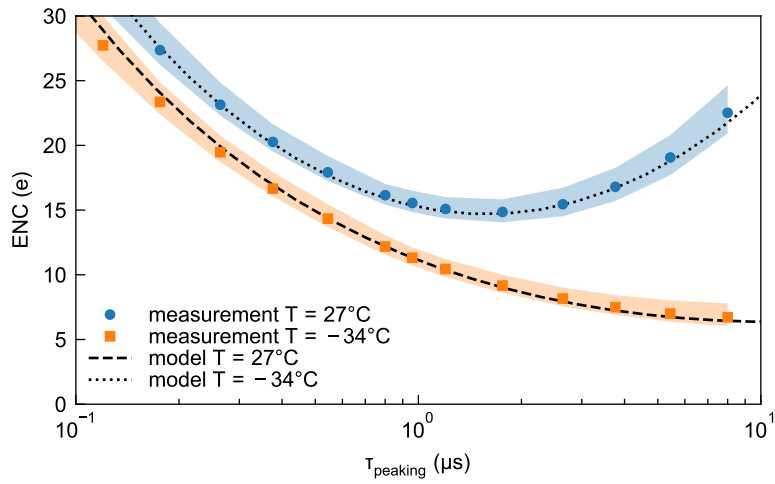
Figure 6.14: Comparison of the root temperature and cooled noise curves of detector S0-166-7. The measurement data points correspond to the median of all 164 pixels of figure 6.12. The band is the 90 % central interval of all pixels. The model uses equation 4.28 with parameters from table 4.2.
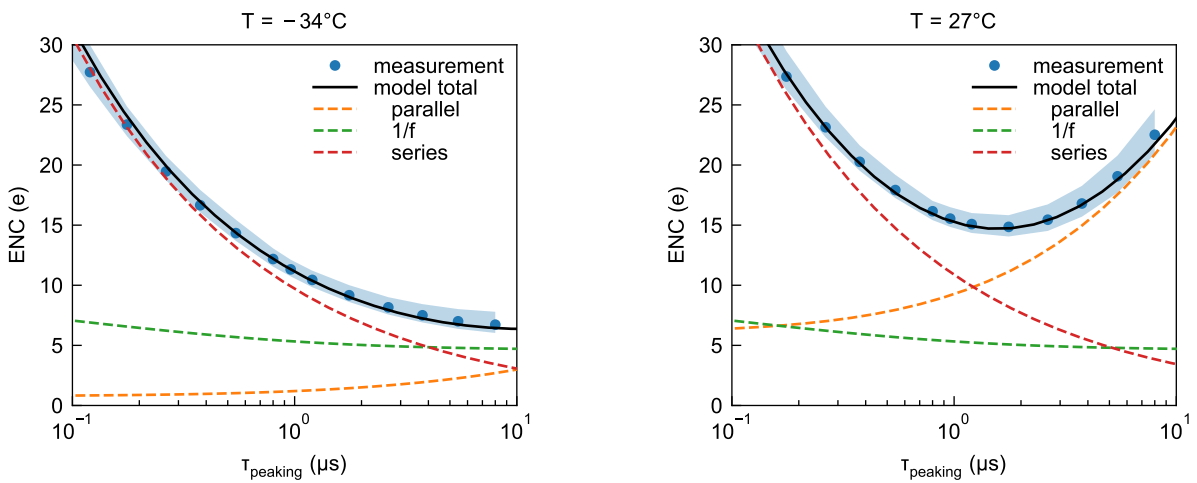
Figure 6.15: Comparison of the measured noise curves of detector S0-166-7 with the noise model. The measurement data points and the band are the same as in figure 6.14. The model uses equation 4.28 with parameters from table 4.2.

Comparison to previous detector generations

The noise performance of an SDD depends on the detector and amplifier design as well as the quality of the wafer processing steps. Therefore, variations can occur in different designs and productions. Figure 6.16 compares the noise curves of four different 7-pixel detectors of different productions, listed in table 6.1. The used bias parameters are given in the appendix table A.6. The room temperature noise curves are compared, as a cooled measurement was not available for all detectors. The noise curves of productions 1, 1b, and 2 were calculated analogous to the description in section 6.2.3, based on the width of the zero-peak. The noise curve of the detector prototype 0, with CUBE readout, is based on the width of the ^{55}Fe K$_\alpha$ peak. The reason for this is that the detectors with CUBE readout do not feature a second stage and, therefore, also use a different DAQ system[8], which is optimized for first stage ramp signals. With this DAQ, the zero-peak method was not available when the data was taken.

Figure 6.16 shows that the equivalent noise charge (ENC) of the detectors compare differently depending on the trapezoidal filter peaking time τ_peaking. At large peaking times the ENC is dominated by shot noise, originating from leakage current. The leakage current can differ for the different detector productions and depends strongly on temperature. Thus, the observed differences at $\tau_\mathrm{peaking} > 1\,\mu\mathrm{s}$ can originate from a different detector temperature, which was not regulated for the measurements. Due to the cooling in the final TRISTAN detector setup, the differences in the noise curve at large peaking times are not of concern.

More interesting is the noise performance at short peaking times, which measures the series noise on the detector signals (see section 4.3 for a noise model). The prototype 0 detector has the best series noise performance of the compared devices (ENC $\approx$ 19 e at $\tau_\mathrm{peaking} = 256\,\mathrm{ns}$). The first tested TRISTAN detector with integrated JFET and ETTORE readout (label prototype 1) has a significantly larger ENC value at short peaking times (ENC $\approx$ 35 e at $\tau_\mathrm{peaking} = 264\,\mathrm{ns}$). After detailed searches for possible origins of the increased series noise, one reason was found: An unexpected high resistance was present between the n-implanted silicon and the aluminum line at the integrated JFET drain and source contacts in production 1. The additional resistor R_contact in the source line, illustrated in the circuit diagram of figure 6.17, worsens the noise performance of the detector. The thermal voltage noise power of $W = 4k_B T R_\mathrm{contact}$ adds to the overall series noise (see equation 4.24)

$$W_\mathrm{out\ amp\ series}^\mathrm{ENC} = C_a^2 4 k_B T \left(\frac{a_n}{g_m} + R_\mathrm{contact} \right). \tag{6.7}$$

---

[8]XGlab DANTE DPP

Table 6.1: Devices used for the noise curve comparison. Bias parameters are listed in the appendix table A.6.

label	# pixels	⌀ pixel	readout	comment
prototype 0	7	2 mm	CUBE	
production 1	7	3 mm	JFET + ETTORE	
production 1b	7	3 mm	JFET + ETTORE	fixed contact resistance issue and other improvements
production 2	7	3 mm	JFET + ETTORE	final TRISTAN design
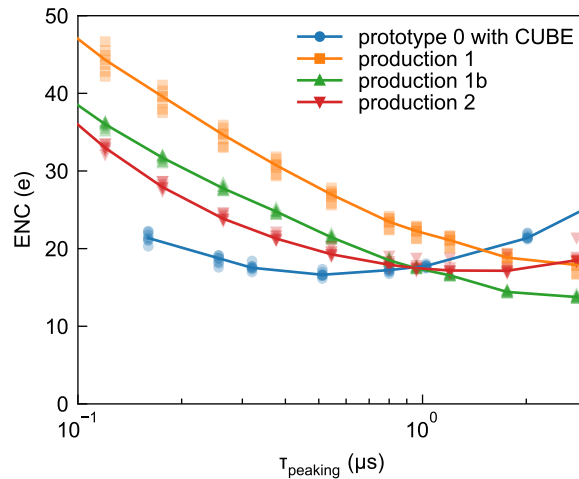
Figure 6.16: Noise curve of 7-pixel devices of different detector productions at room temperature. The markers indicate the individual pixels, and the line represents the mean of the pixels.
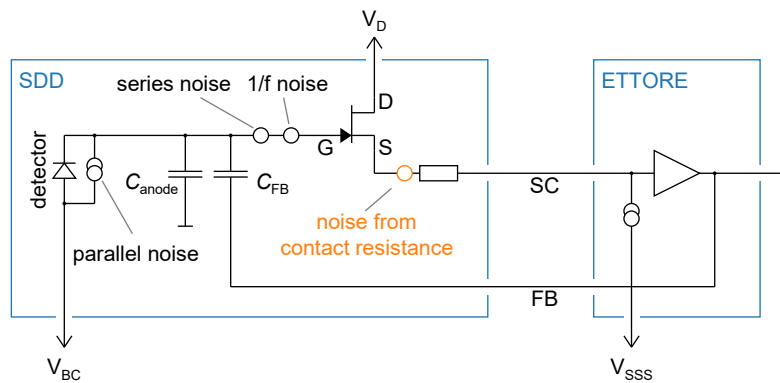
Figure 6.17: Circuit diagram of the TRISTAN readout with additional contact resistance at the JFET source line. The contact resistance comes with a thermal voltage noise source, which adds to the series noise of the detector.

The first term in the bracket corresponds to the series noise of the JFET channel and is approximately $4\,\mathrm{k}\Omega$ (see equation 4.24 in section 4.3). Consequently, a contact resistance $R_{\mathrm{contact}} \approx 4\,\mathrm{k}\Omega$ would double the series noise power. The series ENC, which scales with the square root of the noise power, is thereby increased by a factor 1.4. A measurement done by the semiconductor laboratory showed contact resistance values $\mathscr{O}(\mathrm{k}\Omega)$ for production 1, which can explain a significant increase in the series noise. In the subsequent detector productions, the semiconductor laboratory could solve the contact resistance issue by an additional implantation step. Figure 6.16 shows that production 1b, with the additional implantation, has an improved series noise (ENC $= 28\,\mathrm{e}$ at $\tau_{\mathrm{peaking}} = 264\,\mathrm{ns}$) compared to production 1.

The latest TRISTAN production 2 shows a further improved series noise performance (ENC $= 24\,\mathrm{e}$ at $\tau_{\mathrm{peaking}} = 264\,\mathrm{ns}$) compared to production 1b. This suggests that there may have been further reasons besides the contact resistance issue, which worsened the series noise performance of production 1. The series noise performance of the 7-pixel device of production 2 agrees with the previously presented measurement of a 166-pixel device at room temperature (see figure 6.14). Thus,

91

the noise performance is independent of the device's pixel count. In conclusion, the series noise performance has significantly improved from production 1 to production 1b and production 2. The prototype 0 detectors without integrated JFET, but external CUBE readout, sill have a slightly lower ENC at short τ_{peaking}, which probably originates from the different readout designs.

6.2.4 Response to electrons

The energy resolution for electrons as primary particles is generally larger than the energy resolution for X-rays. The increase is primarily due to the entrance window effect: Electrons lose kinetic energy by scattering at the entrance window, where the charge collection efficiency is reduced. A typical effective thickness of the insensitive layer is about 50 nm [138]. With the electron gun setup developed within this work, a precise measurement of the detector response to electrons is possible. To this end, acquisitions of monoenergetic electrons at 5, 10, 15, 20 and 25 keV are performed. The measurement uses the electron gun, described in section 5.2, at moderate rates of $\mathcal{O}(1\,\mathrm{kcps})$. In the following, a single pixel 0604 of detector S0-166-6 is investigated. More measurements of the detector response of all pixels of several modules are, for example, found in [97] and [143].

Figure 6.18 presents the acquired spectra. Besides the electron peak, there are the Mn-K$_\alpha$ and Mn-K$_\beta$ X-ray peaks of an ^{55}Fe source present at 5.9 keV and 6.5 keV, respectively. The X-ray lines and a zero peak (compare section 6.2.3) are used for the energy calibration. The recorded electron spectra show several features:

- The main electron peak is slightly asymmetric and shifted compared to the energy calibration from X-rays. The reason is the statistical energy loss of electrons at the entrance window.
- The silicon escape peak sits 1.7 keV below the main electron peak. This peak is two orders of magnitude weaker compared to the main peak.
- A tail from the main peak down to zero originates from electrons that are backscattered and leave the detector volume with residual kinetic energy.
- A small amount of events from pileup is found above the main peak. The shape of the pileup spectrum is similar to the convolution of the input spectrum with itself, causing a peak at twice the energy of the main peak.

The FWHM of the main electron peak is plotted in figure 6.19. For comparison, also the resolution of ^{55}Fe (156 eV FWHM at 5.9 keV), the Fano resolution, and the electronic noise contribution are shown. The entrance window effect dominates the energy resolution for electrons with low energies. A minimal energy resolution is observed at around 10 keV. At higher energies, the Fano resolution dominates.

All measurements from 5 keV to 25 keV show an energy resolution below 300 eV FWHM, which was one design goal of the TRISTAN detector [93]. Although this measurement demonstrates the excellent electron performance of the TRISTAN detector, it does not prove the homogeneity of the performance for all pixels and its stability over time. These properties are studied, utilizing the electron gun setup, in other theses [143, 136].
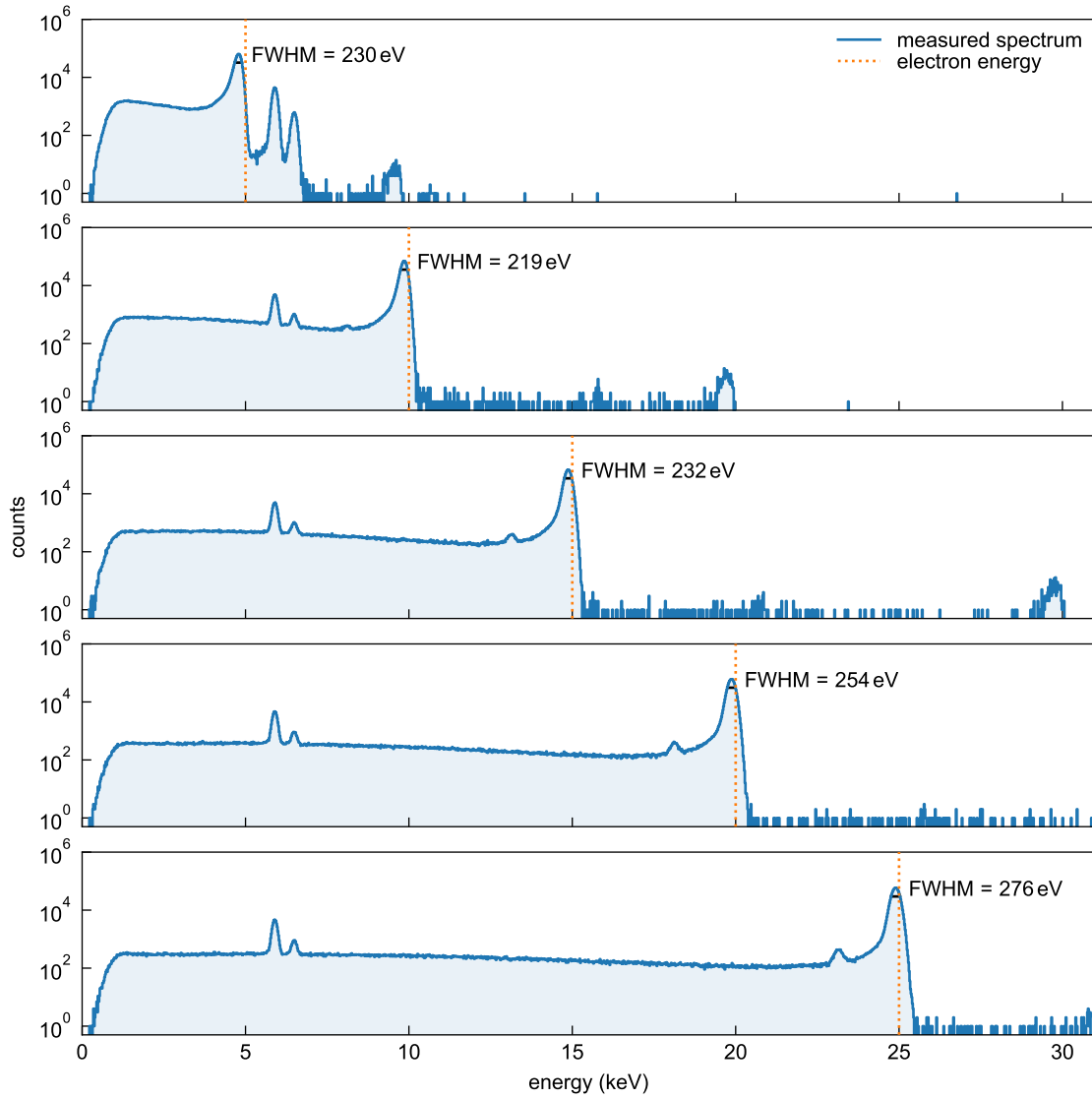
Figure 6.18: Measured electron response of pixel 0604 and detector S0-166-6 at five different energies. The detector was cooled to $-34\,°\text{C}$. Each measurement had a duration of 20 minutes at a count rate of around 1 kcps. The trapezoidal energy filter had the parameters $\tau_{\text{peaking}} = 960\,\text{ns}$ and $\tau_{\text{gap}} = 480\,\text{ns}$.
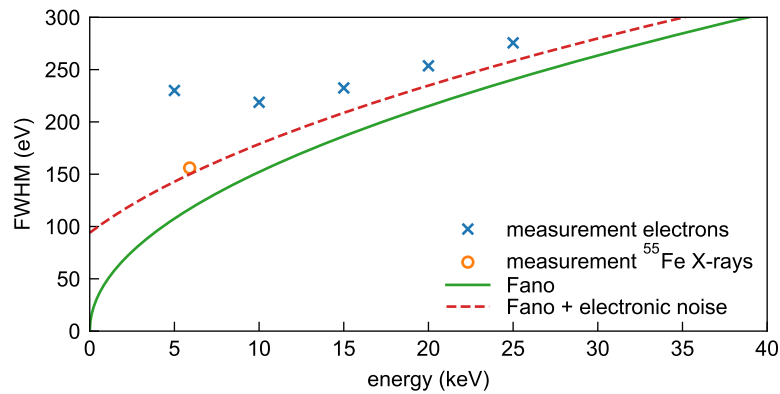
Figure 6.19: Energy resolution (FWHM) as a function of energy. The Fano and electronic noise is calculated according to equation 4.37 with an equivalent noise charge $\text{ENC} = 11\,\text{e}$.

6.3 Crosstalk

The effect of crosstalk describes electric interference of detector signals on different channels. The mitigation of crosstalk in the TRISTAN detector readout is very demanding due to the high readout density and analog signal routing. Crosstalk can change the spectroscopic response of the detector. Therefore, it is a critical systematic effect, which must be taken into account in the sterile neutrino search with the TRISTAN detector.

The first following section 6.3.1 presents a measurement of crosstalk in 7-pixel devices of the first detector production. After that, possible mechanisms of crosstalk are studied (section 6.3.2) and design modifications for mitigation of crosstalk are presented (section 6.3.3). The consecutive section 6.3.4 then compares the measured crosstalk in different detectors where these design modifications are implemented. These measurements were used to find the best design for the detector production 2. Finally, in section 6.3.5 the crosstalk situation in 166-pixel detectors from detector production 2 is shown.

6.3.1 Measurement of crosstalk

Crosstalk is measured by simultaneously capturing the signals on all device channels. A physical event on one channel triggers the data acquisition in all channels. The channel with the physical event is called "aggressor" in the following, and the other channels (without physical events) are called "victims".

An example of a crosstalk acquisition using a 7-pixel device with ^{55}Fe X-ray events is shown in figure 6.20. The plot shows the average of $\mathcal{O}(1000)$ digitized signals of all seven detector channels. The events were selected such that for all events, the central pixel (labeled CC, see pixel map in figure 6.21) is the aggressor, and all other pixels are victims. Without crosstalk, one would expect the averaged output signals of the victim channels to be flat[9]. However, it is observed that distortions, which coincide with the aggressor event, are visible on all six averaged victim signals. Four victim channels show minor distortions with a negative amplitude of around 1 % of the aggressor's event amplitude. Two channels (NN and SS), however, show relatively large distortion with negative amplitudes of around 7 % and 9 %.

This measurement is repeated for all possible aggressor channels. To illustrate all resulting signals, a 7×7 "crosstalk waveform matrix" is used, where the rows define the aggressor channel and the columns define the victim channels. The waveforms of figure 6.20 fill the fifth row of the matrix. The entire matrix of waveforms is shown in figure 6.22. To quantify the amount of crosstalk, the relative crosstalk amplitude is defined as the absolute amplitude of the distortion on the victim channel relative to the amplitude of the corresponding aggressor event. The resulting "crosstalk amplitude matrix" is shown in figure 6.23.

The crosstalk amplitude matrix shows a clear structure: The amplitude of crosstalk is large (around 8 %) within three subgroups of channels: $\{NW, SW\}$, $\{NN, SS, CC\}$, and $\{SE, NE\}$. The three subgroups correspond to one readout column of pixels each, which are visible in figure 6.21. Hence, a lagre crosstalk amplitude is observed between pixels with have readout lines geometrically close to each other. Further properties of the observed crosstalk are:

---

[9]A small imprint of charge sharing is expected. However, if the corresponding amplitude is calculated, it turns out to be negiligble.
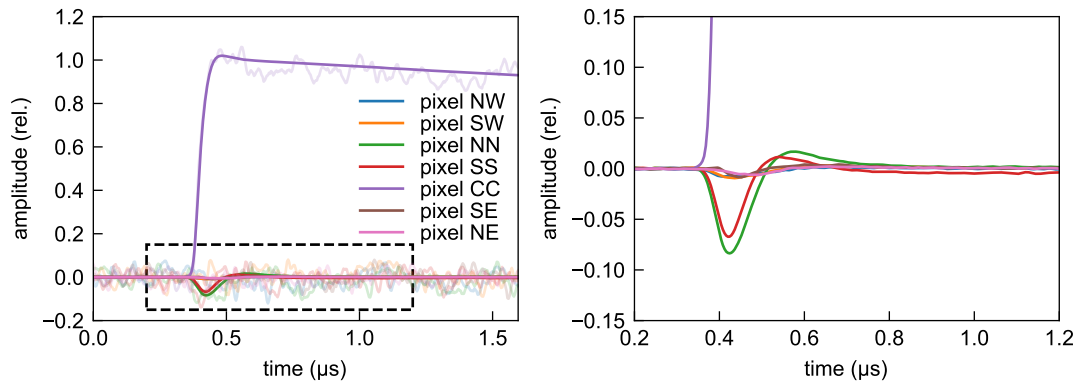
Figure 6.20: Waveform acquisition with a 7-pixel detector to measure crosstalk. The lines correspond to the average of many traces where channel CC has a physical event from an ^{55}Fe X-ray source. The faint lines correspond to one example event to illustrate the noise level on the signals. The right plot zooms in on the distortions on victim channels due to crosstalk.
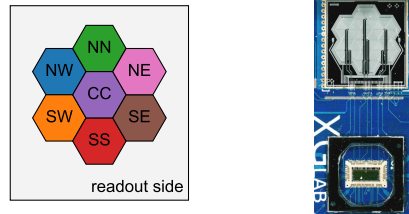
Figure 6.21: Left: Pixel map of a 7-pixel detector (CC: central, NN: north, NE: northeast, ...). Right: picture of a 7-pixel detector mounted on the front-end electronics board with an ETTORE ASIC (black square at the bottom). The readout routing, visible as black traces on the detector chip, is arranged in three readout columns.

- The crosstalk is symmetric, such that the crosstalk between aggressor channel A and victim channel B has a similar amplitude as the crosstalk from aggressor channel B and victim channel A.
- The crosstalk is linear, which means that the relative crosstalk amplitude is independent of the event energy. The linearity was tested with several X-ray lines of an ^{241}Am source.
- The crosstalk amplitudes are robust against detector bias voltages, such as the back contact voltage. The bias settings for the used 7-pixel detector are listed in the appendix table A.6.
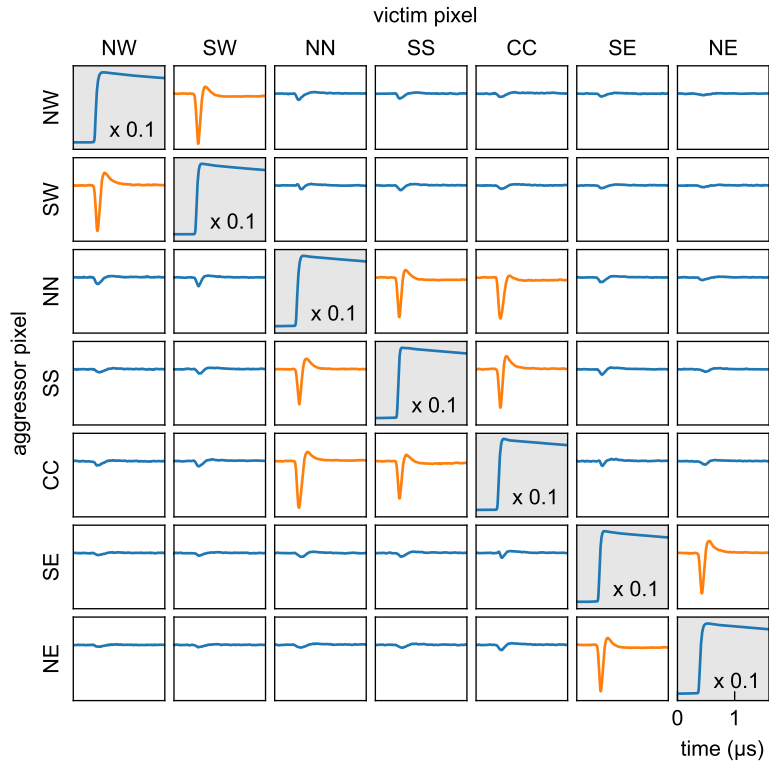
Figure 6.22: Crosstalk waveform matrix of a 7-pixel detector. The plotted signals correspond to the victim channel. The physical pulses on the aggressor channel are shaded in gray and scaled by a factor of 0.1 to fit the full pulse. Each plotted signal averages $\mathcal{O}(1000)$ signals. The victim channels, which share the same readout column as the aggressor channel (see figure 6.21), show significantly enhanced crosstalk and are indicated in orange in the figure.
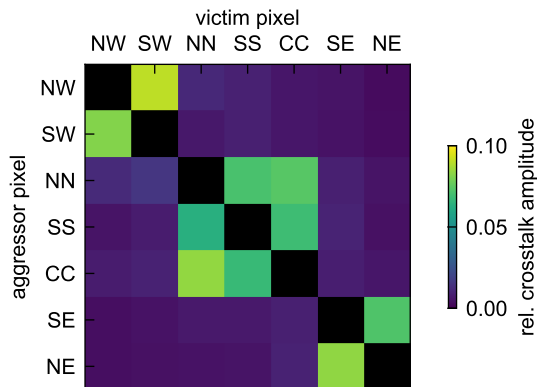
Figure 6.23: Crosstalk amplitude matrix of a 7-pixel detector. The matrix is based on the data of the crosstalk waveform matrix of figure 6.22. The color code is the absolute amplitude of the distortion on the victim channel relative to the amplitude of the aggressor event. The three subgroups of channels in the same detector column are visible due to their increased crosstalk amplitude.

6.3.2 Mechanisms for crosstalk

The most relevant mechanism that can cause crosstalk is related to capacitive couplings on the level of the CSA feedback loop. The high readout routing density and the high driving point impedance, especially of the JFET source (SC) line, make the CSA feedback loop particularly susceptible to crosstalk. Figure 6.24 shows a simplified electric circuit of two detector channels. Four possible cross-capacitance locations are drawn in the figure. The cross-capacitances connect two lines (FB or OUT) of the aggressor channel with sensitive lines (anode, SC or FB) of the victim channel.

An electric trace-level simulation of the circuit is performed to study how the distortion on the victim channel would look with these cross-capacitances. The simulation uses the same method and settings as described in section 4.2.3 but with two CSA circuits simulated in parallel[10]. The simulation calculates the response in time domain of both channels to a δ-shaped input charge pulse at the anode of the aggressor channel. Figure 6.25 plots the simulated signals. Due to the very small size of the cross-capacitance, the system behaves linearly, and the amplitude of the distortion on the victim channel is proportional to the size of the cross-capacitance. The proportionality is described by the crosstalk gain, given in table 6.2. The crosstalk gain is the ratio of the relative crosstalk amplitude to the value of the cross-capacitance. The table also gives the value of the cross-capacitance, which would be necessary to observe a 1 % distortion. The simulation shows that the four different cross-capacitances would have the following effects:

- **FB-anode** A cross-capacitance between the aggressor's FB line and the victim's anode introduces a negative step-like signal on the victim output (sometimes referred to as integral crosstalk). The cross-capacitance acts similar to the feedback capacitance $C_{FB} = 25\,fF$, which is implemented at each channel's anode. Although this is a very sensitive cross-capacitance (250 aF is sufficient to cause a 1 % effect), this cross-capacitance is suppressed geometrically, as the anode is not routed outside of the anode region of each pixel. However, this kind of cross-capacitance could also be implemented via coupling the FB line to a supply line (e.g. IG or R1) and a subsequent coupling of the supply line to the anode.

- **FB-SC** A cross-capacitance between the FB line and the SC line causes a negative dip in the output of the victim channel. The distortion is only present during the voltage transient of the aggressor (sometimes referred to as differential crosstalk). The FB-SC cross-capacitance has a much lower crosstalk gain than the FB-anode crosstalk. However, the FB and SC lines of all channels are routed between the SDD and the ETTORE ASIC using a long parallel routing. Therefore, values of around 100 fF can easily occur in the line routing, which would

---

[10]The only difference compared to the simulation in chapter 4.2.3 is that a value of $C_{p1} = 60\,pF$ is used by default instead of $C_{p1} = 40\,pF$.

Table 6.2: Simulated magnitude of crosstalk for different locations of a cross-capacitance. The crosstalk gain is the relative crosstalk amplitude per unit cross-capacitance.

cross-capacitance	crosstalk gain (10^{12}/F)	capacitance necessary for 1 % rel. crosstalk amplitude (fF)
$C_{FB\text{-anode}}$	40	0.25
$C_{FB\text{-SC}}$	0.5	20
$C_{FB\text{-FB}}$	0.0014	7000
$C_{OUT\text{-SC}}$	5.5	2
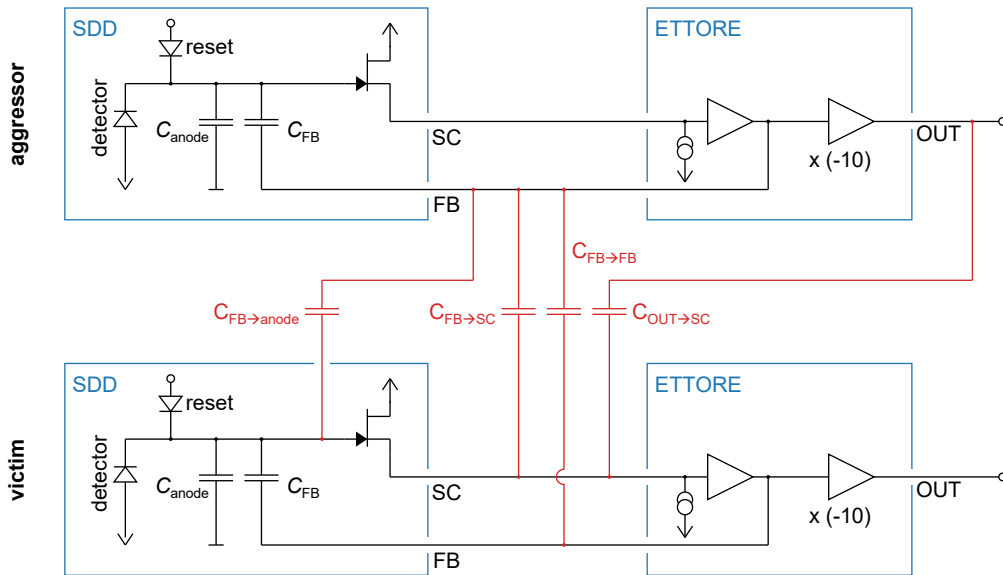
Figure 6.24: Electric circuit of two detector channels to study possible crosstalk mechanisms. The CSA loop extends from the SDD chip to the ETTORE ASIC and involves the feedback line (FB) and JFET source line (SC). Four selected locations of possible cross-capacitances considered most relevant are added in red to the circuit.

correspond to a 5 % crosstalk amplitude. In order to mitigate this crosstalk mechanism, special care was taken when the lines were routed (for example, there are no FB-SC line neighbors of different pixels) [89].

- **FB-FB** A cross-capacitance between the aggressor's FB line and the victim's FB line has a much lower crosstalk gain than the FB-SC cross-capacitance. This is because ETTORE has a smaller output impedance than the JFET source, making the FB line less susceptible to pickup distortions. Furthermore, a distortion on the FB line leads to a smaller output signal compared to a distortion on the SC line. The shape of the victim output signal looks almost like the second derivative of the aggressor's output signal. Although a rather large cross-capacitance is necessary (7 pF to have a 1 % effect), there are many neighboring FB lines of different channels in the line routing between SDD and ETTORE.

- **OUT-SC** The last studied cross-capacitance sits between the aggressor's ETTORE output (OUT) line and the victim's SC line. This cross-capacitance acts similar to the FB-SC capacitance but with the additional gain of −10 of the 2nd stage of ETTORE[11]. Consequently, the crosstalk gain is ten times as large as in the case of FB-SC coupling, and the distortion has the opposite (now positive) sign. Although the crosstalk gain is larger, this cross-capacitance is generally less problematic than the FB-SC capacitance, as there is almost no geometric overlap between the ETTORE output and the SC line routing.

It should be mentioned that the simulated crosstalk gain and distortion shape is a simplified estimation. Many details, for example the total stray capacitances of the SC and FB line, substantially influence the crosstalk distortions. However, these are difficult to measure and can be pixel-dependent.

---

[11]The gain can be changed to −5 by choosing the LG option in the ETTORE settings. However, all crosstalk measurements were done with a gain of −10.
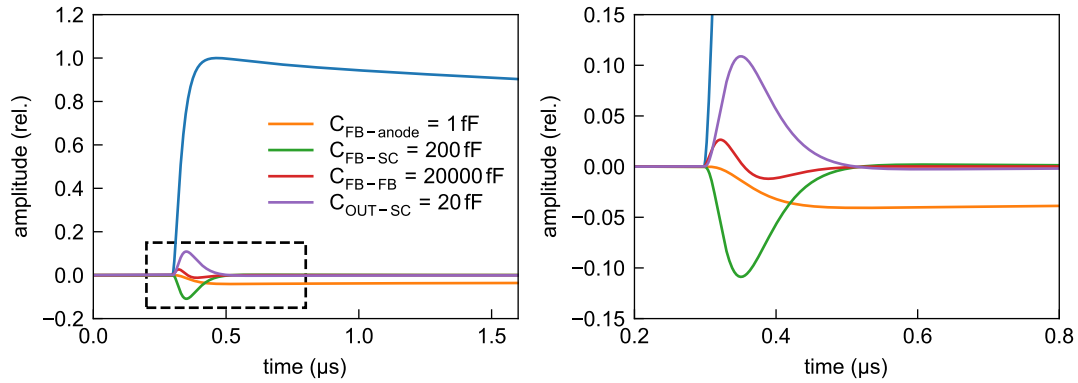
Figure 6.25: Simulated victim output signals of the crosstalk circuit simulation with four different locations of the cross-capacitance. The aggressor signal is shown in blue. The values for the cross-capacitances in the simulation were chosen arbitrarily so that the output distortion has a reasonable magnitude for plotting. The right plot zooms in on the distortions on the victim signal.
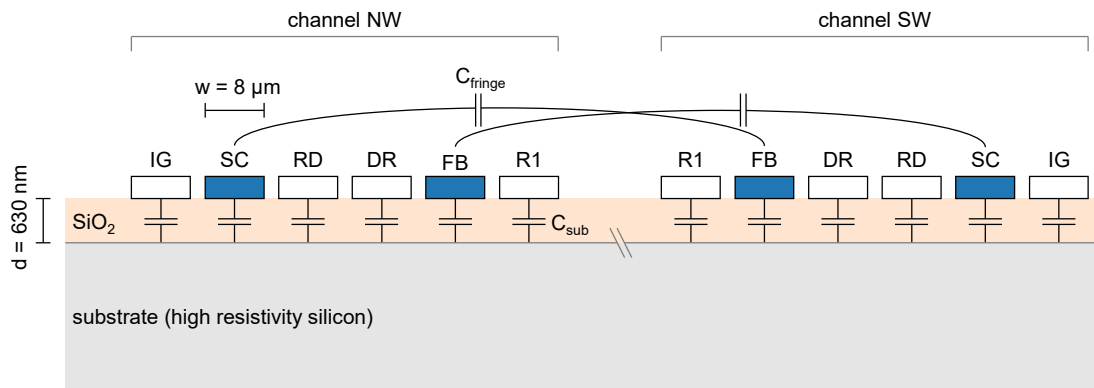
Figure 6.26: Cross section of the readout lines on the SDD chip of two channels of a 7-pixel device (compare figures 6.21 and 2.8). The two pixels have a mirrored line order. The drawn capacitances show possible contributions to the FB-SC cross-capacitance, which could explain the observed crosstalk.

The comparison of the simulated crosstalk signals from figure 6.25 and the measured 7-pixel waveforms from figures 6.20 and 6.22 shows that the most dominant observed crosstalk structure fits to an FB-SC cross-capacitance. The observed channel pattern relates to the column-wise routing of the readout lines on the SDD. This is a strong hint that the cross-capacitance originates mainly from the SDD chip and not from the line routing on the PCB or from ETTORE.

Now, possible origins for cross-capacitance on the SDD chip are studied. Figure 6.26 illustrates the cross section of the readout lines of two pixels on the SDD chip. The SC and FB lines are embedded between supply lines, particularly the innermost ring supply (R1), the JFET drain line (DR), or the reset diode line (RD). A direct cross-capacitance C_{fringe} between FB and SC lines of the two pixels is assumed negligible due to the large distance and the presence of supply lines in between. Another probably more critical coupling path involves the carrier silicon substrate and the corresponding capacitance C_{sub}. C_{sub} has a relatively large value of 0.5 pF/mm, estimated using the equation for

Table 6.3: Design modifications for productions 1a, 1b and 1c compared to production 1.

	contact implantation	modifications for studying crosstalk			
		shifted lines	lines on thick insulator	narrow FB and SC lines	broad GND line
production 1	no	no	no	no	no
production 1a (reference)	yes	no	no	no	no
production 1b (moderate)	yes	yes	yes	yes	no
production 1c (advanced)	yes	yes	yes	yes	yes

the parallel plate capacitance C_{pp} per length l

$$\frac{C_{pp}}{l} = \frac{w}{d}\epsilon_0\epsilon_r,\tag{6.8}$$

with width $w = 8\,\mu\text{m}$, distance $d = 630\,\text{nm}$, and the relative permittivity of SiO_2 $\epsilon_r = 3.9$. Besides depending on C_{sub}, the details of a coupling through the substrate may also be location-dependent on the chip. Where the readout lines pass over an area outside of the active pixels, the high-resistivity substrate is connected to a grounded outer substrate contact. The electric properties (conductive or depleted) of the high-resistivity substrate here depend on the involved potentials and are difficult to predict. Where the readout lines pass over drift rings, C_{sub} connects to the corresponding p^+-implantation of each drift ring. In both regions, the capacitive coupling between FC and SC lines through the substrate is a potential candidate to cause crosstalk.

6.3.3 Design modifications of production 1x

After the first tests of devices of production 1, there was the option to produce two more wafers with modified readout line geometry. Initially, these wafers were dedicated to studying a new entrance window technology. However, they also provided a good opportunity to fix issues found in production 1 and study the influence of the readout design on crosstalk. Devices with three different designs (labeled production 1a, 1b, and 1c) were implemented in the new production. The modifications are listed in table 6.3. The corresponding readout structure designs are shown in figure 6.27. The main modifications are the following ones:

- **Contact implantation** One issue in production 1 was an increased contact resistance, which led to an increased noise on the detector signals. This issue was solved by an additional contact implantation on all three designs 1a, 1b, and 1c. This modification was done independent of the crosstalk investigations.
- **Shifted lines** In designs 1b and 1c, the readout lines were shifted slightly to bypass the anode region of other pixels at a larger distance (see figure 6.27). If crosstalk is caused by the capacitive coupling of lines to the anode structure of other pixels, this would reduce the crosstalk.
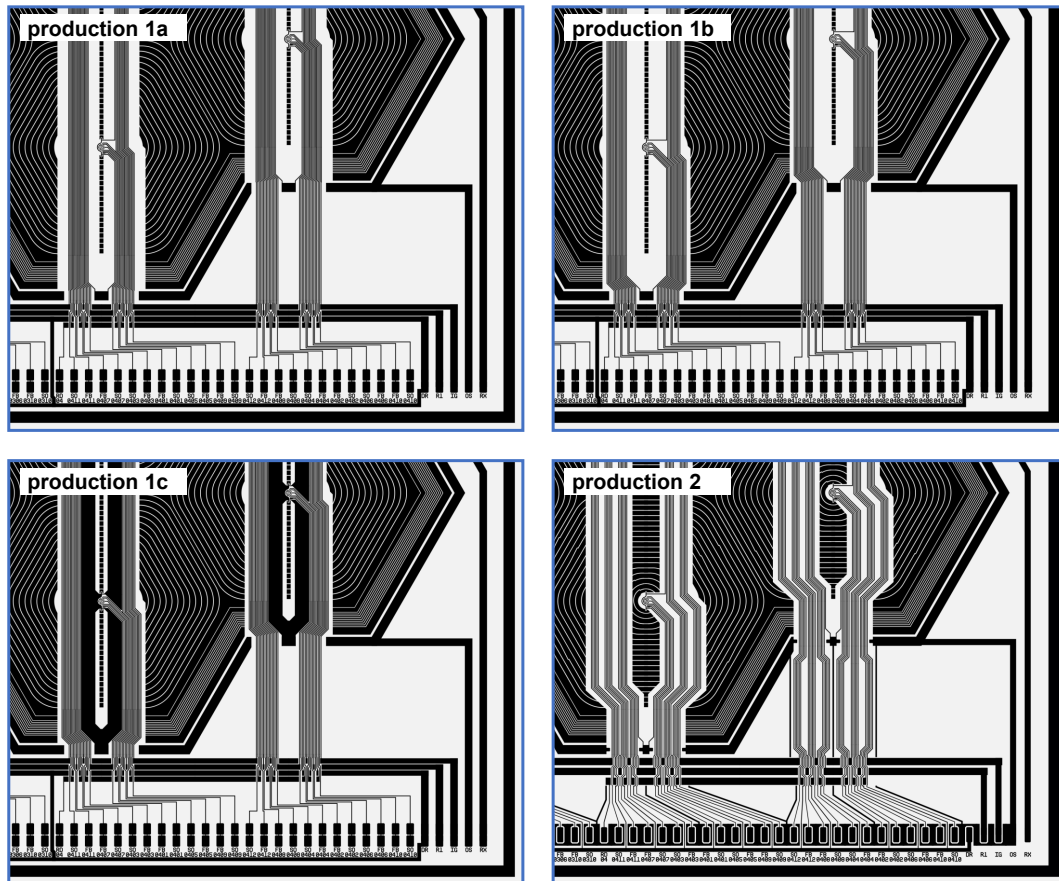
Figure 6.27: Comparison of the aluminum readout structure of SDDs of production 1a, 1b, 1c, and 2. On the bottom of each cutout one can recognize the pond pads, which are connected to the anodes, including the JFET, by vertical aluminum lines. Two anodes are visible in each cutout, which has a size of $6.8\,\mathrm{mm} \times 5.6\,\mathrm{mm}$ and corresponds to a 47-pixel device. The 7-pixel, 12-pixel, and 166-pixel chips have an equivalent readout structure. Production 1 (not shown) has a similar design to production 1a.

- **Lines on thick insulator** In designs 1b and 1c, the thickness of the insulating SiO_2 between the silicon substrate and the aluminum lines was increased from $630\,\mathrm{nm}$ to $1030\,\mathrm{nm}$. This reduces the readout lines' overall capacitance and thereby reduces cross-capacitance between all lines if these are caused by structures below the lines (for example, the drift rings).
- **Narrow FB and SC lines** In designs 1b and 1c, to further reduce the capacitance of the critical FB and SC lines, the width of these lines was reduced from $8\,\mu\mathrm{m}$ to the technological minimum of $6\,\mu\mathrm{m}$.
- **Broad GND line** Design 1c has an extra broad GND plane covering the ring structure (see figure 6.27). This increases the capacitance of the drift rings to GND and thereby reduces the cross-capacitance between all lines if the drift rings are involved.

6.3.4 Comparison of crosstalk with design modifications

The same crosstalk investigations as shown in section 6.3.1 are now presented for 7-pixel devices of production 1, 1a, 1b, and 1c. Based on the results, the design of production 2 was defined. The crosstalk in 7-pixel devices of production 2 is discussed at the end of this section. Figure 6.28
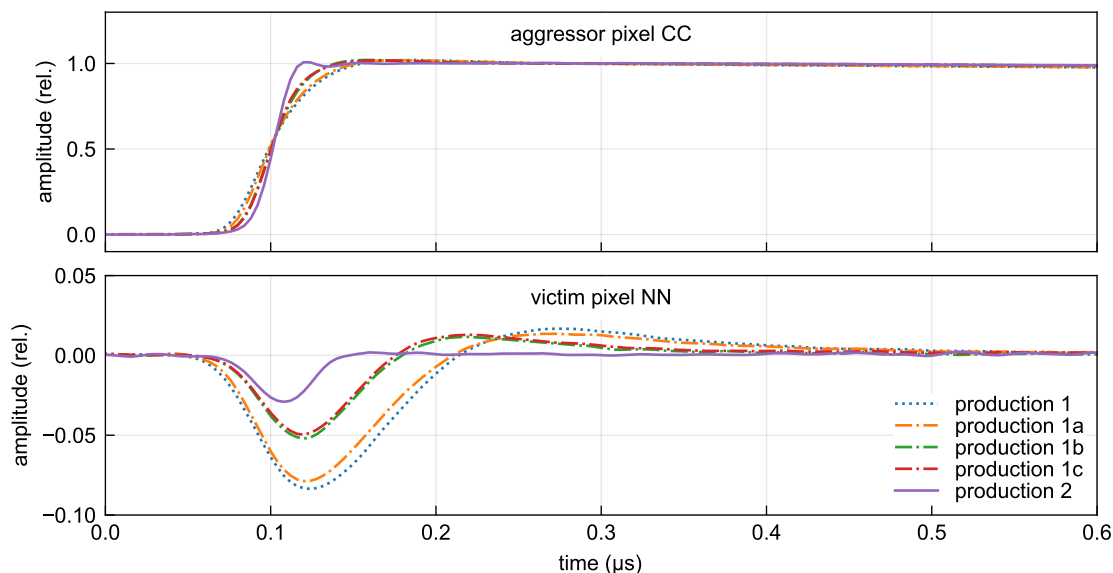
Figure 6.28: Comparison of crosstalk signals for detector production 1, 1a, 1b, 1c, and 2. The two plots show the central (CC) and north (NN) pixel signals of a 7-pixel device. $\mathcal{O}(1000)$ signals were averaged to reduce the electronic noise. The aggressor (pixel CC) and victim (pixel NN) signals become faster, and crosstalk amplitude decreases with the evolving design.

compares the average output signals for one aggressor-victim combination. The evolution of the crosstalk amplitude for all possible pixel combinations is summarized in figures 6.29 and 6.30, showing two different depictions of the crosstalk amplitudes.

Production 1a shows almost no crosstalk reduction compared to production 1, while productions 1b and 1c show a significant crosstalk reduction. Furthermore, the latter two designs also show a faster signal rise time. These observations both fit to a reduced line capacitance in production 1b and 1c, which was intended by the design modifications. Most of the reductionoriginates probably from the increased insulator thickness. The increased insulator thickness should reduce the line capacitance on the SDD chip by around 40 %. The average level of crosstalk (figure 6.29) between production 1b and 1c is reduced slightly from around 4.6 % to 4.1 %. This shows that the coupling through the drift rings is probably not the dominant mechanism of crosstalk. However, it may be one contribution to the overall crosstalk.

In conclusion, the design modifications in production 1a, 1b, and 1c showed that the crosstalk amplitude is related to the readout structure on the SDD. Furthermore, reducing the capacitance of the SC and FB lines to the silicon substrate, and thus also FB-SC cross capacitances, significantly reduced the crosstalk amplitude. This was achieved by increasing the SiO_2 thickness and reducing the line width. A positive side effect of the reduced SC line capacitance is a faster signal rise due to the higher bandwidth limit of the CSA. The crosstalk is probably not dominated by a cross capacitance through the drift ring structure. Therefore, the cross capacitance must originate either from the bond pad region or the region between the bond pads and the active area of the SDD.

Modifications and Crosstalk in Production 2   After the crosstalk analysis of 7-pixel devices of production 1a, 1b, and 1c, the semiconductor laboratory prepared a new design for the upcoming
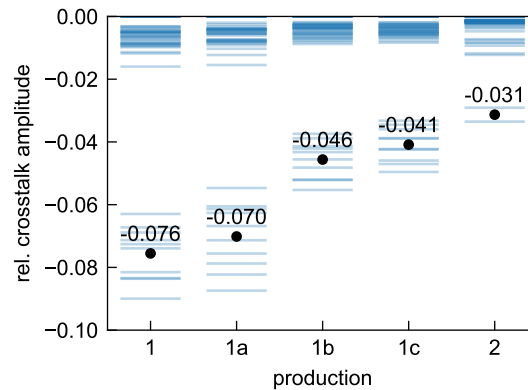
Figure 6.29: Evolution of all crosstalk amplitude matrix entries for 7-pixel devices from production 1, 1a, 1b, 1c, and 2. Each line corresponds to one of 42 aggressor-victim pairs per detector. The bullet point with a number is the average value of the outlier cluster with an amplitude < -0.02. Production 1, 1a, 1b, and 1c have ten outliers each, while production 2 has only two.
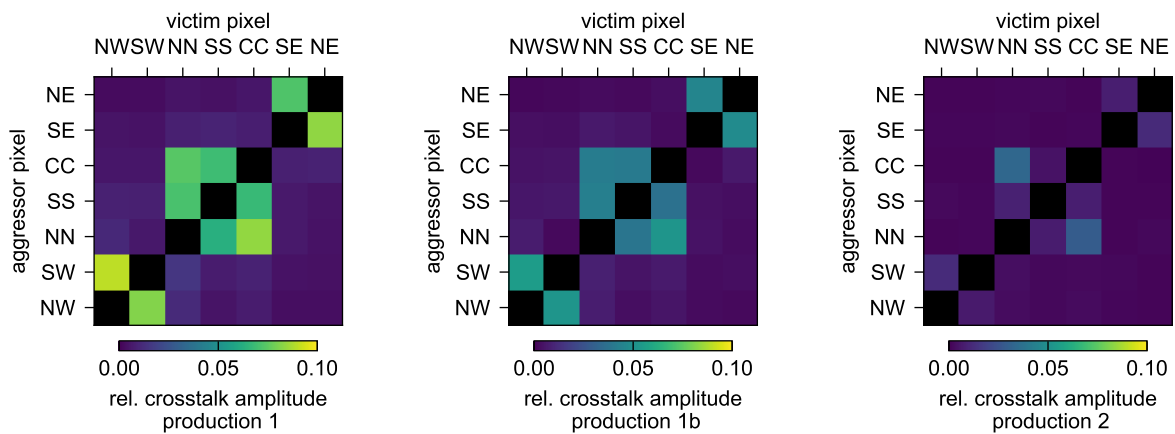
Figure 6.30: Evolution of the crosstalk amplitude matrix for 7-pixel devices of production 1, 1b, and 2. The crosstalk amplitudes describe the negative amplitude of the crosstalk dip relative to the aggressor signal (compare figure 6.28). The color scale is the same for the three matrices. With each production, the amount of crosstalk was reduced.

production 2. The design of production 2 is based on the design of production 1b but has several further improvements. Changes intended to reduce crosstalk are the following:

- A distance between readout lines of different pixels was added within the readout columns.
- The design of the bond pad region was improved to reduce cross-capacitances. For example, there is now only a single bond pad per line.
- Deep n-implantations were added below and between bond pads and readout lines, outside of the active pixel area, to have a better-defined potential below the lines.
- The SiO_2 thickness was increased to 1630 nm compared to 1030 nm in production 1b and 630 nm in production 1.

The readout design of production 2 is shown, besides production 1a, 1b, and 1c, in figure 6.27. The measured crosstalk amplitude of a 7-pixel detector of production 2 is included, besides the previous measurements, in figures 6.28, 6.29, and 6.30. The same positive trend, which is observed when comparing production 1 to production 1b, continues with production 2: The crosstalk amplitude is reduced, and the rise time of the aggressor signal becomes faster.

While the crosstalk amplitude decreases overall, the reduction depends on the channels involved. The channel dependence is visible when comparing the crosstalk amplitude matrices in figure 6.30. Production 1b has a very similar matrix structure as production 1, with ten outliers corresponding to the readout columns. In production 2, however, there are only two matrix elements with large crosstalk amplitude. These correspond to crosstalk between pixel NN and pixel CC, with the most extended parallel readout routing of all pixel combinations of a 7-pixel device.

In summary, the magnitude of differential crosstalk in 7-pixel devices was successfully reduced by a factor of at least 2.5 from production 1 to production 2. For most pixel combinations, the crosstalk amplitude was reduced by more than a factor of 5. The design modifications, causing the reduction, focused on reducing cross-capacitances between readout lines on the SDD.

6.3.5 Crosstalk in 166-pixel detectors of production 2

The previous sections focused on 7-pixel devices, which have a simple and uncritical line routing between the SDD chip and the ETTORE ASIC. Therefore, crosstalk effects could be attributed mainly to the SDD chip. The 166-pixel detector module, however, has a complex high-trace-density interface between ETTORE and the SDD. The interface comprises a rigid-flex PCB, a 200-pin array connector, and the front-end electronic board. These components play an essential role for crosstalk within the 166-pixel module.

The following presents a crosstalk measurement with a 166-pixel detector module. Measuring crosstalk within a 166-pixel detector module is more challenging than 7-pixel devices. This is primarily due to the n^2-scaling of possible aggressor-victim combinations in an n-pixel detector. Nevertheless, a measurement of the full 166-pixel crosstalk matrix is possible and shown in figure A.14 in the appendix. The crosstalk analysis in this section focuses on crosstalk within the first 35 channels of the detector. The reduced number of involved pixels facilitates the analysis and improves the readability of plots, while the results are representative for the full detector. The 35 channels belong to three readout groups, each connected to one 12-channel ETTORE ASIC. A pixel map is shown in figure 6.31. Detector S0-166-11 is used, and the bias settings are found in the appendix in table A.8. The measurement principle is the same as in the previous measurements with 7-pixel devices. Figure 6.32 shows the average aggressor and victim signals for two selected aggressor pixels 0103 and 0311. Some victim signals for aggressor pixel 0103 show a negative dip,
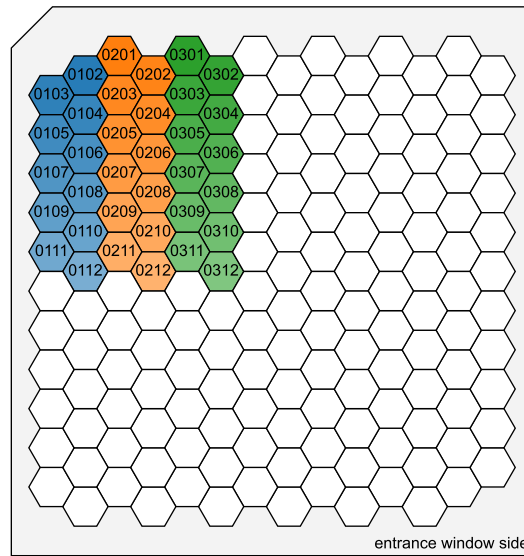
Figure 6.31: Pixel map of connected pixels for the crosstalk measurements with a 166-pixel detector module. The three colors correspond to three readout groups.
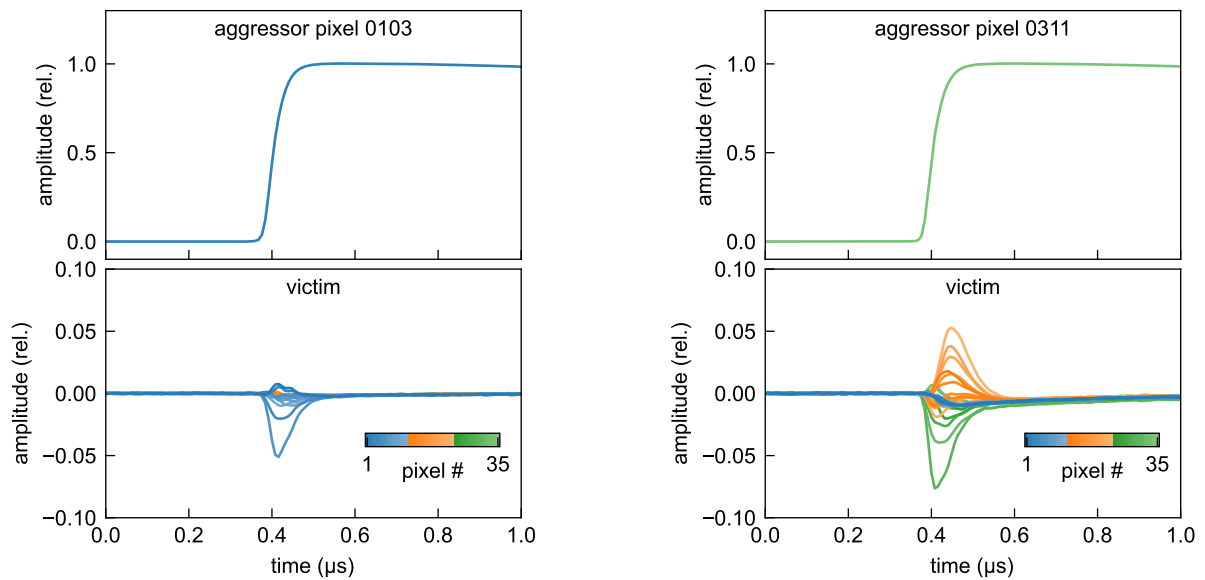
Figure 6.32: Waveform acquisition with a 166-pixel detector to measure crosstalk. The averaged aggressor and victim waveforms for the two aggressor pixels 0103 and 0311 are shown. See figure 6.31 for a pixel map.
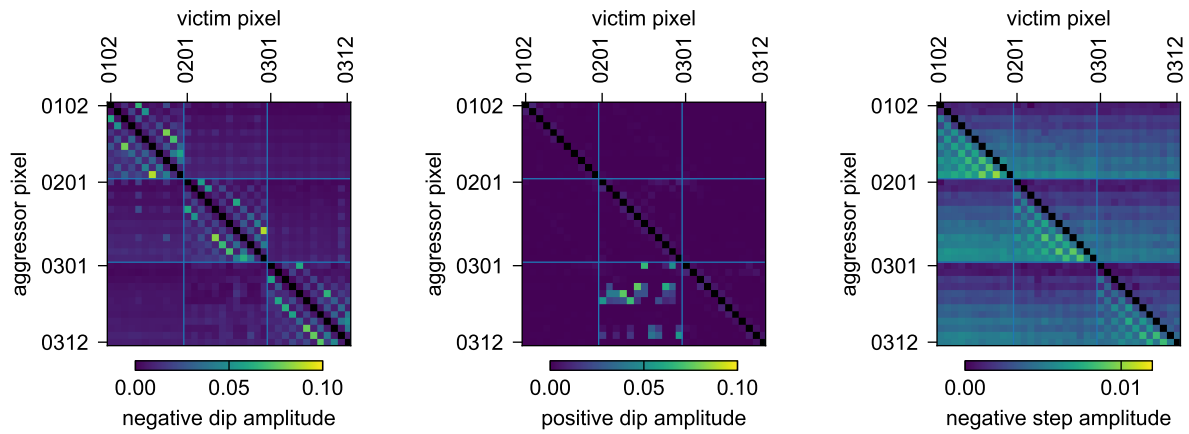
Figure 6.33: Crosstalk amplitude matrices of the 35-channel crosstalk acquisition with a 166-pixel detector module. The three matrices correspond to the three quantities: negative dip, positive dip, and negative step, as described in the text. The three matrices show very different but characteristic patterns.

similar to the 7-pixel case (compare figure 6.20). Additionally, some victim signals show a strong positive dip for aggressor pixel 0311. Such a positive crosstalk dip was not observed in 7-pixel measurements. Furthermore, the measurement indicates a small negative crosstalk component with a relatively long time constant around $\mathcal{O}(1\,\mu s)$. In order to quantify the different shapes and their crosstalk amplitudes, three measures are defined for the following analysis.

- **Negative dip amplitude** The negative dip amplitude measures the minimum of the victim signal distortion.
- **Positive dip amplitude** The positive dip amplitude measures the maximum of the victim signal distortion.
- **Negative step amplitude** The negative step amplitude measures the victim signal level after the main crosstalk dip. To this end, the victim signal is averaged in a time window from 200 ns to 400 ns after the rising edge of the aggressor channel.

These three quantities are determined for each aggressor-victim channel combination in the 35-channel crosstalk acquisition. Consequently, three 35×35 crosstalk matrices are drawn in figure 6.33. Each crosstalk matrix shows a very characteristic but different structure. The three crosstalk structures and their possible origins are studied in the following sections.

6.3.5.1 Negative dip crosstalk

The negative dip crosstalk shows the following characteristic pattern:

- It is present primarily within 12-channel readout groups (blue squares in figure 6.33).
- The pattern is different for each readout group, but the same for both hemispheres (not visible in figure 6.33, but in figure A.14 in the appendix.).
- The pattern is not symmetric.
- The pattern is dominated by some pixel combinations on the second to fourth off-diagonal. The structure matches the order of the bond pads on the SDD, such that all pixel combinations, which show substantial crosstalk, have neighboring bond pads. However, not all pixel combinations with neighboring bond pads show substantial crosstalk.

As shown in section 6.3.2, a negative dip crosstalk most likely relates to a capacitive coupling between FB and SC lines of the involved pixels. To yield a 5 % negative dip crosstalk amplitude,
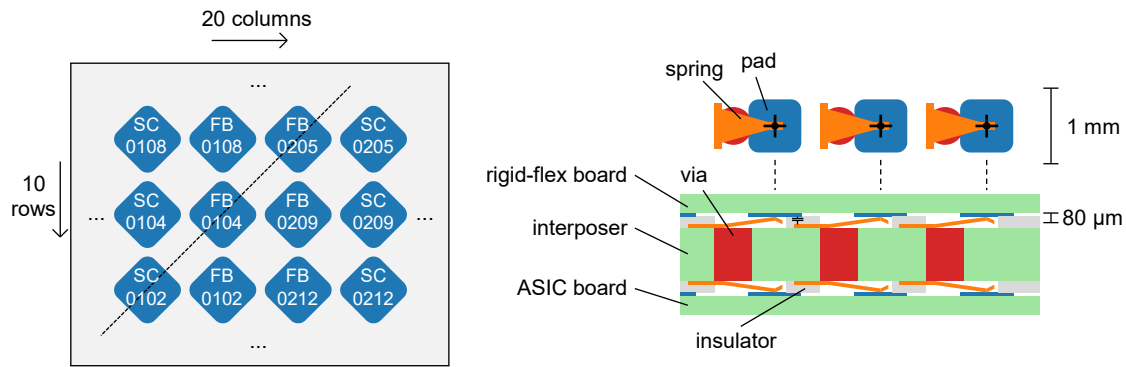
Figure 6.34: Sketch of the Z-ray connector (ZA1-20-2-1.00-Z-10 from Samtec). The connection is a sandwich of three layers (rigid-flex board, interposer, ASIC board), as shown in the cross-section on the right. The cross-section corresponds to a diagonal cut (dashed line) through the pad matrix shown on the left. Due to the diagonal spring geometry on the interposer board, the diagonal neighboring pads have an increased coupling capacitance. For example, there is probably a capacitance $\mathcal{O}(100\,\mathrm{fF})$ between pad FB0104 and pad SC0102, leading to the negative dip crosstalk between pixel 0104 (aggressor) and pixel 0102 (victim). The drawn dimensions are estimated.

which is typical for the pixel combinations with strong crosstalk in figure 6.33, the capacitive coupling between FB an SC lines needs to be $\mathcal{O}(100\,\mathrm{fF})$.

A detailed investigation of all involved routing geometries reveals that the pattern is related to the Z-ray connector between SDD and ASIC board. Figure 6.34 sketches the geometry of the Z-ray connector. The prevention of crosstalk was considered when the pin assignment of the connector was defined: The pin assignment was optimized to maximize the distance between SC and FB pads belonging to different pixels [89]. For instance, there are no directly neighboring SC and FB pads of different pixels. It was found, however, that the pattern of negative dip crosstalk coincides with diagonal neighbors in the pin assignment of the Z-ray connector. The diagonal coupling originates from the geometry of the springs on the connector's interposer: The location of the electric vias on the interposer is shifted diagonally to the pads, such that the diagonal neighbored pads, in one orientation, show an increase capacitance.

More details on the geometry of the Z-ray connector would be necessary to understand the exact cause of the diagonal capacitances further. With this information, one could potentially reduce the crosstalk by adapting the pin assignment on the Z-ray connector. While it is unclear how much the situation could be improved, a new pin assignment would also require redesigning the two involved electronics boards. Therefore, mitigation is currently not possible, and the negative dip crosstalk is expected to be present in the phase 1 measurement of TRISTAN.

6.3.5.2 Positive dip crosstalk

Opposite to the negative dip crosstalk, some pixels show a relatively large positive dip crosstalk, as seen in some signals of figure 6.32. The positive dip crosstalk matrix, shown in figure 6.33, shows a characteristic pattern:

- The positive dip crosstalk is present only in two specific aggressor-victim readout group combinations: Aggressor group 03 affects victim group 02, and aggressor group 05 affects group 06 (the latter is visible only in figure A.14 in the appendix.).
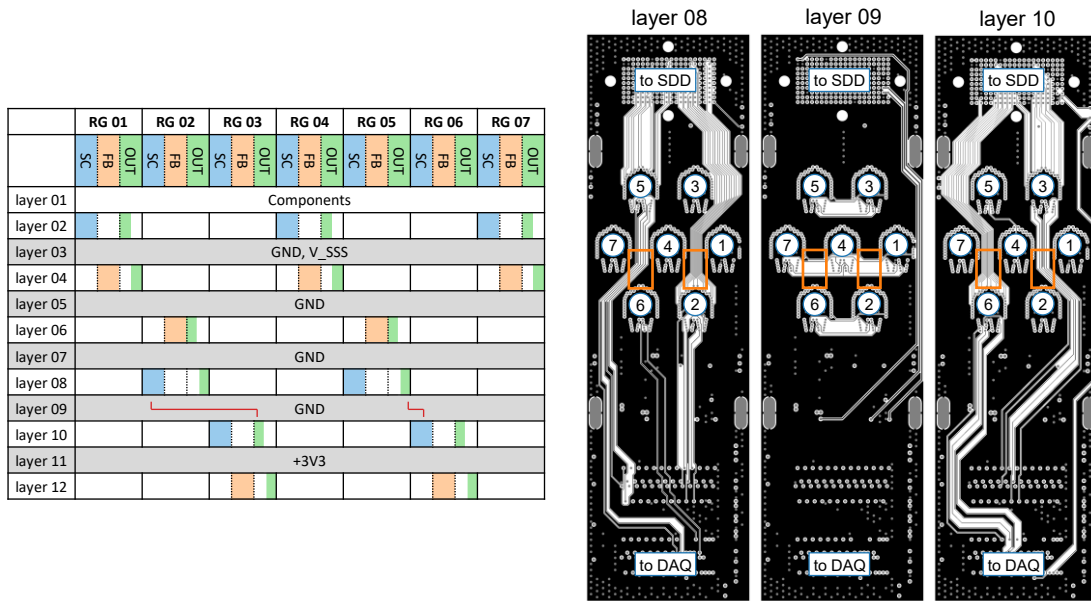
Figure 6.35: Distribution of readout lines on the 12 copper layers of the ASIC board PCB. The SC, FB and OUT lines of seven reset groups (RG 01 to RG 07, connecting to one ETTOR ASIC each) are routed on 6 layers, with ground layers in between. The layout of copper layers 08, 09, and 10 is also drawn. A critical capacitive coupling between OUT and SC lines is present between layers 08 and 10, as indicated by the two red lines (left) and orange squares (right).

- Only six out of twelve channels in the aggressor group cause positive dip crosstalk.
- The pattern is not symmetric.
- The pattern is the same on both hemispheres.

The positive dip crosstalk could be explained by capacitive coupling from the ETTORE output (OUT) to SC lines of different pixels, as demonstrated in section 6.3.2. To obtain a 5 % positive dip crosstalk amplitude, similar to the observation on some pixels, the capacitive coupling between OUT and SC lines of $\mathcal{O}(10\,\mathrm{fF})$ would be sufficient.

A detailed investigation of the involved geometries revealed that the pattern is related to the PCB design of the ASIC board. The FB, SC and OUT signal lines of 83 channels are distributed on 12 layers of the PCB, as illustrated in figure 6.35. The figure also shows the three copper layers, which are critical for positive dip crosstalk. As indicated by the orange squares in figure 6.35, there is a geometric overlap between the SC lines of ETTORE 06 (layer 10) and ETTORE 02 (layer 08) and the OUT lines of ETTORE 05 (layer 08) and ETTORE 03 (layer 10), respectively. In order to mitigate couplings between layers 08 and 10, there is a solid GND plane in layer 09. However, a small cutout in the GND plane, necessary for bias voltage routing, sits at the critical location. This small (length of around 3 mm) cutout in layer 09 is sufficient to cause a $\mathcal{O}(10\,\mathrm{fF})$ capacitance between OUT and SC lines and thereby leads to the observed positive dip crosstalk. The positive dip crosstalk can be mitigated in the future by closing the cutout in layer 09. A new design of the ASIC boards is already produced but remains to be tested for crosstalk. Due to the improved PCB design, no significant positive dip crosstalk is expected in the phase 1 measurement of TRISTAN.

6.3.5.3 Negative step crosstalk

The crosstalk matrix of the negative step amplitude (right matrix in figure 6.33) looks again different from the two previously described crosstalk components.

- The negative step crosstalk is not constrained within one reset group but has a hemisphere-wide component. One aggressor event can distort up to 82 victim pixels within the same hemisphere. The hemisphere-wide component is stronger for longer lines of the aggressor pixel on the SDD.
- In addition to the hemisphere-wide component, there is a component that fills the lower triangle matrix within each readout group with a chessboard pattern. This means those pixel combinations are affected, where the victim pixel lies downstream in the same readout column. The strength of the effect scales with the length of parallel lines of the aggressor pixel and victim pixel.
- The crosstalk amplitude is smaller than 1.2 % on all pixels, and thereby is weaker compared to the previous two crosstalk components.
- The step-like component decays with a time constant of around 1 μs.

Additional investigations would be necessary to better characterize this crosstalk component, especially the correlation to the readout geometry. Thus, the origin of the negative step crosstalk is still unclear. It is likely that the supply lines (R1, DR, or IG) are involved, as the effect is not constrained within one readout group.

6.4 Simulation of the impact of crosstalk on spectroscopy

The central aspect of crosstalk in the TRISTAN detector is its effect on spectroscopy. This section studies the possible effects of the negative dip crosstalk and the negative step crosstalk. Positive dip crosstalk is neglected, as it is expected to vanish with the new ASIC board production. The study utilizes the trace-level simulation of the TRISTAN signal processing `DAQsim`, described in detail in the DAQ chapter of this work in section 7.3.

The signals of many detector channels are simulated in parallel, comprising one victim channel and several aggressor channels. The victim channel has a monoenergetic input spectrum with 30 keV. The monoenergetic spectrum is convenient for directly seeing the influence of crosstalk on the detector response. The aggressor channels have a flat input spectrum from zero to 30 keV. The flat input spectrum is a rough estimate for the acquired tritium spectrum. An empirical cross-response function is applied to the signals to account for crosstalk. The response is such that a pulse on the aggressor channel adds a dip-like or step-like distortion, imitating the measured crosstalk (compare figure 6.32). After adding crosstalk, the simulation adds electronic noise[12]. Subsequently, the complete DAQ processing, as described in section A.4, is applied. The output spectrum is finally compared to a simulation without crosstalk.

---

[12]This is physically not the correct order, as noise on one channel can couple through crosstalk to other channels. This effect increases the overall noise. However, the increase of noise due to crosstalk is also present in the series noise characterization (section 6.2.3) and, therefore, would be added twice if the noise was added before crosstalk.
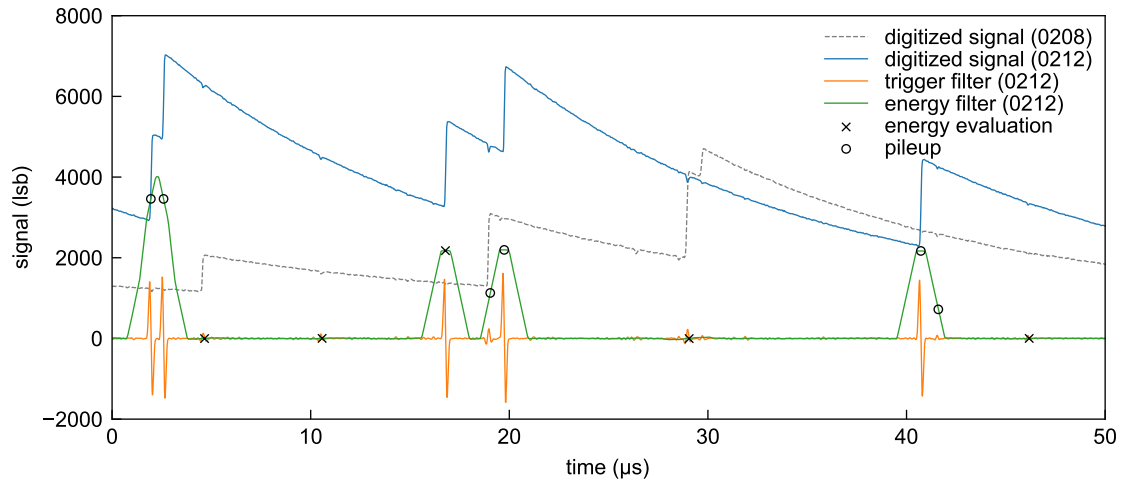
Figure 6.36: Example signal snippet of the trace-level simulation with negative dip crosstalk. The two channels (aggressor 0208 and victim 0212) with the strongest negative dip crosstalk amplitude of 8.9 % (compare figure 6.33) are plotted. The signal on channel 0212 shows, besides actual events at a rate of 100 kcps, the dip-shaped distortions from crosstalk originating from events on the other channels of the same reset group. One other channel (0208) is also shown, which is the aggressor channel for some (but not all) of the visible crosstalk dips. 0208 The dips lead to distortions on the trigger filter and energy filter signal, thereby influencing the spectroscopic performance.

6.4.1 Simulation of negative dip crosstalk

In order to study negative dip crosstalk, the traces of one readout group with 12 pixels are simulated. The measured negative dip amplitude matrix from readout group 02 (figure 6.33) defines the magnitude of crosstalk in the simulation. Pixel 0212 is used to study the detector response. Therefore, it has a monoenergetic input spectrum. The other eleven pixels 0201 to 0211 are considered aggressors and have a flat input spectrum up to 30 keV. An example snippet of the digitized signals of two channels is shown in figure 6.36. The snippet shows the two main implications of the crosstalk dips on the signal of pixel 0212:

1. The dips frequently cause false triggers, as the trigger filter is susceptible to fast dip signals. This happens, for example, at $t = 5\,\mu s$, $11\,\mu s$, $29\,\mu s$ and $46\,\mu s$ in figure 6.36. The crosstalk triggers have little effect on the shape of the acquired spectrum, as the corresponding energy readout is close to zero and does not overlap with the physical spectrum. However, if a crosstalk trigger happens close to a physical trigger (for example, at $t = 19\,\mu s$ and $42\,\mu s$ in figure 6.36) the physical event will be falsely rejected as pileup. The dead time from pileup rejection is thereby increased significantly.
2. The dips can also disturb the reconstructed energy of a physical event if the dip amplitude is too small to cause a trigger. This effect is expected to worsen the energy resolution.

The output spectrum of channel 0212 is analyzed to quantify the two effects. Figure 6.37 shows the corresponding output histograms for different input count rates and crosstalk settings. For each histogram, the RMS width and the efficiency are shown in figure 6.38. The evaluation of the energy resolution in RMS is preferred here because crosstalk can cause a non-Gaussian shape, such that the FWHM is not a representative measure. The Fano resolution is not included in the simulation to make changes in the detector response more visible. The study compares three scenarios:
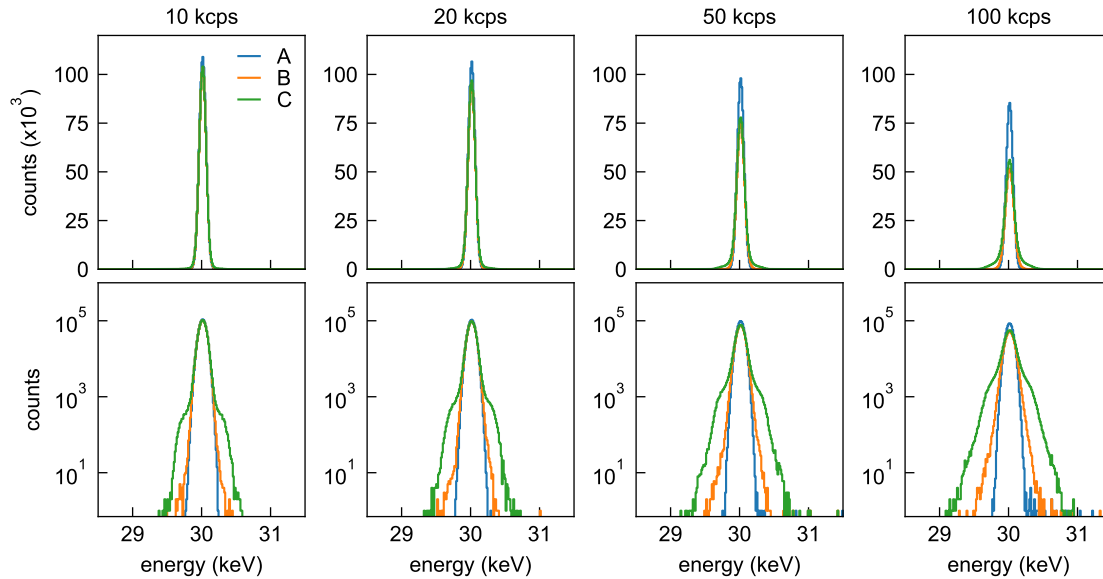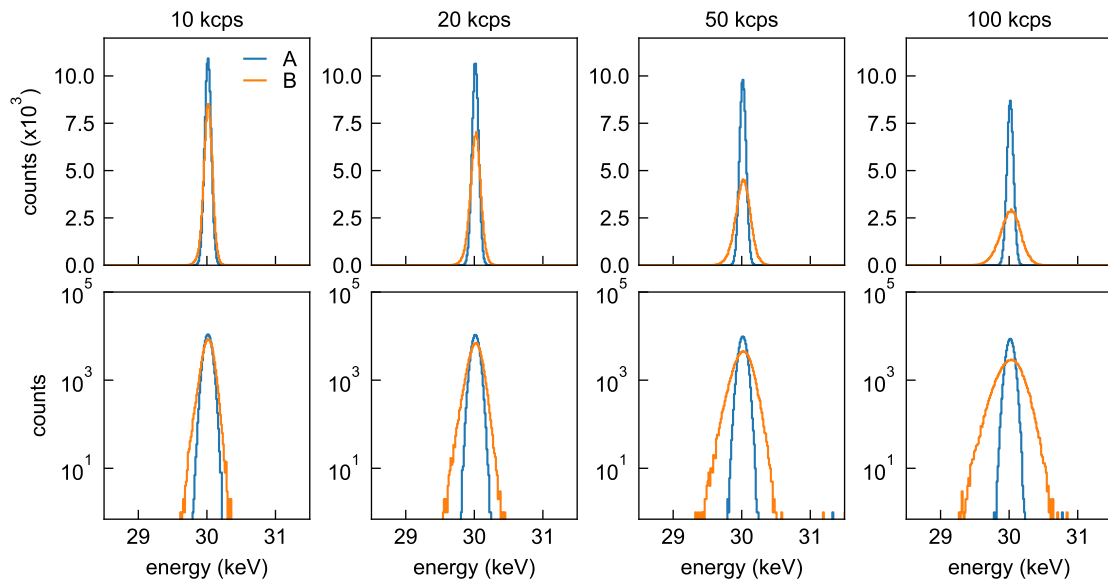
Figure 6.37: Simulated output spectrum of channel 0212 with negative dip crosstalk for different rates in linear (top) and logarithmic (bottom) scale. Three different crosstalk scenarios are compared. **A:** Crosstalk is switched off in the simulation. **B:** Negative dip crosstalk is switched on in the simulation. **C:** Negative dip crosstalk is switched on in the simulation, and the threshold is increased to not trigger on crosstalk.

- **A: No crosstalk** In the first studied scenario, no crosstalk is present in the simulation. The energy resolution is around 49 eV RMS or 115 eV FWHM, originating from the electronic noise included in the simulated signals.
  The energy resolution does not depend on the rate, while the efficiency drops linearly with the rate as the dead time from pileup rejection increases (see table 7.2). At 100 kcps the efficiency is around 76 %.
- **B: Crosstalk** When negative dip crosstalk is switched on, the energy resolution at 100 kcps increases slightly to around 60 eV RMS. Furthermore, the efficiency decreases significantly from 76 % to 56 %. Both effects are disadvantageous for the TRISTAN measurement.
- **C: Crosstalk + increased threshold** To prevent the loss of efficiency due to pileup rejection in combination with the crosstalk triggers, a straightforward counteract is the increase of the trigger threshold. In the last simulated scenario, therefore, the trigger threshold is increased from 80 lsb to 320 lsb, corresponding to a physical threshold of around 1.6 keV and 6.5 keV, respectively. The efficiency is restored to 76 %. However, almost all recovered events have a crosstalk dip influencing their energy filter readout. Therefore, the energy resolution decreases drastically from 60 eV to 110 eV for increasing rates. Figure 6.37 shows that, due to the effect of crosstalk, the detector's response to monoenergetic events is not Gaussian but has pronounced tails.

In conclusion, the simulation of the negative dip crosstalk shows that there is a trade-off between two disadvantageous effects: The loss of efficiency by up to 20 % and a non-Gaussian broadening of the detector response. Which of the two effects dominates depends on whether pileup with crosstalk is rejected or not. This trade-off is explored in the simulation by varying the trigger threshold. More advanced techniques, like a dedicated crosstalk detecting filter, could provide the option to accept pileup with crosstalk while keeping the energy threshold low. However, the
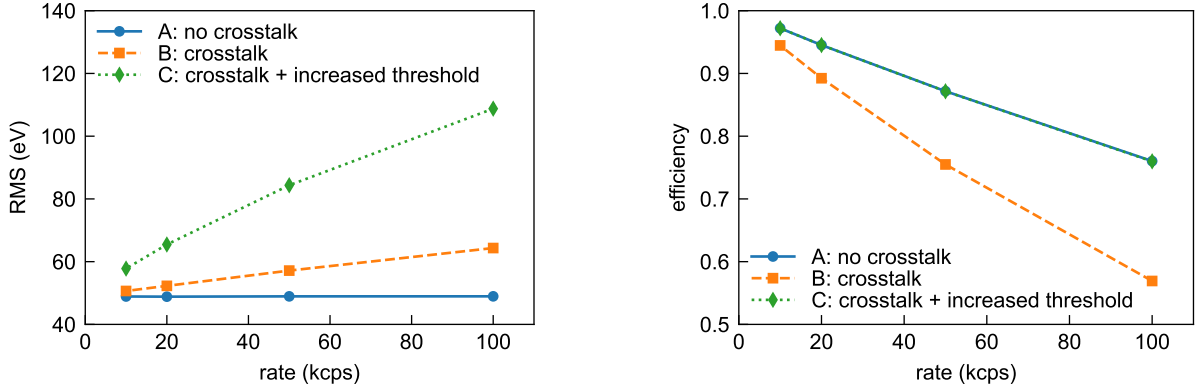
Figure 6.38: Effect of negative dip crosstalk on the energy resolution (left) and the efficiency (right). The negative dip crosstalk causes the efficiency to drop significantly. The efficiency loss can be entirely recovered by increasing the threshold at the cost of a worse (and non-Gaussian, see figure 6.37) energy resolution. Both effects scale approximately linearly with the input count rate per pixel.

fundamental trade-off between efficiency and energy resolution stays independent of whether the threshold or a dedicated filter is used.

The only way this trade-off can, in principle, be overcome is the complete reconstruction of crosstalk. As crosstalk is a linear and time-independent response, its effect can, from a mathematical point of view, be fully recovered. Such a crosstalk recovery, however, requires the correction of a digitized waveform based on the waveform of the other channels. A consequence is that the signals cannot be processed independently from each other, and the complexity of online signal processing increases drastically.

6.4.2 Simulation of negative step crosstalk

Negative step crosstalk is now studied similarly to the negative dip crosstalk. The negative step crosstalk describes the relatively slow crosstalk component, visible in the right plot of figure 6.32. The corresponding crosstalk amplitude is smaller compared to the negative dip crosstalk. However, the amplitude matrix has a pattern that spreads over the entire hemisphere (83 pixels) of the detector (see figure 6.33 and figure A.14). Consequently, the simulation now contains 83 channels. The crosstalk response is implemented in the simulation such that a step-like aggressor signal causes a decaying victim signal with a time constant of $\tau = 1\,\mu s$. The negative step crosstalk amplitude matrix is taken from the measurement in figure A.14.

The effect of negative step crosstalk on the simulated signals is shown in figure 6.39. If negative step crosstalk is switched on, the sum of all crosstalk signals has an effect similar to an increased $1/f$ noise (actually, the superposition of many exponentially decaying signals results in a $1/(1 + (2\pi f \tau)^2)$ power spectrum [109]). Figure 6.40 shows the output spectrum of the victim channel 0208 with a monoenergetic input spectrum. The shape of the response is almost, but not perfectly, Gaussian. The corresponding energy resolution and efficiency as a function of rate is shown in figure 6.41. The energy resolution increases to up to 150 eV RMS, corresponding to around 350 eV FWHM or an additional ENC value of around 40 e. The simulation did not include the Fano resolution, and the energy resolution would increase up to around 440 eV FWHM at 30 keV if it was taken into account. Other than negative dip crosstalk, negative step crosstalk does not affect the detection efficiency as the victim signals do not cause fake triggers. In summary, the
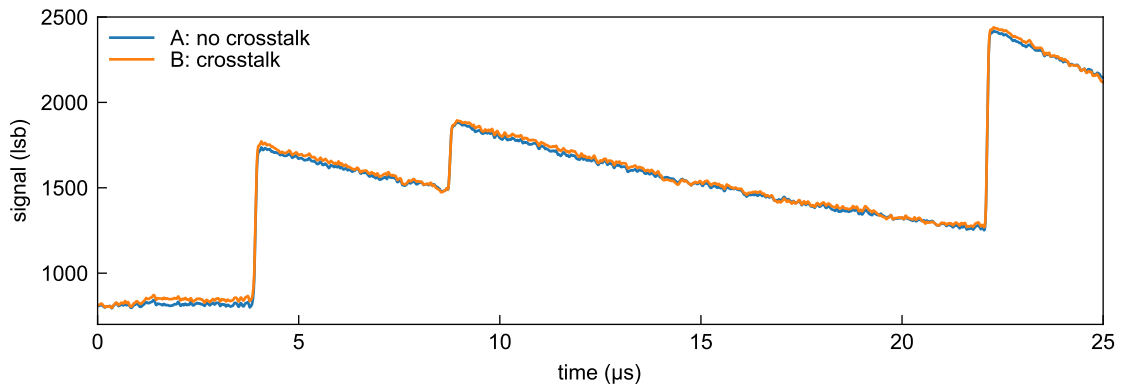
Figure 6.39: Example signal snippet of the trace-level simulation with negative step crosstalk. The shown signal corresponds to channel 0208, which is one out of 83 simulated signals. The input rate is 100 kcps on all channels, and the input spectrum on the aggressor pixels is flat between zero and 30 keV.

Figure 6.40: Simulated output spectrum of channel 0208 with negative dip crosstalk for different rates in linear (top) and logarithmic (bottom) scale. Two cases with negative step crosstalk switched off (**A**) and on (**B**) are compared. The negative step crosstalk causes an almost Gaussian broadening of the detector response.
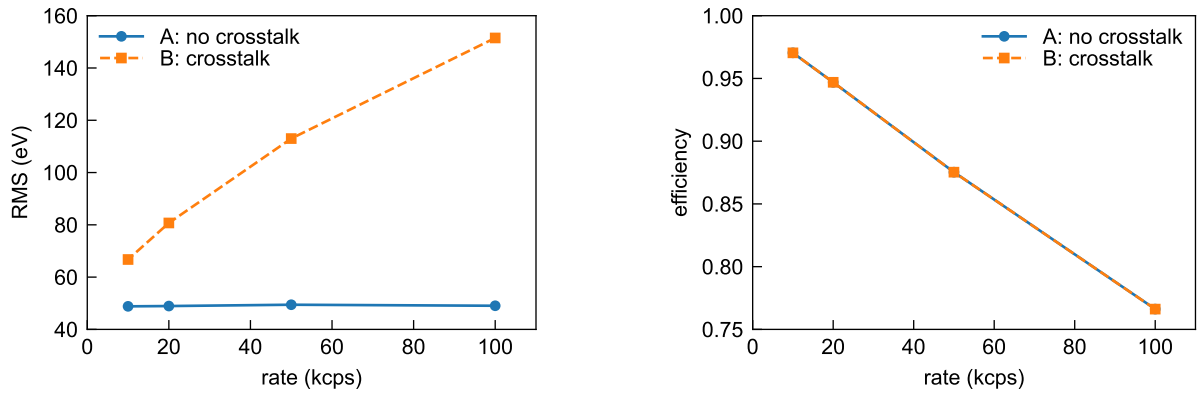
Figure 6.41: Effect of negative step crosstalk on the energy resolution (left) and the efficiency (right). The negative step crosstalk causes a significant worsening of the energy resolution and does not affect the efficiency.

negative step crosstalk causes an effect similar to an additional noise on the signals, which depends on the rate on the entire detector.

6.4.3 Conclusion

The crosstalk simulations in the two previous sections studied the influence of crosstalk on the detector response. The magnitude of the crosstalk effect was extracted from measurements with the latest 166-pixel detector modules. The simulations have two significant simplifications: The input spectrum on the aggressor channels is assumed to be flat between zero and 30 keV. Furthermore, only one representative victim pixel is studied: pixel 0212 for negative dip crosstalk and 0208 for negative step crosstalk.

For negative dip crosstalk, the simulation shows two effects: A non-Gaussian broadening of the detector response and a reduction of detection efficiency. For negative step crosstalk, an almost Gaussian broadening is observed. When interpreting the results, it is important to take into account several constraints which influence the amount of observed crosstalk:

- **Rate-dependence**: The crosstalk effects scale more or less linear with the input count rate per pixel.
- **Pixel-dependence**: The crosstalk effects look different for each pixel due to the individual crosstalk matrix entries. The two chosen pixels 0208 and 0212 are the pixels most affected by crosstalk. Consequently, the result is a conservative estimate.
- **Spectrum dependence** The crosstalk effects depend on the input spectrum on the aggressor pixels. In general, a higher input event energy will cause stronger crosstalk effects. Thus, the tritium spectrum, which differs from the flat spectrum assumed in the simulation, will cause a different crosstalk response than the simulated one.

Due to these dependencies, the resulting magnitudes of the effect are only rough values that depend on the assumed input conditions. Still, a significant broadening, which may be larger than the broadening from electronic noise, and a significant efficiency reduction of around 20 % are observed. Both effects are important to include in the future modeling of the TRISTAN spectrum.

A particular difficulty in the experimental characterization of the detector response due to crosstalk comes from the dependencies on rate and input spectrum, as mentioned above. The high-rate elec-

tron gun described in section 5.2, for example, can only provide a monoenergetic input spectrum on the aggressor pixels. Furthermore, the electron gun cannot illuminate all detector pixels without sequentially scanning the surface. Therefore, a measurement with the high-rate electron gun would not give a reliable result. This is also why the crosstalk implications were simulated and not measured in this work. One possibility for obtaining a reliable crosstalk calibration would be an in-situ approach based on measuring the zero peak during tritium data taking. The shape of the zero peak, which was also used for the noise curve measurement in section 6.2.3, could serve as a direct and reliable measurement of the combined electronic noise and crosstalk response. Therefore, an integrated zero peak acquisition would be beneficial in the TRISTAN DAQ.

6.5 Charge sharing

If the interaction location of an incident particle is close to the border of two adjacent detector pixels, the drifting charge cloud can be shared between several involved anodes. This effect leads to incomplete charge collection and is called charge sharing. Charge sharing affects almost all monolithic pixel detectors and is especially important for small pixel sizes [144, 145].

In SDDs for X-ray spectroscopy, charge sharing often limits the signal-to-background ratio [146]. One method to counteract charge sharing is using a mechanical collimator, which prohibits the illumination of the pixel edge. Another approach is identifying charge sharing events based on their time coincidence [147, 141] or their increased rise time [148, 149]. The identified events can be rejected or even reconstructed to recover the initial event.

Although these mitigation strategies usually improve the spectroscopic performance, they come with substantial drawbacks and challenges in the context of TRISTAN:

- The **mechanical collimator** is unsuitable for TRISTAN due to the unavoidable spectral contribution from electrons scattered at the collimator edge.
- The **time-coincidence method** to identify charge sharing events only works for events where both pulses are above the noise level. This introduces an energy and threshold dependence of the detector response, which is very difficult to model. Furthermore, the time-coincidence method only works for pixels that have six active neighboring pixels. Edge pixels and neighbors of faulty pixels cannot be used for this method.
- The **rise time method** identifies charge sharing events based on their increased rise time with typical threshold values $t_{\text{rise time threshold}} \approx 90\,\text{ns}$ [149]. An efficient identification requires non-charge sharing events to have rise times well below 90 ns. In a test setup, the 166-pixel TRISTAN module shows average rise times from 36 ns to 76 ns, depending on the pixel location (see section 6.2.2). The analog cabling length in the final TRISTAN detector setup may further increase the rise time and reduce the capability of an effective rise-time-based charge sharing identification. Whether the rise time method benefits TRISTAN has to be evaluated once the final detector setup is ready.

Each mitigation strategy increases the spectrum modeling complexity by adding pixel, energy, and noise dependence to the detector response. As the modeling capabilities are most important for TRISTAN, this work focuses on measuring and modeling the charge sharing detector response without any of the three mitigation strategies mentioned above.

The following sections first introduce an analytical model describing the effect of charge sharing on the acquired spectrum. After that, a measurement is presented which determines the characteristic charge sharing width σ_{cs} and evaluates the validity of the analytical model.

6.5.1 Charge sharing model

To describe the effect of charge sharing on the acquired spectrum, the statistical distribution of the fraction

$$\eta = \frac{Q_A}{Q_{\text{tot}}} \tag{6.9}$$

of collected charge Q_A in pixel A relative to the total amount of charge Q_{tot} needs to be known. η depends on the interaction location of the incident particle relative to pixel A, as illustrated in
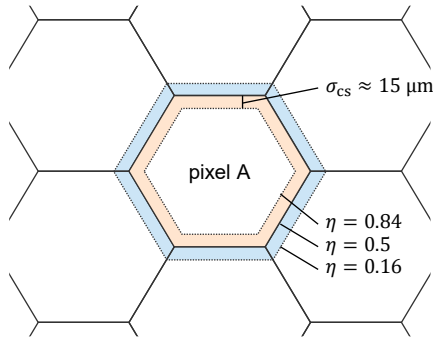
Figure 6.42: Geometric illustration of charge sharing (not to scale). The shaded area is the margin around the pixel border, where 16 % to 84 % of the charge cloud is collected by pixel A ($\pm\sigma_{cs}$). The shape of the margin at the hexagon corners, where three pixels are adjacent, is simplified in this picture.
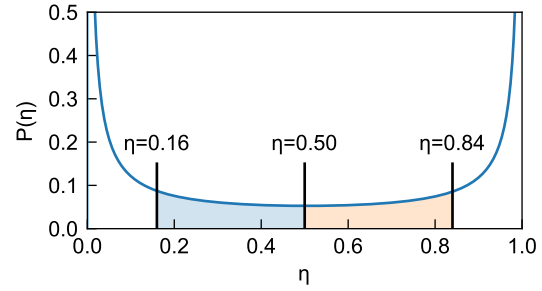
Figure 6.43: Modeled probability density function of the collected charge fraction $P(\eta)$ (equation 6.13) for $\sigma_{cs} = 15\,\mu$m. Only a small fraction of the total area below $P(\eta)$ is visible in the plot, as most of the area is close to the pole at $\eta = 1$. The shaded regions correspond to the shaded regions in figure 6.42

figure 6.42. For simplicity, the model used in this work does not treat the points where three pixel borders meet separately.

All events with an interaction location well inside the pixel area have $\eta = 1$. If the interaction location is precisely at the pixel border, η is 0.5 due to symmetry considerations. The distance from the pixel border, at which around 84 % of the total charge is collected at the anode of pixel A, is the characteristic charge sharing width σ_{cs}.

The charge sharing model, developed in this section, is based on the relation between η and the distance x between the interaction location and the pixel border. $\eta(x)$ is given by a Gaussian integral

$$\eta(x) = \frac{1}{\sqrt{2\pi}} \int_{x/\sigma_{cs}}^{\infty} \exp\left(\frac{-x'^2}{2}\right) dx'. \tag{6.10}$$

This equation empirically describes the complex physical process of the charge cloud drift and its splitting at the pixel border region. Equation 6.10 uses the heuristic picture of a one-dimensional Gaussian charge cloud of width σ_{cs}, which is cut at a straight pixel edge. The different conditions at the corners of the hexagon, where a charge cloud can be shared between three adjacent pixels, are neglected in this model. The Gaussian shape is motivated by the effect of diffusion. If diffusion is the only effect contributing to the spatial extent of the charge cloud, σ_{cs} is expected to be independent of the event energy. The initial extent of the charge cloud along the primary electron track and the electrostatic repulsion within the charge cloud, however, can introduce a slight energy dependence. Both effects have a small effect on the shape of the charge cloud compared to diffusion [88].

To calculate the probability density function $P(\eta)$, the probability density function $P(x)$ and the derivative $\frac{dx}{d\eta}$ are required. This is a random variable transformation:

$$P(\eta) = P(x) \cdot \frac{dx}{d\eta}. \tag{6.11}$$

The probability density $P(x)$ for a homogeneously illuminated detector pixel is given by

$$P(x) = \frac{C}{A} \left(\frac{x}{r_0} + 1 \right), \tag{6.12}$$

with pixel area $A = 7.062\,\mathrm{mm}^2$, pixel circumference $C = 9.892\,\mathrm{mm}$ and with the pixel radius[13] $r_0 = \frac{2A}{C} = 1.428\,\mathrm{mm}$. The final equation for $P(\eta)$ is

$$P(\eta) = \frac{C}{A} \left(\frac{x(\eta)}{r_0} + 1 \right) \cdot \frac{\mathrm{d}x}{\mathrm{d}\eta}(\eta). \tag{6.13}$$

Both $x(\eta)$ and $\frac{\mathrm{d}x}{\mathrm{d}\eta}(\eta)$ are calculated numerically from equation 6.10. $P(\eta)$ is plotted in figure 6.43 for a realistic $\sigma_{cs} = 15\,\mu\mathrm{m}$. One challenging aspect of equation 6.13 is its normalization. Equation 6.13 has an infinite integral for $\eta \to 1$. However, $P(\eta)$ should be normalized to one event per pixel area, which means that $\int_{0.5}^{1} P(\eta) = 1$. This problem is solved by cutting the pole at $\eta \to 1$ such that $\int_{0.5}^{1} P(\eta) = 1$ is fulfilled.

Due to the small σ_{cs} compared to the pixel radius r_0, an incident particle's probability of showing significant charge sharing is relatively small. The probability of falling into the orange areas in figure 6.42 ($0.5 < \eta < 0.84$) is only 0.0208. Due to the small x-dependence of equation 6.12, $P(\eta)$ is slightly asymmetric (not visible by eye), and the blue areas in figure 6.42 correspond to a probability of 0.0210.

The above-presented model for $P(\eta)$ directly serves as a detector response for the effect of charge sharing. For example, assuming $\sigma_{cs} = 15\,\mu\mathrm{m}$, 1000 incident events per pixel area with 10 keV on average cause 1021 events in pixel A above a threshold of 1.6 keV and 979 events above 8.4 keV.

6.5.2 Measurement of charge sharing

There are several possibilities for measuring charge sharing in the TRISTAN detector:
- A direct method uses pulses from a focused laser (see section 5.3) to scan the pixel border and directly measure $\eta(x)$. However, the different initial charge cloud geometry between pulsed light events and electron events is a significant systematic uncertainty of this method.
- A more indirect method is fitting an acquired electron spectrum of a homogeneously illuminated detector with a full detector model, including the properties of $\eta(x)$ as fit parameters. The main challenge with this approach is that detector effects like backscattering and entrance window effects are entangled with the effect of charge sharing.
- A third approach, applied here, uses the time coincidence of charge sharing events in neighboring pixels. This allows for the determination of η of each single event and $P(\eta)$ can be extracted if many events are accumulated.

Within this work, a measurement following the third approach was performed. The measurement uses the electron gun, described in section 5.2, and the steering coil system to illuminate one group of seven pixels homogeneously with electrons of 10 keV, 15 keV and 20 keV kinetic energy at a rate of around 200 cps per pixel. The detector S0-166-6 is used for all measurements, unless otherwise stated. The bias settings are given in table A.8 in the appendix. The rate distribution and pixel selection is shown in figure 6.44.

---

[13]The radius r_0 of the hexagon is defined as the apothem of the hexagon for the charge sharing model derivation.
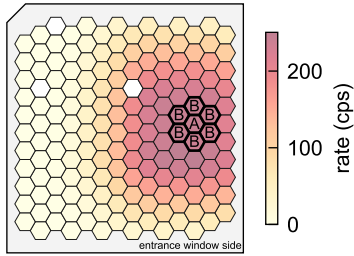
Figure 6.44: Pixel map of electron rate for a charge sharing acquisition. 7-pixels with homogeneous illumination (labels A and B) are used for the analysis.
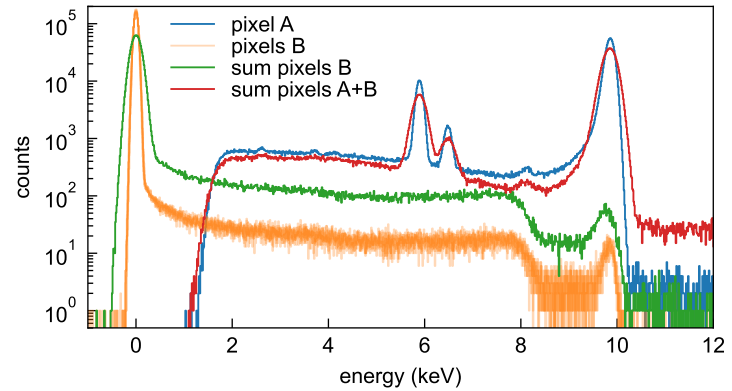
Figure 6.45: Spectra of electons with 10 keV kinetic energy for the charge sharing acquisition. Several different combinations of the energy in pixel A and its six neighbor pixels B are drawn. The event readout on all pixels is triggered solely by pixel A. The spectra of pixels B, therefore, originate from charge sharing with pixel A.
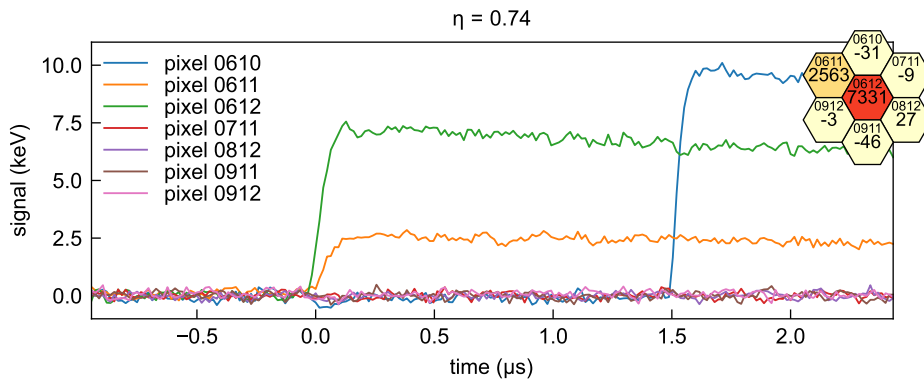
Figure 6.46: Example waveforms of one event in the charge sharing measurement. The central pixel 0612 and one neighboring pixel have pulses from a charge sharing event with $\eta = 0.74$ at the trigger timestamp $t = 0\,\mu s$. Pixel 0610 has a non-charge-sharing random coincidence event at $t \approx 1.5\,\mu s$, which is well separated from the trigger and does not disturb the energy readout. The pixelmap shows the energy readout (in eV) at $t = 0\,\mu s$ for each of the seven pixels.
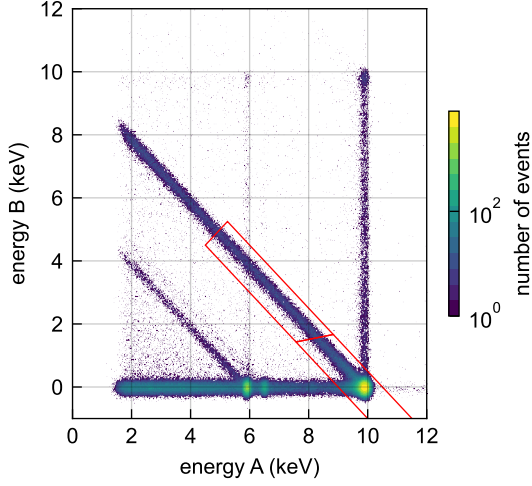
Figure 6.47: 2D histogram of the energy in pixel A and the sum of neighboring pixels B for a charge sharing acquisition at 10 keV. The diagonal lines originate from charge sharing.
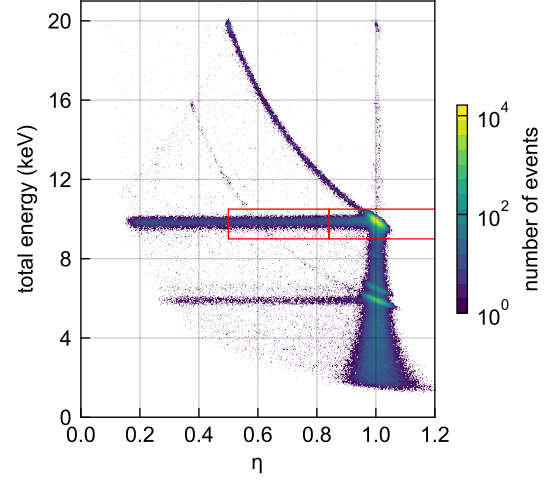
Figure 6.48: 2D histogram of charge sharing fraction η and total energy E_{tot}. This histogram uses the same dataset shown in figure 6.47, and applies equation 6.14 to change the histogram axes. The red boxes indicate the areas used to extract σ_{cs}.

The DAQ records the events in a triggered waveform mode. The trigger is configured such that only a pulse in pixel A triggers an event. For each event, the waveforms of all seven pixels are acquired synchronously. Figure 6.46 shows the waveforms of an example event. The recorded spectra for pixel A, pixels B and the sum of all seven pixels are shown in figure 6.45. For each event, the two quantities E_A and E_B are studied. E_A is the energy of pixel A, and E_B is the sum of the energies of pixels B. A 2D histogram, using E_A and E_B, is shown in figure 6.47

The spectrum of pixel A features the electron peak and two X-ray peaks from an ^{55}Fe source for calibration. The spectra of pixels B contains a zero energy peak, leading to a horizontal line in figure 6.47. Some events share their charge between pixel A and pixels B, causing a diagonal line in the 2D histogram of figure 6.47 A third category of events shows uncorrelated events due to random coincidence in pixel A and pixels B, causing vertical lines in figure 6.47.

6.5.3 Extraction of the charge sharing width

The two-dimensional information of each event (E_A and E_B) enables a precise selection of charge sharing events. To this end, the total energy E_{tot} and charge sharing fraction η are calculated for each event:

$$E_{\text{tot}} = E_A + E_B \qquad \eta = \frac{E_A}{E_A + E_B} \ . \tag{6.14}$$

The 2D histogram of E_{tot} and η is shown in figure 6.48. To measure σ_{cs} for 10 keV electrons, the number of events N_{cs} which fulfill $0.5 < \eta < 0.84$ and are within an E_{tot} region-of-interest $9\,\text{keV} < E_{\text{tot}} < 10.5\,\text{keV}$ are compared to the number of events N_{tot} which fulfill $0.5 < \eta$ in the same E_{tot} region-of-interest. These selections are illustrated by the red boxes in figures 6.47 and 6.48. In the shown case, the fraction $N_{\text{cs}}/N_{\text{tot}}$ is 0.0219. This fraction must be equal to the model prediction $\int_{0.5}^{0.85} P(\eta)\mathrm{d}\eta$ calculated with equation 6.13. As a consequence, σ_{cs}, which enters into
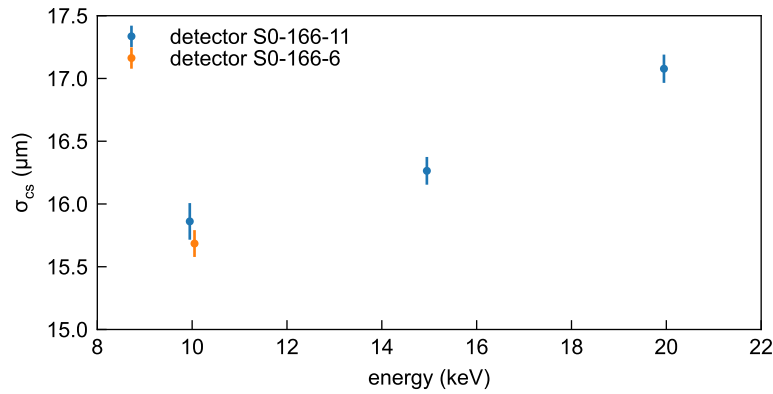
Figure 6.49: Measured charge sharing width σ_{cs} for three different energies. Two different detector modules S0-166-6 and S0-166-11 of the production 2 were used. The error bar is the statistical error.

$P(\eta)$, can be extracted. A numerical solver yields that $\int_{0.5}^{0.85} P(\eta)d\eta = 0.0219$ is fulfilled with $\sigma_{cs} = (15.68 \pm 0.15)\,\mu\text{m}$. The stated uncertainty is the statistical error.

The same measurement was repeated at 10 keV, 15 keV and 20 keV kinetic energy with a different detector module. Figure 6.49 shows the extracted σ_{cs}. An slight energy dependence of σ_{cs} is observed with $\sigma_{cs} = (15.77 \pm 0.13)\,\mu\text{m}$[14] at 10 keV, $\sigma_{cs} = (16.26 \pm 0.11)\,\mu\text{m}$ at 15 keV, and $\sigma_{cs} = (17.08 \pm 0.11)\,\mu\text{m}$ at 20 keV. This energy dependence can be explained by the increasing primary charge cloud size with energy.

6.5.4 Measured η-distribution

So far, only the scalar quantity σ_{cs} was extracted from the measurement. Additionally, also the observed distribution of η can be compared with the modeled $P(\eta)$. In order to obtain the measured distribution, all events in the E_{tot} region-of-interest of the 2D histogram (figure 6.48) are selected, and η is plotted in a histogram. To get a realistic model, $P(\eta)$ is convoluted with a Gaussian function to account for smearing due to noise. Furthermore, the model is normalized to the same number of counts as in the measurement for $\eta > 0.5$. The measured and the modeled η distributions are compared in figure 6.50. It is important to mention here that only two parameters of the model were fitted to the data for this comparison: First, σ_{cs} was chosen such that the ratio of counts in the range $0.5 < \eta < 0.84$ and $\eta > 0.5$ is the same for model and data (see previous section). In the second step, the Gaussian width σ_{peak} of the peak at $\eta = 1.0$ is fit to the data. σ_{peak} is a nuisance parameter and not of interest for charge sharing. In the range $0.25 \lesssim \eta \lesssim 0.95$, a good agreement between measurement and the model is observed. There are, however, slightly fewer counts in the data than modeled in the region $0.85 \lesssim \eta \lesssim 0.95$.

The analysis of the measured $\eta(x)$-distribution proves that the 1D Gaussian model in equation 6.10 is, in general, a suitable choice. However, the slight deficit of counts at high η in the measurement corresponds to a suppression in the tails of the Gaussian charge cloud. The Gaussian model is well motivated by diffusion during the drift of the charge cloud to the saddle point of the electric potential. Other effects, like the shape of the initial charge deposition or coulomb repulsion during the drift, can explain a slightly non-Gaussian character. However, one must be careful when physically interpreting the shape of the heuristic charge sharing model. Even if the charge cloud

---

[14]This is the combined value of the two measurements shown in figure 6.49.
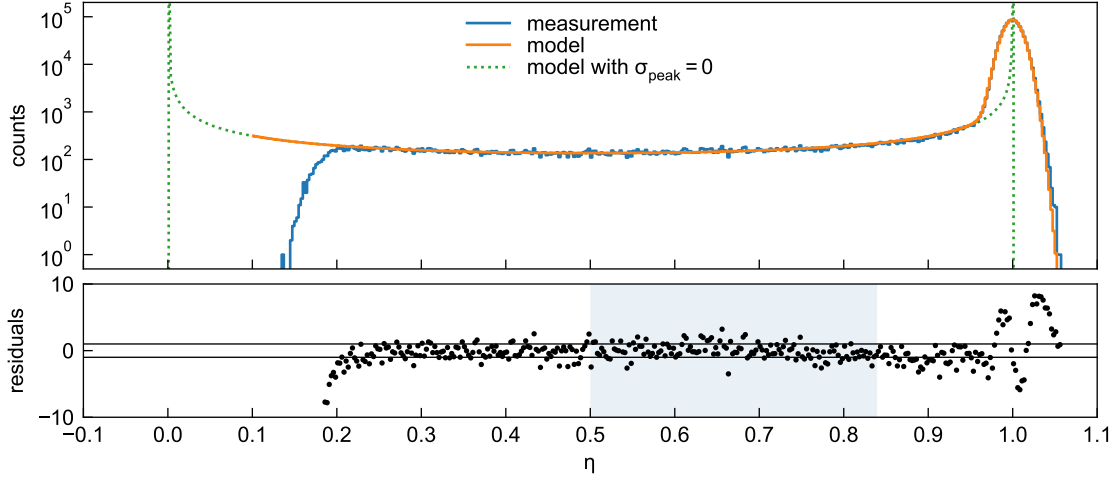
Figure 6.50: Measured and modeled distribution of η at 10 keV. The measured distribution is only valid for $\eta \gtrsim 0.2$ due to the threshold of the measurement. A small discrepancy between the model and the data can be explained by a small contribution from random coincidence events in the data $0.95 < \eta < 1.0$, which is also visible in the 2D histogram in figure 6.48.

would be Gaussian in a homogeneous electric field for a diffusion-only scenario, the real drift in the saddle-shaped electric field of the pixel border may cause non-Gaussian effects.

The slight deficit of counts at high η values could be addressed in the model by artificially cutting or reducing the Gaussian tails. However, more measurements at different energies with less statistical uncertainty would be beneficial to further constrain the charge sharing model $\eta(x)$.

6.6 Summary

In this chapter, general performance parameters of the 166-pixel detector module were measured:

- The leakage current has a negligible effect on the detector performance of a cooled detector due to its low value below 150 fA on all pixels.
- The measured median signal rise ranges between 36 ns and 76 ns, depending on the pixel. The rise times and also the pulse shape are in line with the simulations of the charge drift and readout in sections 4.1 and 4.2.2. The variation of the rise time within the pixels can be related to a variation in the SC line capacitance between the SDD and the ETTORE ASIC. Furthermore, the rise time in the final detector is anticipated to be slightly higher due to the use of longer cables at the output of the ETTORE ASIC.
- The measured equivalent noise charge is ENC $= 11.3^{+1.6}_{-0.9}$ e at a peaking time of 960 ns over all pixels of a detector module. The measured noise aligns with the noise model developed in section 4.3. This is an important achievement for the understanding of the detector.

Furthermore, the two additional aspects of crosstalk and charge sharing in the TRISTAN detector were investigated. The investigation of crosstalk in 7-pixel TRISTAN detectors led to an optimization of the readout design on the SDD. Thereby, the amplitude of crosstalk was reduced significantly. After the successful design improvements, the crosstalk situation in the 166-pixel detectors was examined. As the further mitigation of crosstalk by hardware modifications is not feasible, the

impact of the crosstalk on the spectroscopic performance was investigated by a trace-level Monte Carlo simulation. The simulation indicates that crosstalk will cause a non-Gaussian broadening of the detector response and a reduction in detection efficiency. In the most affected pixel at the target input rate, an additional broadening equivalent to ENC $\approx 40\,e$ is observed in the simulation, clearly dominating the overall noise.

The experimental characterization of the TRISTAN detector concluded with a measurement of the charge sharing effect, which occurs at the boundaries between adjacent pixels. The studies include the development of an empirical model for charge sharing as well as a measurement concept, which extracts charge sharing properties with minimal systematic effects. A measurement with electrons of 10 keV, 15 keV and 20 keV kinetic energy yields a characteristic charge sharing width $\sigma_{cs} \approx 15.8\,\mu$m, 16.3 μm, and 17.1 μm, respectively. A good agreement of model and data could be demonstrated by comparing the simulated and modeled probability distribution of the charge sharing fraction η. The charge sharing measurement is an important input for accurately modeling spectra acquired with the TRISTAN detector.

7 Data acquisition system development and simulation

The Data Acquisition System (DAQ) captures, analyzes, and saves the events of the TRISTAN detector. The TRISTAN detector comes with several challenges for the DAQ:

1. The sterile neutrino search requires the measurement of the spectral shape of tritium β-decay on the 10^{-6} level. Any shape distortion related to the DAQ must be understood precisely.
2. The TRISTAN detector array will measure at a total event rate of around 10^8 counts per second. Due to the high count rate, the DAQ must process and histogram all events in real time. The amount of event-based data would be too large to be stored.
3. The 9-module TRISTAN detector will have more than 1000 analog detector channels, which must be read out. Therefore, the DAQ must feature a high readout density.
4. The detector section of the KATRIN experiment has challenging environmental constraints: The detector and parts of the DAQ will sit on a positive voltage of up to $20\,\mathrm{kV}$ against the ground. Furthermore, a high vacuum is present at the detector. Outside of the vacuum chamber, where DAQ will be located, a stray magnetic field $\mathcal{O}(100\,\mathrm{mT})$ is present.

Due to these requirements, the TRISTAN detector will have a custom-developed DAQ system. It is being developed and built at the Institute for Data Processing and Electronics (IPE)[1] of the KIT in Karlsruhe. The IPE has already developed the DAQ for the current KATRIN focal plane detector [69, 70].

Section 7.1 of this chapter introduces the conceptual design of the DAQ and the signal processing approach. After that, section 7.2 describes the treatment of pileup, which is an essential effect in the high-rate acquisition of TRISTAN. A significant contribution of this work to the DAQ is the development of a trace-level simulation, described in section 7.3. The simulation is used to study the pileup spectrum (sections 7.3.1 and 7.3.2), the amount of deadtime (section 7.3.3), and the effect of a non-perfect exponential devolution (section 7.3.4). Finally, the first hardware tests of a prototype DAQ, operated at the KATRIN monitor spectrometer, are presented in section 7.4.

7.1 Data acquisition concept

The DAQ design follows the modular design of the TRISTAN detector. Each detector module, comprising of 166 pixels, has a dedicated 166-channel frontend DAQ, which features full waveform digitization of all channels. The main advantage of the full waveform digitization approach, compared to approaches like peak-sensing digitization after an analog shaping filter (for example in

---

[1]www.ipe.kit.edu

124
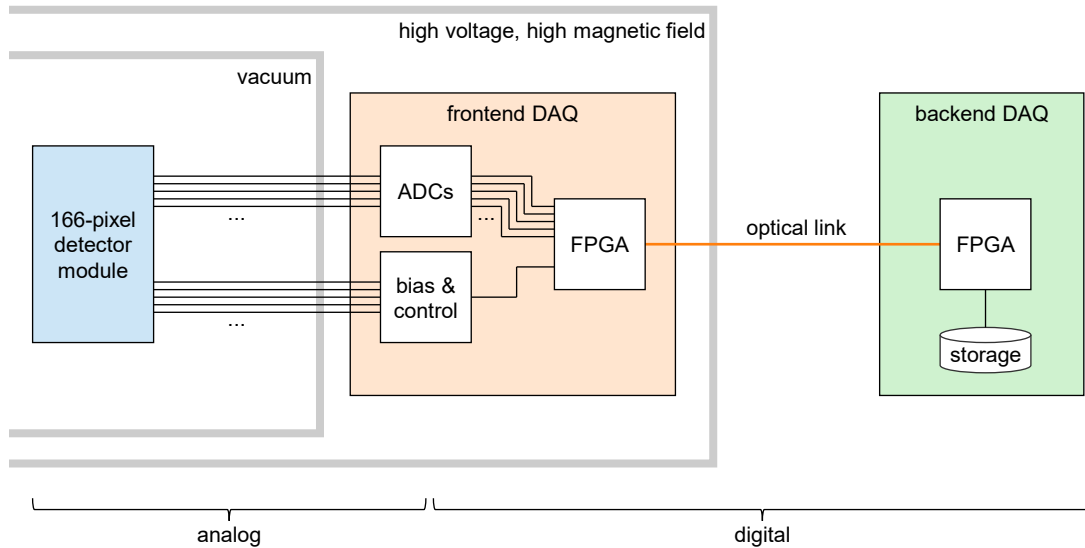
Figure 7.1: Conceptual design of the TRISTAN DAQ. The design follows the "remote ADC" concept, where the digitization on the frontend DAQ is separated from the processing on the backend DAQ.

[150]), is the flexibility and transparency in the processing algorithms. The fully digital processing allows for a detailed study of edge cases on a waveform basis. Furthermore, all pulse-height analysis parameters can be changed by firmware and do not require modifications of the hardware.

A short distance between the detector and the analog-to-digital converters (ADCs) is preferred to reduce possible distortions on the signals due to electromagnetic interference. However, there is limited space, limited cooling capabilities, a high magnetic field, and high voltage near the detector. Therefore, the TRISTAN DAQ follows the "remote ADC" concept, sketched in figure 7.1. The hardware of the DAQ system consists of two separate parts:

- **Frontend DAQ** The custom-developed electronics board of the frontend DAQ is located directly at the ambient air side of the electric feedthroughs of the vacuum chamber. At this location, a high magnetic field $\mathcal{O}(100\,\mathrm{mT})$ is present, which requires a special design and selection of components. The frontend DAQ digitizes the signals of all 166 channels, serializes the data via Field Programmable Gate Arrays (FPGAs), and sends the data stream via high-speed optical links to the backend DAQ. In order to keep the complexity and power consumption of this board at a minimum level, no analysis of the digitized data is done. The frontend DAQ board also provides the detector with the bias and control voltages.

- **Backend DAQ** The backend DAQ receives the digitized waveform stream from the frontend DAQ. Subsequently, it processes the waveforms in terms of a pulse-height analysis, and stores the output histograms. The backend DAQ is located several meters away from the detector, where environmental constraints are relaxed compared to the frontend DAQ location. Thus, high-performance components[2] can be used for digital signal processing.

[2]for instance a Xilinx Virtex UltraScale+ FPGA
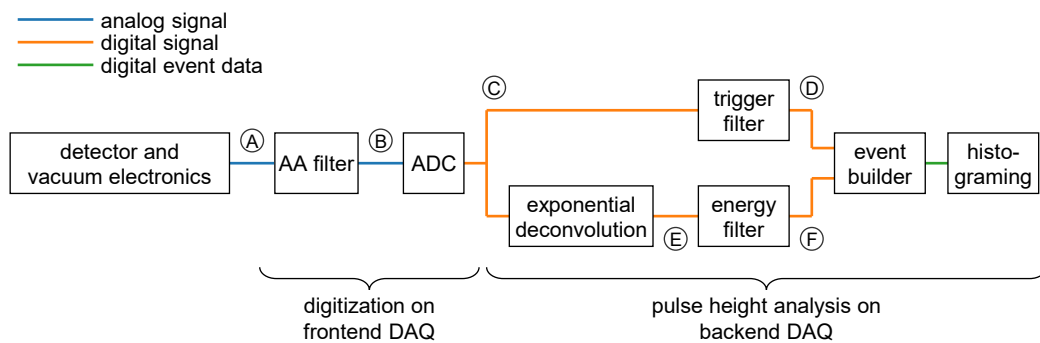
Figure 7.2: Signal chain of one channel in the DAQ system. An illustration of the digital signals of the pulse-height analysis in the backend DAQ is provided in figure 7.3.
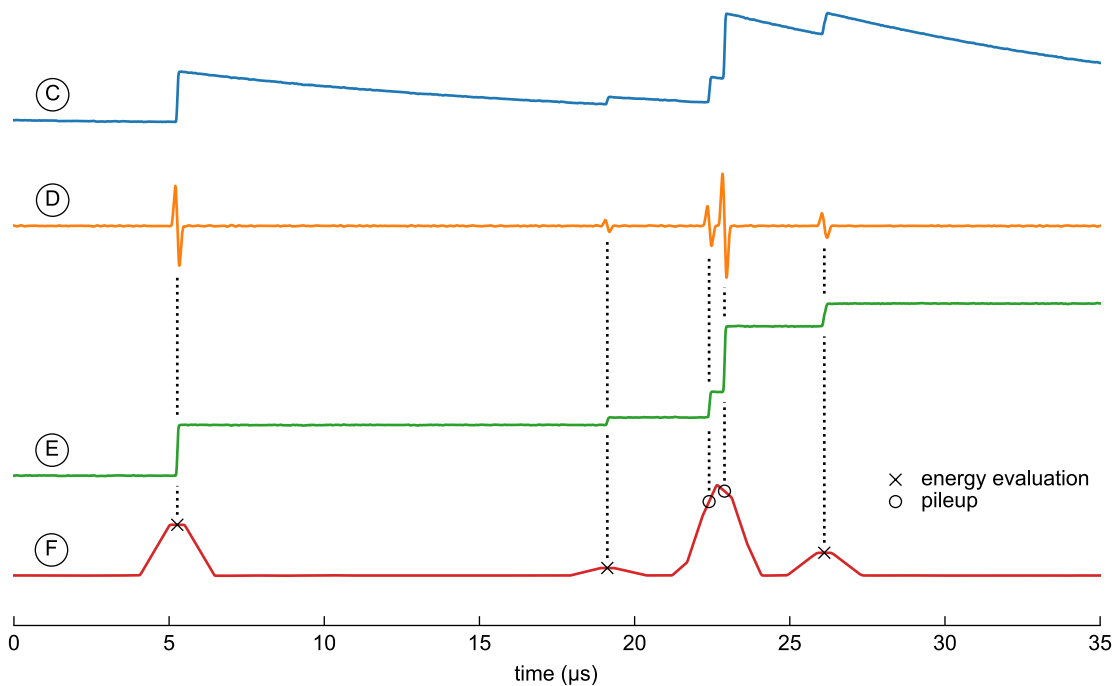
Figure 7.3: Illustratoin of the digital pulse-height analysis of the DAQ system. The four shown signals correspond to signals Ⓒ to Ⓕ in figure 7.2. The trigger filter Ⓓ determines the timestamp of each event (vertical dashed lines). The energy of each event is evaluated at the trapezoidal energy filter Ⓕ. A fast response of the trigger filter is important to discriminate pileup.

Table 7.1: Default parameters for the digital pulse-height analysis for TRISTAN

	symbol	value
trigger filter	τ_{window}	112 ns
	τ_{holdoff}	240 ns
energy filter	τ_{peaking}	960 ns
	τ_{gap}	480 ns
pileup rejection	τ_{pu}	1376 ns

Signal processing

The functional blocks of the DAQ signal processing are illustrated in figure 7.2. The frontend DAQ receives the analog signal, applies an anti-aliasing (AA) filter, and digitizes the signal. The backend DAQ performs an online digital pulse-height analysis (PHA), which has two parallel signal paths: The first path determines each event's timestamp via a trigger filter. A second path extracts the energy of each triggered event by combining an exponential deconvolution block and a trapezoidal energy filter. Figure 7.3 illustrates this method. A detailed description of each functional block of figure 7.2 is provided in the appendix in section A.4.

The most critical parameters of the pulse-height analysis are listed in figure 7.1. A detailed description of the trigger filter and energy filter parameters is given in section A.4.3 and A.4.4 of the appendix, respectively. The pileup rejection parameter is described in section 7.2. Table 7.1 is used as default values for all studies of the DAQ system and for all measurements presented in chapter 6 of this work. This allows for a consistent comparison of simulation and data. Although these parameters are believed to be a wise default configuration for the final TRISTAN measurement, the default values may change in the future.

7.2 Treatment of pileup

If two physical pulses appear close in time, the energy filter responses can overlap, and the reconstruction of the event parameters (especially the energy) can be distorted. This situation is called pileup. Pileup is limiting the performance of most detector systems at high rates. Therefore, the mitigation and understanding of pileup is essential for TRISTAN. This section presents a strategy how to treat pileup in the TRISTAN DAQ. Furthermore, based on the DAQ filtering algorithm, the expected amount of events affected by pileup in the final spectrum is estimated analytically. A simulation of pileup is presented in the next section 7.3.

For illustration, three examples of events that are close in time are plotted in figure 7.4. The three examples belong to three categories which are distinguished:

- **Unresolved pileup** Unresolved pileup occurs if two pulses are so close in time that the individual pulses can not be resolved. The extracted timestamp and pulse height can not be distinguished from a single event with a larger pulse height. Unresolved pileup occurs if the time distance between events is smaller than the minimum resolution time τ_{min}. More details about the trigger algorithm and τ_{min} are given in section A.4.3 in the appendix. There, it is shown that with the used trigger algorithm, τ_{min} depends on the energy of the involved
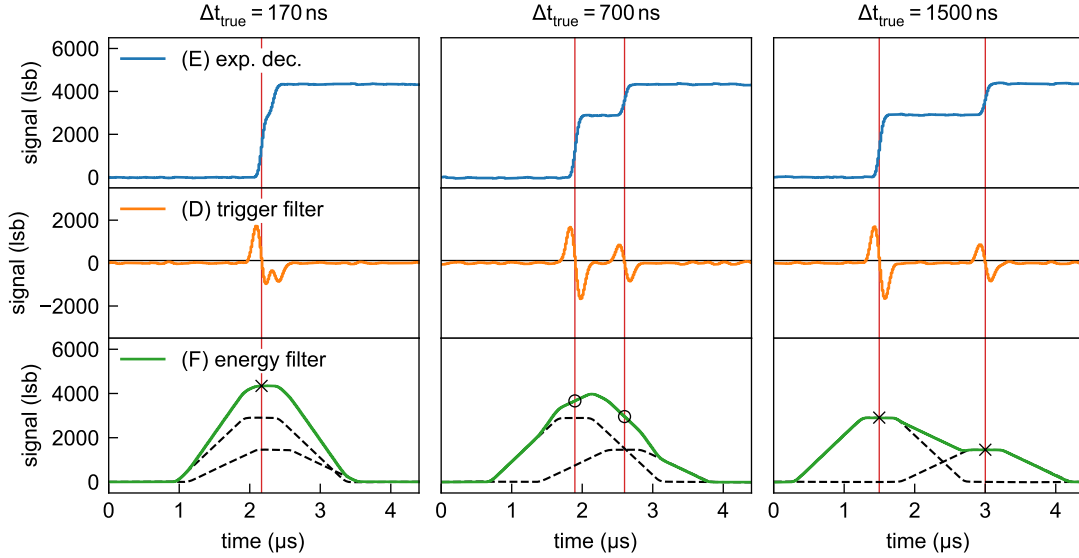
Figure 7.4: Three example simulations to illustrate pileup scenarios. The digitized signal after exponential deconvolution (top), trigger filter output (center), and energy filter output (bottom) are shown. The signals correspond to labels Ⓔ, Ⓓ, and Ⓕ in figure 7.2, respectively. Each simulation has two events with a true time difference Δt_{true}. The energy to the two events is 20 keV and 10 keV. The simulations are classified as unresolved pileup (left), resolved pileup (center), and no pileup (right).

events, which is unfavorable for understanding the unresolved pileup spectrum. Therefore, a trigger holdoff time τ_{holdoff} is introduced, which artificially sets τ_{min} to the defined value of τ_{holdoff}.

- **Resolved pileup** If the time distance between two events is larger than the minimum resolution time τ_{min} but smaller than the pileup threshold time τ_{pu}, the energy readout of the events gives a wrong value. Unlike the previous case, this case can be detected by comparing the timestamps of the two triggers.

- **No pileup** In this case, the time difference is larger than the pileup threshold time τ_{pu} and the event parameters are correctly reconstructed. Note that in the right plot in figure 7.4, the energy readout is correct even if the edges of the trapezoids overlap.

The reconstructed energy of pileup events depends on the time distance and the energy of the involved events. Figure 7.5 shows the reconstructed event energies as a function of their true time distance Δt_{true}. The three pileup categories "unresolved pileup", "resolved pileup", and "no pileup" are marked in the figure. A single event with the sum of the involved events is obtained if the time distance is close to zero. For time distances larger than around $\tau_{\text{gap}}/2$, the reconstructed energy decreases as the trapezoids are not evaluated in the flat-top region. The energies are reconstructed correctly for time distances larger than around $\tau_{\text{gap}}/2 + \tau_{\text{peaking}}$.

In order to keep the pileup-related distortion of the final spectrum low, all events in the resolved pileup region are flagged as pileup and can be rejected for the spectrum. To this end, the pileup threshold time τ_{pu} is defined, which must be set to at least $\tau_{\text{gap}}/2 + \tau_{\text{peaking}}$. This work uses a default value $\tau_{\text{pu}} = 1376$ ns, which provides an additional margin of 176 ns, which ensures undistorted no-pileup events even with signal rise times of around 100 ns.
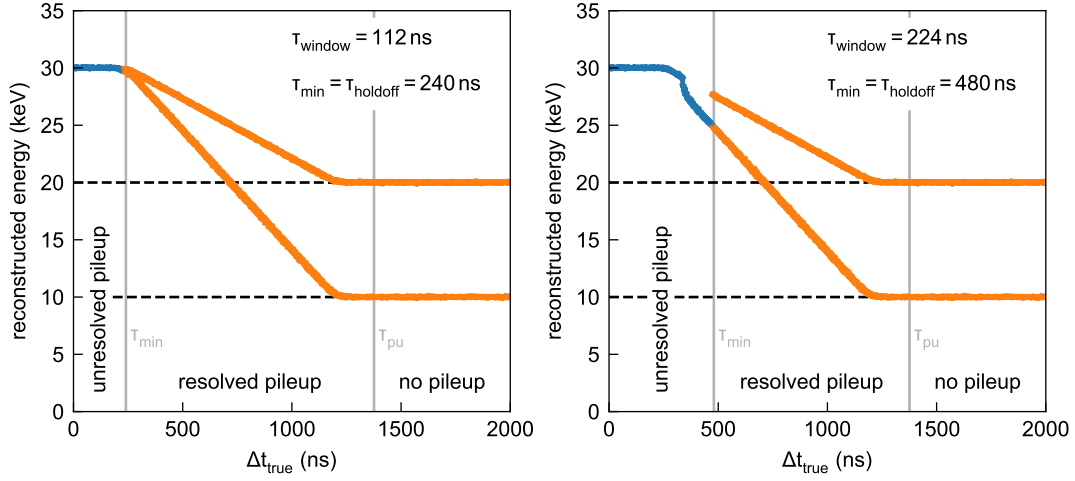
Figure 7.5: Simulated relation between the reconstructed event energy and the time distance Δt_{true} of two events. The curves are obtained by many simulations similar to figure 7.4, with two events with true energy 10 keV and 20 keV, respectively. If the trigger filter detects one event, a blue dot is drawn. If the trigger filter detects two events, two orange dots are drawn. The left plot shows the nominal scenario for TRISTAN, and the right plot shows a scenario with increased trigger filter time τ_{window}. The trapezoidal filter has parameters $\tau_{\text{peaking}} = 960\,\text{ns}$ and $\tau_{\text{gap}} = 480\,\text{ns}$.

The remaining events after rejecting pileup show either no pileup or unresolved pileup. The fast minimal resolution time τ_{min} of the trigger filter, in combination with a flat top time τ_{gap} of the trapezoidal filter, has a beneficial effect: The reconstructed energy of all unresolved pileup events is the sum of the energy of both involved events. This is pictured in the left plot in figure 7.5. The right plot in figure 7.5 shows a less beneficial scenario, where the minimum resolution time is larger than $\tau_{\text{gap}}/2$, such that the energy filter output of unresolved pileup events can partially overlap. In this case, modeling the pileup spectrum would be very challenging.

Probability of pileup   The probability that an input event falls into one of the categories "unresolved pileup", "resolved pileup", or "no pileup" depends on the input rate of events and on τ_{min} and τ_{pu}. The following calculations assume an uncorrelated temporal distribution of events. This assumption is valid in the case of the radioactive tritium decay in the KATRIN source. However, effects like secondary electron emission or backreflection of backscattered electrons can cause correlated arrival times, which would require more sophisticated calculations. The following calculations are based on the Poisson distribution

$$P_{\text{Poisson}}(k; T) = \frac{(TR)^k e^{-TR}}{k!}, \tag{7.1}$$

which describes the probability to have k events in a fixed time window T for a given rate R.

In order to derive the probability of pileup, the picture of figure 7.6 is used, which considers a randomly selected event at time $t = 0$. The event will be classified as no pileup if there is no other event in a time window of size $2\tau_{\text{pu}}$ (orange and blue region in the figure 7.6)

$$P_{\text{no pileup}} = P_{\text{Poisson}}(k = 0; T = 2\tau_{\text{pu}}) = e^{-2\tau_{\text{pu}}R}. \tag{7.2}$$
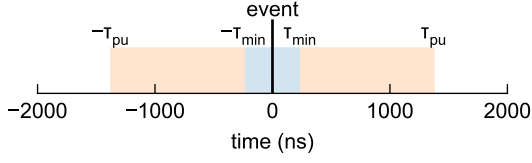
Figure 7.6: Illustration for the derivation of pileup probabilities.
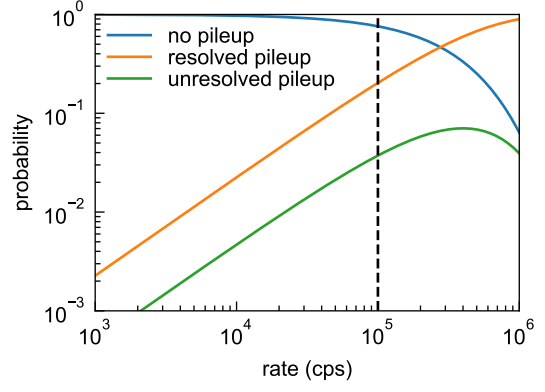
Figure 7.7: Probabilities for the three pileup categories as a function of the event rate. The calculation uses $\tau_{\mathrm{pu}} = 1.376\,\mu s$ and $\tau_{\min} = 240\,\mathrm{ns}$.

Table 7.2: Probabilities (in %) for an input event to fall into one of three pileup categories. The calculation uses $\tau_{\mathrm{pu}} = 1.376\,\mu s$ and $\tau_{\min} = 240\,\mathrm{ns}$.

	$R = 1\,\mathrm{kcps}$	$R = 10\,\mathrm{kcps}$	$R = 100\,\mathrm{kcps}$
$P_{\text{no pileup}}$	99.7	97.3	75.9
$P_{\text{resolved pileup}}$	0.227	2.25	20.3
$P_{\text{unresolved pileup}}$	0.0479	0.468	3.73

The event will be classified as unresolved pileup if there is at least one event in the time window of size $2\tau_{\min}$ (blue region in the figure 7.6) and no event in the time window of size $2\tau_{\mathrm{pu}} - 2\tau_{\min}$ (orange region in the figure 7.6)

$$P_{\text{unresolved pileup}} = P_{\text{Poisson}}(k > 0; T = 2\tau_{\min}) \cdot P_{\text{Poisson}}(k = 0; T = 2\tau_{\mathrm{pu}} - 2\tau_{\min}) \tag{7.3}$$

$$= \left(1 - e^{-2\tau_{\min}R}\right) \cdot e^{-(2\tau_{\mathrm{pu}} - 2\tau_{\min})R} \tag{7.4}$$

$$= e^{-(2\tau_{\mathrm{pu}} - 2\tau_{\min})R} - e^{-2\tau_{\mathrm{pu}}R}. \tag{7.5}$$

Finally, an event will be classified as resolved pileup if there is at least one other event in the window $2\tau_{\mathrm{pu}} - 2\tau_{\min}$ (orange region in the figure 7.6)

$$P_{\text{resolved pileup}} = P_{\text{Poisson}}(k > 0; T = 2\tau_{\mathrm{pu}} - 2\tau_{\min}) = 1 - e^{-(2\tau_{\mathrm{pu}} - 2\tau_{\min})R}. \tag{7.6}$$

The probabilities for the three pileup categories are plotted in figure 7.7 At the maximum target rate of 100 kcps, 76 % of all events are not affected by pileup, 20.3 % of the events are detected as resolved pileup and are rejected, and 3.7 % of the events are unresolved pileup and end up in the pileup spectrum. The pileup spectrum will only contain around 1.9 % of all primary events, as usually two events are merged into one in the case of unresolved pileup.

The derivation of the analytic pileup probabilities $P_{\text{unresolved pileup}}$, $P_{\text{resolved pileup}}$ and $P_{\text{no pileup}}$ assumed some simplifications. For instance, no timestamp jitter and no events below the threshold were considered. The true pileup probabilities, including these effects, are obtained from a trace

level simulation in section 7.3.2. It will be seen, however, that the analytic estimations provide a good approximation of the true pileup probabilities.

7.3 Simulation of the DAQ system

A detailed trace level simulation, called `DAQsim`[3], was developed in the scope of this work. The goal of `DAQsim` is to study the behavior of the full signal processing chain, as illustrated in figure 7.2.

The simulation allocates discrete signal arrays (typical 0.2 s duration each) in memory. These snippets contain Monte Carlo simulated detector events. Subsequently, all steps of signal processing are applied to the signal. Besides the output histograms, many diagnostic data, like small waveform snippets and event data, can be saved. The simulation is written in `python` and is based on `numpy` for efficient array calculations [151]. The simulation runs on parallel processes on a multi-core CPU to have a high simulation speed. With 64 processes in parallel, a total simulation speed $\mathcal{O}(5)$ times as fast as real-time is achieved. This means that a 5 min acquisition with a single channel can be simulated in 1 min calculation time. All processing steps in the simulation are configured with a configuration file. The default configuration is shown in the appendix table A.4.

`DAQsim` is used in the following to simulate DAQ-related systematic effects, which are important for TRISTAN. The first simulation mimics a high-rate tritium acquisition and focuses on the shape of the pileup spectrum. After that, simulations at different count rates are compared in order to confirm the estimated pileup probabilities from section 7.2. Finally, two more studies are done with `DAQsim`, which focus on the dead time from resets and the impact of non-perfect parameters in the exponential deconvolution. `DAQsim` is also used to study the effect of crosstalk on spectroscopy, which was presented in section 6.4.

7.3.1 High-statistic tritium DAQ simulation

The first study with `DAQsim` simulates a realistic scenario of a TRISTAN tritium acquisition at a high rate of 100 kcps. One goal of the simulation is to mimic an actual acquisition. Details like the reset mechanism and the saturation of the second stage output voltage are included in the simulation. Therefore, a complete picture of DAQ-related effects is obtained. A second goal of the simulation is to have many counts in the output spectrum such that small spectral shape effects can be seen. The simulated acquisition time is the order of hours of a single channel with an input count rate of 100 kcps, corresponding to around $\mathcal{O}(10^{10})$ events. Although this is computationally already expensive, it is still a low number compared to the foreseen number of collected events in the TRISTAN acquisition, which will be $\mathcal{O}(10^{16})$ [93].

Simulation parameters   To get a realistic input spectrum, the spectrum calculation software `TRmodel` is used in the "optimized scenario" described in [78]. The obtained charge pulse height spectrum is shown in figure A.21. The primary tritium spectrum extends from 20 keV to 38.8 keV due to the post-acceleration of electrons to the detector. A tail between zero and 20 keV is present in the spectrum, originating from charge sharing and backscattering. Backscattered electrons are assumed to be lost. In the actual setup, the magnetic or electrostatic backreflection of backscattered electrons may significantly change the shape of the tail between zero and 20 keV. As the

---

[3]https://nuserv.uni-muenster.de:8443/kurban/daqsim

Table 7.3: Parameters used for the high statistic tritium simulation. A full list is found in the appendix table A.4.

category	name	symbol	value
input	rate	R_{in}	100 kcps
	duration	T_{sim}	43 200 s
signals	charge signal rise time	τ_{rise}	32 ns to 96 ns
ETTORE	2nd stage gain	g_{ETTORE}	5
	fixed reset period	T_{reset}	220 µs
	inhibit duration	$T_{inhibit}$	20 µs
signal processing	ADC sampling frequency	f_s	62.5 MHz
	trigger filter window	τ_{window}	112 ns
	energy filter peaking time	$\tau_{peaking}$	960 ns
	energy filter gap time	τ_{gap}	480 ns
	trigger holdoff time	$\tau_{holdoff}$	240 ns
	pileup rejection time	τ_{pu}	1376 ns
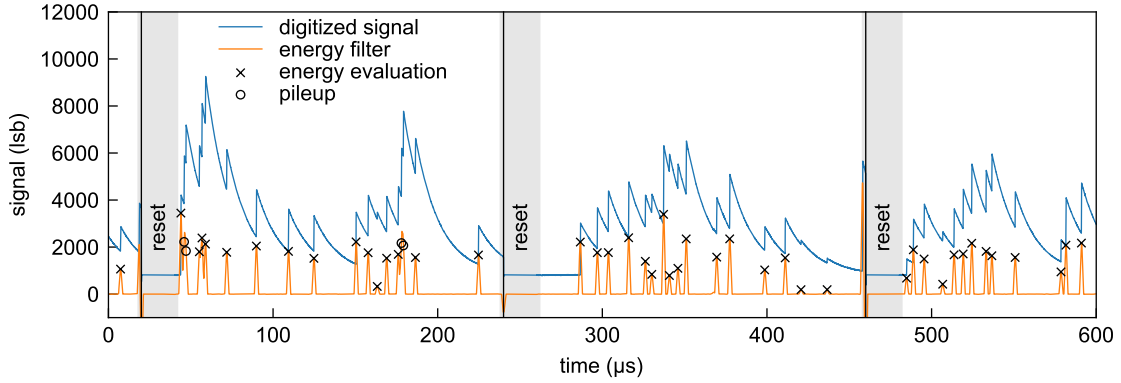
Figure 7.8: Snippet of simulated signals for the high statistic tritium DAQ simulation.

correct calculation of the electron spectrum with backreflection is challenging and depends on various parameters, it is neglected here. The input rate of the simulation is defined as the rate of events following the entire input spectrum. In addition to the input spectrum, `DAQsim` uses the parameters listed in table 7.3. The parameters are a proposed scenario for an actual TRISTAN data acquisition. A fixed external detector reset with period 220 µs is used with an inhibit duration of 20 µs. Considerations that motivate the choice of the reset period are found in section 7.3.3. For illustration, a snippet of the simulated digitized signal and the energy filter output are plotted in figure 7.8. Each event has the two flags *saturation* and *pileup*. The two multiplicity flags *mlt A* and *mlt B* are not filled, as only a single channel is simulated. According to the first two rows of the decision tree option 1 in figure A.12, there are four output histograms.

Results The numbers of events ending up in each histogram are listed in table 7.4. Out of $4.3 \cdot 10^9$ input events, $2.9 \cdot 10^9$ events were reconstructed without the pileup flag, and $0.7 \cdot 10^9$ events were reconstructed with the pileup flag. The fraction of all reconstructed events to all input events is 83.7 %. The missing fraction is explained by the dead time from resets (around 12.1 %), events below the energy threshold, and unresolved pileup events. 19.6 % of all reconstructed events are

flagged as pileup. This fraction is in line with the analytical estimation of 20.3 % given in table 7.2. The slight discrepancy is explained by the energy threshold, which is present in the simulation but not accounted for in the analytical pileup formulas of section 7.2. Less than 2000 events in the simulation saturate the ETTORE 2nd stage voltages range and are flagged accordingly. Although this is a small number, the rejection of these events can still have a small spectral effect, as the saturation probability is higher for high-energy events.

The output spectra of the high-statistic tritium DAQ simulation are shown in figure 7.9. The spectrum of all events has a prominent tail to high energies, which reduces significantly if pileup events are rejected. After rejecting pileup and saturating events, the spectrum has the shape of the input spectrum with an additional unresolved pileup spectrum. This unresolved pileup spectrum extends to around 120 keV, corresponding to 4-fold pileup. Higher orders of pileup should still be present in the spectrum but are too rare to be observed in the simulation. With the used acquisition and DAQ settings, the unresolved pileup spectrum has two interesting and beneficial properties: First, the amount of pileup events is relatively low. In the shown case, the number of events in the unresolved pileup tail above 39 keV is only 1.6 %. Second, the pileup spectrum follows an analytical model. The model is a sum of n-fold convolutions of the input spectrum with itself. Due to the 20 keV post acceleration, the pileup spectrum peaks around 50 keV and is shallow in the region of the primary tritium spectrum.

Comparison to pileup spectrum model

The output spectrum of the high-statistic tritium DAQ simulation is compared to a pileup model in the following. The differential input spectrum is denoted as $S_{\text{in}}(E) = \frac{P_{\text{in}}(E)}{\text{d}E}$. The output spectrum contributions S_n from summing n pulses modeled with

$$S_1(E) = S_{\text{in}}(E),$$

$$S_2(E) = \iint S_{\text{in}}(\epsilon_1)\, S_{\text{in}}(\epsilon_2)\, \delta(E - \epsilon_1 - \epsilon_2)\, \text{d}\epsilon_1 \text{d}\epsilon_2, \qquad (7.7)$$

$$S_3(E) = \iiint S_{\text{in}}(\epsilon_1)\, S_{\text{in}}(\epsilon_2)\, S_{\text{in}}(\epsilon_3)\, \delta(E - \epsilon_1 - \epsilon_2 - \epsilon_3)\, \text{d}\epsilon_1 \text{d}\epsilon_2 \text{d}\epsilon_3,$$

$$\dots .$$

The δ function in the integral ensures that the sum of the individual pulse energies ϵ_i is the output energy E. From a mathematical point of view, the equations for S_n correspond to the $(n-1)$-fold convolution of S_{in} with itself. The total differential output spectrum $S_{\text{out}}(E)$ is the sum of the normalized spectral contributions, weighted by their amplitudes A_n:

$$S_{\text{out}}(E) = \underbrace{A_1 S_1^*(E)}_{\text{no pileup}} + \underbrace{A_2 S_2^*(E)}_{\text{2-fold pileup}} + \underbrace{A_3 S_3^*(E)}_{\text{3-fold pileup}} + \dots . \qquad (7.8)$$

The asterisk denotes that the spectra are normalized to one. The integral of the output spectrum $\int S_{\text{out}} \text{d}E = \sum_i A_i$ gives the friction of output event relative to the number of input events.

Now, the model in equation 7.8 is fitted to the simulated output spectrum. The pileup amplitudes A_1, A_2, A_3, and A_4 are free parameters in the fit. Higher orders of pileup are neglected. A global gain g and a Gaussian broadening with width σ are left free to account for the effect of electronic

Table 7.4: Number of reconstructed events in the high-statistic tritium DAQ simulation. The events are classified by the two flags *saturation* and *pileup*.

	flag saturation	flag pileup	number of events	fraction of input	fraction of output
input events:			4 319 970 724		
output events:			3 615 878 848	83.7 %	
histogram 0:	false	false	2 908 065 603	67.3 %	80.4 %
histogram 1:	false	true	707 811 278	16.4 %	19.6 %
histogram 2:	true	false	164	$< 10^{-6}$	$< 10^{-6}$
histogram 3:	true	true	1803	$< 10^{-6}$	$< 10^{-6}$
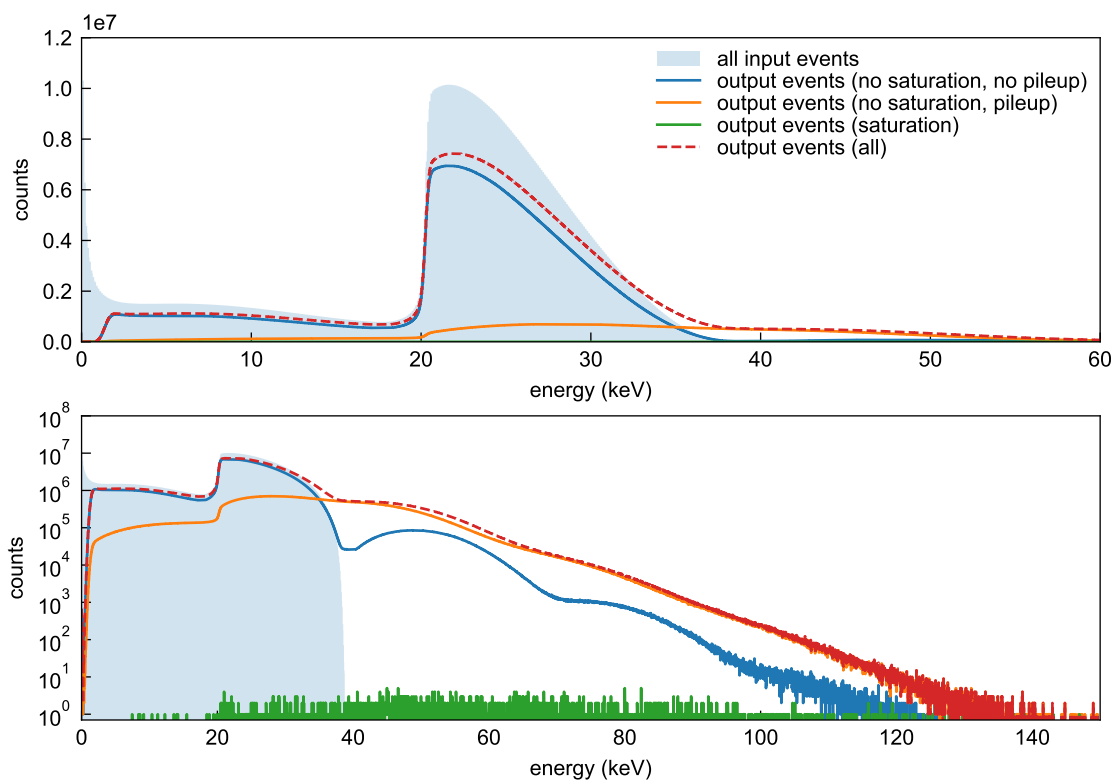
Figure 7.9: Output histograms of the high-statistic tritium DAQ simulation in linear and logarithmic scale. The four shown output histograms are filled with events depending on their saturation and pileup flags. The histogram bin width is 28 eV.
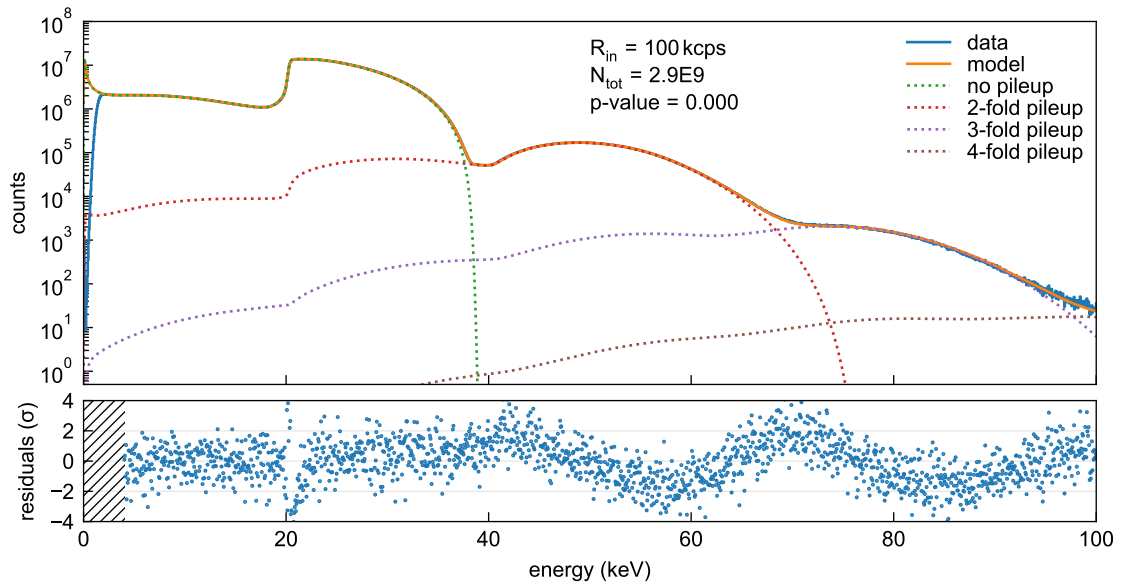
Figure 7.10: Fit of the pileup model (equation 7.8) to the simulated DAQ output spectrum. The bin width is 55 eV. The spectrum below 4 keV is not used for the fit as the threshold effect is not included in the model. The "data" histogram contains all events without pileup flag and saturation flag (histogram 0 in table 7.4).

noise. The fit uses a maximum likelihood approach with the binned (bin width 55 eV) spectrum, assuming a Poissonian likelihood function for each bin.

Figure 7.10 plots the best-fit model. The fitted model, in general, describes the simulated data well. However, a structure is observed in the residuals in the high-energy tail. There are several possible explanations:

- In equation 7.8, the pileup probabilities are assumed independent of the energy E. Although the trigger holdoff mechanism should produce an energy-independent minimal resolution time τ_{min} (and thereby an energy-independent unresolved pileup probability), there could be a small correlation between the actual τ_{min} and the energy of the two involved events.
- The pileup model does not account for the finite trigger threshold. The threshold leads to a small contribution from events, which have an actual time distance in the resolved pileup window but cannot be rejected if one event is below the energy threshold.
- The trapezoidal output is not entirely flat within the flat top of the trapezoid due to the finite rise time of the detector signals. The model does not include this effect.
- A small systematic effect could come from the binning used for the numerical calculation of the model. This is assumed to be a small effect, which cannot explain the residual structure in the pileup tail. It could, however, contribute to the feature at 20 keV in the residuals, which is located where the output spectrum has the highest gradient.

In order to improve the fit, the convolution model 7.7 could, for example, be extended by energy-dependent correction factors in the integral. These factors could depend on the total output energy E and the individual energies ϵ_i.

In summary, the high-statistic tritium DAQ simulation shows that the pileup rejection in the DAQ signal processing works as expected. The shape of the pileup spectrum, which remains after rejection resolved pileup, plays a crucial role for TRISTAN as it overlaps with the tritium spectrum. The spectral investigation in this section showed that the shape of the unresolved pileup spectrum can
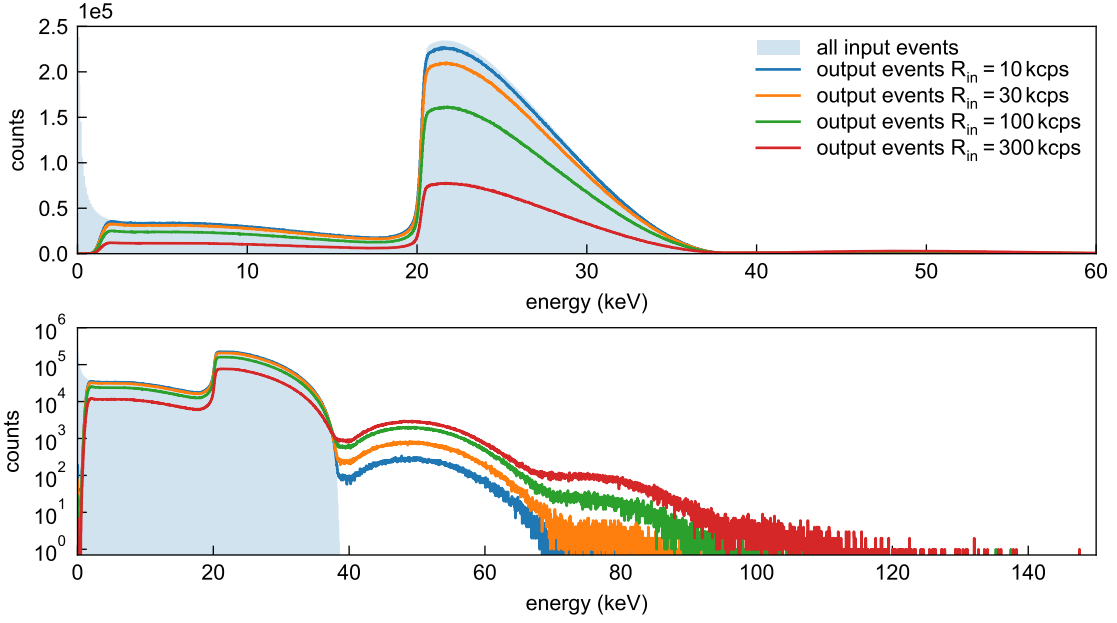
Figure 7.11: Output spectra of the tritium DAQ simulation to study the pileup probabilities at four different input rates R_{in}, in linear (top) and logarithmic scale (bottom). The spectra contain all events with negative pileup and saturation flags. The bin width is 28 eV.

be modeled with a convolution model (equation 7.7). The trace-level DAQ simulation, developed in this work, proved to be a powerful tool to study pileup effects and develop a more accurate analytical pileup model in the future.

7.3.2 Simulation at varying rate

The rate dependence of the pileup spectrum is now studied using four simulations at different input rates $R_{in} = 10$ kcps, 30 kcps, 100 kcps, and 300 kcps. The output spectrum of each simulation is fitted with the same method described in the previous section. Finally, the fitted pileup probabilities can be compared to the simplified analytic expectation from section 7.2.

All simulations use the same settings as described in the previous section (table 7.3) but with varying rates and 10^8 input events. The reduced number of input events compared to the previous simulation was chosen to reduce the computation time. The output spectra are compared in figure 7.11. As expected, the overall efficiency drops with increasing rate while the fraction of events in the pileup tail increases due to unresolved pileup events. Each spectrum is fitted with the model in equation 7.8, and the pileup amplitudes A_1, A_2, A_3, and A_4 are extracted and listed in table 7.5. The individual fits are shown in figures A.17, A.18, A.19, and A.20 in the appendix. For all four cases, the model shows a good agreement with the data and no significant structure is observed in the residuals. The residual structure, which was observed for $R_{in} = 100$ kcps in figure 7.10, is gone due to the reduce number of events in the spectrum. The amplitudes in table 7.5 are normalized to the number of input events in the simulation, considering the dead time from resets. For example, the amplitude $A_2 = 1.8\%$ means that the number of counts in the 2-fold pileup spectrum is 1.8% of the number of input events, which happened during the active phase of the detector.

Table 7.5: Pileup amplitudes A_i, obtained from fitting equation 7.8 to the output spectrum of the DAQ simulation at different rates. The individual fits are shown in section A.5.7 in the appendix. Errors are only shown if larger than the last digit and correspond to the 68 % central interval of the Bayesian output probability distribution.

R_{in}	A_1 no pileup	A_2 2-fold pileup	A_3 3-fold pileup	A_4 4-fold pileup
10 kcps	98 %	0.23 %	$3.6^{+0.4}_{-0.3} \cdot 10^{-6}$	$9^{+159}_{-9} \cdot 10^{-9}$
30 kcps	93 %	0.65 %	$3.5 \cdot 10^{-5}$	$1.2^{+4.0}_{-0.2} \cdot 10^{-7}$
100 kcps	77 %	1.8 %	$3.1 \cdot 10^{-4}$	$2.7^{+0.8}_{-0.4} \cdot 10^{-6}$
300 kcps	45 %	3.2 %	0.15 %	$5.3 \cdot 10^{-5}$
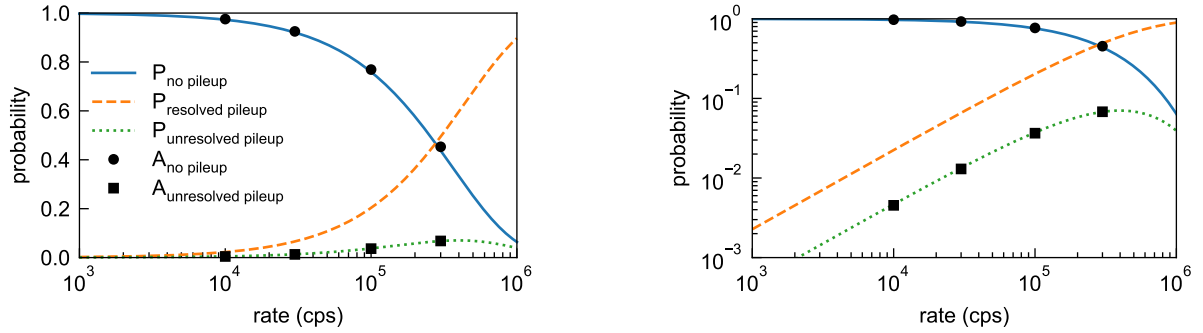
Figure 7.12: Comparison of pileup amplitudes $A_{\text{no pileup}}$ and $A_{\text{unresolved pileup}}$, extracted from fitting the DAQ simulation output spectra, and the analytical equations (labeled P) from section 7.2 in linear scale (left) and logarithmic scale (right).

The fitted pileup amplitudes cannot be compared directly to the analytical model presented in section 7.8. The following two quantities are defined to allow for a meaningful comparison:

$$A_{\text{no pileup}} = A_1 \tag{7.9}$$
$$A_{\text{unresolved pileup}} = 2A_2 + 3A_3 + 4A_4 \tag{7.10}$$

The second equation accounts for merging i input events in case of i-fold unresolved pileup. Figure 7.12 compares the pileup amplitudes (equation 7.9 and equation 7.10) with the analytic equations from section 7.2. The comparison shows a good agreement for all simulated input rates.

In summary, the study at varying rates confirms the estimated pileup probabilities: at 100 kcps, around 77 % of the input event end up in the primary tritium spectrum. The number of events in the unresolved pileup spectrum is 1.8 % compared to the number of input events. The remaining fraction is lost due to the rejection of resolved pileup.

7.3.3 Resets and dead time

The TRISTAN detector is operated in a pulsed reset mode (see section 4.2). During the reset, the acquisition is in an inhibited state and no events are recorded. This section addresses the expected reset periods and gives an estimate for the dead time. Three different options for the pulsed reset operation are studied in the following:
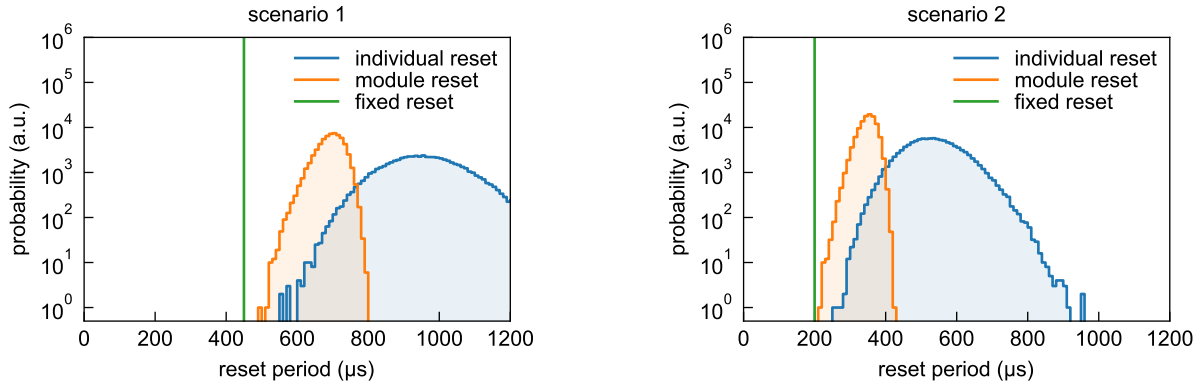
Figure 7.13: Simulated distribution of reset periods for the level sensitive reset. The simulation creates 10^8 events following the spectrum according to scenario 1 (left) or scenario 2 (right) with random timestamps at a rate of 100 kcps. After a cumulative energy of the 1st stage full scale range of 1.15 MeV a reset is triggered. The blue histogram shows the distribution of individual resets periods. The orange histogram shows the minimum reset period of each 166 resets, to simulate the module level reset. The green line corresponds to a fixed reset period of 450 μs (left) or 200 μs (right). Scenario 2 has a input spectrum with higher mean energy and thus requires fore frequent resetting.

- **Individual reset** The first option is the level-sensitive individual reset. In this case each pixel is reset when its first stage ramp exceeds a threshold voltage $V_{th} = 2.6$ V, slightly below the railing of the first stage output. Consequently, each ramp contains a total deposit energy of around 1.15 MeV (see table A.2). This mode cannot be used in the TRISTAN hardware, as a detector module has only one global reset line. Thus, this option is studied here only for completeness.
- **Module reset** When the detector is operated with the level-sensitive module reset option, the reset is applied synchronously to all 166 pixels of one detector module. The reset is triggered when the first pixel crosses $V_{th} = 2.6$ V with its 1st stage ramp. In this reset option, the sequential "or" logic of the SAT_OUT signal of ETTORE is used.
- **Fixed reset** When the detector is operated with the fixed reset option, the reset is applied synchronously to all 166 pixel of one detector module with a fixed frequency. The reset frequency must be chosen high enough, so that the probability of a saturating ramp within a reset period is negligible.

The use of the fixed reset has advantages and disadvantages compared to the level sensitive module reset:

$\oplus$ With fixed reset, the resets are deterministic. Therefore, the fraction of dead time from the resets is fixed and does not depend on the input rate and spectrum.

$\oplus$ With fixed reset, the system is more robust against broken pixels. In level sensitive module reset, a single malfunctioning pixel can disturb the resetting of the entire module.

$\ominus$ With fixed reset, the reset period must be chosen smaller than it is on average with the level sensitive module reset option. Thus, the fraction of dead time is in general higher.

The distribution of the reset duration obtained with the different reset options depends on the input spectrum. In the following, two different scenarios for the input spectrum are compared: "scenario 1" with a mean energy of 12.0 keV and "scenario 2" with a mean energy of 21.4 keV, corresponding to a case without post acceleration and with 20 keV post acceleration, respectively. The spectrum of
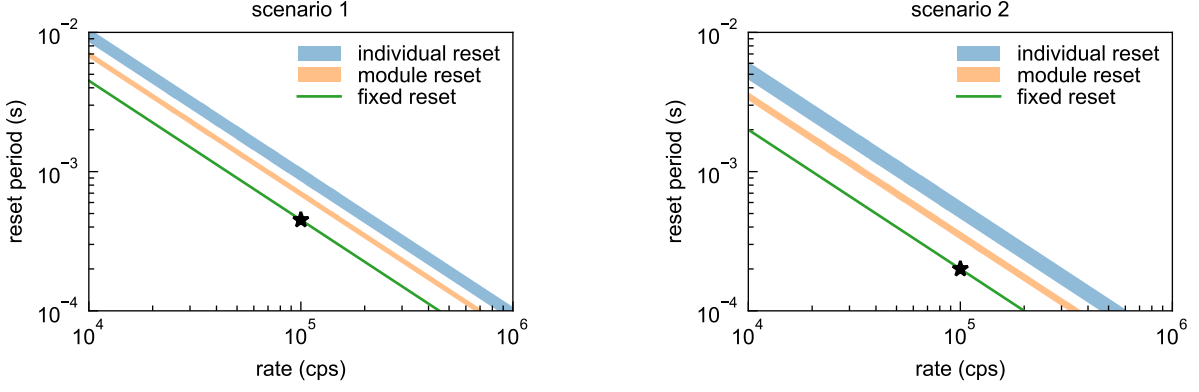
Figure 7.14: Simulated reset period of the TRISTAN detector as a function of the rate. In the level sensitive case "individual reset" (blue) and "module reset" (orange), the band indicates the 68 % central interval. Note that the reset distribution is not symmetric (see figure 7.13). The "fixed reset" case (orange) uses equation 7.11.

scenario 2 is shown in figure A.21 in the appendix. Figure 7.13 shows the simulated distributions of the reset duration for both scenarios.

The level sensitive reset options "individual reset" and "module reset" show a slightly asymmetric distribution. The fixed reset period is chosen below the minimal occurring reset duration in the level-sensitive case (450 µs for scenario 1 and 200 µs for scenario 2). These reset periods were obtained with an input rate $R_{in} = 100$ kcps. If a different rate is used, the product of the fixed reset period T_{reset} and the rate must stay constant:

$$T_{reset} \cdot R_{in} = \overline{N}_{evt} = \text{const.} \tag{7.11}$$

$\overline{N}_{evt}$ denotes the expected number of events per reset period and is $\overline{N}_{evt} = 45$ and $\overline{N}_{evt} = 20$ for scenario 1 and scenario 2, respectively. Figure 7.14 shows the rate dependence of the reset duration for both scenarios.

The overall amount of dead time from resets and pileup rejection is now simulated for the fixed reset option. The simulation uses `DAQsim` with the input spectrum scenario 2 and a fixed reset period according to equation 7.11. All other parameters are as used previously and listed in table 7.3. Each reset in the trace-level simulation is assumed to cause a dead time of $T_{inhibit} = 20$ µs. This value for $T_{inhibit}$ is only a rough estimate. The final value of $T_{inhibit}$ depends on how fast the waveform settles after a reset. As some variations of the settling time were observed in the past in various setups with different cabling, the value can be given only after a first test of the detector in its final detector environment.

Besides the dead time from the reset due to $T_{inhibit}$, there is also a dead time associated to the rejection of pileup, as explained in section 7.2. The resulting overall dead time budget, extracted from eight trace-level simulations of various rates ($R_{in} = 1$ kcps to 300 kcps) is shown in figure 7.15. Both the dead time form $T_{inhibit}$ and the dead time from pileup rejection scale linearly with the input rate and are of similar magnitude. At $R_{in} = 100$ kcps, the total dead time is around 30 %.

Note that result in figure 7.15 assumes that the reset has a fixed period, which is adapted to the input rate according to equation 7.11. If the reset period is not adjusted to the rate, the dead time
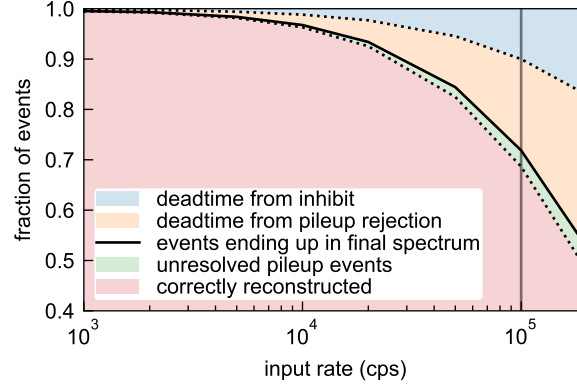
Figure 7.15: Simulated amount of dead time. The y-axis gives the fraction of input events after applying the dead time from $T_{\text{inhibit}} = 20\,\mu s$ and the pileup rejection. The reset period was set according to equation 7.11 with $\overline{N}_{\text{evt}} = 20$. The parameters for the trace-level simulation were chosen according to table 7.3.

from T_{inhibit} does not depend on the rate. The reset period then has to be chosen according to the highest possible rate, which is non-optimal for the amount of dead time at lower input rates.

7.3.4 Non-perfect exponential deconvolution

The exponential deconvolution, which was shortly introduced in section A.4.4, is a signal processing step that compensates for the exponential decay of the second stage of ETTORE. As illustrated in the appendix figure A.15, the exponential deconvolution has two parameters: c_1, and offset. The parameter offset must be adjusted to the baseline of the digitized signal. c_1 must be set according to the constant of the pulses. With a correctly configured exponential deconvolution, the trapezoidal filter output returns to zero after the trapezoid, which is essential to limit the amount of pileup. This, however, is only true if the two parameters offset and c_1 are tuned precisely to the baseline and decay constant of the digitized pulses. This section investigates the influence of an incorrectly set offset and τ on the spectroscopic performance by trace-level simulations with `DAQsim`.

Parameter offset In order to study the influence of a wrongly set offset parameter, a trace-level simulation at an input rate of 100 kcps with monoenergetic events of 30 keV is done. The simulation creates pulses with the decay time $\tau = 15\,\mu s$ on a baseline at 5 % of ADC range, corresponding to offset $= 819\,\text{lsb}$. The signal processing, in contrast, is done with an offset deviation Δoffset and the correct parameter $c_1 = \frac{T_s}{\tau}$, where T_s is the sampling period of the ADC. All other parameters are as used previously and listed in table 7.3.

The simulated traces for five different Δoffset values of 160 lsb, -80 lsb, 0, 80 lsb, and 160 lsb are shown in figure 7.16. Figure 7.17 shows the simulated output spectra of the simulations, and figure 7.18 shows the dependency of the peak position and resolution (FWHM) on the offset.

It is observed that the effect of a wrongly set offset is a slope s in the exponential deconvolution output, given by

$$s = \frac{\Delta\text{offset} \cdot c_1}{T_s} = \frac{\Delta\text{offset}}{\tau}. \tag{7.12}$$

This relation can also be directly derived from the schematic of the exponential deconvolution in the appendix figure A.15. After the trapezoidal filter, the slope corresponds to a shift of the

140
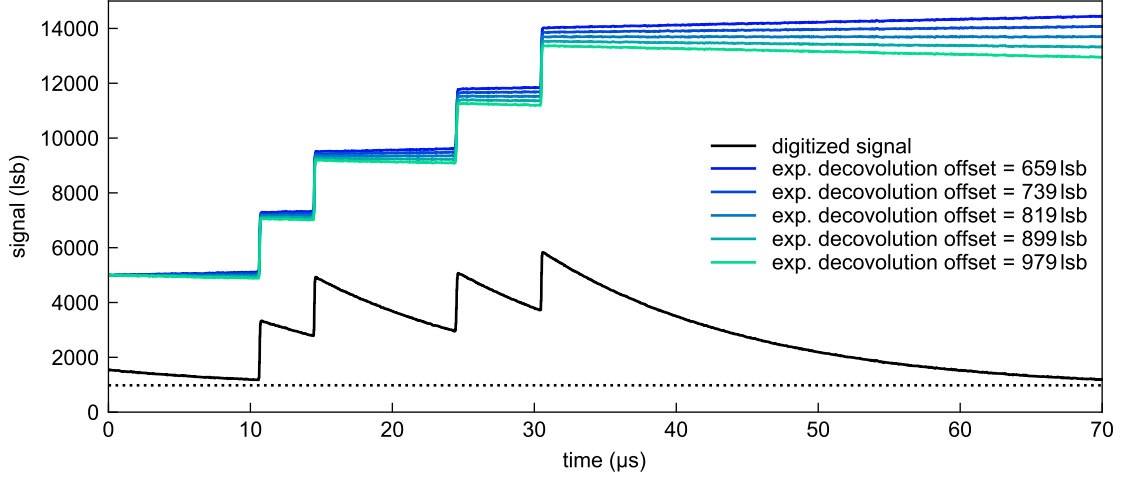
Figure 7.16: Simulated signal after digitization (black) and after exponential deconvolution to study the influence of parameter offset. The signals correspond to labels Ⓒ and Ⓓ in figure 7.2. Five simulations with varying offset parameters are compared. The correct value for offset is 819 lsb.
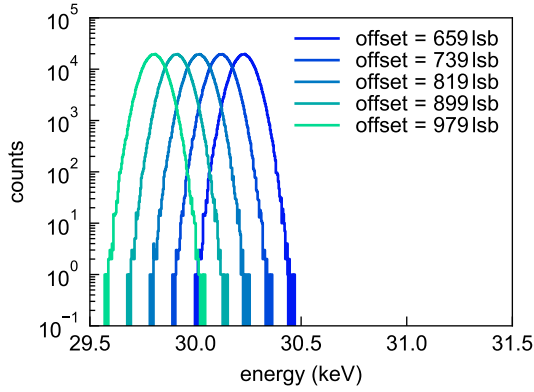
Figure 7.17: Influence of the offset parameter in the exponential deconvolution on the output spectrum of the trace-level simulation with a 30 keV, monoenergetic input spectrum.
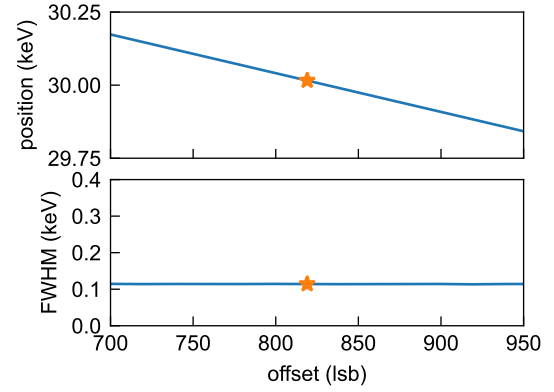
Figure 7.18: Simulation peak position and FWHM of the output spectra from figure 7.17. The star marks the nominal offset value, for which the true peak position at 30 keV is measured.

trapezoidal peak height of

$$\Delta E = s \cdot t_{\text{window dist}} = \Delta\text{offset} \frac{\tau_{\text{peaking}} + \tau_{\text{gap}}}{\tau}. \tag{7.13}$$

Here, $t_{\text{window dist}} = \tau_{\text{peaking}} + \tau_{\text{gap}}$ is the temporal distance of the two averaging windows of the trapezoidal filter. The resulting peak shift ΔE for the case where $\Delta\text{offset} = 160\,\text{lsb}$ (or 2.2 keV, see table A.2) is $\Delta E = 15.4\,\text{lsb}$ (or 212 eV). The offset parameter does not affect the energy resolution. This means that the calibration can fully compensate a wrongly set but constant offset parameter. It is more critical if the offset value varies over time. In this case, the output peak broadening is suppressed by $\frac{\tau_{\text{peaking}} + \tau_{\text{gap}}}{\tau} \approx 10$, such that a fluctuation of the baseline by 100 eV or 0.88 mV leads to a peak broadening of around 10 eV.

During measurements done for this work, no significant fluctuations or drifts of the second stage baseline value have been observed in the hardware. If relevant drifts appear in the future, a possible
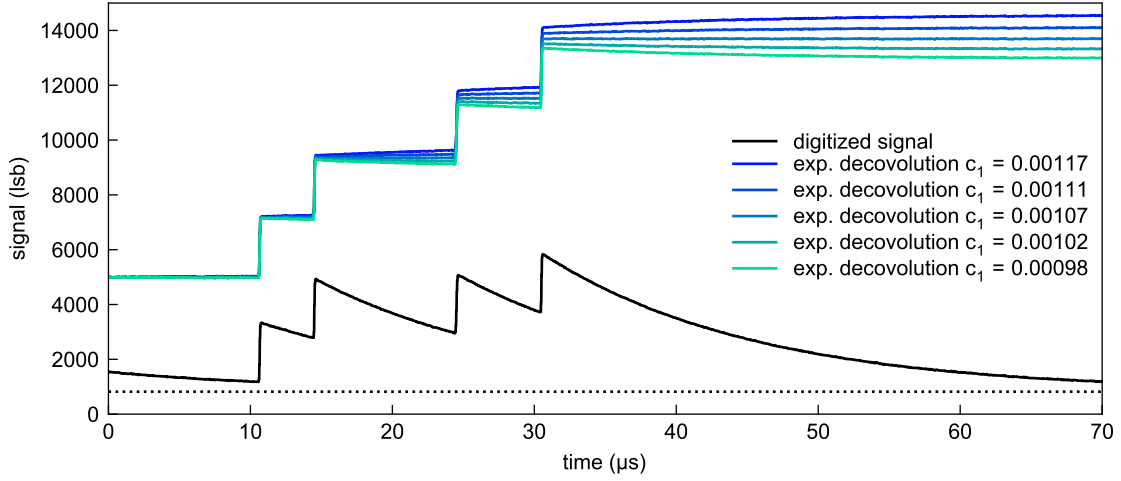
Figure 7.19: Simulated signal after digitization (black) and signal after exponential deconvolution to study the influence of parameter c_1. The signals correspond to labels Ⓒ and Ⓓ in figure 7.2. Five simulations with varying c_1 parameters are compared. The correct value for $c_1 = \frac{T_s}{\tau}$ is 0.00107.

counteract could be a frequent (for example, at every reset) measurement and setting of the offset parameter. The case where the offset is adjusted continuously during the acquisition using the baseline signals between pulses is often referred to as a baseline correction in DAQ settings (for example, [152]). At a TRISTAN acquisition, the signal usually does not return to the baseline between two pulses, and a simple baseline correction is impossible.

Effect of leakage current One of many possible origins for a shift in the second stage baseline is a fluctuation of the detector leakage current I_{leak}. The effect of a leakage current on the offset is $\Delta\text{offset} = w\tau\Delta I_{\text{leak}}$. When plugging this into equation 7.13, τ cancels out:

$$\Delta E = w(\tau_{\text{peaking}} + \tau_{\text{gap}})\Delta I_{\text{leak}}. \tag{7.14}$$

Here, $w = 3.63\,\text{eV/e}$ is the pair creation energy in silicon. With default parameters, a change of the leakage by $1\,\text{pA}$ corresponds to a peak broadening of $\Delta E \approx 34\,\text{eV}$. The actual leakage current is expected to be more stable, as the absolute value of the leakage current is typically below $0.1\,\text{pA}$, see section 6.2.1. Therefore, no significant degradation of the energy resolution is expected due to a baseline shift from a varying leakage current.

Parameter c_1 The conclusion about the offset parameter could also have been derived solely analytically. Still, `DAQsim` provided a simple way to illustrate and confirm the effect. Similarly to the offset parameter, the influence of the parameter c_1 is now studied. For c_1, an analytic derivation is more complicated than for offset. Therefore, the effect is studied solely via `DAQsim`.

c_1 relates to the pulse decay constant τ via $c_1 = \frac{T_s}{\tau}$, where T_s is the sampling period. The same digitized signals from figure 7.16 are now processed with the correct parameter offset $= 819\,\text{lsb}$ but with a wrong value for c_1. The resulting traces for five different cases are shown in figure 7.19. The effect of the wrongly set c_1 parameter is a shape distortion in the exponential deconvolution output. Other than for the offset parameter, now the distortion is not a constant slope, but the slope depends on the absolute level of the digitized signal. This means that events that sit on the
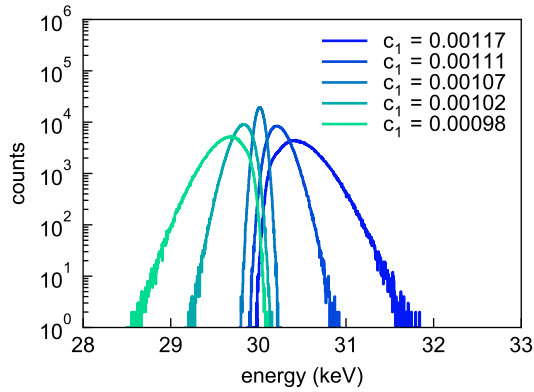
Figure 7.20: Influence of the c_1 parameter in the exponential deconvolution on the output spectrum of the trace-level simulation with a 30 keV, monoenergetic input spectrum at 100 kcps input rate.
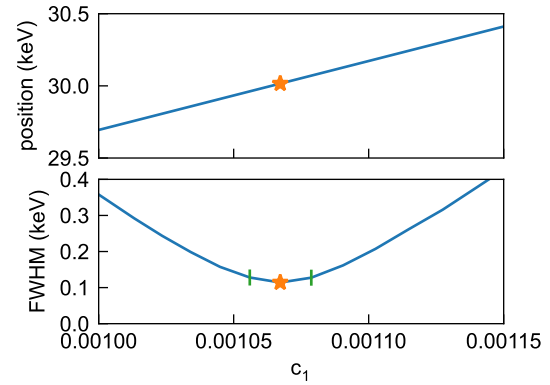
Figure 7.21: Peak position and FWHM of the output spectra from figure 7.20. The green bars indicate a variation of c_1 from the nominal value (star) by ±1%.

decaying tail of a previous event are generally more affected by the wrongly set c_1 parameter than events that are close to the baseline. This has two major implications:

- As the effect differs from event to event, the energy resolution worsens.
- As the baseline distribution changes with rate and input spectrum, this effect also changes with rate and input spectrum.

The trace-level simulation for this study uses an input rate of 100 kcps and a 30 keV, monoenergetic input spectrum. The resulting broadening of the energy resolution is shown in figure 7.20. One observes a combination of a peak shift and an asymmetric broadening. The dependency of the peak position and resolution (FWHM) on the c_1 parameter is shown in figure 7.21.

Conclusion In summary, it was found that the exact setting of the c_1 parameter, related to the decay constant τ, is much more critical for the spectroscopic performance compared to the offset parameter. A wrongly set offset has no negative effect if the baseline is stable over time. If the c_1 parameter is not set to the correct value, events that sit on the exponential tail of previous events are not reconstructed correctly. This leads to a rate and spectrum-dependent degradation of the energy resolution. A realistic goal for the accuracy of the c_1 parameter is to set it with a maximal deviation of 1%, as illustrated by the green bars in figure 7.21. In this case, the energy resolution of the readout system at an input count rate of 100 kcps and a 30 keV, monoenergetic input spectrum would increase from 114 eV FWHM to 127 eV FWHM. Note that this is the value for the energy resolution without Fano noise. If Fano noise were included, the energy resolution would change from 286 eV to 292 eV FWHM.

One implication of the 1% requirement for c_1 is that c_1 needs to be set individually on each channel of the DAQ system. Within the channels of one detector module, the decay constant can spread by almost 10% (for example, from 13.2 µs to 14.3 µs, see figure 6.9). A global setting on one detector module will not be sufficient. A dedicated calibration method will be necessary, which measures the optimal c_1 parameter for each channel. This calibration method could use pulse waveform data to extract c_1 or, alternatively, could scan c_1 for the best energy resolution at high rates. The second method, however, requires a monoenergetic calibration source with high rate for all pixels.
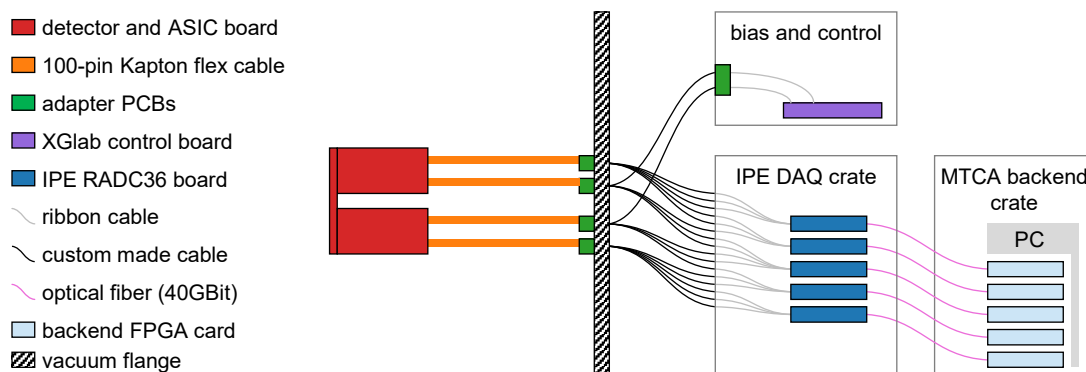
Figure 7.22: Schematic view of the detector readout at the Monitor Spectrometer tests.

7.4 Prototype tests at the KATRIN Monitor Spectrometer

In November and December 2022, a prototype of the TRISTAN DAQ system was tested at the Monitor Spectrometer setup next to the KATRIN beamline. These tests were conducted within the scope of this work. The main goals of the test campaign were:
- to check the analog signal integrity from detector to DAQ in a realistic environment,
- to find possible issues in the frontend-DAQ system before developing the final hardware, and
- to demonstrate the operation of the full chain of a TRISTAN measurement, including beamline, detector and data acquisition.

7.4.1 Experimental setup

The KATRIN Monitor Spectrometer [153, 75] is an MAC-E filter setup next to the KATRIN main beamline, which uses hardware of the former Mainz experiment [74]. It was used for high voltage monitoring in the first KATRIN measurement campaigns. Recently, it was also used as test environment for the TRISTAN detector [97]. This work focuses on the prototype tests of the TRISTAN DAQ system at the Monitor Spectrometer. Figure 7.22 shows a schematic sketch of the setup.

Detector   The setup uses a 166-pixel TRISTAN SDD array. This detector was the first full module operated at the Monitor Spectrometer. The detector was cooled and the bias parameters listed in table A.9 in the appendix.

Frontend DAQ   Due to the prototype phase, the detector bias and readout is split into separate electronic boards. The detector biasing and control board from XGlab provides all detector supply and control voltages. A set of five custom-developed RADC40 boards performs the data acquisition of all analog output signals of the detector. A picture of one RADC40 board is shown in figure 7.23a. Each RADC40 board has five 8-channel ADC daughter boards and digitizes 36 channels (4 ADC channels are not used). Five RADC40 boards are mounted in the IPE DAQ crate (see figure 7.23b), so that 180 channels can be read out in total, which is sufficient for one detector module. The digitized waveform data is sent via four 10 Gbit optical fibers per RADC40 board to the backend DAQ. The RADC40 board was originally designed for the readout of the current KATRIN FPD. Therefore, an interface board is necessary at the input side of the RADC board to adapt the voltage levels of the ETTORE output to the allowed input levels of the ADC boards.
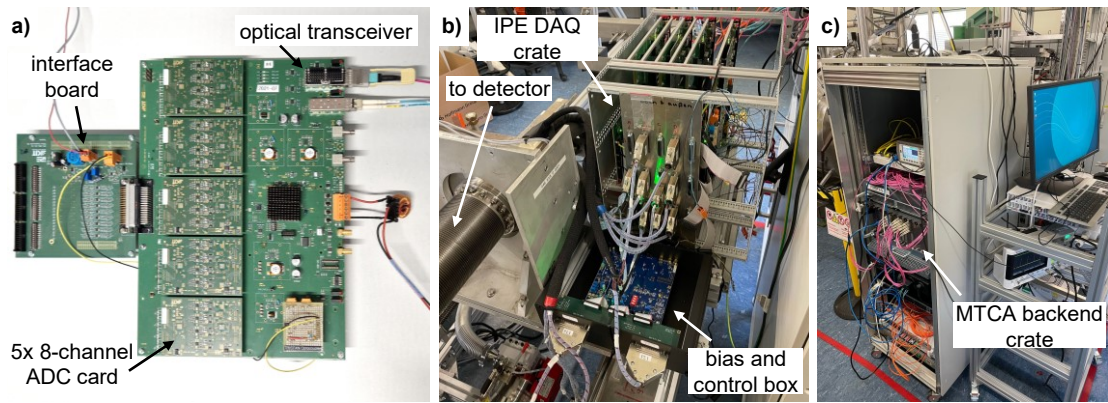
Figure 7.23: Photographs of the TRISTAN DAQ at the KATRIN Monitor Spectrometer. Shown are **a)** the RADC40 board, **b)** the frontend DAQ setup, and **c)** the backend DAQ setup.
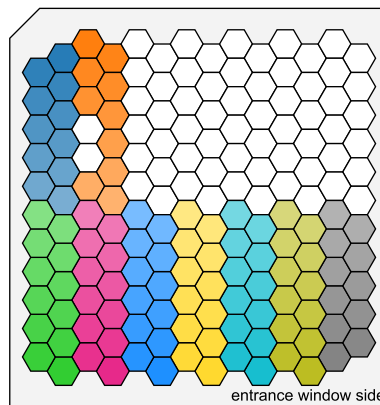
Figure 7.24: Pixel map of the 104 active pixels at the prototype DAQ tests at the Monitor spectrometer. The colormap is the same as in the frequency spectra and energy spectrum later in this section. White pixels were not connected.

Backend DAQ The fully digital backend DAQ receives, processes and saves waveform data from the optical fibers. It is implemented as five HGF-AMC cards[4] in a MicroTCA crate with a hub PC (see figure 7.23c). At the time of the tests, the online pulse height analysis was not yet fully tested in the backend FPGA firmware. Therefore, all data was acquired either in waveform mode or in event mode with waveform saving (see section A.4.5). This allows for an offline processing, but limits the acquisition to low input rates ($\mathcal{O}(10)$ cps per pixel) to not exceed the data throughput of the backend PC. For the main goals of the prototype test at the Monitor Spectrometer, this is not a problem.

At the time of the tests, not all 25 8-channel ADC boards were available. This restricted the readout to 104 channels. A map of the connected pixels is shown in figure 7.24.

7.4.2 Noise analysis

The electronic noise situation was investigated by capturing signal waveforms without events. Two short example snippets of digitized waveforms are shown in figure 7.25. The two snippets

---

[4]developed by DESY and KIT/IPE, see for example this poster.
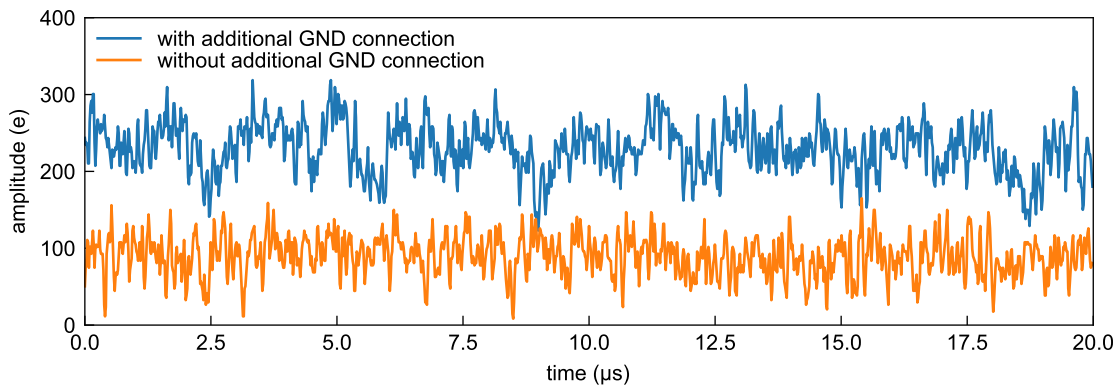
Figure 7.25: Two example waveforms with electronic noise of one detector channel at the Monitor Spectrometer. The sampling frequency is 62.5 MHz. The amplitude is equivalent charge at the anode in electrons e, using the electron spectrum for calibration. 1 e corresponds to one electron at the anode.

correspond to two different grounding scenarios. In scenario "with additional GND connection", a ground connection between the vacuum chamber at the detector flange and the frontend DAQ crate was present. In the scenario "without additional GND connection", this ground connection was removed, as an increased electronic noise was observed in the first tests. The increased noise is visible in figure 7.25 as increased fluctuations on a scale of several µs.

Figure 7.26 shows the noise power density spectrum for the two grounding scenarios. The noise power spectra show the continuous white noise from the preamplifier at around 10^{-4} e^2/Hz, with the cutoff from the anti-aliasing filter at around 10 MHz. Some lines are present at around 600 kHz and above. These lines can be associated with electric interference by switching DC-DC converters on the frontend DAQ. Although these lines are visible in the noise power density spectrum, they do not degrade the spectroscopic performance significantly. More critical are the additional lines at around 200 kHz to 300 kHz, which are visible in the scenario "with additional GND connection". In order to see the influence of the noise frequencies on the energy resolution, a noise curve is calculated from the waveform data. For that, a trapezoidal filter with time constant τ_{peaking} is applied to the noise waveforms, and the standard deviation of the output is calculated. Figure 7.26 shows the result for both grounding scenarios. The noise curves indicate a clear distortion from the expected shape for the "with additional GND connection" scenario, which can be related to the additional lines at around 200 kHz to 300 kHz in the noise power spectrum. The origin of these problematic noise frequencies was found by looking at the ground level of the frontend DAQ boards compared to the detector ground with an oscilloscope. The ground level had a strong (several 100 mV) oscillations at frequencies of 200 kHz to 300 kHz. These ground oscillations probably originate from a ground loop, although the exact mechanism is not fully understood. With the ground connection removed (scenario "with additional GND connection"), the oscillations are gone, and good noise performance is observed (see right noise curve plot in figure 7.27).

The noise investigations showed that a clean and proper grounding of the devices along the analog signal path is important. In this special case, removing a ground connection helped to substantially improve the noise situation.
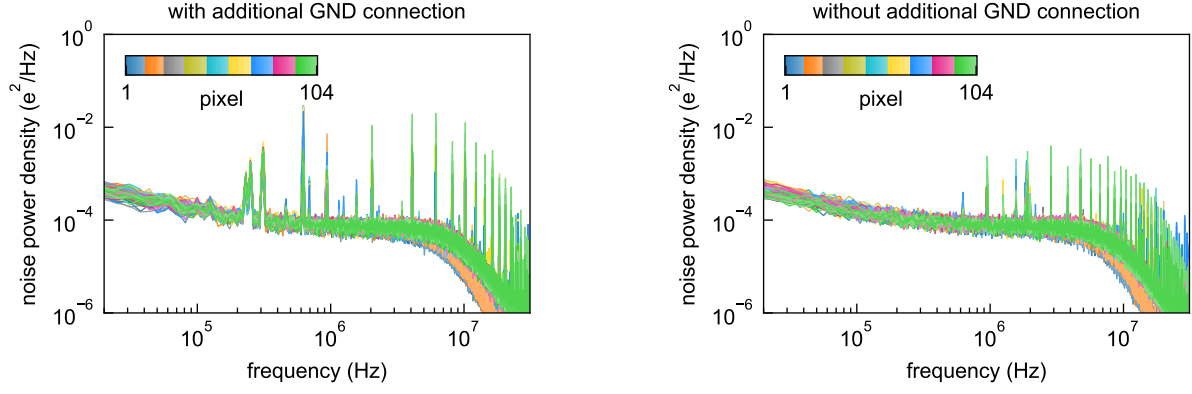
Figure 7.26: Noise power density spectra of the 104 active pixels. Each spectrum uses around 3.6 ms of waveform data and is calculated with the `scipy.signal.welch` algorithm. Two grounding scenarios are compared.
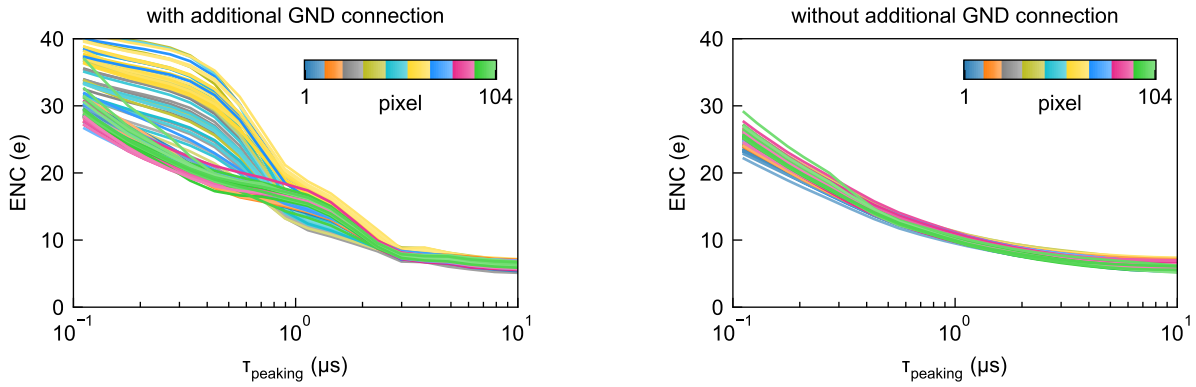
Figure 7.27: Energy resolution in equivalent noise charge (ENC) as a function of the peaking time τ_{peaking}. The calculation uses a trapezoidal filter with fixed $\tau_{\text{gap}} = 480$ ns. Two grounding scenarios are compared.

7.4.3 Electron spectra measurements

A spectrum measurement of monoenergetic electrons was performed to test the response of the detector and readout system to electrons. The electron source is an implanted ^{83}Rb source [114], which is located at the source section of the Monitor Spectrometer beamline. The source emits conversion electrons from the nuclear decay of ^{83m}Kr. The spectrum has several narrow lines with an energy up to 32.137 keV [113]. An additional accelerating source potential increases the electron energy by 500 eV. The MAC-E filter of the Monitor Spectrometer is used to only transmit electrons above 32.5 keV. The resulting electron spectrum at the detector is almost monoenergetic with an energy of 32.637 keV.

The measurement with a 12 h duration used the event mode of the backend DAQ, where a short waveforms snippet is saved for each event. The pulse height of each event was determined by offline processing with a trapezoidal filter with peaking time $\tau_{\text{peaking}} = 0\,\mu$s and $\tau_{\text{gap}} = 0\,\mu$s.

Figure 7.28 shows the count rate and the FWHM of the electron peak. The corresponding electron spectra are shown in figure 7.29. The count rate distribution fits to the expectation from the ^{83}Rb surface activity. The energy resolution of 330 eV FWHM aligns with measurements of the same system with a commercial CAEN VX2740 data acquisition system [143]. There is an area
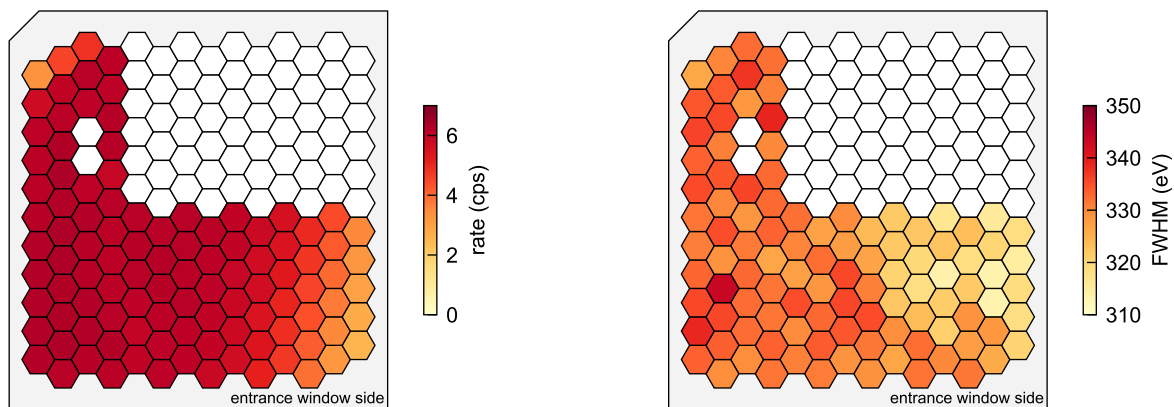
Figure 7.28: Pixel maps of the event rate (left) and the main peak FWHM (right) in the electron spectrum measurement at the Monitor Spectrometer
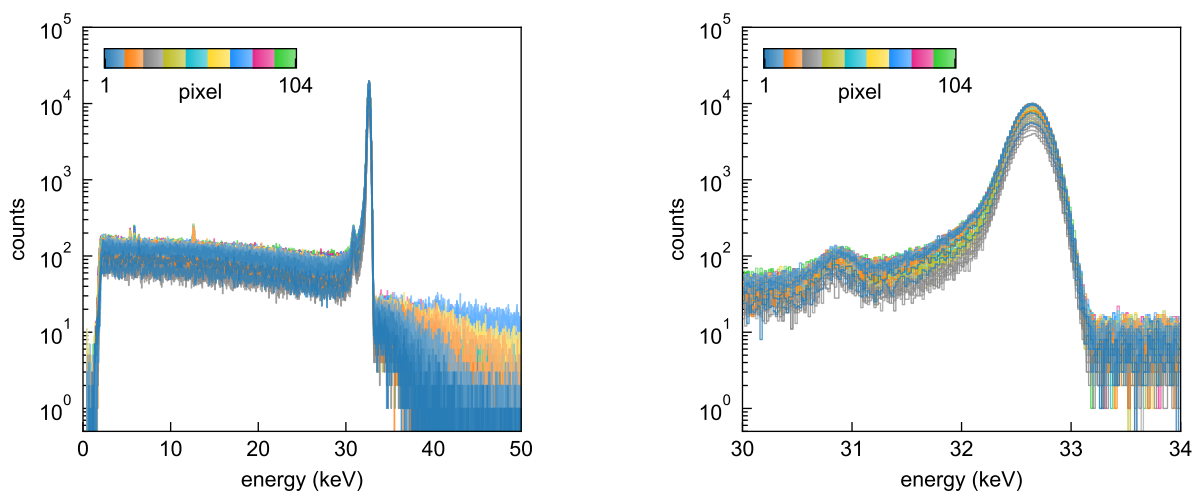
Figure 7.29: Electron spectrum measured at the Monitor Spectrometer. All 104 active channels are super-imposed. The right plot zooms to the main electron peak and the silicon escape peak at 30.9 keV. A simple linear calibration, which centers the main electron peak to 32.637 keV, is used.

on the right half of the detector where the energy resolution is superior to the rest of the surface. This intrinsic effect of the used detector chip is probably attributed to some entrance window contamination. More details about measurements of this detector with the CAEN DAQ system at the Monitor Spectrometer are found in [143, 97], where, besides others, the entrance window effect is addressed.

The shape of the electron response in figure 7.29 looks very homogeneous over the pixels. The main peak, silicon escape peak, and a tail from backscattering are visible. Furthermore, a tail towards higher energies is observed, which originates from higher energy electrons up to > 100 keV emitted in the ^{83}Rb decay. The transport of these electrons from the source to the detector is not adiabatic due to the large kinetic surplus energy in the spectrometer. This explains the pixel-dependent shape of the tail towards high energies, which is observed in figure 7.29.

7.5 Summary

This work contributed to the development and specification of the DAQ for the TRISTAN detector. A key challenge of the pulse-height analysis for TRISTAN is achieving a clear understanding of the pileup spectrum at the high target rate of 100 kcps per channel.

The first step was defining an algorithm to reject pileup events. Subsequently, an analytic model for the remaining pileup contribution to the acquired spectrum was derived. With the proposed filter design, about 1.8 % of the final spectrum counts are expected to come from pileup.

Next, the trace-level simulation tool `DAQsim` was developed, which simulates the entire signal chain of a TRISTAN measurement. The first use-case of `DAQsim` was studying the pileup spectrum shape. It was shown that an analytical convolution model could accurately describe the pileup spectrum when DAQ filter parameters are set correctly.

Two more studies, both using `DAQsim`, were performed. The first study simulated the dead time in the TRISTAN acquisition, showing 30 % dead time at 100 kcps due to 10 % from detector resets and 20 % from pileup rejection. A second study simulated the influence of a non-perfect exponential devolution setting. It was shown that the decay constant is the most critical parameter. The decay constant must meet the hardware value of the ETTORE ASIC by 1 % to prevent a significant worsening of the energy resolution. `DAQsim` proved to be a versatile tool, which can be used for many studies of DAQ-related systematic effects for TRISTAN in the future.

Finally, this work also contributed to the DAQ hardware development. A test of the prototype DAQ at the KATRIN monitor spectrometer assessed the first combination of a TRISTAN detector and the remote ADC readout concept. After a minor adjustment to the grounding scheme, the signal integrity and quality of the digitized signals were deemed satisfactory. This adjustment highlighted the importance of a proper grounding design.

The electron spectrum of 32 keV electrons from ^{83m}Kr decay, measured with the TRISTAN detector and the prototype DAQ, looks promising and confirms the excellent energy resolution and homogeneity of the detector response. While this measurement validated the DAQ performance at low count rates, the high-rate performance remains to be tested once the final hardware is completed.

8 Conclusions

Sterile neutrinos are a minimal extension of the Standard Model of particle physics. If they have masses in the keV range, they could contribute to the abundance of dark matter in the universe. A precise measurement of the spectral shape of β-decay provides a method to search for keV sterile neutrinos in laboratory experiments. A key challenge in these searches the understanding of all experimental factors that could influence the measured spectral shape. This thesis focused on improving the understanding of the TRISTAN Silicon Drift Detector (SDD), helping to fully exploit its potential in the search for sterile neutrinos at the KATRIN experiment. The main results of this work are summarized below.

A custom spectrum model and analysis code were developed to perform a **sensitivity study** for the keV sterile neutrino search via tritium β-decay. The work focused on the effect of fundamental nuisance parameters like calibration and energy resolution. Their influence on the sensitivity could be shown in an illustrative way by comparing spectral residuals. Furthermore, the influence of the energy region-of-interest for the analysis was studied, indicating that a large region-of-interest is, in general, beneficial as it helps to constrain nuisance parameters. However, this also brings the danger of underestimating the effect of nuisance parameters in a sensitivity study.

To advance the **understanding of the SDD signals**, the simulation code `driftsim` was developed within this work. This software simulates the electric fields based on the realistic detector geometry. Subsequently, the drift of an event charge cloud is simulated by a Monte Carlo approach based on single drifting electrons. The simulation reveals that the drift times in the detector can reach up to around 200 ns if the incident location of the primary particle is at the border between two pixels. The signal 10 % to 90 % rise time reaches up to 80 ns, in this case. In addition to the studies with `driftsim`, the TRISTAN amplifier circuit was analyzed, showing that the overall rise time of output signals is significantly affected by the line capacitance between the SDD and the ETTORE ASIC. Finally, a comprehensive model of the noise on the detector signals was developed, predicting an equivalent noise charge of ENC ≈ 11.5 electrons at a trapezoidal peaking time of 960 ns. This reliable noise model, which successfully reproduces the measured data, is an important achievement for understanding the TRISTAN detector performance.

To enable the experimental characterization of the TRISTAN detector, the **development of new calibration tools** was necessary. This includes the development of a custom electron gun, providing monoenergetic electrons at high rates up to more than 100 kcps. The electron gun, based on the thermionic emission of electrons from a tantalum filament, was explicitly designed to characterize the TRISTAN detector in flexible experimental configurations. Design highlights include an off-axis mounting to mitigate the detector illumination with light and a coil system to magnetically steer the electron beam. After the successful commissioning, the electron gun was used for detector characterizations and was established as a central tool for studying TRISTAN detector modules. In addition to the electron gun, a pulsed light characterization approach was explored. This approach induces charge clouds in the detector volume by a short, focused light pulse at a defined time and location. The measurement of the resulting pulse shapes yields information about the drift and

signal formation in the TRISTAN SDD. A measurement using the new approach was performed, and the validity of the SDD signal simulation was confirmed.

The **experimental characterization** of the TRISTAN detector was a central part of this work. The measurements first focused on the general performance parameters of the 166-pixel TRISTAN detector module. The studies include the energy resolution, the pulse shape, the leakage current, and the electron response. An excellent noise performance of $\text{ENC} = 11.3^{+1.6}_{-0.9}$ e was measured homogeneously over all pixels of a detector module. Most notably, a method to measure and quantify crosstalk between pixels in the TRISTAN detector was developed. The investigation showed that the capacitive coupling of readout lines on the monolithic SDD chip causes significant crosstalk, which influences the spectroscopic performance of the detector at high rates. As a consequence of the findings, the design of the readout lines on the SDD was improved, which reduced the effect of crosstalk significantly. After these successful design improvements, the final crosstalk situation in the 166-pixel detectors was analyzed, identifying a remaining crosstalk effect from the readout electronics. As the mitigation of this remaining crosstalk was not possible, the impact of the crosstalk on the spectroscopic performance was investigated by a dedicated trace-level Monte Carlo simulation. The simulation indicates that crosstalk will cause a non-Gaussian broadening of the energy spectrum and a reduction in detection efficiency. In addition to crosstalk, the charge sharing effect, which occurs at the boundaries between adjacent pixels, was studied. An empirical model and a measurement concept were developed to quantify charge sharing and its influence on the detector response. A good agreement of model and data could be shown, with a characteristic charge sharing width of $\sigma_{cs} = (17.08 \pm 0.11)\,\mu\text{m}$ for 20 keV electrons. The charge sharing width is an important input parameter for sensitivity studies and the final data analysis.

Finally, this work contributed to the **development and simulation of the data acquisition system** for the TRISTAN detector. A key challenge of the pulse-height analysis in the DAQ system is achieving a clear understanding of the pileup spectrum at the high target rate. An algorithm for the treatment of pileup was presented based on a fast trigger filter for identifying and rejecting pileup events. It was observed that the implementation of a trigger holdoff time $\tau_{\text{holdoff}} \approx 240\,\text{ns}$ is required to get a well-defined pileup spectrum. With this setting, about 1.8 % of the final spectrum counts are expected to come from pileup at the nominal rate of 100 kcps per channel. In the next step, the trace-level DAQ simulation code `DAQsim` was developed, which simulates the entire signal chain of a TRISTAN measurement. This simulation showed that an analytical convolution model accurately describes the pileup spectrum when the DAQ filter parameters are set correctly. Additionally, the dead time in the TRISTAN acquisition was extracted, showing around 30 % dead time at 100 kcps. The deadtime originates from detector resets (10 %) and from the rejection of pileup events (20 %). Finally, the hardware of a DAQ prototype was tested. The measurement campaign at the KATRIN monitor spectrometer assessed the combination of a TRISTAN detector and the remote ADC readout concept for the first time. The successful tests confirmed the signal integrity between the detector and DAQ and demonstrated the excellent energy resolution and homogeneity of the detector response.

In summary, this work contributed to a deeper understanding of the TRISTAN detector performance through detailed measurements and simulations. Furthermore, the presented work on calibration sources and the data acquisition system has enhanced the overall experimental framework of the TRISTAN detector. Both are important prerequisites for the upcoming search for keV sterile neutrinos at the KATRIN experiment.

Bibliography

[1]   Carlo Giunti and Chung Wook Kim. *Fundamentals of neutrino physics and astrophysics*. Repr. Oxford [u.a.]: Oxford Univ. Press, 2012. 710 pp. ISBN: 9780198508717 (cit. on p. 1).

[2]   C. S. Wu et al. "Experimental Test of Parity Conservation in Beta Decay". In: *Physical Review* 105.4 (Feb. 1957), pp. 1413–1415. ISSN: 0031-899X. DOI: 10.1103/physrev.105.1413 (cit. on p. 1).

[3]   M. Goldhaber, L. Grodzins, and A. W. Sunyar. "Helicity of Neutrinos". In: *Physical Review* 109.3 (Feb. 1958), pp. 1015–1017. ISSN: 0031-899X. DOI: 10.1103/physrev.109.1015 (cit. on p. 1).

[4]   R. N. Mohapatra and A. Y. Smirnov. "Neutrino Mass and New Physics". In: (2006). DOI: 10.48550/ARXIV.HEP-PH/0603118 (cit. on p. 1).

[5]   R L Workman et al. "Review of Particle Physics". In: *Progress of Theoretical and Experimental Physics* 2022.8 (Aug. 2022). ISSN: 2050-3911. DOI: 10.1093/ptep/ptac097 (cit. on pp. 2, 4, 6, 7).

[6]   Raymond Davis, Don S. Harmer, and Kenneth C. Hoffman. "Search for Neutrinos from the Sun". In: *Physical Review Letters* 20.21 (May 1968), pp. 1205–1209. ISSN: 0031-9007. DOI: 10.1103/physrevlett.20.1205 (cit. on p. 2).

[7]   V. Gribov and B. Pontecorvo. "Neutrino astronomy and lepton charge". In: *Physics Letters B* 28.7 (Jan. 1969), pp. 493–496. ISSN: 0370-2693. DOI: 10.1016/0370-2693(69)90525-5 (cit. on p. 2).

[8]   A. Yu. Smirnov. *Solar neutrinos: Oscillations or No-oscillations?* 2016. DOI: 10.48550/ARXIV.1609.02386 (cit. on p. 2).

[9]   Q. R. Ahmad et al. "Direct Evidence for Neutrino Flavor Transformation from Neutral-Current Interactions in the Sudbury Neutrino Observatory". In: *Physical Review Letters* 89.1 (June 2002), p. 011301. ISSN: 1079-7114. DOI: 10.1103/physrevlett.89.011301 (cit. on p. 2).

[10]   K. Eguchi et al. "First Results from KamLAND: Evidence for Reactor Antineutrino Disappearance". In: *Physical Review Letters* 90.2 (Jan. 2003), p. 021802. ISSN: 1079-7114. DOI: 10.1103/physrevlett.90.021802 (cit. on p. 2).

[11]   Y. Fukuda et al. "Evidence for Oscillation of Atmospheric Neutrinos". In: *Physical Review Letters* 81.8 (Aug. 1998), pp. 1562–1567. ISSN: 1079-7114. DOI: 10.1103/physrevlett.81.1562 (cit. on p. 2).

[12]   Ivan Esteban et al. "The fate of hints: updated global analysis of three-flavor neutrino oscillations". In: *Journal of High Energy Physics* 2020.9 (Sept. 2020). ISSN: 1029-8479. DOI: 10.1007/jhep09(2020)178 (cit. on p. 3).

[13]   Ivan Esteban et al. *NuFIT 5.3*. 2024. URL: www.nu-fit.org (cit. on p. 3).

[14] David O. Caldwell. *Current Aspects of Neutrino Physics*. Description based on publisher supplied metadata and other sources. Berlin, Heidelberg: Springer Berlin / Heidelberg, 2001. 1349 pp. ISBN: 9783662045978 (cit. on p. 2).

[15] André de Gouvêa. "Neutrino Mass Models". In: *Annual Review of Nuclear and Particle Science* 66.1 (Oct. 2016), pp. 197–217. ISSN: 1545-4134. DOI: 10.1146/annurev-nucl-102115-044600 (cit. on pp. 2, 3, 6).

[16] S F King. "Neutrino mass models". In: *Reports on Progress in Physics* 67.2 (Dec. 2003), pp. 107–157. ISSN: 1361-6633. DOI: 10.1088/0034-4885/67/2/r01 (cit. on p. 3).

[17] Julien Lesgourgues and Sergio Pastor. "Neutrino cosmology and Planck". In: *New Journal of Physics* 16.6 (June 2014), p. 065002. ISSN: 1367-2630. DOI: 10.1088/1367-2630/16/6/065002 (cit. on p. 4).

[18] Lothar Oberauer. *Neutrinophysik. Grundlagen, Experimente und aktuelle Forschung*. Ed. by Judith Oberauer. 1. Aufl. 2019. Berlin, Heidelberg: Springer Berlin Heidelberg, 2019. 1182 pp. ISBN: 9783662593356 (cit. on p. 4).

[19] Isabelle Tanseri et al. "Updated neutrino mass constraints from galaxy clustering and CMB lensing-galaxy cross-correlation measurements". In: *Journal of High Energy Astrophysics* 36 (Nov. 2022), pp. 1–26. ISSN: 2214-4048. DOI: 10.1016/j.jheap.2022.07.002 (cit. on p. 4).

[20] N. Aghanim et al. "Planck2018 results: VI. Cosmological parameters". In: *Astronomy and Astrophysics* 641 (Sept. 2020), A6. ISSN: 1432-0746. DOI: 10.1051/0004-6361/201833910 (cit. on p. 4).

[21] DESI Collaboration et al. *DESI 2024 VI: Cosmological Constraints from the Measurements of Baryon Acoustic Oscillations*. 2024. DOI: 10.48550/ARXIV.2404.03002 (cit. on p. 4).

[22] Kai Zuber. *Neutrino physics*. Second edition. Series in high energy physics, cosmology, and gravitation. Boca Raton: CRC Press, Taylor and Francis Group, 2012. 1440 pp. ISBN: 9781420064728 (cit. on p. 4).

[23] Christoph Wiesinger. "No neutrinos not found". PhD thesis. Technical University of Munich, 2020 (cit. on p. 4).

[24] L. Pertoldi. "The first year of LEGEND-200 physics data in the quest for $0\nu\beta\beta$ decay". In: Neutrino Conference (Milano). 2024 (cit. on p. 4).

[25] Itaru Shimizu. "Results from KamLAND-Zen". In: Neutrino Conference (Milano). 2024 (cit. on p. 4).

[26] Juan José Gómez-Cadenas et al. "The search for neutrinoless double-beta decay". In: *La Rivista del Nuovo Cimento* (Jan. 2024). ISSN: 1826-9850. DOI: 10.1007/s40766-023-00049-2 (cit. on p. 4).

[27] M. Agostini et al. "Final Results of GERDA on the Search for Neutrinoless Double-β Decay". In: *Physical Review Letters* 125.25 (Dec. 2020), p. 252502. ISSN: 1079-7114. DOI: 10.1103/physrevlett.125.252502 (cit. on p. 4).

[28] E W Otten and C Weinheimer. "Neutrino mass limit from tritium β decay". In: *Reports on Progress in Physics* 71.8 (July 2008), p. 086201. ISSN: 1361-6633. DOI: 10.1088/0034-4885/71/8/086201 (cit. on pp. 4, 5).

[29] G. Drexlin et al. "Current Direct Neutrino Mass Experiments". In: *Advances in High Energy Physics* 2013 (2013), pp. 1–39. ISSN: 1687-7365. DOI: 10.1155/2013/293986 (cit. on pp. 4, 5).

[30] Thomas J. Loredo and Donald Q. Lamb. "Bayesian analysis of neutrinos observed from supernova SN 1987A". In: *Physical Review D* 65.6 (Feb. 2002), p. 063002. ISSN: 1089-4918. DOI: 10.1103/physrevd.65.063002 (cit. on p. 4).

[31] M. Aker et al. *Direct neutrino-mass measurement based on 259 days of KATRIN data*. 2024. DOI: 10.48550/ARXIV.2406.13516 (cit. on pp. 5, 12).

[32] Project 8 Collaboration et al. *The Project 8 Neutrino Mass Experiment*. 2022. DOI: 10.48550/ARXIV.2203.07349 (cit. on p. 5).

[33] L. Gastaldo et al. "The electron capture in 163Ho experiment – ECHo". In: *The European Physical Journal Special Topics* 226.8 (June 2017), pp. 1623–1694. ISSN: 1951-6401. DOI: 10.1140/epjst/e2017-70071-y (cit. on p. 5).

[34] M. Borghesi et al. "An updated overview of the HOLMES status". In: *Nuclear Instruments and Methods in Physics Research Section A: Accelerators, Spectrometers, Detectors and Associated Equipment* 1051 (June 2023), p. 168205. ISSN: 0168-9002. DOI: 10.1016/j.nima.2023.168205 (cit. on p. 5).

[35] Matteo Borghesi and the HOLMES collaboration. *The first neutrino mass limit of HOLMES*. Poster at Neutrino Conference. Milano, June 21, 2024 (cit. on p. 5).

[36] A. Aguilar et al. "Evidence for neutrino oscillations from the observation of $\overline{\nu}_e$ appearance in a $\overline{\nu}_\mu$ beam". In: *Physical Review D* 64.11 (Nov. 2001), p. 112007. ISSN: 1089-4918. DOI: 10.1103/physrevd.64.112007 (cit. on p. 6).

[37] A. A. Aguilar-Arevalo et al. "Updated MiniBooNE neutrino oscillation results with increased data and new background studies". In: *Physical Review D* 103.5 (Mar. 2021), p. 052002. ISSN: 2470-0029. DOI: 10.1103/physrevd.103.052002 (cit. on p. 6).

[38] G. Mention et al. "Reactor antineutrino anomaly". In: *Physical Review D* 83.7 (Apr. 2011), p. 073006. ISSN: 1550-2368. DOI: 10.1103/physrevd.83.073006 (cit. on p. 6).

[39] V. V. Barinov et al. "Results from the Baksan Experiment on Sterile Transitions (BEST)". In: *Physical Review Letters* 128.23 (June 2022), p. 232501. ISSN: 1079-7114. DOI: 10.1103/physrevlett.128.232501 (cit. on p. 6).

[40] M. A. Acero et al. *White Paper on Light Sterile Neutrino Searches and Related Phenomenology*. 2022. DOI: 10.48550/ARXIV.2203.07323 (cit. on p. 6).

[41] Jeffrey M. Berryman et al. "Statistical significance of the sterile-neutrino hypothesis in the context of reactor and gallium data". In: *Journal of High Energy Physics* 2022.2 (Feb. 2022). ISSN: 1029-8479. DOI: 10.1007/jhep02(2022)055 (cit. on p. 6).

[42] A. Boyarsky et al. "Sterile neutrino Dark Matter". In: *Progress in Particle and Nuclear Physics* 104 (Jan. 2019), pp. 1–45. ISSN: 0146-6410. DOI: 10.1016/j.ppnp.2018.07.004 (cit. on pp. 6–8).

[43] Takehiko Asaka and Mikhail Shaposhnikov. "The νMSM, dark matter and baryon asymmetry of the universe". In: *Physics Letters B* 620.1–2 (July 2005), pp. 17–26. ISSN: 0370-2693. DOI: 10.1016/j.physletb.2005.06.020 (cit. on p. 6).

[44] Alexey Boyarsky, Oleg Ruchayskiy, and Mikhail Shaposhnikov. "The Role of Sterile Neutrinos in Cosmology and Astrophysics". In: *Annual Review of Nuclear and Particle Science* 59.1 (Nov. 2009), pp. 191–214. ISSN: 1545-4134. DOI: 10.1146/annurev.nucl.010909.083654 (cit. on p. 6).

[45] R. Adhikari et al. "A White Paper on keV sterile neutrino Dark Matter". In: *Journal of Cosmology and Astroparticle Physics* 2017.01 (Jan. 2017), pp. 025–025. ISSN: 1475-7516. DOI: 10.1088/1475-7516/2017/01/025 (cit. on p. 7).

[46] Alexander Merle. *Sterile Neutrino Dark Matter*. IOP Publishing, 2017. ISBN: 9781681744810. DOI: 10.1088/978-1-6817-4481-0 (cit. on p. 7).

[47] Scott Tremaine and James E. Gunn. "Dynamical Role of Light Neutral Leptons in Cosmology". In: *Physical Review Letters* 42.6 (Feb. 1979), pp. 407–410. ISSN: 0031-9007. DOI: 10.1103/physrevlett.42.407 (cit. on p. 8).

[48] Alexey Boyarsky, Oleg Ruchayskiy, and Dmytro Iakubovskyi. "A lower bound on the mass of dark matter particles". In: *Journal of Cosmology and Astroparticle Physics* 2009.03 (Mar. 2009), pp. 005–005. ISSN: 1475-7516. DOI: 10.1088/1475-7516/2009/03/005 (cit. on p. 8).

[49] Scott Dodelson and Lawrence M. Widrow. "Sterile neutrinos as dark matter". In: *Physical Review Letters* 72.1 (Jan. 1994), pp. 17–20. ISSN: 0031-9007. DOI: 10.1103/physrevlett.72.17 (cit. on pp. 7, 8).

[50] Shunsaku Horiuchi et al. "Sterile neutrino dark matter bounds from galaxies of the Local Group". In: *Physical Review D* 89.2 (Jan. 2014), p. 025017. ISSN: 1550-2368. DOI: 10.1103/physrevd.89.025017 (cit. on p. 8).

[51] Brandon M. Roach et al. "Long-exposure NuSTAR constraints on decaying dark matter in the Galactic halo". In: *Physical Review D* 107.2 (Jan. 2023), p. 023009. ISSN: 2470-0029. DOI: 10.1103/physrevd.107.023009 (cit. on p. 8).

[52] Joshua W. Foster et al. "Deep Search for Decaying Dark Matter with XMM-Newton Blank-Sky Observations". In: *Physical Review Letters* 127.5 (July 2021), p. 051101. ISSN: 1079-7114. DOI: 10.1103/physrevlett.127.051101 (cit. on p. 8).

[53] Xiangdong Shi and George M. Fuller. "New Dark Matter Candidate: Nonthermal Sterile Neutrinos". In: *Physical Review Letters* 82.14 (Apr. 1999), pp. 2832–2835. ISSN: 1079-7114. DOI: 10.1103/physrevlett.82.2832 (cit. on p. 8).

[54] Cristina Benso et al. "Prospects for finding sterile neutrino dark matter at KATRIN". In: *Physical Review D* 100.11 (Dec. 2019), p. 115035. ISSN: 2470-0029. DOI: 10.1103/physrevd.100.115035 (cit. on p. 9).

[55] K -H Hiddemann, H Daniel, and O Schwentker. "Limits on neutrino masses from the tritium beta spectrum". In: *Journal of Physics G: Nuclear and Particle Physics* 21.5 (May 1995), pp. 639–650. ISSN: 1361-6471. DOI: 10.1088/0954-3899/21/5/008 (cit. on p. 10).

[56] E Holzschuh et al. "Search for heavy neutrinos in the β-spectrum of Ni". In: *Physics Letters B* 451.1–2 (Apr. 1999), pp. 247–255. ISSN: 0370-2693. DOI: 10.1016/s0370-2693(99)00200-2 (cit. on p. 10).

[57] E Holzschuh et al. "The β-spectrum of 35S and search for the admixture of heavy neutrinos". In: *Physics Letters B* 482.1–3 (June 2000), pp. 1–9. ISSN: 0370-2693. DOI: 10.1016/s0370-2693(00)00476-7 (cit. on p. 10).

[58] J. N. Abdurashitov et al. "First measurements in search for keV sterile neutrino in tritium beta-decay in the Troitsk nu-mass experiment". In: *JETP Letters* 105.12 (June 2017), pp. 753–757. ISSN: 1090-6487. DOI: 10.1134/s0021364017120013 (cit. on p. 10).

Bibliography

[59] M. Aker et al. "Search for keV-scale sterile neutrinos with the first KATRIN data". In: *The European Physical Journal C* 83.8 (Aug. 2023). ISSN: 1434-6052. DOI: 10.1140/epjc/s10052-023-11818-y (cit. on pp. 10, 11).

[60] Otokar Dragoun and Drahoslav Vénos. "Constraints on the Active and Sterile Neutrino Masses from Beta-Ray Spectra: Past, Present and Future1". In: *Open Physics Journal* 3.1 (Sept. 2016), pp. 73–113. ISSN: 1874-8430. DOI: 10.2174/1874843001603010073 (cit. on p. 10).

[61] E B Norman et al. "Evidence for the emission of a massive neutrino in nuclear beta decay". In: *Journal of Physics G: Nuclear and Particle Physics* 17.S (Dec. 1991), S291–S299. ISSN: 0954-3899. DOI: 10.1088/0954-3899/17/s/031 (cit. on p. 10).

[62] J. L. Mortara et al. "Evidence against a 17 keV neutrino from ^{35}S beta decay". In: *Physical Review Letters* 70.4 (Jan. 1993), pp. 394–397. ISSN: 0031-9007. DOI: 10.1103/physrevlett.70.394 (cit. on p. 10).

[63] K. G. Leach and S. Friedrich. "The BeEST Experiment: Searching for Beyond Standard Model Neutrinos Using ^{7}Be Decay in STJs". In: *Journal of Low Temperature Physics* 209.5–6 (July 2022), pp. 796–803. ISSN: 1573-7357. DOI: 10.1007/s10909-022-02759-z (cit. on p. 10).

[64] C J Martoff et al. "HUNTER: precision massive-neutrino search based on a laser cooled atomic source". In: *Quantum Science and Technology* 6.2 (Feb. 2021), p. 024008. ISSN: 2058-9565. DOI: 10.1088/2058-9565/abdb9b (cit. on p. 10).

[65] Douglas R. O. Morrison. "The rise and fall of the 17-keV neutrino". In: *Nature* 366.6450 (Nov. 1993), pp. 29–32. ISSN: 1476-4687. DOI: 10.1038/366029a0 (cit. on pp. 10, 11).

[66] J. J. Simpson. "Evidence of Heavy-Neutrino Emission in Beta Decay". In: *Physical Review Letters* 54.17 (Apr. 1985), pp. 1891–1893. ISSN: 0031-9007. DOI: 10.1103/physrevlett.54.1891 (cit. on p. 10).

[67] A. Hime and N.A. Jelley. "New evidence for the 17 keV neutrino". In: *Physics Letters B* 257.3–4 (Mar. 1991), pp. 441–449. ISSN: 0370-2693. DOI: 10.1016/0370-2693(91)91922-i (cit. on p. 10).

[68] M. Aker et al. "Improved eV-scale sterile-neutrino constraints from the second KATRIN measurement campaign". In: *Physical Review D* 105.7 (Apr. 2022), p. 072004. ISSN: 2470-0029. DOI: 10.1103/physrevd.105.072004 (cit. on p. 11).

[69] J.F. Amsbaugh et al. "Focal-plane detector system for the KATRIN experiment". In: *Nucl. Instrum. Methods Phys. Res., Sect. A* 778 (Apr. 2015), pp. 40–60. ISSN: 0168-9002. DOI: 10.1016/j.nima.2014.12.116 (cit. on pp. 11, 15, 18, 124).

[70] M. Aker et al. "The design, construction, and commissioning of the KATRIN experiment". In: *J. Instrum.* 16.08 (Aug. 2021), T08015. ISSN: 1748-0221. DOI: 10.1088/1748-0221/16/08/t08015 (cit. on pp. 12, 15, 60, 124).

[71] A. Picard et al. "A solenoid retarding spectrometer with high resolution and transmission for keV electrons". In: *Nuclear Instruments and Methods in Physics Research Section B: Beam Interactions with Materials and Atoms* 63.3 (Feb. 1992), pp. 345–358. ISSN: 0168-583X. DOI: 10.1016/0168-583x(92)95119-c (cit. on p. 13).

[72] V.M. Lobashev and P.E. Spivak. "A method for measuring the electron antineutrino rest mass". In: *Nuclear Instruments and Methods in Physics Research Section A: Accelerators, Spectrometers, Detectors and Associated Equipment* 240.2 (Oct. 1985), pp. 305–310. ISSN: 0168-9002. DOI: 10.1016/0168-9002(85)90640-0 (cit. on p. 13).

[73] M Aker et al. "KATRIN: status and prospects for the neutrino mass and beyond". In: *Journal of Physics G: Nuclear and Particle Physics* 49.10 (Sept. 2022), p. 100501. ISSN: 1361-6471. DOI: 10.1088/1361-6471/ac834e (cit. on p. 14).

[74] Ch Kraus et al. "Final results from phase II of the Mainz neutrino mass searchin tritium *β* decay". In: *The European Physical Journal C* 40.4 (Apr. 2005), pp. 447–468. ISSN: 1434-6052. DOI: 10.1140/epjc/s2005-02139-7 (cit. on pp. 14, 144).

[75] Martin Slezák. "Monitoring of the energy scale in the KATRIN neutrino experiment". PhD thesis. Charles University in Prague, 2015 (cit. on pp. 15, 144).

[76] M. Aker et al. "Direct neutrino-mass measurement with sub-electronvolt sensitivity". In: *Nature Physics* 18.2 (Feb. 2022), pp. 160–166. ISSN: 1745-2481. DOI: 10.1038/s41567-021-01463-1 (cit. on p. 15).

[77] M. Aker et al. "Analysis methods for the first KATRIN neutrino-mass measurement". In: *Physical Review D* 104.1 (July 2021), p. 012005. ISSN: 2470-0029. DOI: 10.1103/physrevd.104.012005 (cit. on p. 15).

[78] Martin Descher. "Differential spectrum modeling and sensitivity for keV sterile neutrino search at KATRIN". en. PhD thesis. Institut für Experimentelle Teilchenphysik (ETP), 2023. DOI: 10.5445/IR/1000166956 (cit. on pp. 17, 19, 22, 25, 131).

[79] William R. Leo. *Techniques for Nuclear and Particle Physics Experiments. A How-to Approach.* 1st ed. Description based on publisher supplied metadata and other sources. Berlin/Heidelberg: Springer Berlin Heidelberg, 1994. 1384 pp. ISBN: 9783642579202 (cit. on pp. 17, 164).

[80] Hermann Kolanoski and Norbert Wermes. *Particle detectors. Fundamentals and applications / Hermann Kolanoski, Norbert Wermes.* Oxford: Oxford University Press, 2020. ISBN: 9780198858362 (cit. on pp. 17, 164).

[81] Helmuth Spieler. *Semiconductor detector systems.* Vol. 12. Oxford science publications. Oxford: Oxford Univ. Press, 2005. ISBN: 9780198527848 (cit. on pp. 17, 36, 55).

[82] R. C. Alig, S. Bloom, and C. W. Struck. "Scattering by ionization and phonon emission in semiconductors". In: *Phys. Rev. B* 22.12 (Dec. 1980), pp. 5565–5582. ISSN: 0163-1829. DOI: 10.1103/physrevb.22.5565 (cit. on pp. 17, 164).

[83] P. Lechner et al. "Silicon drift detectors for high count rate X-ray spectroscopy at room temperature". In: *Nucl. Instrum. Methods Phys. Res., Sect. A* 458.1–2 (Feb. 2001), pp. 281–287. ISSN: 0168-9002. DOI: 10.1016/s0168-9002(00)00872-x (cit. on pp. 18, 58).

[84] Emilio Gatti and Pavel Rehak. "Semiconductor drift chamber — An application of a novel charge transport scheme". In: *Nucl. Instrum. Methods Phys. Res.* 225.3 (Sept. 1984), pp. 608–614. ISSN: 0167-5087. DOI: 10.1016/0167-5087(84)90113-3 (cit. on pp. 18, 47, 55).

[85] Lothar Strüder et al. "Development of the Silicon Drift Detector for Electron Microscopy Applications". In: *Microscopy Today* 28.5 (Sept. 2020), pp. 46–53. ISSN: 2150-3583. DOI: 10.1017/s1551929520001327 (cit. on pp. 18, 58).

[86] XGlab. *APPLICATION Note #1 Find the right CUBE*. 2024. URL: https://www.xglab.it/wp-content/uploads/2020/04/01_App_note_Find_the_right_amplifier.pdf (cit. on p. 18).

[87] Susanne Mertens et al. "A novel detector system for KATRIN to search for keV-scale sterile neutrinos". In: *Journal of Physics G: Nuclear and Particle Physics* 46.6 (May 2019), p. 065203. ISSN: 1361-6471. DOI: 10.1088/1361-6471/ab12fe (cit. on p. 19).

[88] Marc Korzeczek. "Sterile neutrino search with KATRIN - modeling and design-criteria of a novel detector system". en. PhD thesis. Institut für Experimentelle Teilchenphysik (ETP), 2020. DOI: 10.5445/IR/1000120634 (cit. on pp. 19, 22, 36, 71, 77, 117).

[89] Matteo Gugiatti. "Development of a Large-matrix SDD-based Radiation Detector for Beta-decay Spectroscopy in Neutrino Physics". PhD thesis. Milano: Politecnico Milano, 2022 (cit. on pp. 19, 43–45, 78, 98, 107).

[90] Peter Lechner et al. "Silicon drift detectors for high resolution room temperature X-ray spectroscopy". In: *Nuclear Instruments and Methods in Physics Research Section A: Accelerators, Spectrometers, Detectors and Associated Equipment* 377.2–3 (Aug. 1996), pp. 346–351. ISSN: 0168-9002. DOI: 10.1016/0168-9002(96)00210-0 (cit. on p. 19).

[91] Paolo Trigilio et al. "ETTORE: a 12-Channel Front-End ASIC for SDDs with Integrated JFET". In: *2018 IEEE Nuclear Science Symposium and Medical Imaging Conference Proceedings (NSS/MIC)*. IEEE, Nov. 2018. DOI: 10.1109/nssmic.2018.8824675 (cit. on pp. 20, 42, 44).

[92] Anton Huber. "Analysis of first KATRIN data and searches for keV-scale sterile neutrinos". en. PhD thesis. Karlsruher Institut für Technologie (KIT), 2020. DOI: 10.5445/IR/1000128344 (cit. on p. 22).

[93] S Mertens et al. "Characterization of silicon drift detectors with electrons for the TRISTAN project". In: *J. Phys. G: Nucl. Part. Phys.* 48.1 (Dec. 2020), p. 015008. ISSN: 1361-6471. DOI: 10.1088/1361-6471/abc2dc (cit. on pp. 22, 59, 77, 92, 131).

[94] Tim Brunst. "First generation prototype detectors for the TRISTAN project". PhD thesis. Technical University of Munich, 2020. URL: https://mediatum.ub.tum.de/?id=1540377 (cit. on pp. 22, 26, 77).

[95] Yadolah Dodge. *The concise encyclopedia of statistics*. [Updated ed.] Springer reference. New York, NY [u.a.]: Springer, 2010. 622 pp. ISBN: 9780387317427 (cit. on p. 23).

[96] Daniel Foreman-Mackey et al. "emcee: The MCMC Hammer". In: *Publications of the Astronomical Society of the Pacific* 125.925 (Mar. 2013), pp. 306–312. ISSN: 1538-3873. DOI: 10.1086/670067 (cit. on p. 23).

[97] D Siegmann et al. "Development of a silicon drift detector array to search for keV-scale sterile neutrinos with the KATRIN experiment". In: *Journal of Physics G: Nuclear and Particle Physics* 51.8 (June 2024), p. 085202. ISSN: 1361-6471. DOI: 10.1088/1361-6471/ad4bf8 (cit. on pp. 26, 92, 144, 148).

[98] Robert Cimrman, Vladimír Lukeš, and Eduard Rohan. "Multiscale finite element calculations in Python using SfePy". In: *Adv. Comput. Math.* 45.4 (May 2019), pp. 1897–1921. ISSN: 1572-9044. DOI: 10.1007/s10444-019-09666-0 (cit. on pp. 32, 66, 165).

[99] Tommaso Comellato, Matteo Agostini, and Stefan Schönert. "Charge-carrier collective motion in germanium detectors for $\beta\beta$-decay searches". In: *The European Physical Journal C* 81.1 (Jan. 2021). ISSN: 1434-6052. DOI: 10.1140/epjc/s10052-021-08889-0 (cit. on p. 35).

[100] I. Abt et al. "Simulation of semiconductor detectors in 3D with SolidStateDetectors.jl". In: *Journal of Instrumentation* 16.08 (Aug. 2021), P08007. ISSN: 1748-0221. DOI: 10.1088/1748-0221/16/08/p08007 (cit. on p. 35).

[101] C. Jacoboni et al. "A review of some charge transport properties of silicon". In: *Solid-State Electron.* 20.2 (Feb. 1977), pp. 77–89. ISSN: 0038-1101. DOI: 10.1016/0038-1101(77)90054-5 (cit. on p. 36).

[102] W. Shockley. "Currents to Conductors Induced by a Moving Point Charge". In: *Journal of Applied Physics* 9.10 (Oct. 1938), pp. 635–636. ISSN: 1089-7550. DOI: 10.1063/1.1710367 (cit. on p. 39).

[103] S. Ramo. "Currents Induced by Electron Motion". In: *Proceedings of the IRE* 27.9 (Sept. 1939), pp. 584–585. ISSN: 0096-8390. DOI: 10.1109/jrproc.1939.228757 (cit. on p. 39).

[104] A. Niculae et al. "Optimized readout methods of silicon drift detectors for high-resolution X-ray spectroscopy". In: *Nuclear Instruments and Methods in Physics Research Section A: Accelerators, Spectrometers, Detectors and Associated Equipment* 568.1 (Nov. 2006), pp. 336–342. ISSN: 0168-9002. DOI: 10.1016/j.nima.2006.06.025 (cit. on p. 42).

[105] Matthew Romer et al. "A low-power analog front-end amplifier for SiPM based radiation detectors". In: *Nuclear Instruments and Methods in Physics Research Section A: Accelerators, Spectrometers, Detectors and Associated Equipment* 1048 (Mar. 2023), p. 167897. ISSN: 0168-9002. DOI: 10.1016/j.nima.2022.167897 (cit. on p. 42).

[106] F. Edzards et al. "Investigation of ASIC-based signal readout electronics for LEGEND-1000". In: *Journal of Instrumentation* 15.09 (Sept. 2020), P09022–P09022. ISSN: 1748-0221. DOI: 10.1088/1748-0221/15/09/p09022 (cit. on p. 42).

[107] XGLab. "Report on development of ETTORE RUN2, a readout front-end ASIC for SDD arrays with integrated JFET". 2020 (cit. on pp. 43, 81, 83, 84, 167).

[108] Ulrich Tietze, Christoph Schenk, and Eberhard Gamm. *Halbleiter-Schaltungstechnik*. 16., erweiterte und aktualisierte Auflage. Berlin: Springer Vieweg, 2019. 1793 pp. ISBN: 9783662485538 (cit. on pp. 45, 79).

[109] V Radeka. "Low-Noise Techniques in Detectors". In: *Annu. Rev. Nucl. Part. S.* 38.1 (Dec. 1988), pp. 217–277. ISSN: 1545-4134. DOI: 10.1146/annurev.ns.38.120188.001245 (cit. on pp. 47, 48, 53, 55, 112).

[110] Tobias Eggert. "Die spektrale Antwort von Silizium-Röntgendetektoren". PhD thesis. Technische Universität München, 2004. URL: https://mediatum.ub.tum.de/?id=603022 (cit. on p. 58).

[111] Joseph Magill, Raymond Dreher, and Zsolt Sóti, eds. *Karlsruher Nuklidkarte*. 11. Auflage. Karlsruhe: Nucleonica GmbH, 2022. 72 pp. ISBN: 9783000691805 (cit. on p. 58).

[112] Matthew Newville, Christopher T. Chantler, and Darren S. Dale. *X-ray DB*. 2023. URL: https://xraypy.github.io/XrayDB/ (cit. on pp. 58, 59).

[113] D. Vénos et al. "Properties of83mKrconversion electrons and their use in the KATRIN experiment". In: *J. Instrum.* 13.02 (Feb. 2018), T02012–T02012. ISSN: 1748-0221. DOI: 10.1088/1748-0221/13/02/t02012 (cit. on pp. 59, 147).

[114] M Zbořil et al. "Ultra-stable implanted83Rb/83mKr electron sources for the energy scale monitoring in the KATRIN experiment". In: *J. Instrum.* 8.03 (Mar. 2013), P03009–P03009. ISSN: 1748-0221. DOI: 10.1088/1748-0221/8/03/p03009 (cit. on pp. 59, 147).

[115] J. Behrens et al. "A pulsed, mono-energetic and angular-selective UV photo-electron source for the commissioning of the KATRIN experiment". In: *Eur. Phys. J. C* 77.6 (June 2017). ISSN: 1434-6052. DOI: 10.1140/epjc/s10052-017-4972-9 (cit. on p. 60).

[116] A. V. Crewe et al. "Electron Gun Using a Field Emission Source". In: *Rev. Sci. Instrum.* 39.4 (Apr. 1968), pp. 576–583. ISSN: 1089-7623. DOI: 10.1063/1.1683435 (cit. on p. 60).

[117] K. Urban et al. "A thermionic electron gun to characterize silicon drift detectors with electrons". In: *Journal of Instrumentation* 19.06 (June 2024), P06004. ISSN: 1748-0221. DOI: 10.1088/1748-0221/19/06/p06004 (cit. on p. 60).

[118] O. W. Richardson. *The Emission of Electricity from Hot Bodies*. Monographs on physics. Longmans, Green and Company, 1916 (cit. on p. 60).

[119] Neil W. Ashcroft and N. David Mermin. *Solid state physics*. New York: Holt Rinehart and Winston, 1976. ISBN: 0-03-083993-9 (cit. on p. 60).

[120] William M. Haynes. *CRC Handbook of Chemistry and Physics, 95th Edition*. Taylor and Francis Group, 2014, p. 2704. ISBN: 9781482208689 (cit. on pp. 61, 63).

[121] KIMBALL PHYSICS. *KIMBALL PHYSICS CATHODES. CATHODE TUTORIAL AND RESOURCE*. Kimball Physics. 2023. URL: https://www.kimballphysics.com/wp-content/uploads/2023/09/Cathode_Tutorial_Resource_2023_0606.pdf (visited on 01/04/2024) (cit. on p. 61).

[122] The Editors of Encyclopaedia. *Encyclopedia Britannica. Planck's radiation law*. 2023. URL: https://www.britannica.com/science/Plancks-radiation-law (visited on 01/16/2024) (cit. on p. 62).

[123] D.M. Schlosser et al. "Expanding the detection efficiency of silicon drift detectors". In: *Nucl. Instrum. Methods Phys. Res., Sect. A* 624.2 (Dec. 2010), pp. 270–276. ISSN: 0168-9002. DOI: 10.1016/j.nima.2010.04.038 (cit. on p. 62).

[124] R. Hartmann et al. "Ultrathin entrance windows for silicon drift detectors". In: *Nucl. Instrum. Methods Phys. Res., Sect. A* 387.1–2 (Mar. 1997), pp. 250–254. ISSN: 0168-9002. DOI: 10.1016/s0168-9002(96)01000-5 (cit. on p. 62).

[125] Gregor Kramberger. "Advanced TCT Setups". In: *Proceedings of The 23rd International Workshop on Vertex Detectors — PoS(Vertex2014)*. Vertex2014. Sissa Medialab, May 2015. DOI: 10.22323/1.227.0032 (cit. on p. 71).

[126] *Particulars advanced measurement systems*. an. Jozef Stefan Institute. URL: www.particulars.si (visited on 2024) (cit. on p. 71).

[127] G. Prigozhin et al. "Characterization of the silicon drift detector for NICER instrument". In: *SPIE Proceedings*. Ed. by Andrew D. Holland and James W. Beletic. SPIE, Sept. 2012. DOI: 10.1117/12.926667 (cit. on p. 71).

[128] Jinhun Joung et al. "Performance Characterization of a Silicon Drift Detector for Gamma Ray Imaging". In: *IEEE Transactions on Nuclear Science* 57.3 (June 2010), pp. 931–937. ISSN: 1558-1578. DOI: 10.1109/tns.2009.2038696 (cit. on p. 71).

[129]   S. Di Giacomo et al. "Timing Performances of SDD as Photodetector Candidate for Proton Therapy Application". In: *IEEE Transactions on Radiation and Plasma Medical Sciences* 6.7 (Sept. 2022), pp. 811–819. ISSN: 2469-7303. DOI: 10.1109/trpms.2021.3137668 (cit. on p. 71).

[130]   Martin A. Green and Mark J. Keevers. "Optical properties of intrinsic silicon at 300 K". In: *Progress in Photovoltaics: Research and Applications* 3.3 (Jan. 1995), pp. 189–192. ISSN: 1099-159X. DOI: 10.1002/pip.4670030303 (cit. on p. 71).

[131]   Markus Kandler. "Calibration and Characterization of a7-pixel TRISTAN Detector with an LED". MA thesis. Technical University of Munich, 2024 (cit. on pp. 72, 74, 76).

[132]   Dieter Meschede. *Gerthsen Physik*. 25. Aufl. 2015. Springer-Lehrbuch. Berlin, Heidelberg: Springer Berlin Heidelberg, 2015. 11052 pp. ISBN: 9783662459775 (cit. on p. 73).

[133]   Christian Forstner. "Characterization of a TRISTAN Silicon Drift Detector Array with a Laser System". MA thesis. Technical University of Munich, 2023 (cit. on pp. 74, 81).

[134]   Christian Forstner et al. *Investigations of Charge Collection and Signal Timing in a multi-pixel Silicon Drift Detector*. 2024. DOI: 10.48550/ARXIV.2409.08901 (cit. on pp. 74, 76).

[135]   Daniela Spreng et al. *Investigation of Electron Backscattering on Silicon Drift Detectors for the Sterile Neutrino Search with TRISTAN*. 2024. DOI: 10.48550/ARXIV.2405.12776 (cit. on p. 76).

[136]   Verena Wallner. "Detector degradation over time of the TRISTAN SDD detector". MA thesis. Technical University of Munich, 2024 (cit. on pp. 76, 92).

[137]   L. Bombelli et al. ""CUBE", A low-noise CMOS preamplifier as alternative to JFET front-end for high-count rate spectroscopy". In: *2011 IEEE Nuclear Science Symposium Conference Record*. IEEE, Oct. 2011. DOI: 10.1109/nssmic.2011.6154396 (cit. on p. 77).

[138]   Daniel Siegmann. "Investigation of the Detector Response to Electrons of the TRISTAN Prototype Detectors". MA thesis. Technical University of Munich, Apr. 15, 2019 (cit. on pp. 77, 92).

[139]   Manuel Lebert. "Characterization of the Detector Response to Electrons and Test of a New Entrance Window Technology of Silicon Drift Detectors for theTRISTAN Project". MA thesis. Technical University of Munich, Dec. 2, 2019 (cit. on p. 77).

[140]   T. Brunst et al. "Measurements with a TRISTAN prototype detector system at the "Troitsk nu-mass" experiment in integral and differential mode". In: *Journal of Instrumentation* 14.11 (Nov. 2019), P11013–P11013. ISSN: 1748-0221. DOI: 10.1088/1748-0221/14/11/p11013 (cit. on p. 77).

[141]   Konrad Altenmüller. "Search for sterile neutrinos in β-decays". PhD thesis. Technical University of Munich, 2019. URL: https://mediatum.ub.tum.de/1506307 (cit. on pp. 77, 116).

[142]   Korbinian Urban. "Application of a TRISTAN Silicon DriftDetector as Forward Beam Monitor inKATRIN". MA thesis. Technical University of Munich, Dec. 9, 2019 (cit. on p. 77).

[143]   Daniel Siegmann. "Assembly and characterization of the TRISTAN silicon drift detector modules". PhD thesis. Technical University of Munich, 2024 (cit. on pp. 92, 147, 148).

[144]   Aleksandra Krzyzanowska. "Charge Sharing in Single-Photon-Counting Detectors". In: *X-ray Photon Processing Detectors*. Springer International Publishing, Oct. 2023, pp. 27–38. ISBN: 9783031352416. DOI: 10.1007/978-3-031-35241-6_2 (cit. on p. 116).

Bibliography

[145] K Mathieson et al. "Charge sharing in silicon pixel detectors". In: *Nuclear Instruments and Methods in Physics Research Section A: Accelerators, Spectrometers, Detectors and Associated Equipment* 487.1–2 (July 2002), pp. 113–122. ISSN: 0168-9002. DOI: 10.1016/s0168-9002(02)00954-3 (cit. on p. 116).

[146] T. Eggert et al. "Analysis of background events in Silicon Drift Detectors". In: *Nuclear Instruments and Methods in Physics Research Section A: Accelerators, Spectrometers, Detectors and Associated Equipment* 512.1–2 (Oct. 2003), pp. 257–264. ISSN: 0168-9002. DOI: 10.1016/s0168-9002(03)01902-8 (cit. on p. 116).

[147] K. Urban et al. "Characterization measurements of the TRISTAN multi-pixel silicon drift detector". In: *Journal of Instrumentation* 17.09 (Sept. 2022), p. C09020. ISSN: 1748-0221. DOI: 10.1088/1748-0221/17/09/c09020 (cit. on p. 116).

[148] Beatrice Pedretti et al. "Charge Sharing Assessment and Active Collimation in Monolithic Arrays of Silicon Drift Detectors". In: *IEEE Transactions on Nuclear Science* (2024), pp. 1–1. ISSN: 1558-1578. DOI: 10.1109/tns.2024.3429622 (cit. on p. 116).

[149] Christian Forstner. "Pulse Shape Analysis with the TRISTAN Silicon Drift Detector". BA thesis. Technical University of Munich, 2020 (cit. on p. 116).

[150] P. King et al. "Design and characterization of Kerberos: a 48-channel analog pulse processing and data acquisition platform". In: *Journal of Instrumentation* 16.07 (July 2021), T07007. ISSN: 1748-0221. DOI: 10.1088/1748-0221/16/07/t07007 (cit. on p. 125).

[151] Charles R. Harris et al. "Array programming with NumPy". In: *Nature* 585.7825 (Sept. 2020), pp. 357–362. ISSN: 1476-4687. DOI: 10.1038/s41586-020-2649-2 (cit. on p. 131).

[152] CAEN. *CoMPASS User Manual rev. 23. UM5960*. Aug. 6, 2024. URL: https://www.caen.it/products/compass/ (cit. on p. 142).

[153] M Erhard et al. "High-voltage monitoring with a solenoid retarding spectrometer at the KATRIN experiment". In: *Journal of Instrumentation* 9.06 (June 2014), P06022–P06022. ISSN: 1748-0221. DOI: 10.1088/1748-0221/9/06/p06022 (cit. on p. 144).

[154] U. Fano. "Ionization Yield of Radiations. II. The Fluctuations of the Number of Ions". In: *Physical Review* 72.1 (July 1947), pp. 26–29. ISSN: 0031-899X. DOI: 10.1103/physrev.72.26 (cit. on p. 163).

[155] K. Sakai et al. "Demonstration of Fine-Pitch High-Resolution X-ray Transition-Edge Sensor Microcalorimeters Optimized for Energies below 1 keV". In: *J. Low Temp. Phys.* 199.3–4 (Mar. 2020), pp. 949–954. ISSN: 1573-7357. DOI: 10.1007/s10909-020-02409-2 (cit. on p. 164).

[156] Bonnie C. Baker. *Anti-Aliasing, Analog Filters for Data Acquisition Systems. AN699*. microchip. 2002. URL: https://www.microchip.com/en-us/application-notes/an699 (cit. on p. 167).

[157] C. Cottini, E. Gatti, and V. Svelto. "A new method for analog to digital conversion". In: *Nucl. Instrum. Methods* 24 (July 1963), pp. 241–242. ISSN: 0029-554X. DOI: 10.1016/0029-554x(63)90314-8 (cit. on p. 167).

[158] Kai Dolde et al. "Impact of ADC non-linearities on the sensitivity to sterile keV neutrinos with a KATRIN-like experiment". In: *Nucl. Instrum. Methods Phys. Res., Sect. A* 848 (Mar. 2017), pp. 127–136. ISSN: 0168-9002. DOI: 10.1016/j.nima.2016.12.015 (cit. on p. 167).

A Appendix

A.1 Detection of ionizing radiation

This section summarizes the fundamental options of radiation detection and shows why silicon is a good choice as a target material for the TRISTAN detector. Three different mechanisms are frequently used to measure the kinetic energy of ionizing particles. These are

- the detection of scintillation light (secondary quanta: photons),
- the detection of ionization (secondary quanta: electrons and ions), and
- the detection of temperature (secondary quanta: phonons).

In all three cases, the energy resolution of each detection mechanism is limited by statistical properties of the creation process of secondary quanta (photons for scintillation, electron-ion pairs for ionization, and phonons for temperature). The statistical variance of the expected number N of secondary quanta of an event is described by [154]

$$\text{var}(n) = Fn. \tag{A.1}$$

The scalar Fano factor F relates the observed variance to the Poissonian variance $\text{var}(N) = N$. In the most favorable material, there is no statistical fluctuation of the detected number of secondary quanta N, and the Fano factor is $F = 0$. In the worst case, the creation of each secondary quantum is independent of any other secondary quantum, which results in a Poissonian distribution of N with $F = 1$.

The expected number of secondary quanta is proportional to the incident energy E by

$$n = \frac{E}{w}, \tag{A.2}$$

where w is the average creation energy for a single secondary quantum. Both parameters w and F depend on the used material. By combining the two above equations, the uncertainty on the estimated incident energy is given by

$$\sigma_{\text{stat}} = \sqrt{wFE}. \tag{A.3}$$

Both the average creation energy for a single secondary quantum w and the Fano factor F need to be small to achieve a good energy resolution of the detector. In the following, the three detection mechanisms are briefly compared.

Detection of scintillation The light yield of a scintillator describes the number of emitted photons per deposit energy and corresponds to $\frac{1}{w}$ in the picture of equation A.2. Typical values for the light yield are 43 photons per keV for NaI crystals or 61 photons per keV for LaBr crystals. Equation A.3 with Fano factor $F = 1$ yields a lower limit of the energy resolution of around $1.3\,\text{keV}$ FWHM

Table A.1: Selected materials to detect particles by ionization and corresponding pair creation energy w and Fano factor F. Values are from [80, 79, 82]. The column FWHM at 20 keV is calculated with equation A.3.

material	phase	w	F	FWHM at 20 keV
Ar	gaseous or liquid	26 eV	0.15	658 eV
Xe	gaseous or liquid	22 eV	0.15	605 eV
Si	solid	3.63 eV	0.115	215 eV
Ge	solid	2.96 eV	0.13	207 eV
diamond	solid	13.1 eV	0.08	525 eV

at 20 keV. In actual scintillator setups, other detector effects contribute significantly (or may even dominate) the energy resolution [80].

Detection of temperature In a microcalorimeter, the hit of an ionizing particle causes lattice vibrations (phonons), which are measured as an increase in temperature. All deposit energy ends up in phonons in most materials due to energy conservation. Thus, the Fano factor is $F = 0$. Microcalorimiters have recently achieved outstanding energy resolutions below 1 eV at 1 keV incident energy [155]. Nevertheless, this is only possible with tiny detectors (e.g. $45\,\mu\text{m} \times 45\,\mu\text{m}$ detector cells). Furthermore, microcalorimeters must be operated at a temperature in the milli-Kelvin range, making the operation technically very challenging.

Detection of ionization Detectors within this category collect mobile charge carriers created by ionizing radiation. In a drift chamber, an electric field is applied between electrodes, and the electrons and ions created by ionizing radiation can drift in a typically gaseous or liquid target material. Another option for the target material is a semiconducting solid-state material, where electrons in the conduction band and holes in the valence band are mobile. Silicon and Germanium are the most suitable materials to achieve a good resolution at low energy (see table A.1). Germanium is mostly used for high resolution γ-spectroscopy, while silicon detectors are often used for X-ray detection up to around 20 keV.

There are several arguments for choosing silicon as the target material for the TRISTAN detector. The Fano limit of the energy resolution is 207 eV FWHM at 20 keV, which is in line with the target energy resolution of around 300 eV of the TRISTAN detector. Furthermore, silicon detectors are easier to operate than germanium detectors, which require cooling at liquid nitrogen temperature. Microcalorimeters are even more complicated to operate. Last but not least, silicon is widely used with known manufacturing steps.

A.2 Poisson equation in ϕ-symmetric cylindrical coordinates

This section derives the weak formulation of the Poisson equation in cylindrical coordinates, which is used for the field calculation in section 4.1.1.

For a scalar field Φ, the Poisson equation states

$$\triangle \Phi = f(x) \qquad x \in \Omega. \tag{A.4}$$

For the application of electric field calculation in an SDD Φ is the electric potential, $\vec{\nabla}\Phi = \vec{E}$ is the electric field and $f(x) = \frac{N(x)e}{\epsilon_0 \epsilon_r}$ is the space charge in the depleted volume Ω of the SDD. On the surface of volume Ω, boundary conditions are given. These are split into two parts: So-called Dirichlet boundary conditions defined Φ explicitly Γ_D. In the SDD, these are electrodes at a given electric potential. Furthermore, there are so-called Neumann boundary conditions on the surface Γ_N, where the electric field is normal to the surface. Neumann boundary conditions are applied at the border to the next pixel due to symmetry considerations.

$$\Phi = u(x) \qquad x \in \Gamma_D \tag{A.5}$$
$$\vec{\nabla}\Phi \cdot \vec{n} = 0 \qquad x \in \Gamma_N \tag{A.6}$$

The Poisson equation A.4 can be rewritten in a weak formulation, which states

$$\int_{\Omega} \vec{\nabla}\Phi\vec{\nabla}s \mathrm{d}\Omega = -\int_{\Omega} f \cdot s \mathrm{d}\Omega. \tag{A.7}$$

In the weak formulation, a second scalar field s is introduced, called the test function. Equation A.7 has to be fulfilled for any choice of the test function s. In the numerical finite element method approach, the volume is split into a mesh with many nodes $\vec{x}_i$, and each node has its test function s_i, which is only non-zero between $\vec{x}_i$ and its neighboring nodes.

The volume integrals in equation A.7 integrate over the three-dimensional volume $\Omega \subset \mathbb{R}^3$. In the case of a ϕ-symmetric field in cylindrical coordinates, the problem can be written in two-dimensional Cartesian coordinate space with coordinates r and z in $\Omega' \subset \mathbb{R}^2$. When changing from the volume integral in Ω to an area integral in Ω', one has to consider the circumference along ϕ to get the differential correct: $\mathrm{d}\Omega = 2\pi r \mathrm{d}\Omega'$. For the weak formulation in equation A.7 this yields:

$$\int_{\Omega'} \vec{\nabla}\Phi\vec{\nabla}s \cdot 2\pi r \, \mathrm{d}\Omega' = -\int_{\Omega'} f \cdot s \cdot 2\pi r \, \mathrm{d}\Omega' \tag{A.8}$$

This equation is used to solve to scalar field Φ in an SDD detector using the finite element method (FEM) package *sfepy* [98].

A.3 Field Calculation Benchmark

To check if the field calculation is section 4.1.1, using the *sfepy* package and equation A.8, gives the correct result, a simple benchmark test is performed. To this end, a problem that has a known analytical solution is calculated with the FEM code. It was chosen to simulate the potential in a spherical plate capacitor with a given space charge density. The field extends between two spheres at $R_1 = 0.1$ and $R_2 = 1.0$ at voltages $V_1 = 0$ and $V_2 = 1$. A homogeneous space charge is given by $f = -2$ in equation A.8. The analytical solution is given by

$$V(r) = -\frac{f r^2}{6} - \frac{A}{r} + B \qquad \text{with} \tag{A.9}$$

$$A = \frac{1 - \frac{1}{6}f \cdot (R_1^2 - R_2^2)}{\frac{1}{R_1} - \frac{1}{R_2}} \qquad \text{and} \tag{A.10}$$

$$B = \frac{1}{6}f R_1 + \frac{A}{R_1}. \tag{A.11}$$

The analytic solution and the numeric solution from the FEM method on a coarse mesh of 41×41 points are compared in figure A.9.
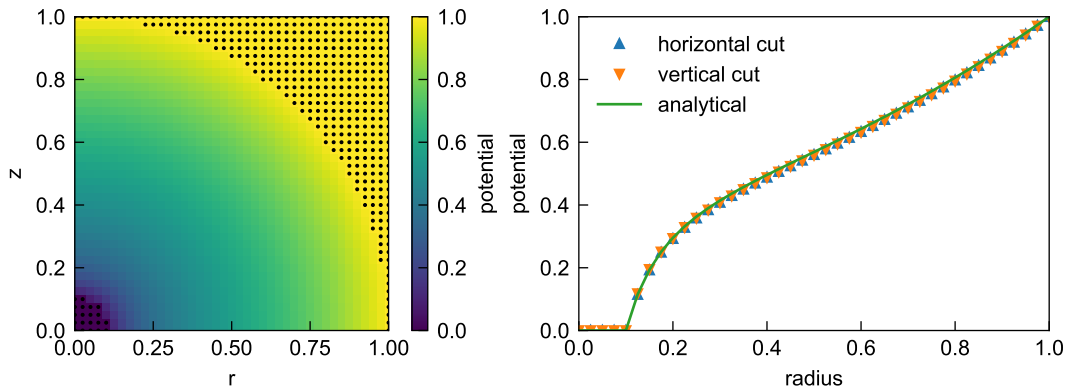
Figure A.1: Benchmark test for the FEM field calculation using a spherical capacitor with negative space charge. The left plot shows the potential Φ on the regular mesh grid. Black dots correspond to nodes where Dirichlet boundary conditions are given. The resulting radial evolution of the potential Φ is plotted on the right for a horizontal and a vertical cut through the mesh and is compared to the analytical solution given in equation A.9.

A.4 Signal path step-by-step

This section gives additional information and illustrations of the TRISTAN signal chain shown in figure 7.2 of section 7.1. The functionality of each block will be addressed in the following sections.

A.4.1 Analog circuit

The frontend DAQ system receives the analog signals from the second amplifier stage of ETTORE, as described in section 4.2.2. The output of ETTORE provides negative pulses with a baseline of 2.7 V [107]. An example of the ETTORE output (labeled Ⓐ in figure 7.2) is plotted in figure A.2.

The analog part of the frontend DAQ system comprises a buffer to map the full ETTORE output dynamic range (0.7 V to 2.7 V) to the ADC and an active anti-aliasing filter. The anti-aliasing filter is a fifth-order bessel low-pass filter [156] with a critical frequency of 13 MHz. An example pulse before and after the anti-aliasing filter is shown in figure A.3. The anti-aliasing filter does not significantly change the rise time or shape of the pulses. At the same time, it efficiently removes all noise components with frequencies above half of the ADC's sampling frequency ($f_s/2 = 31.25$ MHz).

The analog circuit features a "Gatti Slider", a programmable offset added to the analog signal before digitization. By sequentially changing the offset during the measurement, the non-linearity, which originates from the ADC, can be reduced [157, 158].

A.4.2 Analog-to-digital conversion

The analog signals are digitized by AD9257-65 ADCs[1], which are a multistaged, pipelined ADCs with digital error correction and 14 bit resolution. The ADCs are operated at a sampling frequency of 62.5 MHz. The input range of the ADC is adjusted to cover the full-scale range (FSR) of the

---

[1]Datasheet available online.
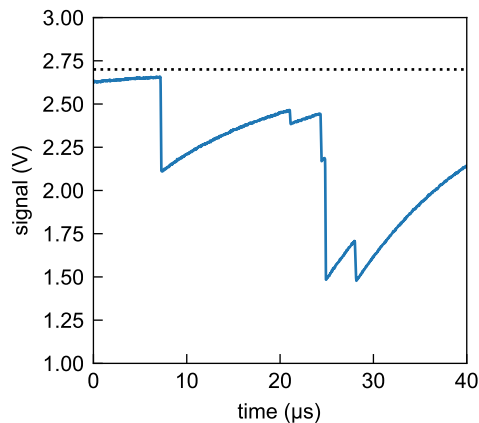
Figure A.2: Simulated detector signal (signal Ⓐ in figure 7.2). This signal is used as input for the step-by-step explanation of the DAQ chain. It was created with a flat input energy spectrum of detector pulses up to $E = 40$ keV at an input rate of 100 kcps.
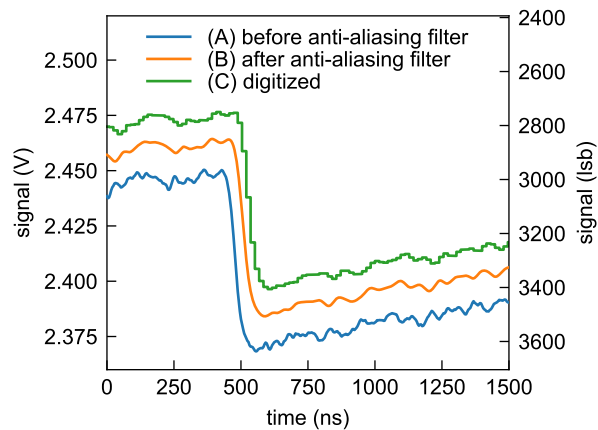
Figure A.3: A simulated pulse before anti-aliasing filter, after anti-aliasing filter, and after digitization (signals Ⓐ, Ⓑ, and Ⓒ in figure 7.2). The pulse is a cutout of the signal in figure A.2 at 20 μs. The corresponding physical event has an energy $E \approx 4.6$ keV. The three signals are shifted slightly for better visibility.

Table A.2: Full-scale range (FSR) and gain of the TRISTAN detector. "Low gain" and "high gain" are two possible gain options of ETTORE 2nd stage.

	detector FSR	ETTORE gain	ADC total gain
low gain	226 keV	8.8 mV/keV	72.4 lsb/keV
high gain	113 keV	17.7 mV/keV	145.8 lsb/keV

detector. According to table A.2, the resulting gain of the full readout circuit is 72.4 lsb/keV and 145.8 lsb/keV for the low gain and high gain mode of ETTORE, respectively[2]. This means that, in low gain mode, a physical event with 10 keV corresponds to a pulse with an amplitude of around 720 lsb in the digitized signal, or, equivalently, one lsb corresponds to a deposit energy of around 14 eV.

The sampling frequency of the ADC was chosen based on the bandwidth of the analog detector signal. The charge sensitive amplifier, consisting of ETTORE and the JFET at the detector anode, has a bandwidth of around 7 MHz, as explained in section 4.2.3. Thus, the sampling frequency of 62.5 MHz is sufficient to maintain all relevant pulse information. Figure A.3 shows, besides the anti-aliasing filter output, the digitization signal. The analog detector signals of the second stage of ETTORE have a negative polarity. In the following plots, the signals in the digital domain are shown with positive polarity to have a more natural visual view of the pulses.

The digitized signals of one TRISTAN detector module have a total data rate of

$$R_{\text{data}} = N_{\text{channels}} \cdot f_s \cdot N_{\text{bit}} = 145.25 \cdot 10^9 \,\text{bit/s} = 18.2 \,\text{GB/s} \tag{A.12}$$

with the number of channels $N_{\text{channels}} = 168$ (166 detector pixels and two spare channels), sampling frequency $f_s = 62.5 \,\text{MHz}$ and sample resolution $N_{\text{bit}} = 14 \,\text{bit}$. The high value of 18.2 GB/s of raw data for a single detector module (the first phase will have nine modules) shows that saving the raw data rate is not feasible. The frontend DAQ sends the digital waveform data via 12 fiber optic transceivers with 16 Gbit/s each to the backend DAQ.

A.4.3 Trigger algorithm

The first signal processing step in the backend DAQ detects events and their corresponding timestamps using a trigger algorithm. This algorithm is illustrated in figure A.4 and works the following way:

- A digital trigger filter is applied to the signal. It produces a fast bipolar, zig-zag-like response at a rising edge of a pulse, similar to the second derivative. This filter is called "heartbeat" trigger filter in this work[3]. The impulse response $h(t)$, step response $a(t)$, and frequency response of the heartbeat trigger filter are illustrated in the appendix figure A.16.
- Any rise of the trigger filter output above a threshold level causes the trigger logic to switch to an armed state. The trigger threshold is set above the noise level of the trigger filter output.
- The consecutive zero crossing of the trigger filter output defines the timestamp of the event.

---

[2]The digital unit of one ADC code is called least significant bit (lsb) in this work.
[3]The name "heatbeat" trigger filter was chosen because of the shape of the trigger filter output. A similar filter is called a triangular trigger filter in a CAEN user manual (available online).

Figure A.4: Simulated digitized pulse sequence (top) and the corresponding trigger filter output (bottom). The signals correspond to signals Ⓒ and Ⓓ in figure 7.2, respectively. The insert shows a zoom to the trigger filter output of one event and illustrates the trigger algorithm described in the text.

Two important properties characterize the trigger algorithm: First, the ability of the trigger to correctly separate two fast consecutive events is important. Especially for the treatment of pileup, this minimum resolution time plays an important role. Second, the trigger should have a low detection threshold.

Minimum resolution time

The minimum resolution time τ_{min} describes the minimal time difference between two consecutive pulses, where the trigger algorithm detects two triggers. To reach a short minimum resolution time, the window length τ_{window} of the trigger filter (compare figure A.16) should be small. The lower constraint for τ_{window} comes from the limited rise time of the digitized pulses: If τ_{window} is much smaller than the pulse rise time, the trigger filter amplitude depends strongly on the pulse rise time, which is undesired. In this work, the window length $\tau_{\text{window}} = 112\,\text{ns}$ is chosen.

In order to study the minimal resolution time, trace-level simulations of two consecutive events with known true time distance Δt_{true} were performed. Figure A.5 shows three example simulations with $\Delta t_{\text{true}} = 150\,\text{ns}$. At this time distance, the trigger algorithm can, in principle, detect both events correctly (central plot). However, depending on the pulse heights, there are cases where the trigger algorithm detects only one event. In this case, the trigger filter output has only one threshold and zero crossing (left and right plot). The reconstructed event timestamps t_{reco} of many MC simulations with known Δt_{true} are plotted in figure A.6. The extracted minimum resolution time is $\tau_{\text{min}} \approx 170\,\text{ns}$. However, there is a soft transition between the two regimes. For $\Delta t_{\text{true}} < 150\,\text{ns}$, usually a single event centered at the mean of the two events around $t_{\text{reco}} = 0$ is reconstructed (blue dots). For $\Delta t_{\text{true}} > 200\,\text{ns}$ the trigger algorithm correctly reconstructs two events at $t_{\text{reco}} \approx \pm 0.5\Delta t_{\text{true}}$ (orange dots). Between these two regimes, the decision on one or two detected events is influenced by the event's pulse height and noise.

Figure A.5: Three example simulations of the digitized signal after exponential deconvolution (top) and the trigger filter output (bottom). The signals correspond to signals Ⓔ and Ⓓ in figure 7.2, respectively. Each simulation has two input events with a time difference of 150 ns. The energy of the two events is 10 keV and 30 keV for the left plot, 20 keV and 20 keV for the central plot, and 30 keV and 10 keV for the right plot. The simulation in the central plot correctly reconstructs two events (green lines), while the other two simulations only have one output event.

The energy dependence of the minimum resolution time $\tau_{\min}$ is undesired for TRISTAN, because it strongly distorts the unresolved pileup spectrum. In this case, the modeling of the unresolved pileup spectrum, as it will be shown in section 7.3.1, would not be possible. In order to mitigate the energy dependence of the minimum resolution time, a trigger holdoff time τ_{holdoff} is defined. Any trigger that happens within τ_{holdoff} after a previous trigger is ignored. Thereby, the minimum resolution time $\tau_{\min}$ is fixed to τ_{holdoff}, which is set to $\tau_{\text{holdoff}} = 240\,\text{ns}$ in this work.

Threshold

The lowest achievable detection threshold depends on the amount of noise at the trigger filter output. The trigger filter output fluctuation can be calculated similarly to the noise calculation of the trapezoidal filter in section 4.3. The difference is that the filter integral B_{series} (equation 4.29) has to be evaluated for the heartbeat filter instead of the trapezoidal filter. The result is $B_{\text{series}} = \frac{3}{\tau_{\text{window}}}$, so the heartbeat filter is three times more affected by the series noise compared to a trapezoidal filter with the same time constant. Due to the short τ_{window}, the 1/f and parallel noise contributions can be neglected. According to equation 4.28, the equivalent noise charge (ENC) at the trigger filter output is

$$\text{ENC}^2_{\text{heartbeat}} = \underbrace{\frac{3C_a^2 4k_B T a_n}{g_m}}_{\approx 2.96\,\cdot\,10^{-4}\,\text{e}^2\text{s}} \frac{1}{\tau_{\text{window}}}. \tag{A.13}$$

The constant factor is calculated from the default parameters in the noise section 4.3. With $\tau_{\text{window}} = 112\,\text{ns}$, the equivalent noise charge is $\text{ENC}_{\text{heartbeat}} \approx 51\,\text{e}$. Together with the pair creation energy $w = 3.63\,\text{eV}$, this corresponds to fluctuation of the trigger filter output baseline of $\sigma \approx 185\,\text{eV}$. To have a low chance that a random sample causes a noise trigger, the threshold should be set to at least $5\sigma \approx 0.9\,\text{keV}$.

The achievable threshold observed in practice usually differs from this value for two reasons: First, if the rise time of a pulse is similar to the time constant of the trigger filter τ_{window}, the amplitude of the trigger filter output depends on the pulse rise time. This effect causes an increased threshold
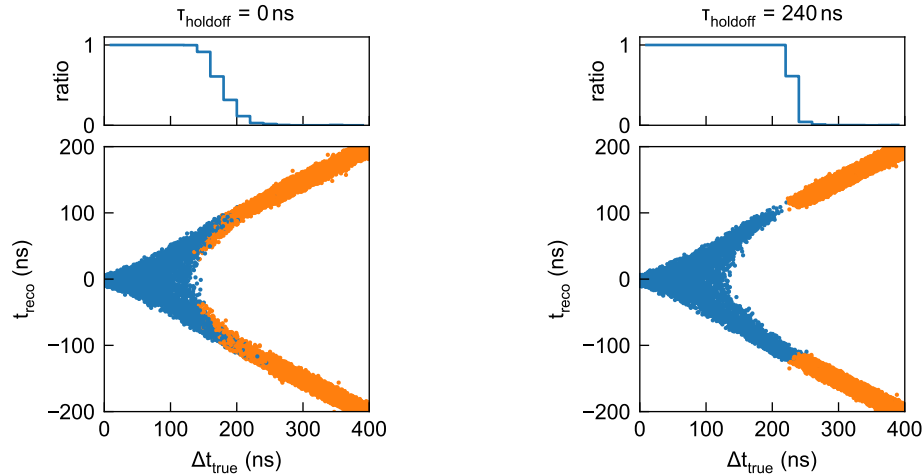
Figure A.6: Simulated relation between reconstructed timestamps t_{reco} and true time difference Δt_{true} of two consecutive pulses. The simulation in the left figure uses no trigger holdoff. The simulation shown on the right uses a trigger holdoff $\tau_{\text{holdoff}} = 240\,\text{ns}$ and ignores any second trigger during this time after the first trigger. Each blue dot corresponds to a simulated signal with a single output trigger. The orange dots indicate that the simulated signal snippet had two output triggers. Two triggers are reconstructed correctly only if the time difference Δt_{true} is large enough Each pulse had a random amplitude between 1.5 keV and 40 keV.

for signals with a large rise time. Second, at high frequencies, the electronic noise is influenced by the limited bandwidth of ETTORE and the anti-aliasing filter. In this case, the noise calculation is not fully accurate.

A trace-level Monte Carlo simulation is performed to study the threshold in a realistic scenario. The simulation generates trigger filter signals for pulses with energies from 0 keV to 4 keV and for two different values of the rise time of the charge pulse in the detector (32 ns and 100 ns). For each signal, the maximum of the trigger filter output is evaluated in a time window of $\pm 1\,\mu s$ around the true position of the pulse. The maximum indicates at which threshold the pulse would cause a trigger. Figure A.7 shows the simulated relation between the maximum of the trigger filter output and the true pulse energy.

It is observed that a pulse with a rise time of 32 ns needs to have at least 0.5 keV of energy to have a 1 % chance of causing a threshold crossing. A 1.5 keV pulse has a 99 % chance to cause a trigger. If the rise time of the pulse is increased to 100 ns, a 2 keV pulse is necessary to have a 99 % chance to cause a trigger. The simulation shows that the energy threshold increases by one-third if the rise time of a signal is 100 ns compared to 32 ns. Such a variation in the rise time is realistic for events close to the pixel border in the TRISTAN SDD, as shown in section 4.1.3. Therefore, the proposed trigger filter settings and a threshold setting of 120 lsb achieve a physical threshold of around 2 keV. This means that an event with an energy of around 2 keV has a probability > 99 % to cause a trigger.
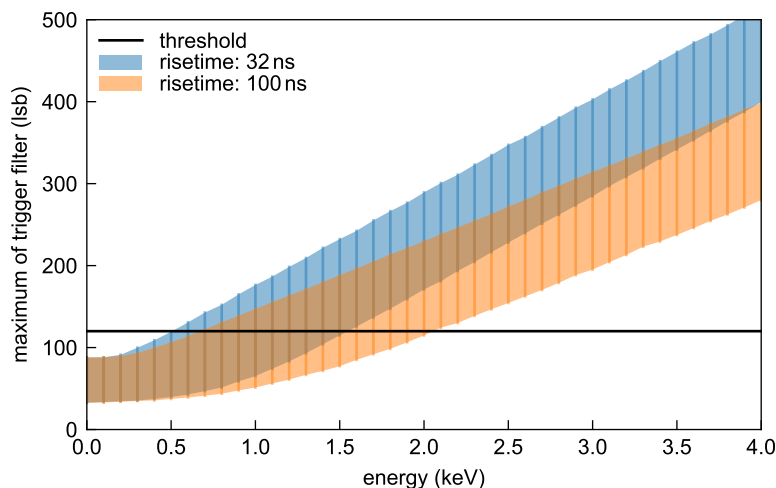
Figure A.7: Monte Carlo simulation of the trigger filter maximum (in a $\pm 1\,\mu s$ window) as a function of the true energy of a pulse. Due to noise on the signal, a distribution of trigger filter maxima is observed for each pulse energy (vertical lines). The plotted band corresponds to the central 98 % interval of observed maxima. Two simulations with different rise times of the anode signals are compared. The black line shows a realistic threshold value. The simulation uses $\tau_{\text{window}} = 112\,\text{ns}$.

A.4.4 Energy filter

For each detected event, the DAQ measures the pulse height, which is a estimate of the event energy. The pulse height is extracted after the signal has passed through a pulse shaping filter (here called energy filter). The primary function of the energy filter is to enhance the signal-to-noise ratio. Furthermore, for high-rate operation, a fast energy filter is essential to limit the amount of pileup events.

The energy filter in TRISTAN converts an ideal detector pulse into a trapezoid with a rise time of τ_{peaking} and a flat top of τ_{gap}, as illustrated in figure A.8. The pulse height is determined by sampling a value at the center of the flat top, with the evaluation time dictated by the trigger timestamp. The flat top of the trapezoidal filter ensures that the pulse height remains independent of the rise time of the detector pulses. Moreover, a flat top is highly advantageous for pileup treatment, as further discussed in section 7.2. In this work, a value of $\tau_{\text{gap}} = 480\,\text{ns}$ is chosen for the flat top, corresponding to twice the trigger holdoff time t_{holdoff}.

The rise time of the trapezoid is a key factor in determining the energy resolution of the detector, as demonstrated by the noise curve calculations in section 4.3.3. The optimal energy resolution for a cooled detector is typically achieved at around $\tau_{\text{peaking}} \approx 10\,\mu s$. For TRISTAN, a shorter rise time is preferable to minimize pileup events at high rates. Therefore, a value of $\tau_{\text{peaking}} = 960\,\text{ns}$ is chosen in this work.

The amount of pileup at high rates depends on the duration of the filter response. An ideal trapezoidal filter has a finite response duration of $2\tau_{\text{peaking}} + \tau_{\text{gap}}$. However, the overall response duration is much longer if the energy filter is applied to the second stage signal of ETTORE. This comes from the infinite AC-filter characteristic with $\tau = 15\,\mu s$ of the second stage of ETTORE.

To counteract the infinite response length of the exponential decaying signals after the second stage of ETTORE, a step called "exponential deconvolution" is applied to the digitized signal before the
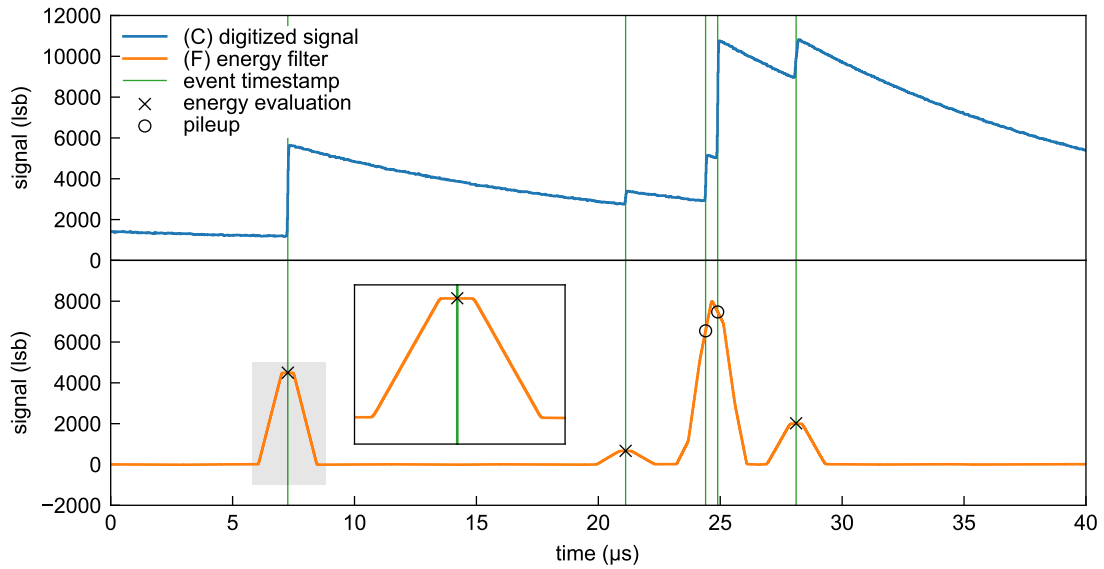
Figure A.8: Simulation of a digitized pulse sequence (top) and the energy filter output (bottom). The signals correspond to labels Ⓒ and Ⓕ in figure 7.2, respectively. The trapezoidal filter parameters are $\tau_{\text{peaking}} = 960\,\text{ns}$ and $\tau_{\text{gap}} = 480\,\text{ns}$. The insert shows a zoom to the energy filter output of one event and illustrates the energy evaluation at the center of the trapezoidal top.
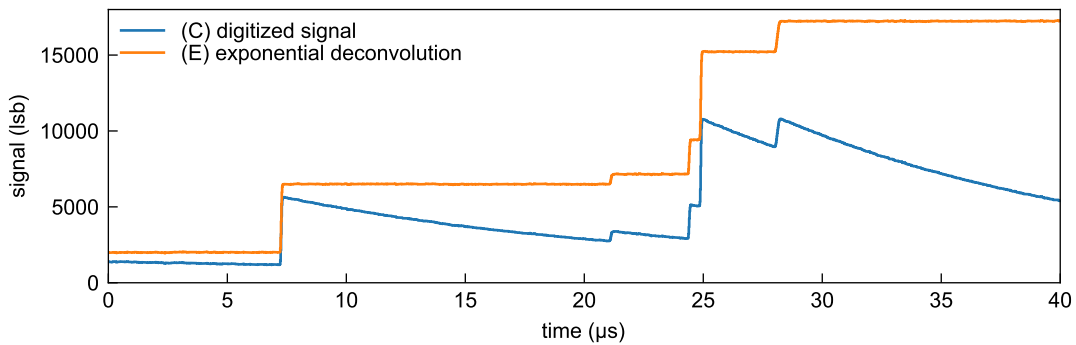
Figure A.9: Simulation of a digitized pulse sequence before (blue) and after the exponential deconvolution (orange). The signals correspond to labels Ⓒ and Ⓔ in figure 7.2, respectively. The exponential deconvolution removes the exponential decay of the pulses.

173

Figure A.10: Illustration of the stored data for one channel in the three readout modes. Saving a waveform snipped in event mode is optional.

energy filter (see sketch of signal chain in figure 7.2). This step digitally restores the step-like first stage signal, as illustrated in figure A.9.

Details about the parameters and implementation of the exponential deconvolution filter are given in the appendix in section A.5.5.

A.4.5 Readout modes

The DAQ system can operate in different readout modes, which define what kind of information is stored. This section gives a possible definition of the readout modes and describes their output data format. The sketch of the DAQ chain in figure 7.2 shows the DAQ in a histogramming mode, where all events are histogramed according to their energy. Three readout modes are distinguished:

- **Waveform mode** In waveform mode, the entire digital waveform of each channel is stored. The data can originate from any of the four digital waveforms (Ⓒ to Ⓕ in figure 7.2). No individual triggering is involved in this mode. Due to the high data rate, this mode can operate only for a short duration $\mathcal{O}(1\,\mathrm{ms})$. This mode is useful for diagnostics.
- **Event mode** The event mode uses an event builder to collect information for each triggered event. The information can include timestamp, energy, channel, flags, and a waveform snippet of the pulse. The waveform snippet will only be included in low-rate diagnostic measurements. The small event memory size of 16 byte is important to prevent data throughput limitations at high rates.
- **Histogram mode** The histogram mode uses the stream of events from the event builder to fill energy histograms. Several histograms can be recorded for each channel, depending on event flags. If ten histograms are recorded per channel, the total number of histograms is $K = 1660$. The proposed number of bins is $L = 2^{16} = 65\,536$, which gives a bin width of $1.7\,\mathrm{eV}$ in low gain mode (compare table A.2).

The structure of the output data in the three modes is shown in figure A.10. Table A.3 estimates the amount of output data for the different cases. The waveform and event modes have extremely high output data rates. Both of these modes, therefore, can only be used for diagnostics. In this case, the parameters acquisition time, number of enabled pixels, or event rate must be reduced to have a manageable amount of output data. For measurements lasting several days or weeks at thigh count rates, as is foreseen for tritium measurements, a manageable amount of output data

Table A.3: Amount of stored data per 166-pixel detector module for the three readout modes. In histogram mode, the amount of data is independent of the measurement time and input rate.

| | waveform mode | event mode | | histogram mode |
| | | w/ wfm | w/o wfm | |
	(MB/s)	(MB/s)	(MB/s)	(MB)
rate 1 kcps/px		420	2.7	
rate 10 kcps/px	21 000	4200	27	440
rate 100 kcps/px		42 000	270	
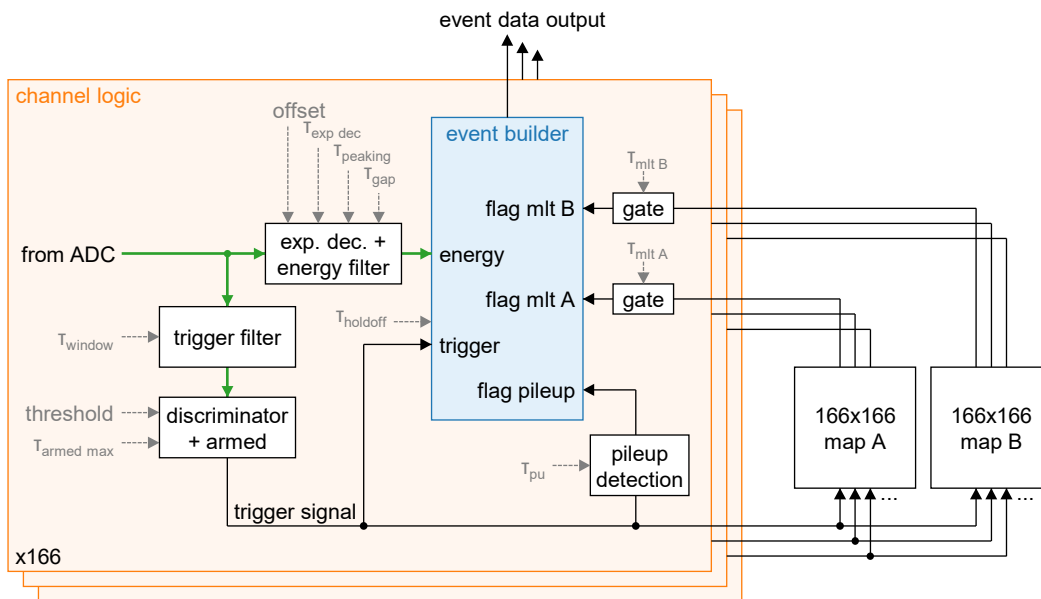
Figure A.11: Sketch of a possible architecture of the event builder. The green paths are digital signal vectors with at least 14 bits. The black lines are single logic signals. Selected configuration parameters are also shown in gray.

is only achieved in histogram mode. In this mode, a single acquisition has a fixed data amount independent of its length. If a histogram is saved every five minutes, the data amount is around 130 GB per day per detector module.

A.4.6 Event builder and histograming

The event builder is an essential part of the DAQ system. It is involved in the event mode and the histogram mode. In histogram mode, the events are not stored but are used to fill histograms. A possible implementation of the event builder is illustrated in figure A.11.

An exciting part of the event builder is the inter-pixel logic. The drawn case contains two 166 × 166 boolean maps. Via these maps, each channel can use the information if there is at least one coincident signal in a defined set of other channels. One configuration could be:

- Map A defines the physical neighbors of each pixel. The flag *mlt A* then contains the information if at least one neighboring pixel had a coincident event, which hints at charge sharing.

175
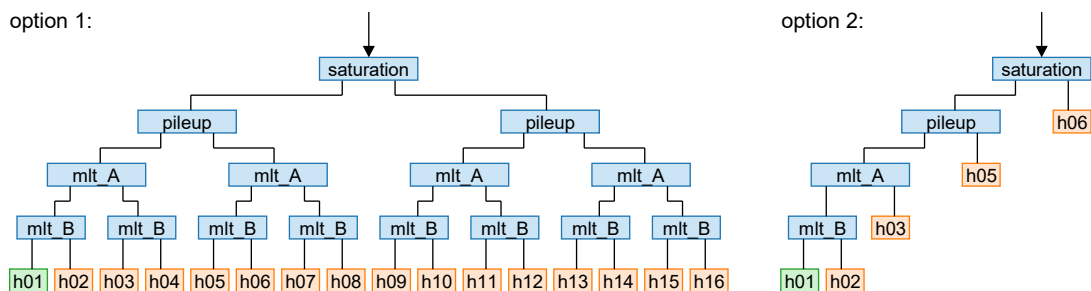
Figure A.12: Decision trees for histograming of events based on their flags. Each flag (blue box) can either be negative (left output line) or positive (right output line). The green box is the "golden" histogram, which contains only events with all negative flags. All other histograms are drawn in orange.

- Map B defines pixels in the same readout group of the detector. The flag *mlt B* then contains the information if at least one pixel in the same readout group had a coincident event, which hints at crosstalk.

The final histogram would then only contain events with neither the *mlt A* nor *mlt B* flag set.

In the drawn case, the inter-pixel logic is limited to the flagging of events. A 166×166 map could, in principle, also be used to distribute the trigger signal itself. This trigger distribution feature is very useful to study effects like crosstalk or charge sharing (as done, for example, in section 6.5). This option is not foreseen in the regular tritium acquisition, and the trigger distribution is not shown in figure A.11.

For simplicity, only three flags are shown in the event builder sketch (figure A.11), which are *mlt A*, *mlt B* and *pileup*. Additionally, a saturation flag, set if the ADC saturates during the trapezoidal filter window, is essential to prevent railing events from ending up in the spectrum. Other flags, like a "baseline" flag or a "time after reset" flag, could also be helpful but are not addressed here.

In histograming mode, the events are used to fill several histograms based on their energy and flags. Two options for a decision tree of which histogram to fill when are shown in figure A.12. Option 1 uses all available flag information and has 2^n histograms for n binary flags. Option 2 is a reduced version, where some information is neglected. The advantage of option 2 is the reduced number of output histograms and, therefore, a reduced amount of output data. In the decision trees in figure A.12, the four flags are sorted by their "importance". A flag with high "importance" indicates that a flagged event is not very useful for any further analysis. The *saturation* flag, for example, is the most "important" flag, as a saturating event should for sure not end up in the final spectrum. The *mlt B* flag, on the other hand, is less "important", as the flagged events could still be used for spectral analysis. In the decision tree of option 2, the order of the flags plays an essential role, as all consecutive flag information is lost after one positive flag. In the decision tree of option 1, the order is unimportant as no information is lost. The two shown decision trees have the beneficial property that each event fills exactly one histogram, which simplifies the histograming implementation.

In general, saving histograms according to the decision tree option 1 is preferred, as no flag information is lost. However, this option can lead to many output histograms. With six flags, already $2^6 = 64$ histograms are required. Therefore, a combination of option 1 and option 2 is a good

compromise, where "important" flags like the saturation rejection are treated as in option 2, and some flags are treated as in option 1.

A.5 Supplementary figures and tables

A.5.1 Circuit diagram of the HV battery box for the electron gun
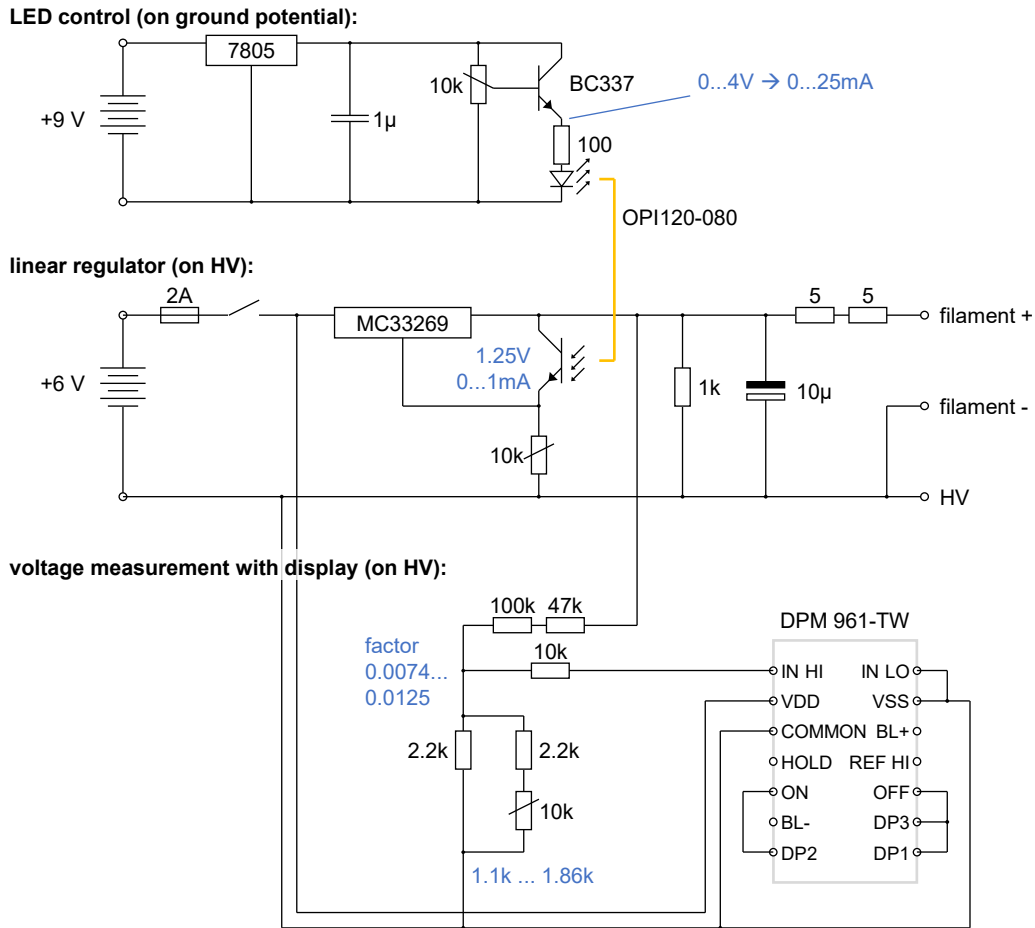
Figure A.13: Circuit diagram of the battery box for biasing the electron gun filament.

A.5.2 166-pixel crosstalk amplitude matrices
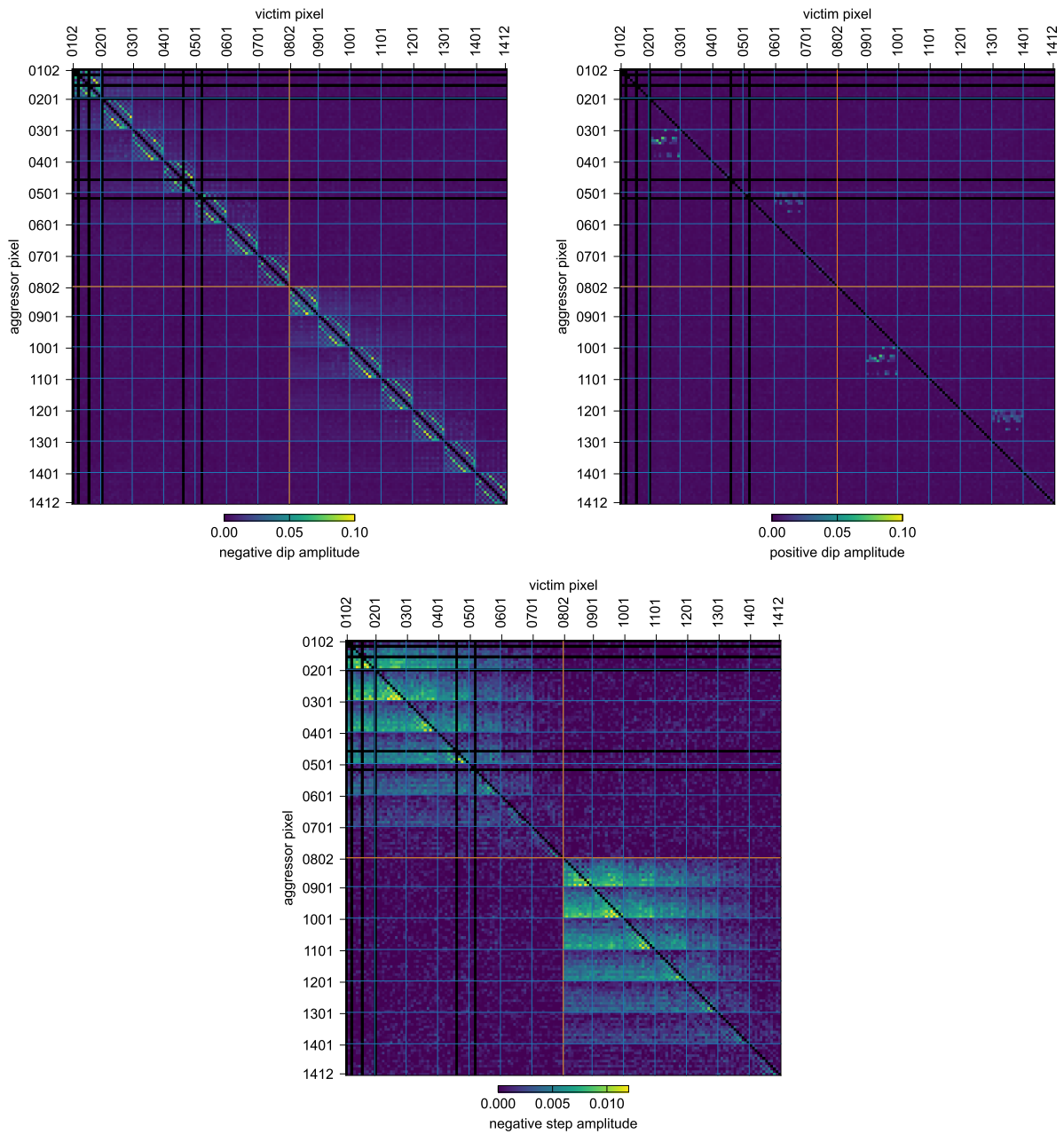
Figure A.14: Crosstalk amplitude matrices of an entire 166-pixel detector module, as described in section 6.3.5. Blue lines mark the readout groups. Orange lines mark the hemispheres. Six pixels were malfunctioning, indicated by the horizontal and vertical black lines. The measurement uses detector S0-166-6 with bias settings given in table A.8. The detector is of production 1b. Therefore, the negative dip crosstalk is slightly increased compared to production 2 in figure 6.33. Furthermore, the statistical noise in the measurement is increased due to the limited amount of data for averaging per matrix element. The characteristic structures of crosstalk and the symmetry of the two hemispheres are visible.

A.5.3 `DAQsim` **default parameters**

Table A.4: Parameters of the DAQ simulation (`DAQsim`) and their default values. The configuration parameters are grouped into functional parts of the simulation. Some parameters which are only used is special investigations are not shown.

General This part defines general settings about the simulation.			
`int seed`	=42		seed for drawing random numbers
`float duration`	=0.2		duration of waveform in one process [s]
`float log_duration`	=0.002		duration where waveforms are saved [s]
`float dt`	=16E-9		sampling period of the ADC [s]
`int dt_factor_analog`	=1		oversampling factor for analog signals
`int n_processes`	=64		number of processes running in parallel
Part 0 draws a list of events with time and amplitude.			
`str spectrum_name`	=`"s001"`		name which defines the spectrum
`float rate`	=100E3		input count rate [cps]
`bool add_fano`	=True		fluctuate amplitudes according to Fano statistics
Part 1 simulates the charge signal from the detector with Gaussian pulses with random width.			
`list risetime_range`	=[32E-9,96E-9]		range of 10 % to 90 % pulse widths [s]
Part 2 adds noise and the effect of ETTORE preamplifier to the waveform, including resets.			
`float c_fb`	=25E-15		feedback capacitance [F]
`float ettore1st_bw`	=7.0E6		bandwisth of ETTORE 1st stage [V]
`float ettore1st_vbsl`	=0.6		baseline voltage of ETTORE 1st stage [V]
`float ettore1st_vth`	=2.6		threshold voltage for level sensitive reset [V]
`float ettore_reset_period`	=inf		reset period of external reset [s]
`float ettore_reset_delay`	=10E-6		delay of level sensitive reset [s]
`float ettore_inhibit`	=20E-6		inhibit duration [s]
`float ettore2nd_tau`	=15E-6		time constant of 2nd stage of ETTORE [s]
`float ettore2nd_gain`	=5		absolute voltage gain of 2nd stage of ETTORE
`float ettore2nd_vbsl`	=2.7		baseline voltage of ETTORE 2nd stage [V]
`int ex_n`	=20		exponent for fft in noise calculation ($2^{\text{ex-n}}$ samples)
`bool reuse`	=True		reuse noise waveforms of $2^{\text{ex-n}}$ samples
`float noiseconfig.gm`	=150E-6		JFET transconductance [A/V]
`float noiseconfig.I`	=1E-12		leakage current [A]
`float noiseconfig.C`	=220E-15		anode capacitance [A/V]
`float noiseconfig.T`	=250		temperature [K]
`float noiseconfig.A`	=5E-11		1/f factor [V^2]
`list noiseconfig.parts`	=[`"N1"`,`"N2"`,`"N3"`]		include parallel (`"N1"`), pink (`"N2"`), or series (`"N3"`) noise
Part 3 applies the antialiasing filter and simulates the ADC.			
`float aa_bw`	=12.9E6		−3 db bandwidth of the antialiasing filter [Hz]
`list adc_range`	=[1.0,3.0]		input voltage range of the ADC [V]
`int nbit`	=14		number of bits of the ADC
Part 4 simulates the trigger logic.			
`float tf_window`	=112.0E-9		window length of heartbeat trigger filter [s]
`int threshold`	=70		threshold for triggering [lsb]
`float max_armed_buffer`	=100E-9		maximal time the trigger stays armed [s]
`float holdoff_buffer`	=240E-9		minimal time between two consecutive triggers [s]
`float pileup_reject_buffer`	=1376E-9		window to flag two consecutive triggers as pileup [s]

continued on next page

`int saturation_threshold`	=16374	threshold to flag ADC input as saturating [lsb]

Part 5 simulates the energy filter.

`int ed_offset`	=2458	offset parameter for exp. deconvolution [lsb]
`float ed_tau`	=15E-6	decay constant for exp. deconvolution [s]
`float ef_peaking`	=960E-9	peaking time of trapezoidal energy filter [s]
`float ef_gap`	=480E-9	gap time of trapezoidal energy filter [s]

Part 6 histograms the events.

`list hist_xspace`	=[-1024,16383,0.25]	left border, right border and binsize [lsb]
`bool keep_lm`	=False	save all reconstructed event data

A.5.4 Block diagram for digital filtering
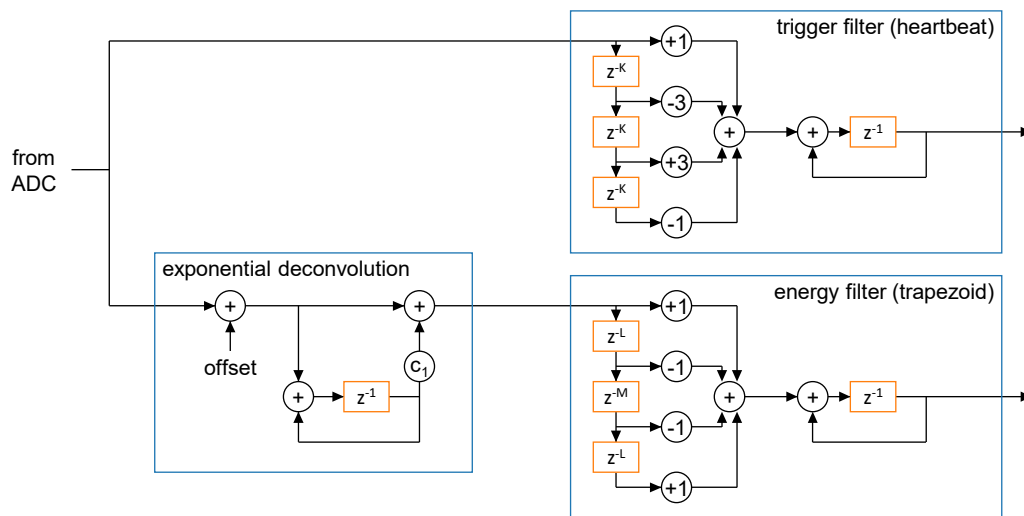
Figure A.15: Block diagram of a possible digital filtering implementation in the TRISTAN DAQ. The diagram uses the z-domain notation, where a multiplication with z^{-n} delays the digital signal by n samples. K corresponds to the trigger filter window τ_{window}, L corresponds to the trapezoidal filter peaking time τ_{peaking}, and M corresponds to the trapezoidal filter gap time τ_{gap}.

A.5.5 Exponential deconvolution filter calculation

The exponential deconvolution can be implemented as a first-order Infinite Impulse Response (IIR) filter, as shown in figure A.15. For the exponential deconvolution, the transfer function of the second stage of ETTORE in frequency domain

$$H_{\text{second stage}}(\omega) = \frac{i\omega\tau}{i\omega\tau + 1} \tag{A.14}$$

with $\tau \approx 15\,\mu\text{s}$ needs to be compensated by the transfer function of the exponential deconvolution. The z-domain transfer function of the exponential deconvolution IIR filter is

$$H(z) = \frac{1 - (1 - c_1)z^{-1}}{1 - z^{-1}} \,. \tag{A.15}$$

The frequency domain transfer function is obtained by setting $z = \exp(i\omega T_s)$, where T_s is the sampling frequency of the digital system. Additionally, the approximation $\exp(i\omega T_s) \approx 1 - i\omega T_s$ is applied, which is valid for frequencies $f = \frac{\omega}{2\pi}$ well below the sampling frequency. This yields

$$H_{\text{exp. dec.}}(\omega) \approx \frac{i\omega \frac{T_s}{c_1} + 1}{i\omega \frac{T_s}{c_1}}\,. \tag{A.16}$$

By comparing equation A.16 and A.15, the parameter c_1 of the exponential deconvolution must be set to

$$c_1 = \frac{T_s}{\tau}\,, \tag{A.17}$$

such that the total response $H_{\text{tot}}(\omega)$ is unity

$$H_{\text{tot}}(\omega) = H_{\text{second stage}}(\omega) \cdot H_{\text{exp. dec.}}(\omega) = 1\,. \tag{A.18}$$

A.5.6 Heartbeat filter response
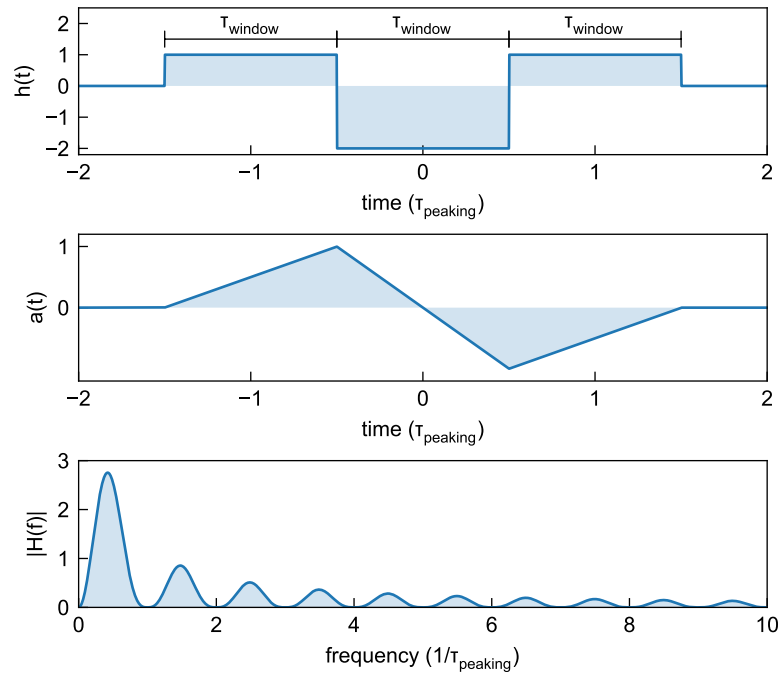
Figure A.16: Impulse response $h(t)$, step response $a(t)$ and transfer function $|H(f)|$ of heartbeat trigger filter. The filter is normalized such that the step response has amplitude 1.

A.5.7 Pileup spectrum fits
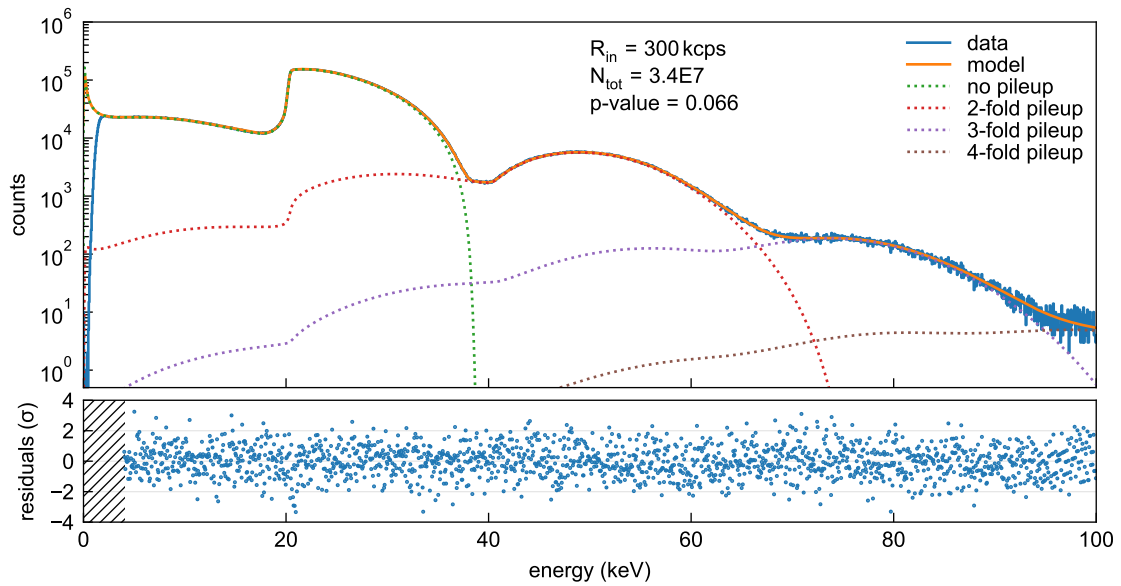
Figure A.17: Fit of the pileup model (equation 7.8) to the simulated DAQ output spectrum of tritium with an input rate $R_{in} = 300\,$kcps. The fit parameters are used in section 7.3.2. The `DAQsim` settings are found in table 7.3 and table A.4.
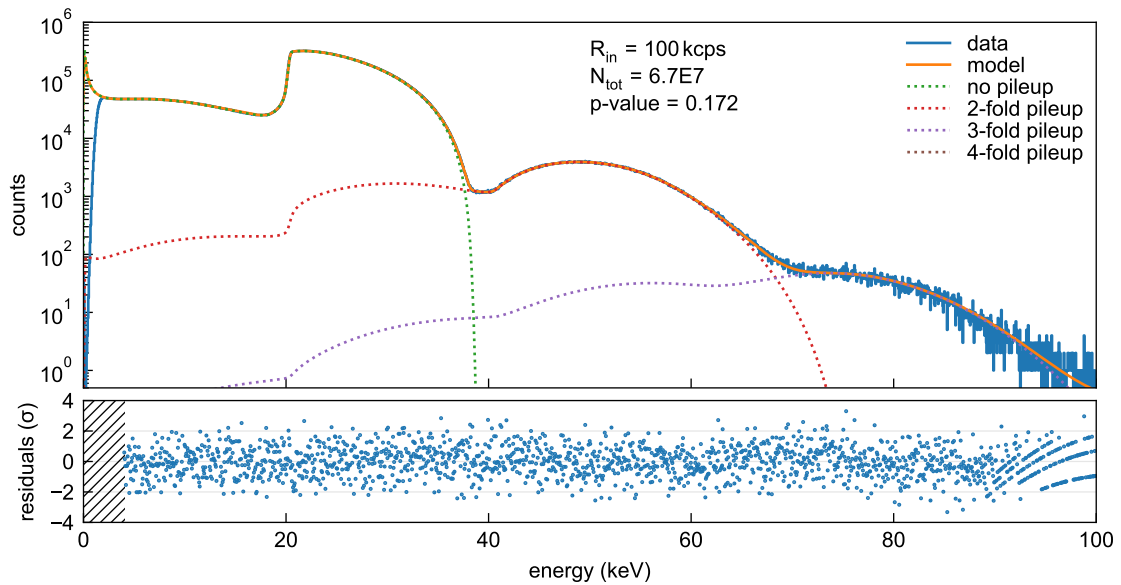
Figure A.18: Fit of the pileup model (equation 7.8) to the simulated DAQ output spectrum of tritium with an input rate $R_{in} = 100\,$kcps. The fit parameters are used in section 7.3.2. The `DAQsim` settings are found in table 7.3 and table A.4.
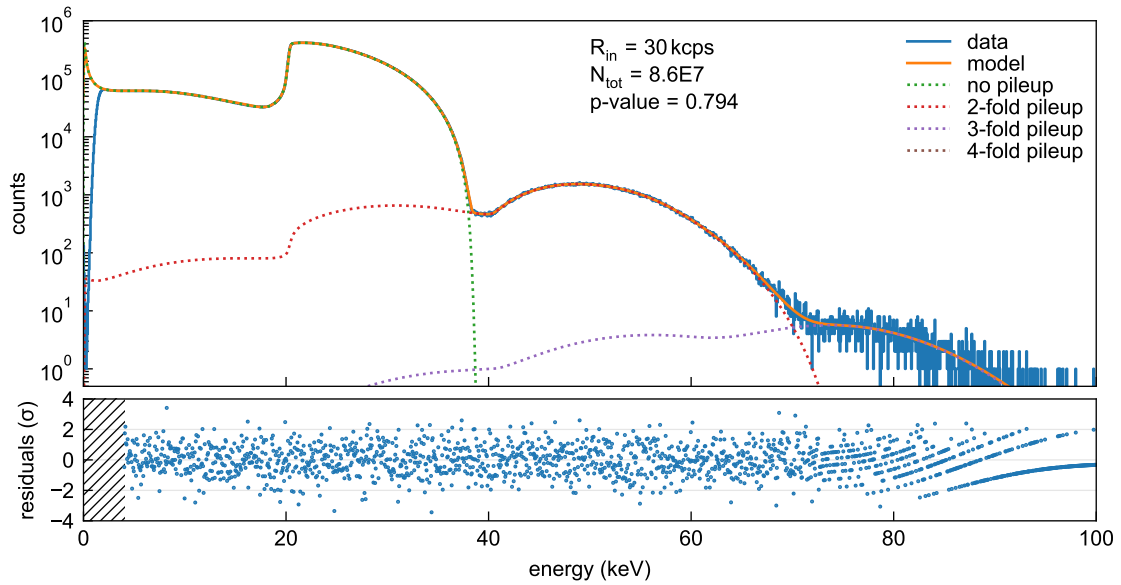
Figure A.19: Fit of the pileup model (equation 7.8) to the simulated DAQ output spectrum of tritium with an input rate $R_{in} = 30$ kcps. The fit parameters are used in section 7.3.2. The `DAQsim` settings are found in table 7.3 and table A.4.
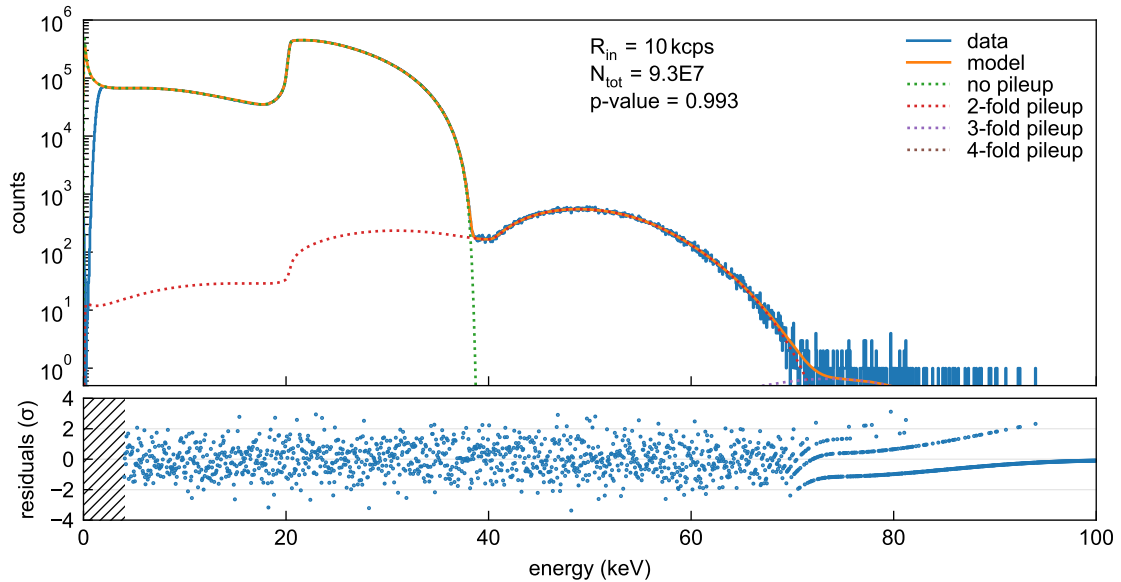
Figure A.20: Fit of the pileup model (equation 7.8) to the simulated DAQ output spectrum of tritium with an input rate $R_{in} = 10$ kcps. The fit parameters are used in section 7.3.2. The `DAQsim` settings are found in table 7.3 and table A.4.

A.5.8 Input spectra for DAQ simulations
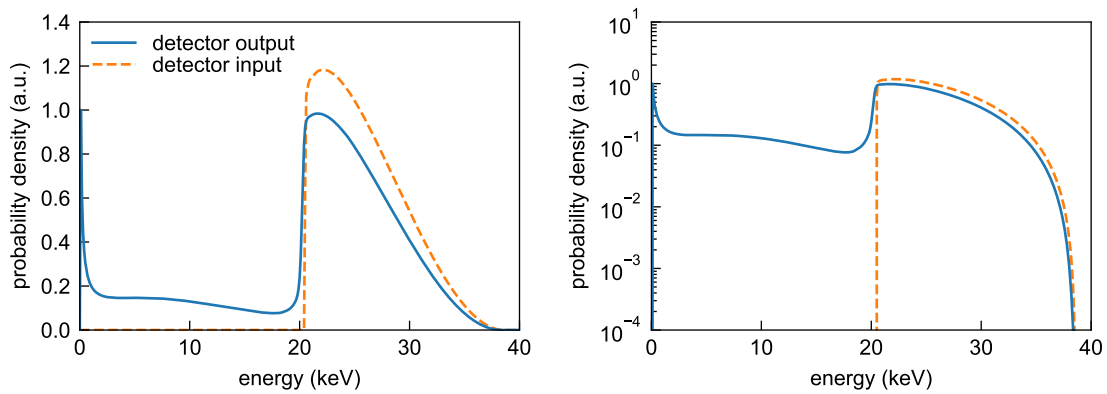
Figure A.21: Input spectrum for DAQ simulations in linear scale (left) and logarithmic scale (right). The spectrum is calculated with TRmodel (https://nuserv.uni-muenster.de:8443/katrin-git/tristan/trmodel, commit bd210bd7f2dfc3e0610ab3571c8da5813e315ae). The beamline configuration from "scenario 2: Optimized" in file lib/scenarios.py is used. The "detector input" shows the tritium spectrum shifted by 20 keV by the post acceleration. The "detector output" shows the spectrum after applying detector effects like backscattering, Fano resolution and charge sharing. The average of the spectrum is at 21.4 keV.

A.5.9 Detector bias setting tables

Table A.6: Detector biasing settings of 7-pixel detectors at room temperature.

detector	**S0-1** (prototype 0) elog 60	**S0-7-4**, production 1, elog 225
		S0-7-5, production 1a, elog 225
		S0-7-6, production 1b, elog 225
		S0-7-7, production 1c, elog 225
		S0-7-9, production 2, elog 344
d pixel	2 mm	3 mm
readout	CUBE	JFET + ETTORE
V_{BC}	−86.0 V	−100.0 V
V_{BF}	−98.0 V	−110.0 V
V_{IG}	-	−19.0 V
V_{R1}	−20.0 V	−9.0 V
V_{RX}	−110.0 V	−120.0 V
V_{SSS}	-	−6.8 V
V_D	-	6.6 V
V_{RESH}	-	4.0 V
V_{RESL}	-	−10 V
I_D	-	2.2 mA
$I_{D\ channel}$	-	314 μA

Table A.7: Detector biasing settings for the general detector characterization.

parameter	value	parameter	value
detector	**S0-166-6**, Kiriko, elog 316		
temperature	−34 °C	V_{SSS}	−3.8 V
V_{BC}	−100.0 V	V_D	−6.9 V
V_{BF}	−110.0 V	V_{RESH}	4.0 V
V_{IG}	−22.0 V	V_{RESL}	−10.0 V
V_{R1}	−10.0 V	I_D	32.2 mA
V_{RX}	−120.0 V	$I_{D\ channel}$	194 µA
detector	**S0-166-7**, Reinhardt, elog 318, warm		
temperature	27 °C	V_{SSS}	−3.8 V
V_{BC}	−100.2 V	V_D	−6.9 V
V_{BF}	−110.0 V	V_{RESH}	3.9 V
V_{IG}	−21.9 V	V_{RESL}	−10.0 V
V_{R1}	−9.5 V	I_D	31.6 mA
V_{RX}	−120.4 V	$I_{D\ channel}$	190 µA
detector	**S0-166-7**, Reinhardt, elog 318, cold		
temperature	−34 °C	V_{SSS}	−3.9 V
V_{BC}	−105.0 V	V_D	−6.9 V
V_{BF}	−115.0 V	V_{RESH}	3.9 V
V_{IG}	−21.9 V	V_{RESL}	−10.0 V
V_{R1}	−10.3 V	I_D	33.0 mA
V_{RX}	−120.0 V	$I_{D\ channel}$	199 µA

Table A.8: Detector biasing settings for measurements of charge sharing.

detector	**S0-166-6**, Kiriko, production 2		
documentation	charge sharing: elog 313, crosstalk: elog 313		
temperature	−34 °C	V_{SSS}	−3.8 V
V_{BC}	−100.0 V	V_D	−6.9 V
V_{BF}	−110.0 V	V_{RESH}	4.0 V
V_{IG}	−25.0 V	V_{RESL}	−10.0 V
V_{R1}	−10.2 V	I_D	32.2 mA
V_{RX}	−120.0 V	$I_{D\ channel}$	194 µA
detector	**S0-166-11**, Junker Queen, production 2		
documentation	charge sharing: elog 333, crosstalk: elog 327		
temperature	−34 °C	V_{SSS}	−3.8 V
V_{BC}	−100.0 V	V_D	−6.9 V
V_{BF}	−110.0 V	V_{RESH}	4.0 V
V_{IG}	−22.1 V	V_{RESL}	−10.0 V
V_{R1}	−10.5 V	I_D	32.0 mA
V_{RX}	−120.0 V	$I_{D\ channel}$	193 µA

Table A.9: Detector biasing settings for measurements at the KATRIN monitor spectrometer.

parameter	value	parameter	value
detector	**S0-166-4**, Winston, production 1b		
documentation	elog 295		
temperature	$-28\,°\mathrm{C}$	V_{SSS}	$-3.9\,\mathrm{V}$
V_{BC}	$-115.0\,\mathrm{V}$	V_{D}	$-7.0\,\mathrm{V}$
V_{BF}	$-125.0\,\mathrm{V}$	V_{RESH}	$4.0\,\mathrm{V}$
V_{IG}	$-20.3\,\mathrm{V}$	V_{RESL}	$-10.0\,\mathrm{V}$
V_{R1}	$-9.7\,\mathrm{V}$	I_{D}	$32.0\,\mathrm{mA}$
V_{RX}	$-120.0\,\mathrm{V}$	$I_{\mathrm{D\ channel}}$	$193\,\mathrm{\mu A}$

A.5.10 Second stage waveforms plots
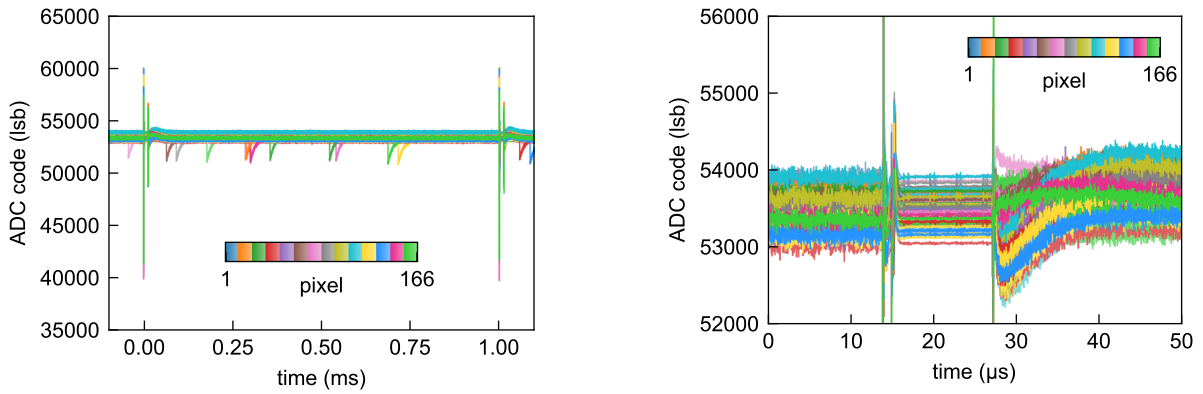
Figure A.22: Long waveform acquisition of second stage signals of all channel with ^{55}Fe events at a low rate. The reset period is $1\,\mu s$. The right plot shows a zoom-in around a reset, where a $10\,\mu s$ inhibit, used in this acquisition, is visible.
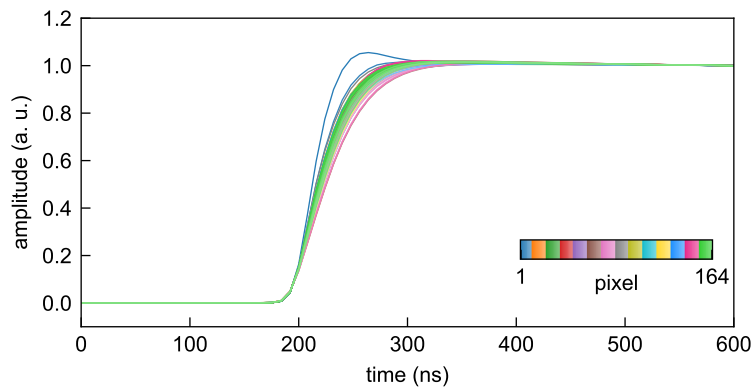
Figure A.23: Average pulse shape of $\mathcal{O}(3000)$ $25\,keV$ electron events. All 164 pulse shapes of one detector module are superimposed. A variation in the rise time, as described in section 6.2.2 is observed.

Acronyms

ADC	Analog-to-Digital Converter
ASIC	Application-Specific Integrated Circuit
CL	Confidence Level (in the context of a frequentist analysis approach)
cps	Counts Per Second
CSA	Charge Sensitive Amplifier
DAQ	Data Acquisition System
ENC	Equivalent Noise Charge
FHWM	Full Width at Half Maximum
FIR	Finite Input Response
FPD	Focal Plane Detector of the KATRIN experiment
FPGA	Field Programmable Gate Array
FSR	Full-Scale Range
IIR	Infinite Input Response
JFET	Junction Field-Effect Transistor
lsb	Least Significant Bit
MAC-E	Magnetic Adiabatic Collimation combined with an Electrostatic filter
MC	Monte Carlo (a simulation technique based on random numbers)
PCB	Printed Circuit Board
PHA	Pulse-Height Analyzer
PIN-diode	Diode with layers (Positive, Intrinsic, Negative)
PMNS	Pontecorvo-Maki-Nakagawa-Sakata matrix
RMS	Root Mean Square
ROI	Region Of Interest
SDD	Silicon Drift Detector
SM	Standard Model of particle physics

SDD connection lines

BC	back contact (on entrance window side)
BF	back frame (on entrance window side)
DR	JFET drain
FB	feedback
IG	inner guard ring
R1	innermost drift ring
RD	reset diode
RX	outermost drift ring
SC	JFET source

List of Figures

List of Tables

Acknowledgements

I would like to take this moment to sincerely thank everyone who has supported me throughout my PhD journey. Without your encouragement and assistance this thesis would not have been possible.

- My deepest gratitude goes to **Prof. Susanne Mertens**, for offering me the opportunity to work on this fascinating project and motivating me to pursue a PhD on the TRISTAN detector. I really appreciate your great supervision and support during the last few years. I also want to thank you for supporting various trips to conferences, workshops, and meetings.
- I am grateful to **Prof. Marco Carminati** and **Prof. Carlo Fiorini** for their assistance with all questions on the TRISTAN readout electronics and for hosting many fruitful meetings in Milan.
- Special thanks to **Dr. Peter Lechner** from HLL for sharing his expertise on SDDs and for his great efforts in optimizing the TRISTAN detector.
- I also want to thank **David Fink** from MPP for his friendly support with all electronics-related matters and many more general discussions.
- I thank **Dr. Sascha Wüstling** from IPE, especially for his advices in electronics debugging and many fruitful discussions in the DAQ call.
- My thanks to the TRISTAN group in Munich, especially **Dr. Thibaut Houdy**, **Dr. Anthony Onillon**, **Dr. Frank Edzards**, **Dr. Tim Brunst**, **Dr. Daniel Siegmann**, **Daniela Spreng**, **Christian Forstner**, and **Andrew Gavin**. Working together on both successes and hardware problems has been a rewarding experience.
- I am also grateful to the broader TRISTAN groups in Karlsruhe and Milan, including **Dr. Martin Descher**, **Andrea Nava**, **Dr. Dominic Hinz**, **Dr. Markus Steidl**, **Matthias Balzer**, **Denis Tcherniakhovski**, **Dr. Matteo Biassoni**, **Dr. Pietro King**, and **Dr. Matteo Guggiatti**. The numerous meetings and discussions were instrumental in shaping this work. Furthermore, the friendly, optimistic, and motivating atmosphere in the group was great.
- A special thank you to my office mates **Christoph Köhler**, **Matthias Meier**, **Florian Henkes**, and **Daniel Siegmann**, for having so much fun in the loveliest office of the physics department.
- I thank all members of E47 for the joyful time, especially during lunch breaks, coffee breaks, movie nights, Weißwurst-breakfasts, Ringberg Trips, etc.
- Last but not least, my biggest thanks goes to **my family** and **my friends**, and especially to **Babsi**, for their never-ending support and patience during my work on this thesis.